Ingestion of micro- and nanoplastic perturbs tissue homeostasis and macrophage core functions

Dissertation

zur

Erlangung des Doktorgrades (Dr. rer. nat.)

der

Mathematisch-Naturwissenschaftlichen Fakultät

der

Rheinischen Friedrich-Wilhelms-Universität Bonn

vorgelegt von

Nikola Makdissi

aus Homs, Syria

Bonn, März 2025

Angefertigt mit Genehmigung der Mathematisch-Naturwissenschaftlichen Fakultät

der Rheinischen Friedrich-Wilhelms-Universität Bonn

Gutachterin/Betreuerin: Prof. Dr. Elvira Mass

Gutachterin: Prof. Dr. Dagmar Wachten

Tag der Promotion: 01.09.2025

Erscheinungsjahr: 2025

Table of Contents

Declaration

The work presented in this thesis was conducted at The Rheinische Friedrich-Wilhelms-Universit.t Bonn in the laboratories of Prof. Elvira Mass (Life & Medical Sciences Institute in Bonn, Germany)

I hereby declare that:

(i) This thesis comprises only my original work towards the degree of Doctor of Philosophy (PhD), except where otherwise stated in the contributions

(ii) Proper acknowledgment has been given in the text to all other sources and materials used

Bonn, 10th of March, 2025

Nikola Makdissi

Summary

Plastic pollution has emerged as a global environmental crisis of unprecedented scale. Micro- and nanoplastic (MNP) pervade ecosystems, resulting in persistent exposure for all living organisms, including humans. MNP have been detected in human blood. Additionally, animal studies indicate MNP ability to cross biological barriers and accumulate in organs such as the liver, spleen, and brain. Nevertheless, the impact of plastic accumulation on tissue homeostasis and immune cell function remains poorly understood. This study investigates the consequences of chronic polystyrene particle ingestion using a mouse model.

Following oral ingestion, MNP breach tissue barriers and accumulate in multiple organs. Hepatic and splenic macrophages are pivotal in the uptake and retention of MNP, leading to their long-term persistence in these tissues. This prolonged presence disrupts metabolic homeostasis in the liver and adipose tissues without inducing systemic inflammation. Moreover, MNP ingestion exacerbates metabolic dysregulation under additional stress, such as a high-fat diet, worsening glucose intolerance.

On a cellular level, MNP accumulation in Kupffer cells, the liver-resident macrophages, impairs their phagocytic function, reducing their ability to clear circulating bacteria. Additionally, MNP-exposed mice exhibit signs of an autoimmune phenotype.

Altogether, our results demonstrate the hazardous nature of MNP ingestion on tissue homeostasis, metabolism, and macrophage functionality. These findings suggest that chronic exposure to plastic particles could contribute to the rising prevalence of environmentally linked metabolic and autoimmune diseases.

1 Introduction

1.1 Micro- and nanoplastic: environmental spread and consequences for human health

The year 1907 marked the invention of Bakelite, the first synthetic plastic, by Leo Baekeland, which is widely recognized as the beginning of the era of modern plastics (1). Since then, plastic has become an indispensable part of modern life, with global production exceeding 360 million tons in 2020 (2). Due to its stability and flexibility, plastic is now used in nearly every aspect of human life. However, the poor management of plastic waste has created a significant environmental problem. Current estimates indicate that approximately 5 billion tons of plastic waste exist globally, with projections suggesting this figure could rise to 12 billion tons by 2050 (3).

This excessive accumulation of plastic waste circulates around the globe in a variety of sizes, types, shapes, and modifications (3). Based on size, environmental plastic is categorized into: macroplastic (>25 mm), mesoplastic (5-20 mm), microplastic (1 µm-5 mm) and nanoplastic (1-1000 nm) (4). However, for nanoscale particles, some reports define 100 nm as the upper limit for nanoparticles (5–7). In this thesis, particles ≤ 100 nm will be referred to as nanoplastic, while those > 100 nm will be classified as microplastics.

In the environment, plastics are subjected to mechanical, photochemical, and microbial processes, breaking them down into smaller particles, reaching the micro- and nanoscale (8,9). Additionally, plastics are directly manufactured at these small sizes for use in cosmetics and medicine (10,11). Consequently, micro- and nanoplastic (MNP) have been detected in environmental samples, murine models, and human food and drinking water (3,8,12–15). For instance, the most abundant plastic polymers in drinking water are ranked as follows: polyethylene (PE), followed by polypropylene (PP), polystyrene (PS), polyvinyl chloride (PVC), and polyethylene terephthalate (PET) (14).

Through contamination of the food chain, humans are exposed to MNP on a daily basis, even from unexpected sources such as beer and sea salt (16,17). Globally, it is estimated that individuals ingest between 39,000 and 52,000 plastic particles annually via food consumption (18). Furthermore, a 2020 Australian study estimated that humans may consume 0.1–5 grams of microplastics weekly (19). Upon ingestion, plastic particles can surpass human protective barriers and have been detected in the blood (20), liver (21), lungs (22), breast milk (23) and even the placenta (24). However, determining the exact amount of plastic ingested and its accumulation within the human body remains challenging due to technical difficulties associated with detecting MNP in human tissues. These challenges stem from limitations in current analytical methods and the potential for sample contamination during analysis (25).

The presence of plastic particles in human tissues raises concerns about their potential health effects, particularly their implications for physiological systems. In recent years, numerous studies have explored the effects of MNP ingestion on physiological systems. These studies have consistently demonstrated the potential harmful impacts of MNP exposure, including disruptions of metabolic and immune systems, as well as adverse effects on reproduction and neurobehavioral health.

MNP ingestion has been widely linked to hepatotoxicity and metabolic dysregulation. Huang et al. demonstrated that long-term exposure to MNP induces hepatotoxicity, characterized by liver injury and dysregulation of lipid metabolism (26). Consistent findings across multiple studies have reported disruptions in lipid homeostasis, highlighting a reproducible phenotype of metabolic imbalance (27–29). Moreover, Luo et al. provided evidence of intergenerational transmission of metabolic disturbances following maternal exposure to microplastics (30). The authors observed hepatic lipid accumulation in the first generation, particularly in adult female offspring, indicating an elevated risk of metabolic disorders. However, it is important to note that these studies were conducted using either relatively high concentrations of plastic particles or shorter exposure durations, which may not fully capture the effects of chronic low-dose exposure observed in environmental or dietary settings.

Beyond the liver, recent studies have highlighted the impact of microplastic ingestion on white adipose tissue. Moon et al. demonstrated that microplastics can induce cellular senescence and inflammation, disrupting the normal formation of fat cells (31). Consistently, numerous studies have shown that exposure to MNP accelerate cellular aging processes though the production of reactive oxygen species (ROS), which can trigger cellular senescence (32).

These disturbances are not confined to metabolic organs but also affect other systems, including the central nervous system. MNP ingestion has been shown to affect the central nervous system, leading to behavioral changes. Several studies have reported anxiety-like behaviors following plastic ingestion, along with impairments in learning ability and memory formation (33,34).

In addition to metabolic and neurological impacts, MNP exposure has been linked to significant impairments in the innate immune system. Huang et al. showed that the accumulation of microplastic disrupted the extracellular matrix, impairing immune signaling (35). Notably, mice exposed to microplastic exhibited diminished immune cell activation upon lipopolysaccharide challenge (35). Additionally, the uptake of microplastics by macrophages impaired efferocytosis *in vitro* (36), the process by which macrophages clear apoptotic cells (ACs) (37). These findings suggest that microplastic exposure may compromise immune homeostasis and contribute to the development of chronic inflammatory conditions.

These diverse physiological and behavioral disruptions are thought to stem from the ability of MNP to interact directly with cell membranes, leading to structural damage and increased

permeability (38,39). Such disruptions may undermine the integrity of vital barriers, such as the intestinal and blood-brain barriers, potentially impairing their protective functions. Additionally, MNP have been shown to induce reactive oxygen species (ROS) production (40), resulting in oxidative stress, DNA damage, and interference with normal cellular functions (41). This oxidative stress serves as a key trigger for apoptosis, which has been observed in various cell types and tissues, including the ovaries (42), heart (43) and neuronal cells (44) following MNP exposure.

1.2 **Macrophage ontogeny**

The first description of macrophages was provided by Elie Metschnikoff in the late 19th century, based on his observations in starfish (45,46). He named the cells he identified "phagocytes," derived from the Greek words *phagein* (to eat) and *kytos* (cell). These specialized eaters are found across vertebrate and invertebrate species (47), where their functions have evolved significantly among species. For instance, amoebocytes, present in *Cnidaria* and *Porifera*, and coelomocytes, found in *Caenorhabditis elegans*, are macrophage-like cells that rely on phagocytosis primarily for nutrient digestion. In contrast, plasmatocytes, the predominant immune cells in *Drosophila melanogaster*, are specialized solely for immune defense, performing critical roles in antimicrobial signaling and wound healing (47). In vertebrates, however, macrophages have evolved to exhibit more advanced and specialized functions, often tailored to specific tissue environments. These roles enable macrophages to meet the specific demands of tissues in both mice and humans (48,49).

In terms of ontogeny, macrophages were traditionally believed to be derived from bone marrow, with hematopoietic stem cells (HSCs)-derived monocytes giving rise to tissue-resident macrophages (50). While this model remains valid for certain tissue-resident macrophages (51–54), genetic fate mapping techniques have revealed a distinct origin for the majority of these cells.

The new model of hematopoiesis has been characterized extensively in mice, and it occurs in three distinct waves each contributing to the development of blood and immune cells (**Figure 1**). The first wave, known as primitive hematopoiesis, begins at embryonic day 7.5 (E 7.5) in the yolk sac. During this phase, primitive erythroid progenitors originate in the yolk sac and give rise to primitive erythroblasts, which enter the embryo to initiate circulation (55–57).

The second wave, transient hematopoiesis, occurs between E 8.5 and E 10.5, also originating in the yolk sac. During this phase, erythro-myeloid progenitors (EMPs) expand and migrate to the fetal liver. EMPs give rise to pre-macrophages (pMacs), which begin migrating to the embryo at E 9.5. These pMacs colonize tissue niches in a Cx3cr1-dependent manner, differentiating into fetal macrophages (58–61), that give rise to macrophages that can and sustain their populations independently throughout life, such as microglia in the brain, Kupffer

cells (KCs) in the liver, red pulp macrophages (RPMs) in the spleen and alveolar macrophages (AMs) in the lung (62–67). In addition to macrophages, EMPs have the potential to produce a variety of cell types, including monocytes, granulocytes, megakaryocytes, mast cells, erythrocytes, and natural killer cells (56,68–70). Although fetal monocytes derived from EMPs are suggested to contribute to the tissue-resident macrophage pool, genetic tools capable of distinguishing monocytes from different hematopoietic waves remain unavailable (71–73).

The third wave, definitive hematopoiesis, begins at E 10.5 with the emergence of HSCs from the hemogenic endothelium within the aorta-gonad-mesonephros (AGM) region. Subsequently, HSCs migrate to the fetal liver, where they expand and differentiate (74,75). By E 17.5, HSCs migrate to the forming bone marrow cavity, which becomes the lifelong primary site of hematopoiesis (56,76).

At birth, all tissues harbor fetal-derived macrophages; however, macrophages originating from HSCs gradually populate various tissues postnatally. Specifically, HSC-derived monocytes differentiate into macrophages and acquire tissue-specific signatures influenced by their local niches, making circulating monocytes the predominant source of macrophages in certain tissues, such as the intestine (51), heart (52), and pancreas (52,53). In contrast, many organs maintain a mixed population of macrophages derived from both fetal progenitors and HSCs under steady-state conditions. This dual population has been described in the peritoneal cavity (77), lung (78), adipose tissue (79), and liver (80), where fetal-derived and HSC-derived macrophages coexist, exhibiting distinct phenotypes and functions. Of note, under specific conditions such as inflammation, monocytes are actively recruited to tissues, differentiating into HSC-derived macrophages. These inflammation-induced macrophages play a critical role in establishing and regulating the local inflammatory response, as well as in promoting its resolution (81).

Macrophage ontogeny is highly conserved among mammals, birds, and fish, with successive waves of hematopoiesis generating macrophages during embryonic development (82). Human hematopoiesis seems to follows a similar "wave" model. Definitive erythroid progenitors and bipotential granulocyte/macrophage progenitors originate in the yolk sac and subsequently localize to the liver (83–85). Human HSCs first emerge in AGM region and later populate the yolk sac and liver (84). While genetic fate-mapping tools are limited in humans, single-cell RNA sequencing of human embryos has provided evidence suggesting that human macrophages are also predominantly embryonically derived (86).

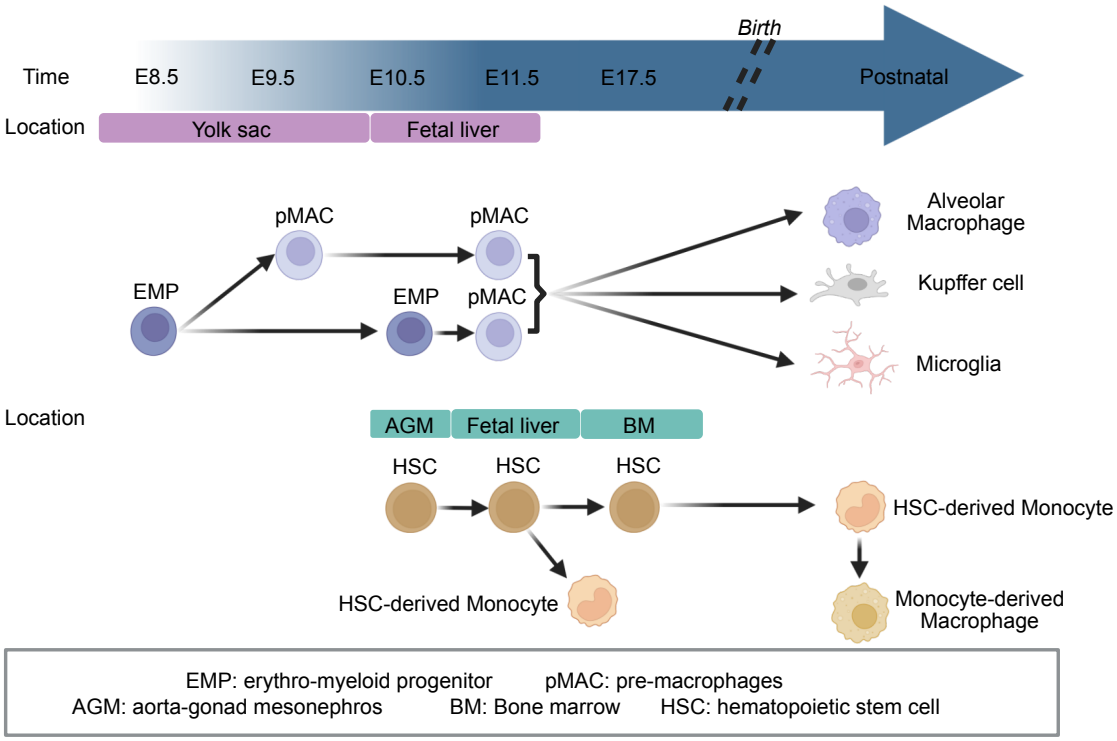

Figure 1 Macrophage ontogeny: erythro-myeloid progenitors (EMPs) arise and expand in the YS (between E8.5 and E10.5), and give rise to Pre-macrophages (pMacs). Both EMPs and pMacs then migrate to and seed the fetal liver, further pMacs colonizes the different peripheral tissue and give rise to tissue-resident macrophages (long-lived). Hematopoietic stem cells (HSCs) emerge intra-embryonically in the aorta-gonad-mesonephros region (AGM) at E10.5. They afterward migrate first to the fetal liver and eventually around E17.5 to the bone marrow, where they persist and self-renew. HSC-derived monocyte circulating in the blood could enter the peripheral tissues and give rise to monocyte-derived macrophages (short-lived).

1.3 **Macrophage functions**

1.3.1 Roles of macrophages in steady-state conditions

Macrophages are resident cells within their niches, where they adapt their phenotype in response to the local microenvironment (60,87) and fulfill tissue-specific roles (88). Throughout life, they orchestrate proper tissue development and function under steady-state conditions (89).

In the central nervous system, microglia begin populating the brain at E9.5 (90,91). During embryogenesis, microglia regulate neurogenesis by phagocytosing neuronal progenitor cells (92) and influence vessel formation and neocortical interneuron migration through interactions with endothelial cells and neurons (93–95). Postnatally, microglia can promote neuronal survival (96) and modulate neural circuits through synaptic pruning, guided by the complement system (97–99). In adulthood, microglia continue to monitor neuronal activity, support synaptic maturation, and facilitate myelin turnover (100–102).

In the liver, KCs reside in the hepatic sinusoids and play critical roles at different stages of development. During the fetal stage, KCs are crucial for the maturation of erythroblasts (103). Postnatally, they contribute to clearing damaged erythrocytes and apoptotic cells (104,105),

recycling iron (106), and eliminating pathogens (107,108). Metabolically, KCs are involved in lipid and cholesterol (109,110), especially because of their location in close proximity to hepatocytes (111) and their ability to produce paracrine factors that could modulate the activity of hepatocytes (112). For instance, KCs secrete pro-inflammatory cytokines such as, interleukin-6 (IL-6) and tumor necrosis factor-alpha (TNF-α), which can influence hepatic lipid and glucose homeostasis. While, IL-6 plays an essential role in maintaining liver glucose homeostasis by modulating insulin signaling(113), TNF-α promotes lipogenesis and contributes to insulin resistance (114,115). Additionally, KCs secrete insulin-like growth factor-binding protein 7 (IGFBP7), a non-inflammatory mediator that plays a critical role in promoting both lipogenesis and gluconeogenesis in the liver (116). Furthermore, KCs influence hepatocyte fatty acid oxidation through peroxisome proliferator-activated receptor delta (PPARδ) signaling (117).

In the lung, AMs are localized in the alveoli, where they continuously surveil the surrounding environment. These macrophages are responsible for clearance of inhaled pathogens and particles, effectively maintaining lung homeostasis without triggering an inflammatory response (118,119).

Splenic macrophages are categorized based on their localization within the spleen's anatomical zones: red pulp macrophages (RPMs), marginal zone macrophages (MZMs), marginal metallophilic macrophages (MMMs), and white pulp macrophages (WPMs). These macrophage subsets differ in their specialized roles attached to their microenvironment.

RPMs are fetal-derived, colonizing the spleen during embryogenesis (67). These macrophages play a critical role in maintaining systemic iron homeostasis by clearing aberrant red blood cells, metabolizing hemoglobin, and recycling iron (67).

In contrast, MZMs and MMMs emerge postnatally between days 7 and 14. Although their precise ontogeny remains unclear, they are suspected to originate from HSCs (67). Both MZMs and MMMs are crucial for pathogen recognition and clearance but differ in their interactions with lymphocytes. MMMs specialize in activating cytotoxic T cells by transferring antigens to $CD8^+$ dendritic cells (120). On the other hand, MZMs capture antigens from the bloodstream and present them to marginal zone B cells, initiating immune responses and facilitating antibody production (121).

WPMs appear later, around the time of weaning, coinciding with the activation of germinal centers upon exposure to external antigens (67). These macrophages are primarily responsible for phagocytosing apoptotic B cells in germinal centers, ensuring the maintenance of immune homeostasis and preventing autoimmunity (113).

Adipose tissue macrophages (ATMs) play a role in tissue remodeling and clearing apoptotic cells (122,123), ATMs are essential to the metabolic functions of adipose tissue. These include

regulating fat storage (124–126) and facilitating cholesterol efflux (127), highlighting their critical involvement in maintaining adipose tissue homeostasis and systemic metabolic health. The intestine harbors the largest macrophage compartment in the body (128). Macrophages are anatomically divided into two main groups: lamina propria macrophages and muscularis macrophages. Intestinal macrophages are crucial for clearing antigens and pathogens that breach the gut barrier, a process that is crucial for oral tolerance (128,129). Moreover, macrophages indispensable for maintaining the integrity of the gut epithelial barrier (128,130). Recent studies have also identified additional subsets of long-lived, self-maintaining macrophages (128,131). These subsets are closely associated with blood vessels and enteric neurons within the intestinal wall, playing critical roles in maintaining blood vessel integrity and supporting neuronal survival (132).

1.3.2 Roles of macrophages in disease conditions

While macrophages are essential for maintaining tissue homeostasis under steady-state conditions, their dynamic functions and plasticity can also contribute to the pathogenesis of various diseases. This plasticity allows them to orchestrate immune responses but also makes them susceptible to dysregulation, which can contribute to disease progression.

Macrophages are critical for sensing tissue injury and pathogens, secreting chemokines, cytokines, and other bioactive molecules essential for initiating and coordinating tissue responses (119,133–135).However, macrophages can also contribute to disease progression when their functions become dysregulated. Excessive production of pro-inflammatory cytokines, failure to clear apoptotic cells, or an inability to resolve inflammation can sustain pathological immune activation. Additionally, certain macrophage-derived factors, such as ROS, reactive nitrogen species (RNS), proteases, and pro-inflammatory lipid mediators, can exacerbate tissue damage (136). The resulting oxidative and nitrosative stress can damage proteins, lipids, and DNA, leading to necrosis, apoptosis, and dysfunction of key transcription factors, such as nuclear factor κB (NF-κB) (136). These mechanisms collectively contribute to chronic inflammation and tissue pathology in various diseases.”

1.3.2.1 Macrophages in Neurological Diseases

In the central nervous system, dysfunctional microglia are implicated in various neurological and psychiatric disorders, such as Parkinson's disease (137), Alzheimer’s disease (138), schizophrenia (139), and amyotrophic lateral sclerosis (140). Mutations in the colony-stimulating factor 1 receptor (CSF1R) are associated with diseases like microgliopathy (141) and pediatric-onset leukoencephalopathy (142), the latter being characterized by a deficiency of microglia. Additionally, the somatic mutation $BRAFV^{600E}$ in microglia leads to their chronic activation, causing neurodegeneration (143).

Furthermore, macrophages play a major role in the pathology of ischemic stroke. Following the stroke, disruption of the blood-brain barrier (BBB) allows increased infiltration of

monocytes into the injury site. These monocytes differentiate into macrophages, which have a dual role, contributing both to tissue injury and repair processes (144). Additionally, border-associated macrophages—specialized macrophages residing in the perivascular spaces surrounding brain blood vessels, the meninges, and the choroid plexus—further exacerbate tissue injury and vascular leakage by recruiting granulocytes in response to the stroke(145).

1.3.2.2 Macrophages in pulmonary diseases

Similarly, in the lung, dysfunctional AMs are linked to pulmonary alveolar proteinosis (PAP), a condition characterized by surfactant accumulation within the alveoli (146). PAP is primarily caused by disruptions in granulocyte–macrophage colony-stimulating factor (GM–CSF), a crucial factor for the development and maintenance of AMs (72).

1.3.2.3 Macrophages in infectious diseases

Macrophages possess a unique ability to recognize and clear invading pathogens. KCs for instance, play a critical role in bacterial clearance, with up to 60% of bacteria being cleared by the liver within 10 minutes of intravenous infection (147). The interaction between macrophages and pathogens is primarily mediated by pattern recognition receptors (PRRs), which identify pathogen-associated molecular patterns (PAMPs) (148). PRRs, including Toll-like receptors (TLRs), C-type lectin receptors (CLRs), NOD-like receptors (NLRs), and scavenger receptors, are localized on the surface, within vesicles, or in the cytoplasm of macrophages. These receptors recognize microbial components such as lipopolysaccharides, peptidoglycans, and nucleic acids, triggering a variety of responses that lead to macrophage activation and/or pathogen engulfment (148).

Scavenger receptors, such as CD36 and scavenger receptor class A (SR-A), mediate non-opsonic phagocytosis of bacterial pathogens including *Neisseria meningitidis*, *Staphylococcus aureus*, *Streptococcus pneumoniae*, *Salmonella typhimurium*, and *Escherichia coli* (*E. coli*) (149). Similarly, CLRs, such as Dectin-1 and the mannose receptor (CD206), play essential roles in recognizing pathogens like *Mycobacterium tuberculosis*, *Mycobacterium leprae*, *Streptococcus pneumoniae*, and *Candida albicans* (150).

In tuberculosis, although macrophages play a crucial role in restricting *Mycobacterium tuberculosis*, the bacteria have evolved mechanisms to evade host defenses, leading to macrophage dysfunction. This dysfunction promotes granuloma formation and sustained inflammation, which ultimately results in tissue damage and fibrosis (151,152).

Beyond bacterial infections, macrophages also play a pivotal role in parasitic infections. In malaria, for example, during the liver stage of Plasmodium infection, KCs recognize and phagocytose sporozoites, the infective form of the parasite that enters hepatocytes (153,154). Following replication within hepatocytes, the rupture of these infected cells releases merozoites into the bloodstream, marking the transition to the blood stage of malaria. At this stage, the parasites invade red blood cells, where they undergo an asexual replication cycle

(155). Macrophages in the spleen phagocytose infected red blood cells (iRBCs) and free merozoites, utilizing both opsonic mechanisms (via Fc receptors (FcRs) and non-opsonic mechanisms (via scavenger receptors such as CD36) to clear these parasites (153). Additionally, KCs also play a role in clearing damaged or altered RBCs, which may include iRBCs, through mechanisms involving scavenger receptors (156).

Macrophages also express FcRs, which bind the Fc region of antibodies, bridging innate and adaptive immunity. Upon activation, FcRs induce phagocytosis, antibody-dependent cellular cytotoxicity (ADCC), and modulation of inflammatory processes (157,158). FcRs are critical for the defense against a wide range of pathogens, including Staphylococcus aureus, Streptococcus pneumoniae, Bordetella pertussis, Legionella pneumophila, Leishmania, and Toxoplasma gondii (159). Notably, several studies have demonstrated that FcRs can also directly interact with non-opsonized bacteria, suggesting their involvement in early antibacterial defense mechanisms (160).

1.3.2.4 Macrophages in autoimmune diseases

Autoimmune diseases are a group of disorders characterized by the inability of the immune system to distinguish between self and non-self-antigens. This breakdown in self-tolerance triggers inappropriate immune responses against the body's own tissues, leading to chronic inflammation and tissue damage mediated by B cells, T cells, and macrophages (161).

Macrophages play pivotal roles in the onset and progression of autoimmune diseases through various mechanisms that drive inflammation and tissue destruction. In systemic lupus erythematosus (SLE), defective clearance of apoptotic cells by macrophages promotes the accumulation of autoantigens, leading to the formation of immune complexes and triggering chronic autoimmune responses (162).

In type 1 diabetes, the accumulation of unengulfed apoptotic cells leads to secondary necrosis, releasing self-antigens in the pancreas. Macrophages in this environment secrete high levels of pro-inflammatory cytokines, such as tumor necrosis factor-alpha (TNF-α) and interleukin-1 beta (IL-1β), which contribute to the immune-mediated destruction of pancreatic beta-cells (162).

In multiple sclerosis (MS), macrophages in the central nervous system contribute to the degradation of myelin sheaths by phagocytosing myelin debris and releasing inflammatory mediators, exacerbating neuronal damage (163). Additionally, macrophages process and present myelin antigens to autoreactive T cells, facilitating their activation and perpetuating the autoimmune response in MS (164).

1.3.2.5 Macrophages and metabolic syndrome

Metabolic syndrome, characterized by conditions such as obesity, insulin resistance, and dyslipidemia, is closely linked to chronic liver injuries, including those caused by non-alcoholic fatty liver disease (NAFLD) (165). In NAFLD, KCs undergo a shift toward a pro-inflammatory

phenotype. This activation results in the secretion of inflammatory factors, including TNF-α and IL-6 (166). This pro-inflammatory signature further contributes to the liver injury and disease progression to non-alcoholic steatohepatitis (NASH), fibrosis, and hepatocellular carcinoma(167). Alongside their inflammatory role, KCs also secrete transforming growth factor-beta 1 (TGFβ1) and platelet-derived growth factor (PDGF) during the progression of liver injury (168,169). These factors activate hepatic stellate cells, leading to increased extracellular matrix production and, ultimately, liver fibrosis.

Similarly, obesity is closely associated with significant alterations in macrophage function, particularly in the liver and adipose tissue. In the liver, KCs have been implicated in the development of hepatic insulin resistance, through the production of pro-inflammatory cytokines (e.g., TNF-α, IL-6) (170,171). However, other studies suggest that KCs may play a protective role against insulin resistance and inflammation in obesity through the production of interleukin-10 (IL-10) and other anti-inflammatory cytokines (172–174).

In adipose tissue, obesity triggers the recruitment of monocytes, which differentiate into ATMs (175). Numerous studies have established a strong link between pro-inflammatory mediators secreted by ATMs and the development of insulin resistance in obesity (176,177). Furthermore, macrophages contribute to inflammation in the adipose tissue by forming crown-like structures around apoptotic adipocytes (178).

Atherosclerosis is another chronic metabolic disease in which macrophages play a crucial role in the onset and the progression of atherosclerosis plaques (110). Macrophages engulf oxidized low-density lipoproteins (oxLDL) via scavenger receptors, such as CD36 and SR-A, transforming into foam cells(179). This lipid accumulation disrupts macrophage homeostasis, promoting pro-inflammatory responses and contributing to plaque growth (110).

Thus, macrophage dysfunction plays a central role in disease progression by shifting from protective to pathological responses. Whether through Kupffer cell-driven inflammation promoting insulin resistance in metabolic disorders or impaired apoptotic clearance fueling autoimmunity, dysregulated macrophages contribute to tissue damage and chronic disease states.

1.3.3 Metabolism and inter-organ communication

Metabolism is a highly coordinated process carried out across various organs, including the liver, adipose tissue, skeletal muscles, and gut. Inter-organ communication is essential for maintaining systemic energy homeostasis. This communication is mediated through a network of signaling molecules, including hormones, cytokines, metabolites, and extracellular vesicles. Dysregulation of this communication, often driven by metabolic stress, disrupts systemic energy balance and contributes to the development of metabolic diseases such as obesity, diabetes, and NAFLD (180).

The liver, as the central metabolic hub, integrates signals from peripheral organs to regulate glucose, lipid, and protein metabolism. Glucose and lipid homeostasis are tightly controlled by the interplay between pancreatic hormones—insulin and glucagon—as well as adipokines and cytokines. Under feeding conditions, insulin promotes glycolysis and lipogenesis in the liver while inhibiting gluconeogenesis. In parallel, adipose tissue increases lipogenesis and glucose uptake, storing excess energy and secreting leptin to suppress food intake (180,182).

Conversely, during fasting, glucagon stimulates hepatic gluconeogenesis and mobilizes stored energy. Simultaneously, adipose tissue enhances lipolysis, releasing non-esterified fatty acids into circulation. These fatty acids are subsequently taken up by hepatocytes and metabolized via beta-oxidation to produce energy (180,182). Additionally, fibroblast growth factor 21 (FGF21), secreted by both the liver and adipose tissue, supports lipolysis and energy balance during fasting (180,183).

Moreover, adipose tissue functions as an endocrine organ by releasing adipokines such as resistin, asprosin, and adiponectin, which modulate systemic metabolism. Specifically, asprosin promotes hepatic gluconeogenesis, while adiponectin enhances fatty acid oxidation and reduces lipogenesis in the liver (180). Cytokines like interleukin-6 (IL-6) and interleukin-13 (IL-13) also play crucial roles in maintaining glucose homeostasis (113,181).

Another critical inter-organ interaction is the gut-liver axis, which plays a key role in maintaining systemic energy homeostasis. The gut influences hepatic metabolism through multiple mechanisms. For instance, gut hormones such as glucagon-like peptide 1 (GLP-1) regulate glucose homeostasis by stimulating insulin secretion, thereby indirectly modulating hepatic glucose production (184).In addition to hormonal signals, bile acids act as key mediators of gut-liver communication. These molecules are synthesized in the liver, modified by the gut microbiota, and subsequently activate the farnesoid X receptor (FXR) in enterocytes (185,186). This activation triggers the release of fibroblast growth factor 15/19 (FGF 15/19) into circulation, which promotes hepatic glycogen synthesis and contributes to energy balance (186).

The intricate crosstalk between metabolic organs maintains systemic energy balance, yet its disruption contributes to metabolic disease pathogenesis. For instance, elevated levels of adipokines such as leptin, resistin, and pro-inflammatory cytokines like IL-6 in obesity are strongly linked to insulin resistance (187). Similarly, gut-derived metabolites, including short-chain fatty acids, ethanol, and trimethylamine, play a significant role in the progression of NAFLD (188). This interplay between metabolic tissues underscores the critical role of inter-organ communication in both maintaining homeostasis and driving disease processes.

1.4 **Aim of the thesis**

The aim of this thesis is to investigate the impact of chronic micro- and nanoplastic (MNP) ingestion on tissue homeostasis, metabolism, and immune function using a mouse model. Specifically, this study explores how prolonged exposure to polystyrene particles influences cellular and metabolic processes across key organs, including the liver, spleen, and adipose tissues.

To comprehensively assess MNP-induced effects, this study evaluates both baseline metabolic and immune responses, as well as the consequences of MNP exposure under conditions of heightened metabolic stress, such as a high-fat diet (HFD). Employing an HFD model provides deeper insight into whether MNP-related disruptions are intensified by metabolic overload. This approach further clarifies how environmental pollutants and dietary stressors may interact to impair tissue homeostasis, disrupt lipid metabolism and glucose regulation, and potentially increase the risk of metabolic disorders.

This study focuses on macrophages, especially Kupffer cells, evaluating their role in MNP retention and how this impacts phagocytic capacity, systemic immunity, and overall immune homeostasis. Macrophage functionality is quantified using an in vivo phagocytosis model. Furthermore, acute and recurrent infection models are utilized to determine whether chronic MNP exposure impairs pathogen clearance and increases infection susceptibility. This study also examines whether MNP-induced macrophage dysfunction contributes to the development of autoimmune traits, specifically by investigating impaired apoptotic cell clearance and dysregulated immune signaling as potential triggers for autoimmunity.

Ultimately, this research aims to provide novel insights into the health risks associated with MNP ingestion and its broader implications for public health amid the escalating plastic pollution crisis.

2 Materials and Methods

2.1 **Materials**

2.1.1 Devices

Device	Company
Luminex® xMAP493	Thermos Scientific
Thermo Q Exactive ™ Plus	Thermo Scientific
Tecan Infinite M200	Tecan
SpeedVac Vacuum	Eppendorf
Centrifuge 5810 R	Eppendorf SE
Centrifuge 5424	Eppendorf SE
Cryostat CM3050 S	Leica Biosystems
Dissection equipment	Fine Science Tools
Gel Doc Imager	BioRad
Mastercycler X50s	Eppendorf
NextSeq2000 Sequencer	Illumina
Eppi Shaker (37°C)	Eppendorf
37°C incubator	BINDER
PCR cycler	Applied Biosystems
Pipetboy Easypet 3	Eppendorf
BeadBug homogenizer	Benchmark Scientific
AccuChec Instant test strips	Roche
Axio Lab.A1	Carl Zeiss AG
Tapestation 4200	Agilent
Advia 2120 Hemocytometer	Siemens
FACS Symphony	BD Biosciences
FACS ARIA III	BD Biosciences
Luminex Guava System	Cytek
Airyscan 880 microscope	Zeiss
Precellys 24 Tissue Homogenizer	Bertin Instruments
JS13.1 rotor	Beckman Coulter
high-speed centrifuge (Avanti)	Beckman Coulter
NextSeq2000 Sequencer	Illumina

2.1.2 Softwares

Software	Version
FlowJo software	FlowJo 10.10.0
Fiji software	v2.1.0/1.53c
QuPath software	version 0.5.1
Imaris software	

BioRender	https://www.biorender.com/
QIIME 2	version 2022.8
GraphPad Prism 10	Version 10.4.1 (532)
R	4.2.1
R Studio	2022.07.1
FACSDiva	9.0

2.1.3 Consumables

Name	Vendor
Deepwell Plate 96/500 µL Low bind, PP	Eppendorf, 0030504100
ZR BashingBead lysis tubes	Zymo Research, S6012-50
1.5 ml, 2.0 ml Eppendorf tubes	Eppendorf
15 ml, 50 ml Falcon tubes	Sarstedt, Inc.
5 ml, 10 ml Pipettes	BRAND
1 ml syringes	Braun
6 well plate	VWR
96 well plate U-bottom	VWR
Heparinized micro-hematocrit capillary tubes	VWR, MODU163613
Microvette	Sarstedt
Microvette, EDTA	Sarstedt
Pipet-tips (10 µl, 200 µl, 1000 µl)	Sarstedt, Inc.
VWR cell strainer	Avantor
FACS tubes	Sarstedt, Inc.
Pasteur pipette	avantor
Serological pipettes	Sarstedt, Inc
Superfros Plus Adhesion Microscope Slides	Epredia
Microtome blades	FEATHER
Micro cover glasses	BRAND
Tissue-Tek O.C.T. Compound	Sakura Finetek Germany
glass beads	Sigma-Aldrich G1152-100G
Glass douncer 2 ml	KIMBLE, 885300-0002

2.1.4 Commercial kits

Kit	Vendor	Catalog number
Alanine aminotransferase (ALT) ELISA	abcam	ab282882
Aspartate aminotransferase (AST) ELISA	abcam	ab263882
ProcartaPlex™ Panel	Invitrogen™	EPX480-20834-492901
PureLink™ RNA Mini Kit	Invitrogen	12183018A
FastStart Universal SYBR Green Mastermix	Roche® Life Science	4913914001

iScriptTM cDNA Synthesis Kit	BioRad	1708890
Oil-Red-O Stain Kit	Sigma-Aldrich	O0625
KAPA HiFi Hotstart Readymix PCR Kit	Kapa Biosystems	KK2602
Nextera XT DNA Library Preparation Kit	Illimina	FC-131-1024
High Sensitivity D5000 assay	Agilent	5067-5592
Qubit high-sensitivity dsDNA assay	Invitrogen	Q33231
TMB Substrate Kit	Thermo Fisher	34021
Chemagic DNA Stool 200 Kit H96 (,)	Perkin Elmer	CMG-1076
Qubit dsDNA HS Assay Kit	Thermo Fisher Scientific	Q32851
MiSeq Reagent Kit v3	Illumina	20037124
Chromium Single Cell 3' Gene Expression v3.1 Dual Index Kit	10x Genomics	PN-1000269
Chromium Next GEM Chip G Single Cell Kit	10x Genomics	PN-1000127
Dual Index TT Set A	10x Genomics,	PN-1000215)

2.1.5 Reagents and chemicals

Reagent	**Vendor**	**Catalog number**
Green Fluorescent Carboxylated PS Latex Particles (50 nm, 100 nm, 200 nm, 500 nm)	Polysciences	15700-10, 17149-10, 16662-10, 09834-10
Carboxylated PS Latex Particles (50 nm500 nm)	Polysciences	15913-10, 09836-15
Red Fluorescent Carboxylated PS Latex Particles (50 nm, 100 nm, 200 nm, 500 nm)	Magsphere, Inc.	CAF050NM, CAF100NM, CAF200NM, CAF500NM
Ketamin	Vetoquinol,	NARKETAN 100 mg/ml
Xylazine	Bayer	4007221031017
Hoechst	Thermo Fisher Scientific	H1398
EDTA	Sigma-Aldrich	E5134-500G
Collagenase D	Roche	11088858001
DNase I	Sigma-Aldrich	DN25
Dispase	Gibco	17105041

Type II collagenase	Sigma-Aldrich	C6885-1g
Triton-X-100	Fisher Scientific	BP151-100
Rat serum	Bio-Rad	C13SDZ
Sodium chloride for anesthesia	Braun	
Normal goat serum	VWR	ICNA 08642921
DAPI	BioLegend	42281
Fluoromount G	Thermo Scientific	00-4958-02
BSA (microscope analysis)	Thermo Scientific	37525
Insulin	Caninsulin® 40 I.E./ml	
Dulbecco's phosphate-buffered saline (DPBS, 10x, w/o Ca and Mg)	PAN-Biotech	P04-53500
Ethanol	Carl Roth	K928.6
xylene	Carl Roth	8749
Periodic acid solution	Carl Roth	HP00
Schiff's reagent	Carl Roth	X900.2
Entellan	Merck	107961
Hematoxylin	Carl Roth	T865.2
Eosin	Carl Roth	X883.2
Picrosirius Red solution	ScyTek Laboratories	SRS500
Euparal	Carl Roth	7356.1
D.sucrose	Fisher Scientific	10638403
Kaiser's glycerol gelatin	Carl Roth	6474.1
Methanol (for LC-MS)	Sigma-Aldrich	1.06035.2500
Isopropanol (for LC-MS)	Merck	1.02781.2500
ddH2O (for LC-MS)	Merck	7732-18-5
Acetic acid (for LC-MS)	Thermo Fisher Scientific	10860701
Ammonium acetate (for LC-MS)	Merck Millipore	5330040050
16% Formaldehyde	Thermo Scientific	11586711
RPMI	PAN-Biotech	P04-16500
Fetal bovine serum (FBS), South America origin, 0.2 µm sterile filtered	PAN-Biotech	P30-3031
Flavopiridol	Sigma	F3055
Bovine serum albumin (BSA)	Sigma-Aldrich	A9647
Ampicillin	Carl Roth	K029.2
Dexamethasone	Sigma-Aldrich	D4902

Annexin V	BioLegend	640941
7-aminoactinomycin D (7-AAD)	Merck	SML1633
Methylated BSA	Sigma-Aldrich	A1009-1G
Calf thymus DNA	Sigma-Aldrich	D4522
Gelatin	Thermo Scientific	10075660
Sulfuric acid	Sigma-Aldrich.	258105-500ML
Evans Blue dye	Sigma-Aldrich	E2129
Formamide	Thermo Fisher Scientific	AM9342
CD45 Microbeads	Miltenyi	130-052-301)

2.1.6 Antibodies

Flow cytometry

Antigen	Conjugation	Dilution	Clone	Vendor
CD115	APC	1:200	AFS98	biolegend
CD11b	PECy7	1:800	M1/70	biolegend
CD11b	BUV-661	1:200	M1/70	BD Biosciences
CD11b	BUV737	1:200	M1/70	BD Biosciences
CD11c	BV605	1:200	N418	biolegend
CD16.2	BV786	1:200	9E9	biolegend
CD163	BV421	1:800	S15049I	Biolegend
CD169	BV605	1:200	3D6.112	Biolegend
CD172a	PE-Cy7	1:400	P84	Biolegend
CD19	APC/Cy7	1:100	6D5	Biolegend
CD19	BV421	1:200	6D5	Biolegend
CD19	Biotin	1:100	6D5	Biolegend
CD206	BV711	1:200	C068C2	Biolegend
CD209b	BV711	1:50	22D1	BD Biosciences
CD3	APC-eF780(Cy7)	1:400	17A2	Biolegend
CD31	FITC	1:100	390	Biolegend
CD31	BUV661	1:200	390	BD Biosciences

CD32b	APC	1:100	AT130-2	Thermo Fisher Scientific
CD43	BUV-496	1:600	S7	BD Biosciences
CD45	BUV-805	1:800	30-F11	BD Biosciences
CD64	FITC	1:800	X54.5/7.0	Biolegend
CD64	PerCP-Cy5.5	1:50	X54.5/7.0	Biolegend
CD64	PE/Cy7	1:100	X54.5/7.0	Biolegend
Clec2	APC	1:100	17D9	Biolegend
Cx3cr1	APC	1:400	SA011F11	Biolegend
CX3CR1	BV711	1:200	SA011F11	Biolegend
F4/80	APC-Cy7	1:400	BM8	Biolegend
F4/80	BV510	1:100	T45-2342	BD Biosciences
F4/80	BV421	1:150	BM8	Biolegend
Ly6C	APC-Cy7	1:200	HK1.4	Biolegend
Ly6C	BV510	1:200	HK1.4	Biolegend
Ly6G	PerCP/Cy5.5	1:200	1A8	Biolegend
Ly6G	Biotin	1:100	1A8	Biolegend
MARCO	APC	1:100	579511	R&D Systems
MerTK	PE-Cy7	1:800	2B10C42	Biolegend
MERTK	PE	1:200	2B10C42	Biolegend
MHC class II	A-700	1:200	M5/113.15.2	Biolegend
NKp46	BV711	1:100	29A1.4	Biolegend
NKp46	Biotin	1:100	29A1.4	Biolegend
Nkp46	APC/Cy7	1:200	29A1.4	Biolegend
SiglecF	BUV-395	1:100	E50-2440	BD Biosciences
Tcr-ß-Bio	APC/Cy7	1:50	H57-597	Biolegend
TCR-β	Biotin	1:100	H57-597	Biolegend
TER-119	APC/Fire™ 750	1:100	TER-119	Biolegend

Tim4	AF647	1:400	RMT4-54	Biolegend
Tim4	BUV-563	1:200	RMT4-54	BD Biosciences
Vsig4	PE-Cy7	1:200	NLA14	Thermo Fisher Scientific
XCR1	APC-Cy7	1:200	ZET	Biolegend
XCR1	BV650	1:200	ZET	Biolegend
Streptavidin	BV785	1:100	-	Biolegend

Immunofluorescent staining

Antibody	**Conjugate**	**Dilution**	**Catalog number**	**Vendor**
Iba1 (rabbit)	-	1:500	ab178847	Abcam
CD31 (arminian hamster)		1:100	MA3105	Thermo Scientific
CD68 (rat)	-	1:500	137001	Biolegend
Goat α-rabbit	AF488	1:1000	A-11008	Thermo Fisher Scientific
Goat α-rabbit	AF647	1:1000	A21244	Thermo Fisher Scientific
Goat α-rat	AF647	1:1000	405416	Thermo Fisher Scientific
Goat α-hamster	DyLight™ 649	1:1000	405505	Biolegend

ELISA:

Antibody	**Conjugate**	**Dilution**	**Catalog number**	**Vendor**
Goat α -Mouse	Horseradish Peroxidase conjugated (HRP)	1:4000	A90-116P	Bethyl Laboratories

2.2 **Methods**

2.2.1 Mice

All investigations concerning mouse work conform to the guidelines from Directive 2010/63/EU of the European Parliament on protecting animals used for scientific purposes. In detail, all animal experiments were conducted according to the German law of animal protection and in agreement with the approval of the local institutional animal care committee (Landesamt für Natur, Umwelt und Verbraucherschutz (LANUV), North Rhine-Westphalia, Az 81-02.04.2019.A167). Mice were housed under specific pathogen-free conditions with 12-h light/dark cycle, with food and water provided *ad libitum*. As wildtype strain, C57BL/6JRcc was

used. To generate the double fate-mapper *Tnfrsf11a*^{Cre}; *Rosa26*$^{LSL\text{-}YFP}$ (JAX stock #006148); *Ms4a3*^{FlpO}; *Rosa26*$^{FSF\text{-}tdTomato}$ (JAX stock #032864), we bred *Tnfrsf11a*$^{Cre/+}$; *Rosa26*$^{FSF\text{-}tdTomato/FSF\text{-}tdTomato}$ animals with *Ms4a3*^{FlpO}; *Rosa26*$^{LSL\text{-}YFP/LSL\text{-}YFP}$ animals. The *Tnfrsf11a*^{Cre} was provided by Prof. Yasuhiro Kobayashi, while *Ms4a3*^{FlpO} was provided by Prof. Florent Ginhoux. All mice were originally of C57BL/6J background and crossed to C57BL/6Jrcc for 2-5 generations. All lines were back-crossed to their respective wildtype line (C57BL/6Jrcc) once per year. Male mice were used for all experiments.

2.2.2 Genotyping of the DFM mouse model

Upon weaning, the mice were ear-tagged. The tissue was used for genotyping and dissolved in 200 µl of 50 mM NaOH for 30 min at 95 °C. 20 µl of 1M TRIS-HCl (pH 8) were added for neutralization. After spinning for 5 min at full speed in an Eppendorf centrifuge, 1 µl of the supernatant was used for genotyping. Per sample 1 µl of the isolated DNA was added to 9 µl of a master mix solution (consisting of 0.5 µl of each primer (**Table 2**), 5 µl DreamTaq Green PCR Master Mix and H_2O to receive a total volume of 10 µl). The genetic material was amplified in 35 cycles in a PCR cycler (**Table 3**). Samples were applied on a 1.5 % agarose gel and separated via electrophoresis at 120 V for 30 min. The DNA was stained with the Sybr-safe dye for visualization via UV light.

Table 1 PCR reagents

Reagent	Vendor
Taq-Polymerase Mastermix	VWR
Nuclease-free water	GE Healthcare
TRIS-Hydrochlodide	AppliChem Panreac
DNA ladder	New England Biolabs

Table 2 Genotyping primers

Genotype	Primer sequence	results
Tnfrsf11a-Cre	P1: TCA AGG GTG ACA TCA TCG TGG T P2: ACT TCT CCA TGG TAG CCT CC P3: TAT GGG GGT GGG GTG ATA C	529 bp: wt 270 bp: Cre
Ms4a3-FlpO	P1: AGA GAA ATC ATC AGG GCA GAA AT P2: GAA AGG GGA ACA AGC GAA GAT P3: TTG GCG AGA GGG GAA AGAC	517 bp: wt 412 bp: FlpO
R26-FrtStoptdTom	P1: ACG GGC AGT AGG GCT GAG P2: AGC CTG CCC AGA AGA CTC C P3: GGT GTT GGG TCG TTT GTT CA P4: TCT AGC TTG GGC TGC AGG T	402 bp: wt 290 bp: FrtStop-tdTom
R26-LoxStopeYFP	P1: CTG GCT TCT GAG GAC CG P2: CAG GAC AAC GCC CAC ACA P3: AGG GCG AGG AGC TGT TCA P4: TGA AGT CGA TGC CCT TCA G	142 bp: wt 384 bp: LoxStop-eYFP

Table 3 PCR program used for genotyping

Step	Temperature	Time	Cycles
Initial denaturation	95 °C	3. min	1
Denaturation	95 °C	30 sec	35
Annealing	60°C	30 sec	
Elongation	72 °C	30 sec	
Final extension	72 °C	5 min	1
Soak	10 °C	hold	1

2.2.3 Chronic Plastic Administration Model

8-12 week old male mice received either PBS or polystyrene particles once per week via oral gavage for a total of 12 weeks. For plastic titration experiments, 1 mg/kg, 10 mg/kg and 100 mg/kg were used, for all other experiments a standard dose of 100mg/kg of body weight was used. To assess plastic particle bioavailability a range of sizes of fluorescent-labeled negatively charged polystyrene particles were used (50nm, 100nm, 200nm and 500nm; Polysciences, Megasphere), however throughout subsequent experiment 50nm and 500nm polystyrene particles were used to mimic nanoplastic and microplastic exposure respectively. For the DFM ontogeny tracing unlabeled negatively charged polystyrene particles were used.

2.2.4 Preparation of cell suspension for flow cytometry

2.2.4.1 Preparation of liver, spleen and brain

Mice were anesthetized with Ketamine/Xylazine mix (20 mg/ml Xylazine100 mg/ml Ketamine in NaCl (0.9 %)) and perfused with ice-cold PBS. For flow cytometry analysis of myeloid cells, 300 mg of adult liver, 20 mg of spleen, as well as the brain, were collected. One brain hemisphere was processed further as described by Aboghazleh et al. (189) to dissect the hippo campus and the cortex. All tissues were finely minced and incubated in a digestion mix containing PBS, 1 mg/mL collagenase D (Roche, 11088858001), 100 U/mL DNase I (Sigma-Aldrich, DN25), 2.4 mg/mL dispase (Gibco, 17105041), and 3% fetal bovine serum (FBS) (PAN-Biotech, P30-303) for 30 minutes at 37 °C, followed by mechanical disruption through a 100 µm filter. The cell suspension was diluted in 3 ml of FACS buffer (0.5 % BSA, 2 mM EDTA in PBS). For the liver, the suspension was centrifuged at 50 x g for 3 min to remove hepatocytes. Then, the supernatant containing hepatic myeloid cells and the spleen suspension were centrifuged at 400 x g for 7 min, 4 °C. The pellets of the spleen and the liver were resuspended in 1 ml RBC lysis buffer (0.1 mM EDTA, 12 mM NaHCO3, 155 mM NH4Cl in Aqua Bidest) for 5 min on ice then washed with FACS buffer. Afterward, cell pellets were resuspended in 50 µl blocking buffer (anti-CD16/32 and 2 % rat serum (Bio-Rad, C13SDZ) in FACS buffer) and incubated for 15 min at 4 °C. For the FcγR assessment blocking was done

only with rat serum. Subsequently, the volume was topped up to 200 µl, out of which 150 µl cell suspension were used cell surface marker staining. The remaining 50 µl were diluted 1:200 in FACS buffer for cell counting using the Luminex Guava System. Cell surface marker staining was performed for 30 minutes at 4°C. For directly conjugated antibodies, cells were incubated with primary antibodies and washed once with FACS buffer before acquisition. In cases where secondary antibody staining was required, cells were first incubated with the primary antibody, washed, and then stained with the appropriate secondary antibody for an additional 30 minutes at 4°C, followed by a final wash before being acquired using the FACS Symphony (BD Biosciences)

2.2.4.2 Preparation of blood

Of the collected blood, 200 µl were transferred into a 15 ml tube containing 3 ml RBC-lysis, mixed and incubated for 5 min on ice. After the addition of 7 ml FACS buffer, the suspension was centrifuged at 400 g, 4 °C for 5 min. The supernatant was aspirated and the pellet resuspended in 3 ml RBC-lysis buffer again. After adding 7 ml FACS buffer, the suspension was centrifuged (400 g, 4 °C 5 min). The supernatant was aspirated and the pellet was resuspended in 50 µl blocking buffer (anti-CD16/32 and 2 % rat serum in FACS buffer). After an incubation for 5-10 min on ice, the volume was measured and adjusted to 200 µl with FACS buffer. 150 µl of the cell suspension was then used for surface marker staining. The remaining 50 µl were diluted 1:50 in FACS buffer for cell counting using the Luminex Guava System. Cell surface marker staining was performed for 30 minutes at 4°C, and the cells were washed before acquiring on the FACS Symphony.

2.2.4.3 Preparation of gWAT

For the flow cytometry analysis of myeloid cells in adipose tissue, 200–300 mg of adipose tissue were excised, minced into small pieces and incubated in a digestion mix containing PBS, 2 mg/ml type-II collagenase (Sigma-Aldrich, C6885-1g), 2.5 mM CaCl2, and 0.5% BSA. The digestion was carried out for 25 minutes at 200 rpm and 37°C. The cell suspension was diluted in 10 ml of FACS buffer (0.5 % BSA, 2 mM EDTA in PBS), and centrifuged at 500 x g for 10 min, 4 °C. The pellet was resuspended in 50 µl blocking buffer (anti-CD16/32 and 2 % rat serum in FACS buffer), and incubated for 15 min at 4°C. Thereafter, the volume was measured and adjusted to 200 µl with FACS buffer. 150 µl of the cell suspension was then used for surface marker staining. The remaining 50 µl were diluted 1:100 in FACS buffer for cell counting using the Luminex Guava System. Cell surface marker staining was performed for 30 minutes at 4°C and the cells were washed before acquiring on the FACS Symphony.

2.2.4.4 Analysis of flow-cytometry data

Labeled cells were acquired with the BD Symphony flow cytometer and the Diva software. Exported data were analyzed with the FlowJo software.

2.2.5 Immunofluorescent analysis

For fluorescent microscopy, tissues were collected in 4 % formaldehyde for 24-48 hours, dehydrated by treatment with D-Sucrose (30 % (w/v) in PBS) (Fisher Scientific, 10638403) until they sink, then embedded in Tissue Tek. Cryo-preserved blocks were cut then air-dried for at least 30 minutes in RT. Liver, spleen and brain were cut at 40 µm, 20 µm and 60 µm thickness, respectively. The sections were washed in PBS, permeabilized with 0-4 %PBT (0.4 %triton-X-100 (Fisher Scientific, BP151-100) then blocked in 100 µl blocking buffer (2 % normal goat serum (VWR, ICNA 08642921), 1% BSA (Thermo Scientific, 37525) in 0.4 % PBT) for one 2 hours at RT. Subsequently the tissues were incubated with primary antibodies overnight at 4°C, then secondary antibodies hosted in goat for 2 hours at RT. Nuclei were stained with 1 µg/mL DAPI (Biolegend, 42281) (in PBS) for 10 min at RT, then the tissue were mounted with Fluoromount G (Thermo Scientific, 00-4958-02). Immunofluorescence images were acquired with a Zeiss LSM Airyscan 880 microscope (Zeiss) and processed with Fiji software. Volumetric reconstruction analysis to visualize PS-engulfment in KCs was carried out using Imaris software according to the protocol described in Schafer et al.(190).

2.2.6 Histological analysis

The livers and adipose tissues were fixed in 4% Formaldehyde (Thermo Scientific, cat. No: 11586711) for 24-48h then washed in PBS and stored in 70% ethanol. The fixed tissues were processed by the histology core facility of the university clinic (UKB). Briefly, tissues were dehydrated and cleared, embedded in paraffin, cut (5 µm thick) and then stained with H&E, PAS-H or Sirus Red staining. Prior to the staining, tissue sections were deparaffinized at 65 °C for 30 minutes and rehydrated by passing through a series of steps, each for 3 minutes: 2 changes of xylene (Carl Roth, 8749), followed by 100 %, 95 %, 90 %, 80 %, and 70 % ethanol, and finally distilled water.

2.2.6.1 Periodic acid Schiff (PAS)-hematoxylin (H) staining

Sections were incubated in periodic acid solution (Carl Roth, HP00) for 10 minutes to oxidize glycogen, rinsed in tap water for 3 minutes, and then briefly rinsed in distilled water. The sections were placed in Schiff's reagent (Carl Roth, X900.2) for 15 minutes. Following staining, sections were washed in running tap water for 10 minutes then briefly rinsed in distilled water. Counterstaining was performed using hematoxylin (Carl Roth, cat. No: T865) for 45 seconds to visualize nuclei. Excess hematoxylin was removed by washing in tap water for 3 minutes, followed by a brief rinse in distilled water. Sections were passed through distilled water, 70%, 80%, 90%, 95%, and 100% ethanol, each for 3 minutes, and then cleared in 2 changes of xylene. Sections were mounted with Entellan (Merck, 107961) and covered with glass coverslips. Images were acquired with Axio Lab.A1 (Carl Zeiss AG) with the 10X objective, in which 3-10 images per liver was taken. For analysis of acquired images Fiji software was

used. First, the color threshold was set for the images and they were converted to 8-bit images. After setting an auto threshold, they were reverted, and the color deconvoluted. Signal intensity for the PAS image plane was measured.

2.2.6.2 Hematoxylin and Eosin (H&E)

Sections were incubated in hematoxylin (Carl Roth, T865.2) for 90 seconds, then rinsed in tab water to stabilize the color. The sections were placed in eosin (Carl Roth, X883.2) for 3 minutes, followed by a brief rinse in distilled water. The sections were dehydrated then mounted with Entellan as descripted in PAS-H staining. Images were acquired with Axio Lab.A1 with the 10X objective.

2.2.6.3 Sirus Red staining

Sections were incubated for 60 minutes with Picrosirius Red solution (ScyTek Laboratories, SRS500) to stain collagen fibers. After incubation, sections were briefly rinsed in 0.5% acetic acid solution (ScyTek, AAD), followed by a quick rinse in 100% ethanol. Samples were then mounted in Euparal (Roth, 7356.1) and allowed to dry overnight. Images were acquired with Axio Lab.A1 with the 10X objective.

2.2.6.4 AdipoQ analyisis

H&E-stained gWAT sections were assessed for adipocyte size using AdipoQ software as previously described (191). Briefly, the image was preprocessed by segmenting into the fore- and background, creating a mask of each adipocyte. Subsequently, the mask was quantified and parameters such as area of the object and number of objects are determined. This allowed to calculate the frequency distribution for different adipocyte sizes between conditions.

2.2.6.5 Histological assessment

Histological evaluation of HE stained gWAT and BAT was performed by the lab of Prof. Dr. Lukas Kenner at the Medical University of Vienna.

For the gWAT, the analysis focused on identifying inflammatory cell infiltrates, including lymphocytes, plasma cells, neutrophils, and mast cells, as well as evaluating vascular and structural abnormalities. Specific criteria included the presence of round cell infiltrates, mixed-cell infiltrates, perivascular and sub peritoneal immune cell aggregations, and focal areas of hemorrhage. Additionally, tissue samples were examined for artifacts that might influence histological interpretation. The degree of inflammation was systematically graded as absent, mild, or multifocal, with particular attention to lymphocytic and mixed-cell infiltrates. Distinct regions, such as the mesothelial areas and epididymal adipose tissue, were assessed for immune cell clusters, including foamy cytoplasmic changes indicative of macrophage involvement or altered adipocyte morphology.

The size distribution of vacuoles in BAT was assessed through a histological scoring method that quantified vacuole size as a percentage of the total tissue area. The analysis differentiated

between large vacuoles, medium-sized vacuoles and small vacuoles, providing a detailed profile of lipid droplet morphology within the BAT.

To quantify the vacuole size distribution, a scoring formula was applied:

$$\text{Vacuole Score} = \frac{(\%\text{large vacuoles} \times 3) + (\%\text{medium vacuoles} \times 2) + (\%\text{small vacuoles})}{100}$$

The evaluation was conducted blinded to experimental groups to ensure unbiased interpretation, and representative images were captured to support both qualitative and quantitative assessments.

2.2.7 Oil-Red-O (ORO) staining

For the assessment of neutral lipid content. liver tissues were fixed in 4% formaldehyde for 24-48 hours, dehydrated by treatment with 30 % D-Sucrose (in PBS) (Fisher Scientific, 10638403) until they sink, then embedded in Tissue Tek. Cryo-preserved liver blocks were cut at 12 µm thickness and dried for 1 h, RT. Sections were rinsed with 60 % isopropanol (Merck, cat. No: 1027812500). Thereafter, the tissue sections were stained using an Oil-red-O Stain Kit (Sigma-Aldrich, O0625) according to the manufacturer's instructions. The sections were then stained with hematoxylin for 5-10 min to visualize nuclei, rinsed with distilled water, and mounted with Kaiser's glycerol gelatin (pre-heated at 55°C) (Carl Roth, 6474.1). Images were taken with an Axio Lab.A1 microscope. For Oil-red-O staining quantification, 10 images of each sample with a 40X objective were taken and quantification was performed using QuPath software.

2.2.8 Lipidomics

To evaluate differences in hepatic lipid metabolism tandem mass spectrometry of extracted lipids was performed based on the method established by the lab of Prof. Christoph Thiele. For this purpose, 10 mg liver tissue was homogenized in 500 µL ddH2O on ice. Then, 50 µL of the homogenate was transferred into a fresh Eppendorf tube and 500 µL Extraction Mix ($CHCl_3$/MeOH 1/5 containing the following internal standards provided by Prof. Christoph Thiele: 210 pmol PE(31:1), 396 pmol PC(31:1), 98 pmol PS(31:1), 84 pmol PI(34:0), 56 pmol PA(31:1), 51 pmol PG (28:0), 28 pmol CL(56:0), 39 pmol LPA (17:0), 35 pmol LPC(17:1), 38 pmol LPE (17:0), 32 pmol Cer(17:0), 99 pmol, SM(17:0), 55 pmol GlcCer(12:0), 14 pmol GM3 (18:0-D3), 339 pmol TG(50:1-d4), 111 pmol, CE(17:1), 64 pmol DG(31:1), 103 pmol MG(17:1), 724 pmol Chol(d6) and 45 pmol Car(15:0) was added. After 2 min of sonication in a bath sonicator, the samples were spun at 20,000 g for 2 min. The supernatant was collected in a new Eppendorf tube and 200 µL chloroform and 750 µL of 1 M NH_4Ac in ddH_2O were added. Following quick manual shaking, the samples were centrifuged at 20,000 g for 2 min again. The upper phase was carefully removed, and the lower phase was transferred into a new

Eppendorf tube. The solvent was evaporated using a SpeedVac Vacuum Concentrator at 45 °C for 20 min. The dried lipids were dissolved in 500 µL Spray Buffer (8:5:1 of Isopropanol, Methanol, ddH2O (all MS grade), 10 mM ammonium acetate, 0.1 % acetic acid by sonication for 5 min.

Lipid extracts were diluted 1:5 and measured with Thermo Q Exactive ™ Plus (Thermo Scientific) using positive mode. For analysis, the raw spectrum files generated by the instrument were converted to .mzML format and imported into LipidXplorer software (192). The software calibrates the mass spectra using both the sample lipids and the previously added internal standard, allowing for mass-based discrimination of different lipid species. The concentration of each lipid species (pmol) was determined by normalizing its signal intensity to the peak intensity of the internal standard, considering the known concentration of the added internal standard in each sample. Samples with a high deviation of the internal standard were excluded from analysis. The overall abundance of the respective lipid class was obtained by summarizing the species' amounts, and finally normalized to tissue weight.

2.2.9 Measurement of Serum ALT and AST Levels

Serum levels of alanine aminotransferase (ALT) and aspartate aminotransferase (AST) were quantified using commercially available ELISA kits (Abcam, ab282882 for ALT and ab263882 for AST) according to the manufacturer's instructions. Serum samples were collected from mice via cardiac puncture, stored at -80°C, and diluted 1:150 prior to analysis. Absorbance was measured at 450 nm using a Tecan Infinite M200 plate reader, and ALT and AST concentrations were calculated by interpolating optical density values against the standard curve.

2.2.10 Multiplexed cytokine and chemokine assay

Multiplexed cytokine and chemokine assay The Immune Monitoring 48-Plex Mouse ProcartaPlex™ Panel (Invitrogen™, EPX480-20834-492901) was used. 25 µl of sera were thawed and analytes were evaluated using Luminex® xMAP493 system. All reagents were prepared and used according to the manufacturer's instructions.

2.2.11 Quantitative RT-PCR

RT-PCR was performed by the lab of Prof. Dagmar Wachten (institute of innate immunity, UKB). For qRT-PCR, 50 mg of fresh liver was snap-frozen and stored at -80°C. Samples were disrupted using a BeadBug homogenizer (Biozym Scientific) in lysis buffer from the PureLink RNA Mini Kit (Cat# 12183018A, Invitrogen) followed by RNA isolation using silica-based RNA spin column enrichment. The eluted RNA was resuspended in RNAse/DNAse-free water, and concentrations were measured using a Nanodrop (ThermoFisher Scientific) spectrophotometer. Reverse transcription was performed with iScriptTM cDNA Synthesis Kit (Cat# 1708890, BioRad). Gene expression was quantified using the SYBR Green-based

method (FastStart Universal SYBR Green Mastermix Cat# 4913914001, Roche Life Science), with mRNA abundance calculated using the relative quantification method (Pfaffl Method(192)). Transcript levels were normalized to Hypoxanthine-guanine phosphoribosyl transferase (Hprt) and tata-box binding protein (Tatabp) expressions. Primer sequences are provided in (Table 4)

Table 4 qRT-PCR primers

Col1a1	GAGATGATGGGGAAGCTGGC	CTCGGTGTCCCTTCATTCCG
Col5a1	CTTGTCCGATGGCAAGTGGC	CATCATCCAGAATCCGGGAGC
Fibronectin	CTCCGAGACCAGTGCATCG	GAATCTTGGCACTGGTCAATGG
Tenascin C	CCACACTCACAGGTCTAAGGC	GATGGTTGCTGGATCACTCTCC
Tgfb	GACCGCAACAACGCCATCTAT	CAATGGGGGTTCGGGCACTG
Tatabp	GAGCTCTGGAATTGTACCGCAG	CATGATGACTGCAGCAAATCGC
Hprt	TCCCAGCGTCGTGATTAGCGATGA	AATGTGATGGCCTCCCATCTCCTTCATGACAT

2.2.12 HFD Model

8-10 weeks old mice (C57BL/6JRcc) were orally gavaged with 50 nm and 500 nm polystyrene particles as described in the chronic ingestion model. Two weeks prior to the start of MNP exposure, mice were switched from a chow diet to a control diet (CD, 13 kJ % fat) (Sniff, E15748-047). After 8 weeks of MNP administration, the diet was switched to a high-fat diet (HFD, 60 kJ % fat) (sniff, E15742-347) for 10 weeks. This included 4 weeks of simultaneous MNP and HFD exposure, followed by 6 weeks on HFD alone after the final MNP gavage.

2.2.13 Glucose and insulin tolerance test

Glucose tolerance tests (GTT) or insulin tolerance tests (ITT) were performed were performed after 9-10 weeks on CD and after 9-10 weeks on HFD. A drop of blood from the nicked tail vein was used to determine the basal glucose concentration using AccuChec Instant test strips (C216796165-IMP, Roche) after 6 h of fasting for GTT and without fasting for ITT. Then, mice were injected intraperitoneally (i.p.) with 0.5 µg/µL glucose at a dose of 2 mg/g of body weight or 0.25 U/ml insulin (Caninsulin® 40 I.E./ml) at a dose of 2.5 U/kg of body weight. Blood glucose levels were subsequently measured at 15, 30, 45-, 60-, 90- and 120-minutes post-injection.

2.2.14 Platelet depletion assay

To assess KC phagocytic function, platelet depletion assay was used. To measure the platelet baseline levels, blood was harvested via retro-orbital bleeding using heparinized micro-hematocrit capillary tubes (VWR, MODU163613). The collected blood was then immediately transferred into EDTA-coated tubes to prevent coagulation. Samples were gently inverted several times to ensure thorough mixing with the anticoagulant. Platelet levels were measured in blood harvested retro-orbitally using a Advia 2120 Hemocytometer (Siemens). Next,

0.37 µg/gr BW of 6A6-IgG2c anti-platelet antibody (provided by Prof. Falk Nimmerjahn, chair of genetic, Erlangen university) was injected i.p., and blood was sampled after 4-, 8-, 24- and 72-hours to assess for platelet counts using an ADVIA 2120 hemocytometer.

2.2.15 *E. coli* infection model

To assess Kupffer cell (KC) capacity to clear circulating pathogens, mice were injected intravenously (i.v.) with either a single dose of 1×10^7 CFU/20 g body weight (BW) or a lower dose of 1×10^6 CFU/20 g BW of ampicillin-resistant E. coli K-12 (provided by the lab of Prof. Imgard Förster, LIMES institute). The high-dose group was sacrificed 5 minutes post-injection, while the low-dose group was maintained for 24 hours, with an interim blood collection from the facial vein 2 hours post-infection.

At the designated endpoints, mice were anaesthetized, and blood was collected from the vena cava. Cardiac perfusion with ice-cold PBS was then performed, then liver and spleen were collected. Subsequently, liver and spleen were homogenized in PBS using Precellys 24 Tissue Homogenizer with glass beads (Sigma-Aldrich G1152-100G). To determine colony-forming units (CFUs), serial dilutions of blood, as well as liver and spleen homogenates, were plated on LB agar plates containing 100 µg/ml ampicillin (Carl Roth, K029.2) and incubated overnight at 37°C. Colonies were counted the next day to calculate CFUs, which were normalized to organ weight.

2.2.16 Malaria infection model

To assess KC function in a chronic, recurring malaria infection model, mice were injected i.p. with 200 µL of a suspension containing 10,000 *Plasmodium chabaudi*-infected red blood cells (iRBCs), harvested from a donor mouse. The *Plasmodium chabaudi* is from the lab of Prof. William Heath, Peter Doherty Institute, Melbourne (provided by Prof. Kevin Couper). Parasitemia, defined as the percentage of iRBCs in blood, was monitored on post-infection days 3, 7, 10, 14, 17, 21, 24, 28, and 31.

For parasitemia quantification, blood samples were collected from the tail vein, stained with Hoechst (10 µg/mL) (Thermo Fisher, H1398) for 1 hour at 37°C, and analyzed using a BD FACS Symphony flow cytometer. iRBCs were gated as illustrated in **Figure 2**.

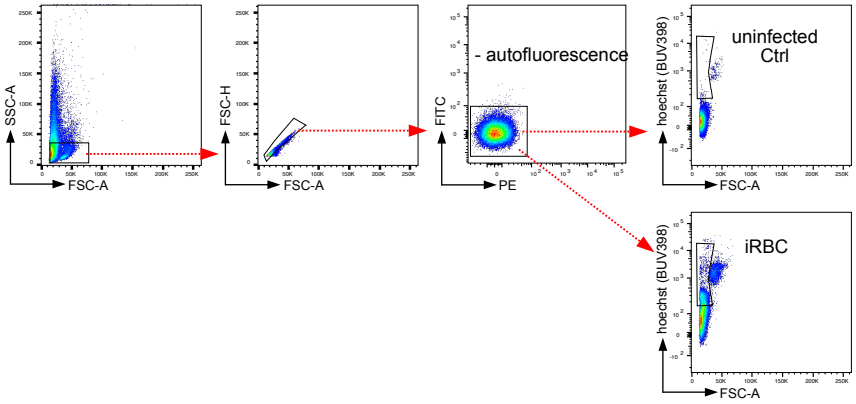

Figure 2 Gating strategy to determine parasitemia.

2.2.17 Apoptotic cell-induced autoimmune response model

2.2.17.1 Apoptosis induction and *in vivo* administration of apoptotic cells

Thymocytes were isolated from 4- to 5-week-old, sex-matched B6 mice and cultured for 6 hours in complete RPMI (PAN-Biotech, P04-16500) supplemented with 5 µM dexamethasone (Sigma-Aldrich, D4902) at 37°C and 5% CO_2. Apoptosis was confirmed by Annexin V (BioLegend, 640941) and 7-aminoactinomycin D (7-AAD) (Merck, SML1633) staining following the manufacturer's instructions., showing approximately 50-60% apoptotic cells and 2% necrotic cells. For the autoimmune response induction, 2 × 10^7 ACs per mouse were administered i.v. as described in Duhlin et al. (193). Briefly, the mice received i.v. injection of ACs over five weeks to break immune tolerance. At days 105 and 140, additional booster injections were administrated to assess the memory response to self-antigens.

2.2.17.2 Anti-DNA IgG autoantibodies ELISA

Serum anti-DNA IgG autoantibodies levels were quantified by ELISA, as previously described (193). Briefly, ELISA plates (Deepwell low binding 96-well plate, Eppendorf, 0030504100) were precoated with 100 µL per well of 5 µg/mL methylated BSA (Sigma-Aldrich, A1009-1G) in PBS and incubated for 2 hours at room temperature (RT). After coating, plates were washed three times with PBS (200 µL per well).

The plates were then incubated overnight at 4°C with 100 µL per well of 50 µg/mL calf thymus DNA (Sigma-Aldrich, D4522) in PBS. The following day, plates were washed three times with PBS and blocked with 150 µL per well of blocking buffer (PBS containing 3% BSA, 1 mM EDTA, and 0.1% gelatin) for 2 hours at RT then washed.

Serum samples were diluted 1:100 in blocking buffer, and 100 µL per well were incubated at RT for 2 hours. Following the incubation, plates were washed three times with blocking buffer (150 µL per well), and 100 µL per well of Horseradish Peroxidase conjugated (HRP) Goat anti-Mouse IgG Antibody (Bethyl Laboratories, A90-116P) (1:4000 in blocking buffer) was added for 1 hour at RT.

The wells were washed three times with blocking buffer, followed by two washes with PBS (200 µL per well). TMB substrate solution (Thermo Fisher, 34021) (100 µL per well) was added and the plates were incubated at RT until the desired color intensity developed. The reaction was stopped by adding 100 µL of 0.16 M sulfuric acid (Sigma-Aldrich. 258105-500ML).
The absorbance was measured at 450 nm using a Tecan Infinite M200 plate reader. All samples were run in duplicates and corrected for background binding.

2.2.18 Assessment of blood-brain barrier permeability using Evans Blue dye

To evaluate BBB integrity, mice were injected i.p. with 4 µl/g body weight of Evans Blue dye (Sigma-Aldrich; E2129) (2% (w/v) in PBS). After 30 minutes, mice were anesthetized, and brains were collected before perfusion. For microscopic analysis, one hemisphere was processed as described in method section 2.5.
For the Evans Blue assay, the other hemisphere was weighed, finely minced in 1 ml of formamide (Thermo Fisher Scientific, AM9342), and incubated for 48 hours at 60°C to extract the dye. Thereafter, the tissue was centrifuged at 300 x g for 5 minutes, filtered through 100 µm strainer, then and centrifuged at 10,000 × g for 20 minutes to precipitate proteins. The supernatant was collected, and the absorbance of Evans Blue was measured at 620 nm using a Tecan Infinite M200 plate reader. The concentration of extravasated Evans Blue was quantified by comparison to a standard curve and expressed as micrograms of dye per gram of brain tissue.

2.2.19 Behavioral assays

All behavioral assays were performed by the lab of Prof. Martin Fuhrmann (DZNE, Bonn).

2.2.19.1 Open field

To assess the exploratory behavior of MNP-exposed mice compared to control mice, an open field test was conducted. Mice were individually placed in a 50 × 50 cm open field arena for 15 minutes. Their movements during exploration were recorded using a video camera and analyzed with EthoVision XT software (Noldus).

2.2.19.2 Novel object recognition test

To assess recognition memory and exploratory behavior, a novel object recognition (NOR) test was conducted over two consecutive days. On Day 1, mice underwent a habituation phase followed by an initial testing phase. During habituation, four mice were simultaneously placed in individual 50 × 50 cm open field arenas, each containing two identical objects (cell culture bottles with blue liquid, designated as objects A). Mice explored the arena for 3 trials each for 5 minutes, with a 15-minute break between trials. Five hours after habituation, the initial testing phase (Trial 1) was conducted by replacing one of the A objects with a colorful Lego building block structure (object B) in each arena. Mice were again placed in the arenas for 5 minutes,

and their interactions with the familiar (object A) and novel (object B) objects were recorded using a video camera and analyzed as described in the open field test.

On Day 2, 24 hours after Trial1, memory retention was evaluated by introducing a new novel object. The Lego structure (object B) was replaced with a small bottle containing clear water (object C). Mice were reintroduced to the arenas for a 5-minute exploration period, and their interactions with both the familiar (object A) and the new novel (object C) objects were recorded and analyzed using the same method.

Discrimination index DI is calculated as the following:

$$DI\ (\%) = \frac{time\ spent\ at\ the\ novel\ object}{time\ spent\ at\ both\ objects} \times 100$$

2.2.19.3 Social discrimination test

To evaluate social discrimination behavior, a social discrimination test was conducted over four days. During the first three days (habituation phase), four mice were simultaneously placed in individual 50 × 50 cm open field arenas, each two empty metal cages. Mice were allowed to acclimatize to the environment for 5 minutes per session.

On Day 4, social interaction was assessed through two trials. In Trial 1, a second mouse was placed inside one of the metal cages, while the other cage remained empty. One experimental mouse was placed in the arena for a 6-minute exploration period. The interaction with the caged mouse and the empty cage were recorded and analyzed as described in the open field test. After a 1.5-hour interval, Trial 2 was conducted to assess social discrimination. A third mouse was introduced into the previously empty metal cage in arena. The experimental mice were reintroduced to the arenas for an additional 6-minute exploration period. The exploration behavior, including the preference for the novel mouse over the familiar one, was recorded and analyzed using the same methodology as in Trial 1. Discrimination index DI is calculated as the described in the novel object recognition test.

Throughout all behavioral tests, arenas were cleaned between sessions to minimize olfactory cues.

2.2.20 Single-cell RNA-sequencing library preparation and analysis

Single-cell suspensions of the cortex were prepared as previously described. Subsequently immune cells were enriched using CD45 MicroBeads (Miltenyi, Cat130-052-301) according to the manufacture's instruction. The cells were resuspended in 500 µl RPMI (PAN-Biotech, P04-16500) and 2 mM flavopiridol (Sigma, Cat. F3055). Cell loading, barcoding and library preparation primarily followed the Seq-Well S3 protocol (194), with two arrays per sample. Seq-Well arrays were set up as described by (195). Each array was loaded with approximately 110,000 barcoded mRNA capture beads (ChemGenes, Cat: MACOSKO-2011-10) and 30,000 cells. Following cell loading, cells were lysed, mRNA captured, and cDNA synthesis was performed. For whole transcriptome amplification, beads from each array were divided into

18-24 PCR reactions with approximately 3,000 beads per reaction (95°C for 3 min, 4 cycles of 98°C for 20 s, 65°C for 45 s, 63°C for 30 s, 72°C for 1 min; followed by 16 cycles of 98°C for 20 s, 67°C for 45 s, 72°C for 3 min; final extension at 72°C for 5 min) using the KAPA HiFi Hotstart Readymix PCR Kit (Kapa Biosystems, Cat: KK2602) and SMART PCR Primer (AAGCAGTGGTATCAACGCAGAGT). Pooled PCR reactions (6-8 per pool) were purified using AMPure XP SPRI Reagent (Beckman Coulter) with sequential 0.6x and 1x volumetric ratios. For library tagmentation and indexing, 200 pg of DNA from each purified WTA pool was tagmented with the Nextera XT DNA Library Preparation Kit (8 min at 55°C) (Illimina, FC-131-1024), followed by Tn5 transposase neutralization (5 min at RT). Illumina indices were then attached to the tagmented products (72°C for 3 min, 98°C for 30 s; 16 cycles of 95°C for 10 s, 55°C for 30 s, 72°C for 1 min; final extension at 72°C for 5 min). The library products were purified using AMPure XP SPRI Reagent at 0.6x and 1x volumetric ratios. The final library quality was assessed using a High Sensitivity D5000 assay on a Tapestation 4200 (Agilent) and quantified with the Qubit high-sensitivity dsDNA assay (Invitrogen). Seq-Well libraries were pooled equimolarly and clustered at a 1.25 nM concentration with 10 % PhiX on a NovaSeq6000 system (S2 flow cell, 100 bp v1.5 chemistry). The sequencing was performed in PRECISE Platform for Single Cell Genomics and Epigenomics (DZNE, Bonn). Sequencing was paired-end, using a custom Drop-Seq Read 1 primer for 21 cycles, 8 cycles for the i7 index, and 61 cycles for Read 2. Single-cell data were demultiplexed using bcl2fastq2 (v2.20). Fastq files from Seq-Well were processed in a snakemake-based pre-processing pipeline (v0.31, available at https://github.com/Hoohm/dropSeqPipe) that utilizes Drop-seq tools provided by the McCarroll lab (196) STAR alignment within the pipeline was performed using the murine GENCODE reference genome and transcriptome (mm10 release vM16; Team 2014).

Downstream analysis was performed using Seurat (v4.1.1) with default preprocessing parameters. Cells expressing at least 200 genes in a minimum of three cells were retained. Further filtering excluded cells with fewer than 200 detected features or more than 2500, alongside cells with more than 5% mitochondrial RNA content. Normalization and scaling followed Seurat's standard pipeline.

UMAPs were generated using the first 10 principal components (PCs), with clustering performed at a resolution of 0.8 Cell clusters were annotated using a known marker gene panel. For microglia sub-clustering, the first 10 PCs were used with a clustering resolution of 0.3. Differential expression and overrepresentation analyses (ORA) were performed for microglia, comparing each plastic treatment to the PBS control. Genes were included in the analysis if expressed in at least 5% of cells using adjusted p value ≤ 0.1, $\log_2$FC ≥ 0.25 or ≤ -0.25. The ORA utilized the clusterProfiler (v4.10.0) package, querying the Hallmark, Reactome, and Gene Ontology (GO)-Biological Process (BP) databases. To maintain

biological relevance, GO BP terms were restricted to the first four hierarchical levels, excluding highly specific child terms (e.g., positive or negative regulation). Gene sets with fewer than 10 or more than 300 genes were omitted. Pathways were considered significant if they had a false discovery rate (FDR) ≤ 10% and included at least three genes.

2.2.21 Single nuclei RNA sequencing: preparation and analysis

2.2.21.1 Tissue homogenization

Nuclei were isolated from approximately 100 mg of fresh-frozen adult liver tissue to enable single-nucleus RNA sequencing (snRNA-seq). Liver tissue was minced, and then immediately transferred into a homogenizer containing 1 ml of ice-cold homogenization buffer (**Table 5**). Tissues were homogenized using a glass douncer with five strokes of pestle A and ten strokes of pestle B. The homogenate was passed through a 70 µm cell strainer into a 50 ml falcon tube, and the strainer was washed with 1.65 ml homogenization buffer to achieve a final volume of 2.65 ml. Subsequently, 2.65 ml of gradient medium (**Table 5**) was added to the sample to reach a total volume of 5.3 ml.

2.2.21.2 Nuclei Isolation and sorting

A 4 ml layer of 29% cushion (**Table 5**) was prepared in ultracentrifuge tubes. The homogenized sample was carefully layered on top of the cushion using a low retention P1000 pipette to avoid disturbing the interface. Tube weights were balanced using homogenization buffer. Centrifugation was performed using an JS13.1 rotor in Avanti high-speed centrifuge (Beckman Coulter) at 10,000 x g, with low acceleration and maximum deceleration at 4°C for 30 minutes. Following centrifugation, supernatants were gently removed, the nuclei were resuspended in 400 µL of resuspension buffer (**Table 5**) and passed through a 0.35 µm filter into a FACS tube. Nuclei were stained with 1 µg/ml DAPI, and mononuclei were sorted using Aria III cell sorter (BD biosciences) into 200 µl of 10X resuspension buffer. After sorting the volume was adjusted in which the nuclei were in 1X resuspension buffer.

2.2.21.3 snRNA-seq Library Construction

Next, the nuclei were centrifuged at 400 × g for 3 minutes, followed by 600 × g for 5 minutes at 4°C. The pellet was then resuspended in 100 µl of resuspension buffer. After assessing the nuclei count, the concentration was adjusted to 1100 nuclei/µl to prepare the nuclei stock suspension. Further, 16,000 nuclei were loaded and used for analysis with the Chromium Single Cell 3' Gene Expression v3.1 Dual Index Kit (10x Genomics, PN-1000269) and Gel Beads in Emulsion (GEMs) using the Chromium Next GEM Chip G Single Cell Kit (10x Genomics, PN-1000127). After GEM-RT cleanup, pre-amplification of the sample was performed, producing material for cDNA amplification for gene expression library construction. During the reverse transcription (RT) reaction, cDNA tagging was achieved with 16-nucleotide barcodes and 10-nucleotide molecular identifiers followed by using 35 µl for further cDNA amplification. For snRNA-seq library preparation, 25 % of the total cDNA was used to generate

gene expression (GEX) libraries. Libraries were prepared and sequenced according to the manufacturer's protocol using the Dual Index TT Set A (10x Genomics, PN-1000215). Final library quality was assessed using a High Sensitivity D5000 assay on a Tape station 4200 (Agilent) and quantified using the Qubit high-sensitivity dsDNA assay (Invitrogen). Pooled and barcoded libraries were sequenced on an Illumina NextSeq 2000 system with P4 flow cells, achieving an average depth of 30,000 reads per nucleus. The sequencing was performed by Genomics Core Facility (EMBL, Heidelberg) All plastic tubes used for this nuclei isolation where precoated with 1 % BSA in PBS overnight.

2.2.21.4 Bioinformatics analysis

Single-nuclei RNA sequencing data were processed using CellRanger (v7.1.0) for read alignment and gene quantification. Downstream analysis was performed using Seurat (v5.0.1) with default preprocessing parameters. Nuclei expressing at least 200 genes in a minimum of three nuclei were retained. Further filtering excluded nuclei with fewer than 600 detected features or more than 30% mitochondrial RNA content. Normalization and scaling followed Seurat's standard pipeline. UMAPs were generated using the first 20 principal components (PCs), with clustering performed at a resolution of 0.5. Cell clusters were annotated using a known marker gene panel. Doublet detection and removal were conducted using DoubletFinder (v2.0.4) with an assumed doublet rate of 25%. The optimal pK parameter (0.001) was determined using the paramSweep function. After doublet exclusion, singlet neclei were re-embedded with the same UMAP parameters, and clustering was repeated at a resolution of 0.2. Mixed annotation clusters were removed before further analysis. For Kupffer cell sub-clustering, the first 20 PCs were used with a clustering resolution of 0.3. Differential expression and overrepresentation analyses (ORA) were performed for hepatocytes and Kupffer cells, comparing each plastic treatment to the PBS control. Genes were included in the analysis if expressed in at least 5% of cells. The ORA utilized the clusterProfiler (v4.10.0) package, querying the Hallmark, Reactome, and Gene Ontology (GO)-Biological Process (BP) databases. To maintain biological relevance, GO BP terms were restricted to the first four hierarchical levels, excluding highly specific child terms (e.g., positive or negative regulation). Gene sets with fewer than 10 or more than 300 genes were omitted. Differentially expressed genes were defined using adjusted p-value and $\log_2$ fold change ($\log_2$FC) thresholds: Hepatocytes: Adjusted $p \leq 0.05$, $\log_2FC \geq 0.75$ or ≤ -0.75, Kupffer cells: Adjusted $p \leq 0.1$, $\log_2FC \geq 0.25$ or ≤ -0.25. Pathways were considered significant if they had a false discovery rate (FDR) ≤ 10% and included at least three genes. Cell-cell communication between hepatocytes and Kupffer cells under each plastic treatment relative to PBS was assessed using CellChat (v1.6.0) with default parameters. Genes were considered overexpressed if detected in at least 10% of cells, with a minimum of 10 cells per group required for interaction inference.

Table 5 snRNA-seq buffers

	Ingredient	Final concentration
Homogenization buffer	Sucrose	320 mM
	$CaCl_2$	5 mM
	Mg Acetate	3 mM
	Tris pH = 8	10 mM
	EDTA	0.1 mM
	Igepal	0.10%
	PMSF	0.1 mM
	RNase inhibitor	0.2 U/µL
	Flavopiridol	1 µM
	β-mercaptoethanol	1 mM
		In UltraPure H_2O
Gradient Medium	$CaCl_2$	5 mM
	OptiPrep	50%
	Mg Acetate	3 mM
	Tris pH = 8	10 mM
	PMSF	0.1 mM
	β-mercaptoethanol	1 mM
	In UltraPure H_2O	
Optiprep Diluent Medium (ODM)	KCl	150 mM
	$MgCl_2$	30 mM
	Tris pH = 8	60 mM
	Sucrose	250 mM
	In UltraPure H_2O	
29% Cushion	OptiPrep	29%
	in ODM	
Resuspension buffer	BSA cell culture based	1%
	RNase inhibitor	0.2 U/µL
	Flavopiridol	1 µM
	in PBS	

2.2.22 Microbiome analysis

2.2.22.1 DNA extraction

DNA was isolated from approximately 100 mg of fecal and cecal samples of using ZR BashingBead lysis tubes (Zymo Research, S6012-50) combined with the chemagic DNA Stool

200 Kit H96 (Perkin Elmer, CMG-1076), according to the manufacturer's instructions (197–199). An additional mechanical lysis step was carried out by adding the lysis buffer and using the Precellys 24 Tissue Homogenizer (Bertin Instruments). After DNA extraction, the samples were stored at -20°C until further processing.

2.2.22.2 16S rRNA library preparation & sequencing

Amplicon sequencing was carried out on fecal and cecal samples to assess their metagenomic composition. The V3-V4 region of the 16S rRNA gene was amplified in the initial PCR step using the primer pair Bakt_341F (5'-CCTACGGGNGGCWGCAG-3') and Bakt_805R (5'-GACTACHVGGGTATCT AATCC-3'). The amplified products were barcoded and pooled in equimolar concentrations at 4 nM, as described in Seel et al. (200). The final pooled sample was quantified using the Qubit dsDNA HS Assay Kit (Thermo Fisher Scientific, Q32851), and the fragment sizes were validated with a D1000 ScreenTape. Sequencing was performed on an Illumina MiSeq platform with the MiSeq Reagent Kit v3 (Illumina, 20037124), employing a 2 × 300 cycle configuration. Clustering was performed at a final loading concentration of 8 pM with a 30 % Phi-X spike-in.

2.2.22.3 Bioinformatics

The 16S sequencing data were processed using QIIME 2 version 2022.8 (201), with sequence quality control and denoising performed using DADA2 (202). The denoised sequences were classified using SILVA SSU 138 database to annotate amplicon sequencing variants (ASVs) for sequences with >99% sequence similarity. A rarefied table with a sampling depth of 14904 reads was used to calculate alpha and beta diversity metrics as alpha diversity metrics including Observed features, Shannon entropy for alpha diversity, and Bray-Curtis for beta diversity.

2.2.23 Illustrations and schematic representations

Illustrations and schematic representations were created using BioRender.

2.2.24 Statistics

Statistical tests were carried out with GraphPad Prism 10 (GraphPad Software Inc). To test for normal distribution of data, D'Agostino-Pearson omnibus normality test was used for sample sizes of n>6 and the Shapiro-Wilk normality test for n<6. One-way ANOVA with FDR correction for multiple comparison test were performed on normally distributed data sets, if normally distributed. For not normally distributed data sets the Kruskal-Wallis test was performed with FDR correction for multiple comparisons. When analyzing data with two independent factors (e.g., condition and time), Two-way ANOVA with Geisser-Greenhouse correction and multiple testing correction with false discovery rate. If not indicated differently, data are represented as mean ± SD. Outliers were identified using Grubbs' test (alpha = 0.05).

3 Results

3.1 **MNP cross the intestinal barrier and are engulfed by macrophages**

3.1.1 MNP cross the intestinal barrier

Numerous studies have demonstrated that MNP can cross the intestinal barrier and accumulate in various organs. To investigate the translocation of MNP into the body after ingestion, C57BL/6JRcc male mice were gavaged orally with negatively charged polystyrene (PS) particles in various sizes (50 nm, 100 nm, 200 nm, 300 nm and 500 nm) in a concentration of 100 mg/kg. Additionally, control mice received PBS (**Figure 3**A). Fluorescently labelled beads were used to allow for detection within tissues after administration. Within 24 hours post-gavage, MNPs crossed the gut barrier and were detected in various organs. Initially, the liver was examined as it is the first organ to receive blood from the gut. All the different sizes of polystyrene beads were detected in the liver by confocal microscopy (**Figure 3**B). Furthermore, immunofluorescence (IF) staining was performed using anti-Iba1 antibodies, a macrophage-specific calcium-binding protein. The MNP signals were overlapping with Iba1 signal, indicating the uptake of the beads by KCs (**Figure 3**B, white arrows). Similar observations were made in the spleen, which is responsible for the filtering of the blood, where also splenic macrophages were found to be engulfing MNP (**Figure 3**C).

Despite the protective function of the BBB in shielding the brain from substances in the bloodstream, nanoparticles measuring 50 nm and 100 nm were detected within the brain parenchyma. These particles were observed to be engulfed by microglia, as indicated by the overlap with the Iba-1 signal (**Figure 3**D, white arrows). In contrast, 300 nm and 500 nm microplastic particles were not detected in the brain (**Figure 3**D).

Altogether, ingested MNP can cross the intestinal barrier reaching the liver and the spleen where macrophages engulf them. Notably, only nanoplastic can pass the BBB and reach the brain parenchyma.

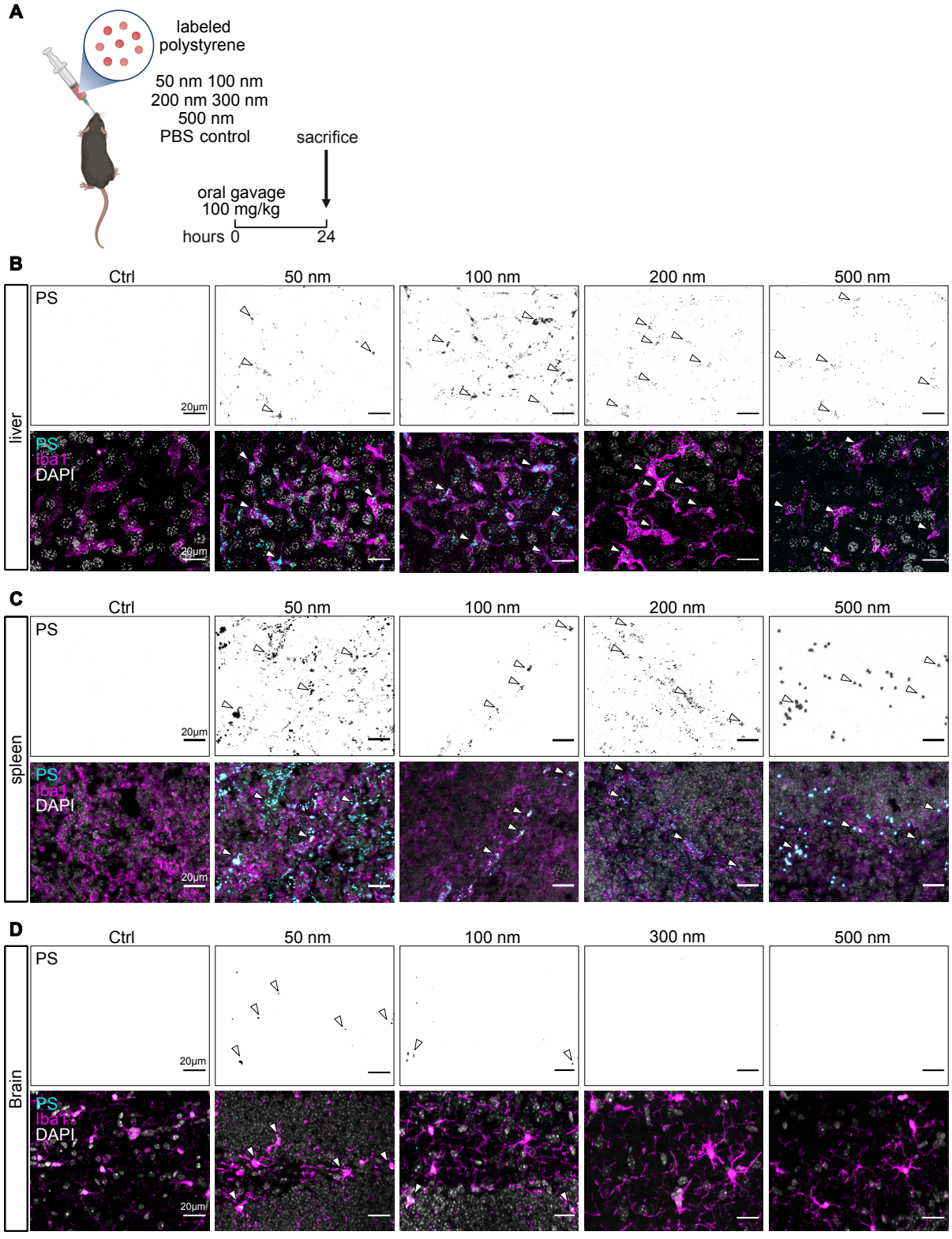

Figure 3 MNP cross the intestinal barrier: (A) Schematic representation of the experimental setup for MNP administration. (B-D) Representative images of immunofluorescence staining of the liver (B), the spleen (C), and the brain (D), upper panel showing the fluorescent PS-particles (indicated by arrows), lower panel showing the fluorescent PS-particles (cyan, arrows), Iba1 (magenta) and DAPI-stained nuclei (gray). Scale bars indicate 20 µm

3.1.2 MNP accumulate in tissue-resident macrophages across different organs over time

After demonstrating that MNP can pass the intestinal barrier, their subsequent accumulation in various organs was examined following chronic ingestion. Oral gavage was performed weekly with negatively charged, fluorescently labelled nanoplastic (50 nm PS) or microplastic (500 nm PS) for 12 weeks. MNP were administered at a dose of 100 mg/kg. Control mice were gavaged weekly with PBS (**Figure 4**A). MNP accumulated in both the liver and spleen as shown by confocal microscopy analysis. In the liver, MNP were primarily engulfed by KCs. Furthermore, MNP signals overlapped with CD68, a macrophage marker that labels phagosomes (**Figure 4**B white arrows). Additionally, MNP were detected within $CD31^{+}$ endothelial cells (**Figure 4**C white arrows).

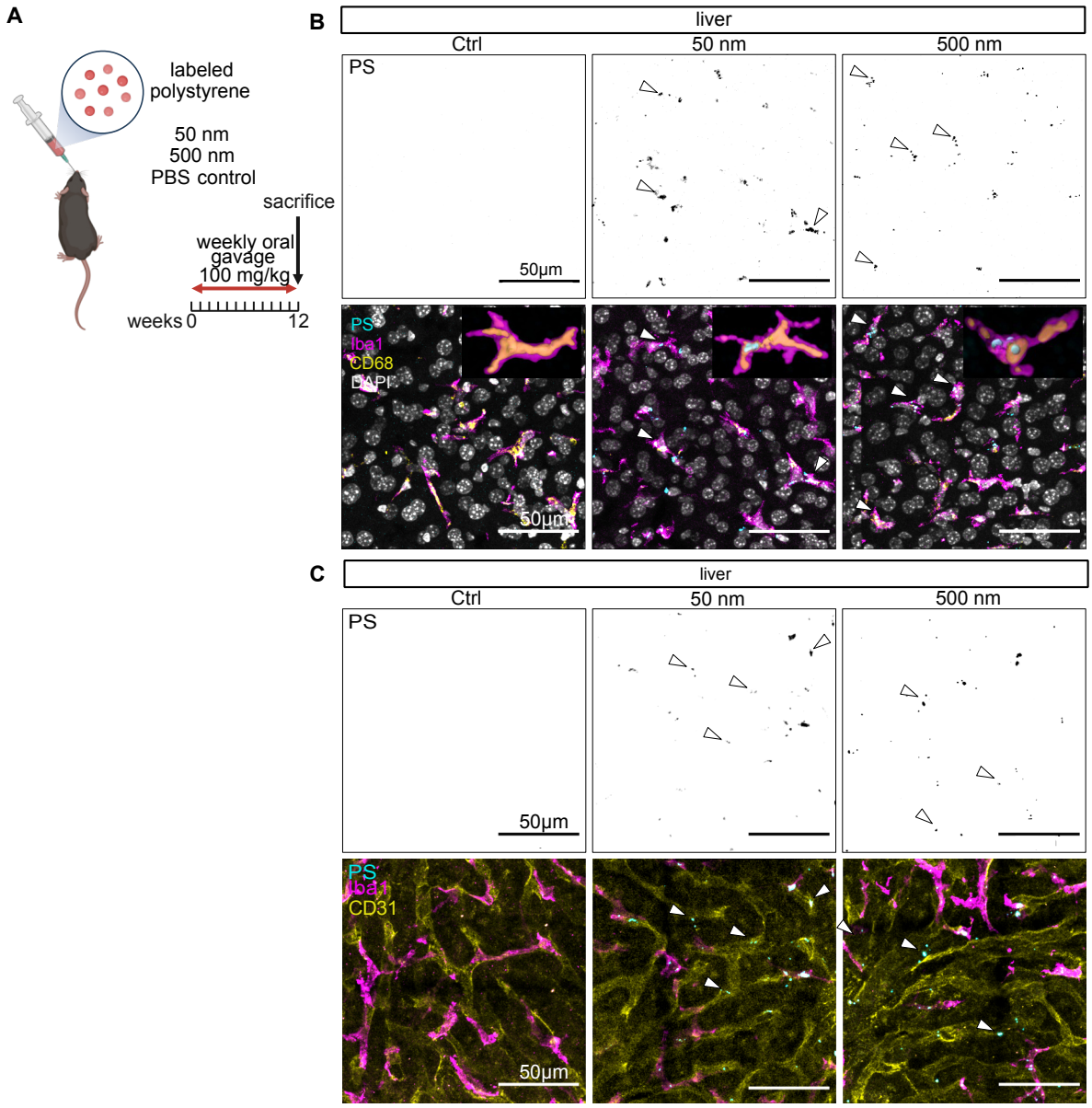

Figure 4 MNP accumulate in the liver following chronic ingestion: (A) Schematic representation of the experimental setup for chronic MNP administration. (B-C) Representative images of immunofluorescence staining of the liver. (B) Upper panel showing the fluorescent PS-particles (indicated by arrows), middle panel showing the fluorescent PS-particles (cyan, arrows), Iba1 (magenta), CD68 (yellow) and DAPI-stained nuclei (gray), lower panel

showing a 3D rendering of PS-particles within the phagosomes of KC. (C) Upper panel showing the fluorescent PS-particles (indicated by arrows), lower panel showing the fluorescent PS-particles (cyan, arrows), Iba1 (magenta), CD31 (yellow). Scale bars indicate 50 µm.

To further investigate the distribution of MNP among different cell types in the liver, flow cytometry analysis was performed. Flow cytometry analysis revealed no changes upon chronic plastic administration in the abundance of various myeloid cell populations in the liver, including KCs ($CD45^+$ $CD11b^{int}$ $F4/80^+$ $TIM\text{-}4^+$), monocytes ($CD45^+$ $CD11b^+$ $Ly6C^+$), granulocytes ($CD45^+$ $CD11b^+$ $Ly6G^+$), conventional dendritic cells- 1 and 2 (cDC1: $CD45^+$ $CD11c^+$ $MHCII^+$ $CD11b^{low}$, cDC2: $CD45^+$ $CD11c^+$ $MHCII^+$ $CD11b^{hi}$) (**Figure 5** A, B).

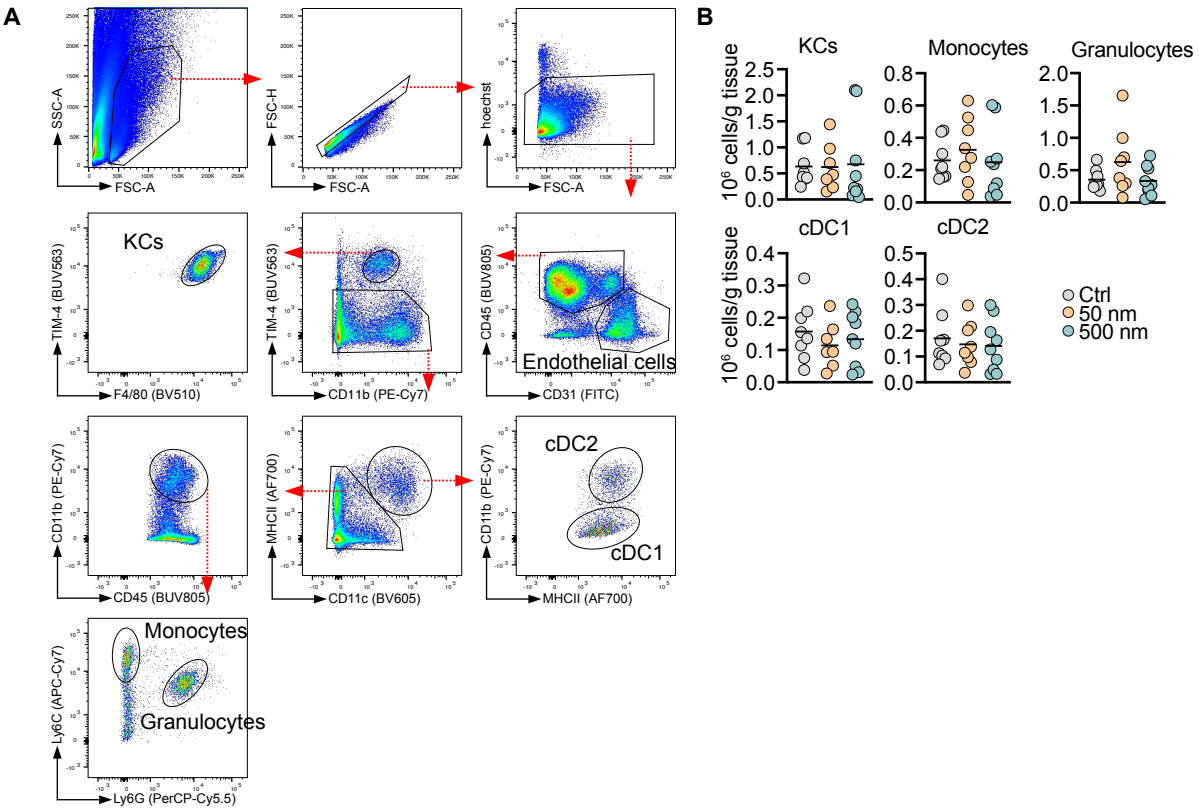

Figure 5 MNP ingestion does not affect the abundance of hepatic myeloid cells (A) Gating strategy of the myeloid cells in the liver. **(B)** the abundance of KCs, monocytes, granulocytes, cDC1 and cDC2, each dot represents an individual mouse, the horizontal line indicates the mean. n= 7-9 animals per condition. Ordinary one-way ANOVA.

It is important to note that the 50 nm particles exhibited lower fluorescence intensity than the 500 nm particles due to their smaller size. MNP-positive cells were gated on single live cells (**Figure 6**A) followed by the gating of various liver cell populations (Figure 5A). The data revealed that KCs were the primary scavengers of both 50 nm (~50 %) and 500 nm (~60 %) particles (**Figure 6**B). Additionally, endothelial cells ($CD45^-$ $CD31^+$), considered non-professional phagocytes, also engulfed MNP. Endothelial cells internalized a greater proportion of 50 nm particles (~25 %) compared to 500 nm particles (~8 %) (**Figure 6**B). Granulocytes and cDC2 internalized ~2 % and ~1.5% of MNP, respectively. Moreover, approximately 14% of the 50 nm and 24% of the 500 nm particles were taken up by

unidentified cells (**Figure 6**B). In contrast, cDC1 and monocytes, unlike KCs and endothelial cells, showed minimal particles uptake (**Figure 6**B).

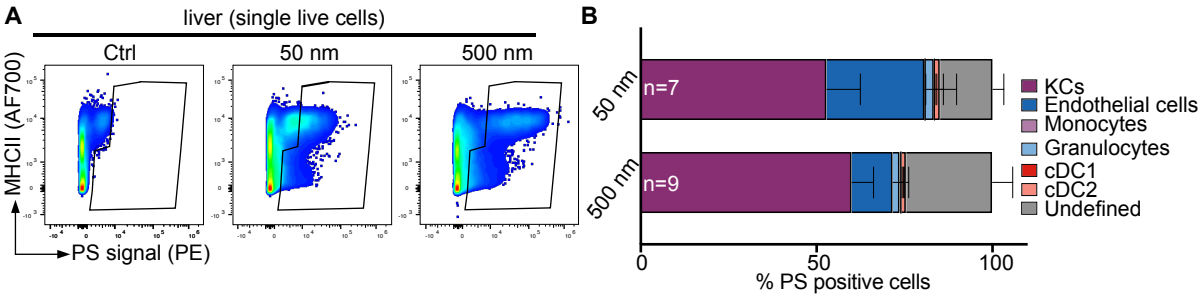

Figure 6 MNP are taken up by various of hepatic cell populations: (A) PS-positive cells gated on liver single live cells. **(B)** The distribution of PS-positive cells among the hepatic cell populations. n= 7-9 animals per condition.

After characterizing MNP distribution in hepatic cell types, the next objective was to examined MNP distribution in the spleen, another key organ involved in blood filtration and immune responses. Immunofluorescence images of the spleen also revealed MNP accumulation in the different splenic regions (**Figure 7**), including the red pulp, white pulp and the marginal zone, with their signals overlapping with Iba1 signal, suggesting uptake by macrophages.

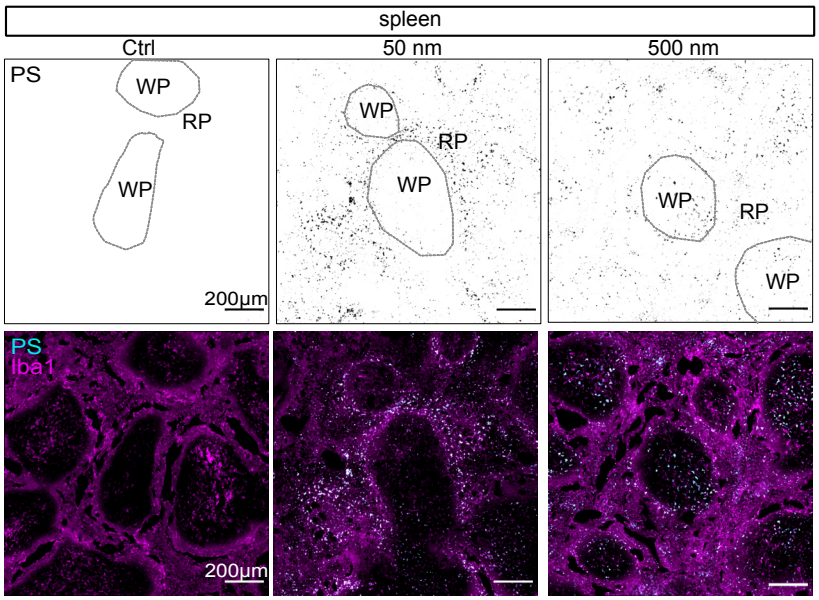

Figure 7 MNP accumulate in the spleen following chronic ingestion: Representative images of immunofluorescence staining of the Spleen: upper panel showing the fluorescent PS-particles and highlighting the regions of the white pulp (WP) and the red pulp (RP), lower panel showing the fluorescent PS-particles (cyan), Iba1 (magenta). Scale bars indicate 200 µm.

Similar to the liver, flow cytometry analysis was used on splenic cells to assess the uptake of 50 nm and 500 nm particles. The abundance of the different myeloid cell populations in the spleen, including CD163^{+} and CD163^{-} RPMs (CD45^{+} CD64^{+} F4/80), WPMs (CD45^{+} CD64^{+} F4/80^{-} CD11b^{hi} TIM-4^{-} MerTK^{+}), MMMs (CD45^{+} CD64^{+} F4/80^{-} CD11b^{hi} TIM-4^{+} CD169^{+}), MZMs (CD45^{+} CD64^{+} F4/80^{-} CD11b^{hi} TIM-4^{-} MACRO^{+}) granulocytes and cDCs (CD45^{+} CD11c^{+} MHCII^{+}), was not changed between the control and the MNP-exposed mice (**Figure 8**A, B).

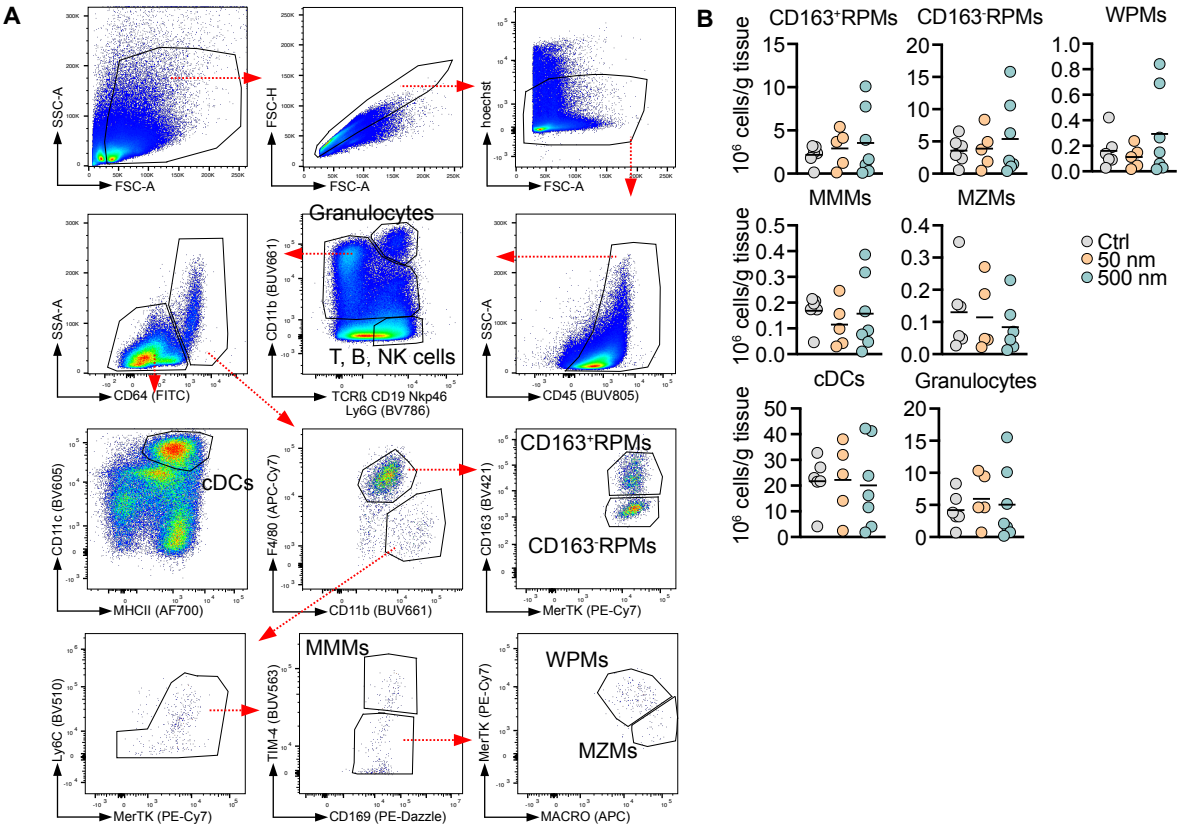

Figure 8 MNP chronic ingestion does not alter the abundance of splenic myeloid cells (A) Gating strategy of the myeloid cells in the spleen. **(B)** the abundance of CD163+ RPMs, CD163- RPMs, WPMs, MMMs, MZMs, granulocytes, cDCs, each dot represents an individual mouse, the horizontal line indicates the mean. n= 5-7 animals per condition. Ordinary one-way ANOVA.

MNP-positive cells were gated from live, single-cell populations (**Figure 9**A), followed by the identification of different immune cell populations (**Figure 9**A).The results revealed distinct patterns of particle uptake in the spleen compared to the liver. However, macrophages composed the majority of MNP-positive cells, accounting for 32 % of captured MNP, which is consistent with observations in the liver (**Figure 9**B). The $CD163^{+}$ and $CD163^{-}$ RPMs, captured 28 % of 50 nm and 26% of 500 nm particles. WPMs and MMMs each captured approximately 1.1-3 % of the MNP, whereas MZMs contribution to MNP clearance was minor (**Figure 9**B). In contrast, other myeloid cell populations, such as cDCs and granulocytes, exhibited higher MNP uptake compared to the liver. cDCs constituted 8 % and 5 % of the 50 nm and 500 nm positive cells, respectively, while granulocytes accounted for 14 % of the 50 nm and 16 % of the 500 nm positive cells (**Figure 9**B).

Interestingly, lymphocytes and natural killer (NK) cells, identified as a mixed $CD19^{+}$ $TCR\beta^{+}$ $Nkp46^{+}$ population, also captured MNP, representing 7 % and 19 % of 50 nm and 500 nm positive cells, respectively. Finally, 37 % of 50 nm and 27 % of 500 nm positive cells remained unidentified (**Figure 9**B).

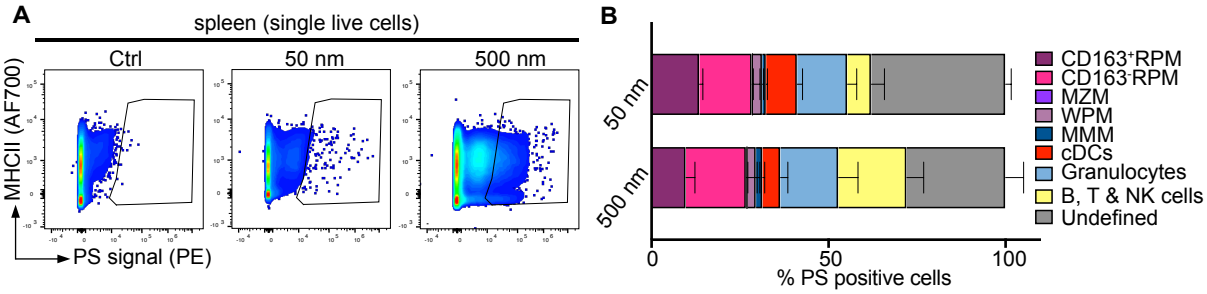

Figure 9 MNP are taken up by different splenic cells: (A) PS-positive cells gated on splenic single live cells. **(B)** The distribution of PS-positive cells across splenic cell populations. n= 3-6 animals per condition

Taken together, chronic exposure to MNP results in their accumulation in various organs. The liver and spleen play a major role in clearing the particles, with tissue-resident macrophages capturing the highest proportion.

3.1.3 Long-term retention of MNP in organs following chronic exposure

After confirming the accumulation of MNP, attention was directed toward their long-term retention within organs following chronic exposure, especially given the non-biodegradable nature of PS. Similar to the previous experimental design, oral gavage was performed weekly for 12 weeks using 50 nm and 500 nm negatively charged, fluorescently labeled PS particles, while control mice received PBS. After the 12-week treatment period, mice were maintained for another 26 weeks prior to sacrifice (**Figure 10**A). Interestingly, the immunofluorescence staining of the liver sections revealed the retention of the MNP even after 26 weeks from the last gavage (**Figure 10**B). This finding suggests that MNP have a prolonged presence in the liver, which may contribute to cumulative long-term biological effects or toxicity.

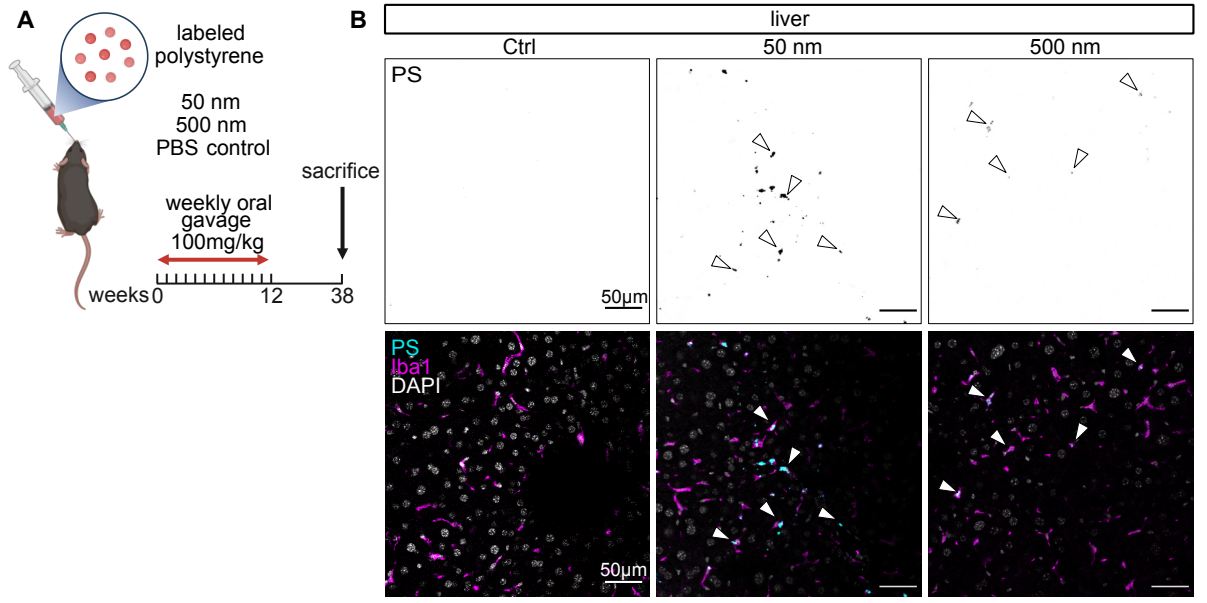

Figure 10 MNP long-term retention in the liver: (A) Schematic representation of the experimental setup for chronic MNP ingestion. **(B)** Representative images of immunofluorescence staining of the liver, upper panel showing the fluorescent PS-particles (indicated by arrows), lower panel showing the fluorescent PS-particles (cyan, arrows), Iba1 (magenta) and DAPI-stained nuclei (gray). Scale bars indicate 50 µm.

3.2 **Chronic ingestion of MNP alters physiological functions**

3.2.1 MNP do not trigger systemic inflammatory response after chronic ingestion

The next objective was to investigate how MNP affect physiological functions. Given their accumulation in various organs, particularly in immune cells, it was important to determine whether they could trigger systemic inflammation. To assess this, serum levels of several inflammatory markers were measured using the xMAP® INTELLIFLEX system from Luminex, a flow-based multiplex platform.Serum was collected from mice that had received MNP via oral gavage for 12 weeks (**Figure 4**A). No evidence of systemic inflammation was observed based on cytokine profiling. Key pro-inflammatory cytokines, including IL-1β, interleukin-1α (IL-1α), the bioactive form of interleukin-12 (IL-12p70), interleukin-18 (IL-18), interleukin-22 (IL-22), interleukin-23 (IL-23), granulocyte colony-stimulating factor (G-CSF), granulocyte-macrophage colony-stimulating factor (GM-CSF), receptor activator of nuclear factor κb ligand (RANKL), and B-cell activating factor (BAFF), as well as chemokines such as C-C motif chemokine ligand 7 (CCL7) and C-X-C motif chemokine ligand 5 (CXCL5) were all comparable between MNP-treated and control mice (**Figure 11**). However, interleukin-17A (IL-17A) displayed lower levels especially in serum from 50 nm plastic-treated mice (**Figure 11**). Similarly, serum levels of interleukin-2 receptor (IL-2R), a marker of immune activation, were reduced, with a significant decrease observed in the 50 nm group (**Figure 11**).

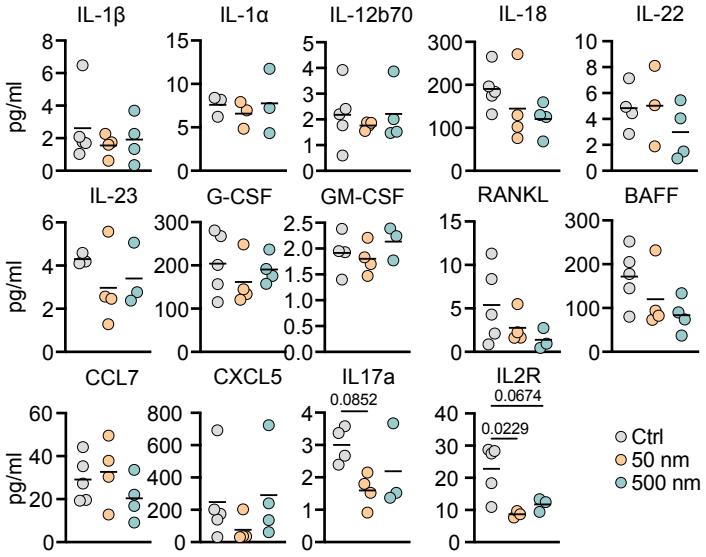

Figure 11 MNP chronic Ingestion triggers no systemic inflammation: serum levels of various cytokines and chemokines, each dot represents an individual mouse, the horizontal line indicates the mean. n= 3-5 samples per condition. Ordinary one-way ANOVA.

Additionally, flow cytometry analysis of blood revealed no changes in Ly6C^{high} and Ly6C^{low} monocytes (gated as CD115^{+} CD11b^{+}) or granulocytes (gated as Ly6G^{+} CD11b^{hi}) in MNP-treated mice compared to control mice (**Figure 12** A, B). Similar findings were observed for T cells (CD3^{+} or TCRß$^{+}$), B cells (CD19^{+}) and NK cells (NKp46^{+}) (**Figure 12**A, B).

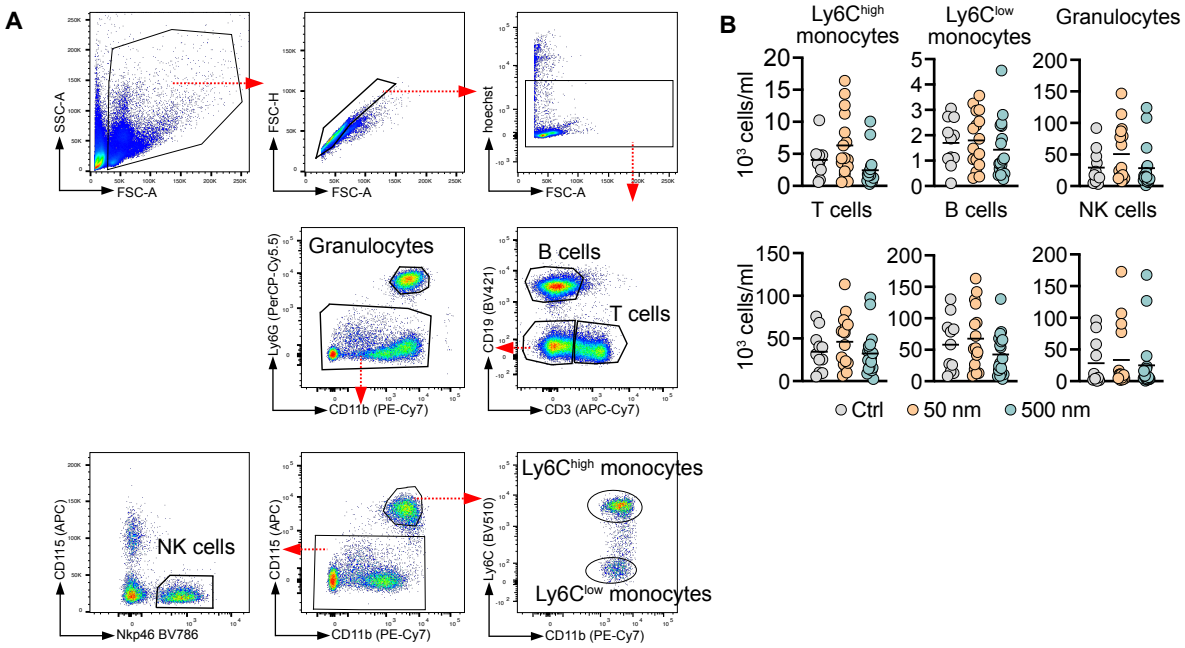

Figure 12 MNP chronic ingestion does not change the abundance of immune cells in the blood: (A) Gating strategy of the blood immune cells. **(B)** the abundance of Ly6C^{high} monocytes, Ly6Cl^{ow} monocytes, granulocytes, T cells, B cells and NK cells, each dot represents an individual mouse, the horizontal line indicates the mean. n= 11-18 animals per condition. Ordinary one-way ANOVA

In summary, these findings suggest that despite the accumulation of MNP in various organs, they do not lead to systemic inflammation or significant changes in immune cell populations within the blood.

3.2.2 Chronic MNP ingestion does not trigger behavioral deficit

3.2.2.1 Limited microglial response and preserved BBB integrity following chronic MNP exposure

Since PS-nanoparticles were shown to cross the BBB within 24 hours (**Figure 3**D), the brain was assessed to evaluate the influence of chronic MNP ingestion (**Figure 4**A). At the cellular level, flow cytometry analysis indicated no significant changes in the abundance of microglia (gated as CD45$^+$CD11b$^+$ CX3CR1$^+$), MHCII$^+$ and MHCII$^-$ border-associated macrophages (BAMs, gated as CD45$^+$CD11b$^+$ F4/80$^+$ CD206$^+$), monocytes (CD45$^+$ CD11b$^+$ Ly6C$^+$) and granulocytes (CD45$^+$ CD11b$^+$ Ly6G$^+$) in the cortex and hippocampus (**Figure 13**A, B).

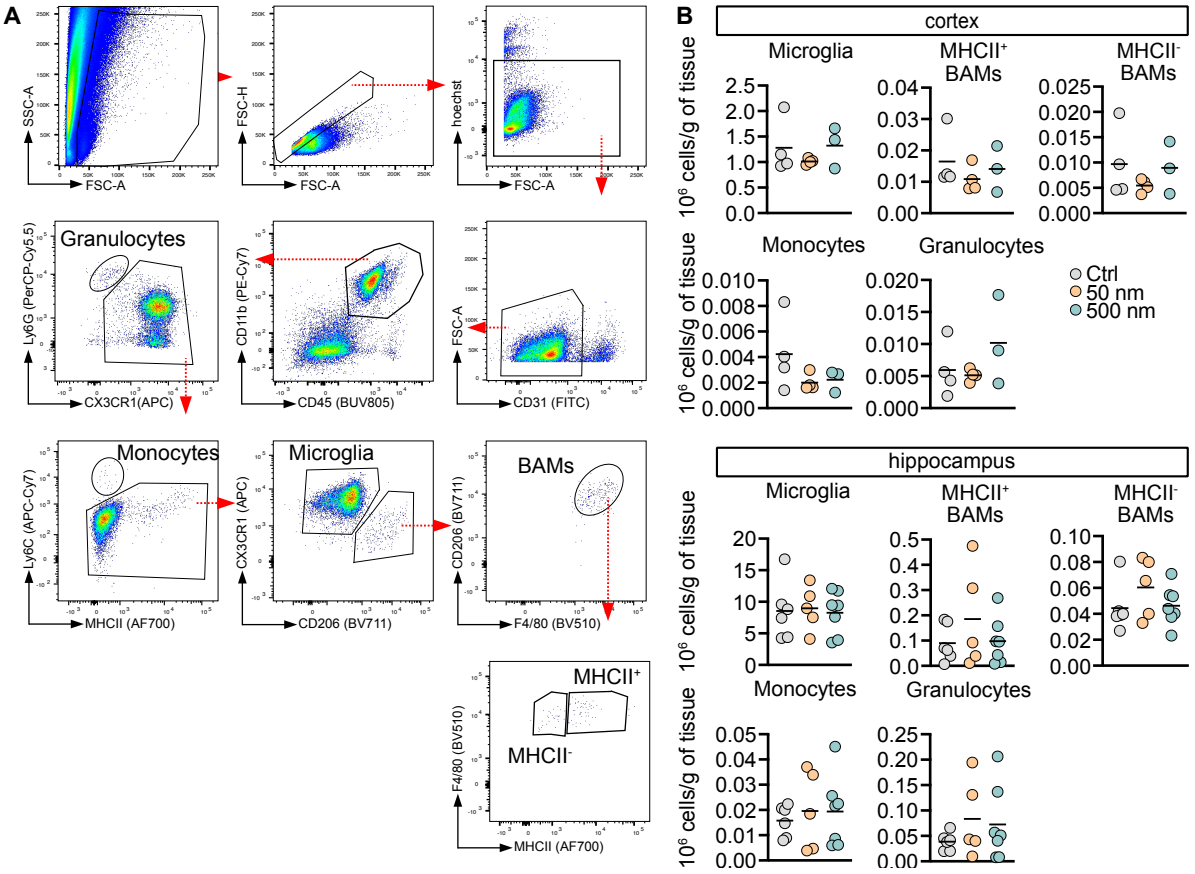

Figure 13 MNP chronic ingestion does not alter the abundance of immune cells in the brain: (A) Gating strategy of the brain myeloid cells. **(B)** The abundance of microglia, BAMs, monocytes and granulocytes in the cortex (upper panel) and the hippocampus (lower panel), each dot represents an individual mouse, the horizontal line indicates the mean. n= 5-7 animals per condition. Ordinary one-way ANOVA.

To gain a comprehensive understanding of molecular changes, single-cell RNA sequencing (scRNA-seq) was performed on immune cells ($CD45^+$) isolated from the brain cortex, following the Seq-Well protocol (203). After quality control, which involved removing low-quality cells based on unique gene counts (<200 or >2500) and mitochondrial gene content (>5 %), a total of 2930, with 318 from controls, 1120 from the 50 nm-exposed group, and 1492 from the 500 nm-exposed group.

To visualize this high-dimensional dataset, Uniform Manifold Approximation and Projection (UMAP), a dimensionality reduction technique (204), was applied (**Figure 14**A). UMAP helps to visualize high-dimensional gene expression data by preserving local and global structures, enabling the identification of distinct cell clusters. Based on cell specific marker expression, clusters were annotated, revealing microglia (expressing *Cx3cr1*, *Csf1r* and *Hexb*), B cells (expressing *Ly6d*, *CD79b* and *CD19*), T cells (expressing *Gimap6*, *Trbc2* and *Cd8a*) and proliferating cells (expressing *Mki67* and *Top2a*) (**Figure 14**B).

After annotating the different cell types, microglia were further assessed to investigate the potential influence of MNP ingestion on their function (**Figure 14**C). Microglia subclustered into two clusters: cluster 0 and cluster 1. Cluster 1 expressed hemoglobin related genes (*Hbb-*

bs, *Hbb-bt*, *Hba-a1* and *Hba-a2*) suggesting potential contamination with RBCs (**Figure 14**D). Consequently, this cluster was excluded from further analysis (**Figure 15**A). Notably, no BAMs were identified in this dataset, as indicated by the absence of Mrc1 expression (**Figure 14**D).

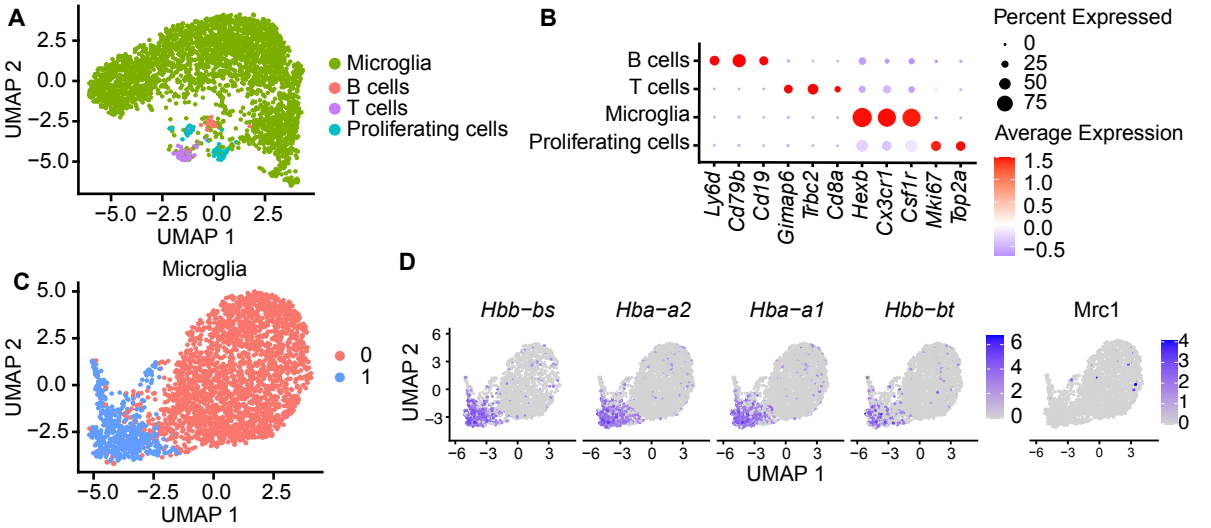

Figure 14 scRNA-seq analysis of myeloid cells in the cortex: (A) UMAP plot of annotated cell types. **(B)** Expression of marker genes across all cell types, visualized as a dot plot. Dot color represents the Z-score of gene expression, dot size indicates the percentage of cells expressing each marker within a given cluster. **(C)** UMAP plot of microglia subclusters. **(D)** Feature plot illustrating the expression of hemoglobin related genes in microglia.

Differentially expressed genes (DEGs) between MNP-exposed and control microglia were identified using an adjusted p-value threshold of ≤ 0.05, and a $\log_2$ fold change threshold of ≥ 0.35 or ≤ -0.35. Furthermore, genes needed to be expressed in more than 5 % of the cells. This analysis revealed 59 and 48 downregulated genes in 50 nm and 500 nm-exposed microglia, respectively. However, three genes, *Hspa1a* (heat shock protein family A member 1A), *Gadd45b* (growth arrest and DNA damage inducible beta), and Hsp90aa1 (heat shock protein 90 alpha family class A member 1), were upregulated in 500 nm-exposed microglia (**Figure 15**B, C). Among the downregulated genes, 19 genes and were shared between both MNP groups.

For over-representation analysis (ORA), a less stringent DEG threshold (adjusted p-value threshold of ≤ 0.1, and a $\log_2$ fold change threshold of ≥ 0.25 or ≤ -0.25) was applied, allowing the inclusion of genes with borderline significance for exploratory analysis. Under these settings, 137 and 106 genes were downregulated, while 1 and 3 genes were upregulated in 50 nm- and 500 nm-exposed microglia, respectively. Nevertheless, ORA revealed only two significant upregulated pathways, ‘regulation of cell death’ and cellular response to stimuli’, in the 500 nm-exposed microglia (**Figure 15**D).

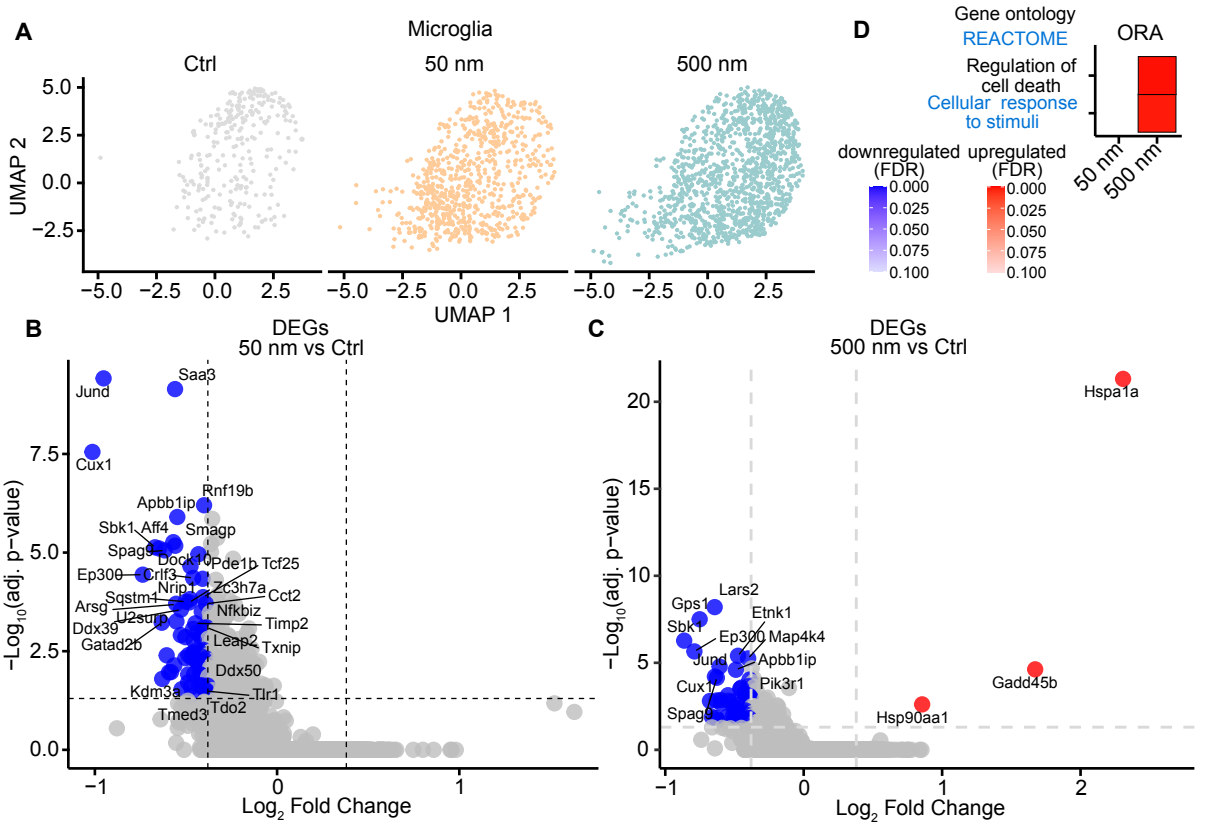

Figure 15 Chronic MNP exposure elicits minimal microglial transcriptomic changes: (A) UMAP plot of microglia across conditions. **(B, C)** Volcano plots displaying DEGs between MNP-exposed and control KCs, each dot represents a gene, with the x-axis showing the $\log_2$ fold change and the y-axis showing the $-\log_{10}$ adjusted p-value. Significantly upregulated genes (adjusted p-value ≤ 0.05, $\log_2$ fold change ≥ 0.38) are shown in red, downregulated genes (of ≤ 0.05, $\log_2$ fold change ≤ -0.35) are shown in blue, non-significant genes are displayed in gray. (E) Heatmap displays significantly enriched pathways based on DEGs (DEGs: adjusted p-value ≤ 0.1, $\log_2$ fold change ≥ 0.25 or ≤ -0.25). **(D)** Pathways enriched among upregulated genes are shown in red, while those enriched among downregulated genes are shown in blue. The color gradient reflects the false discovery rate (FDR)-adjusted significance, with more intense colors indicating stronger enrichment.

Given reports linking nanoparticles to BBB disruption(205), BBB integrity was assessed following chronic MNP ingestion. After 12 weeks of MNP ingestion, mice were injected with 4 µl/g of 2% Evans Blue (EB) intraperitoneally (i.p.) and the dye leakage within the brain parenchyma was assessed. Mice were then sacrificed 30 minutes post-injection, and brains were evaluated using confocal microscopy and a colorimetric assay (**Figure 16**A). The colorimetric assay revealed no significant differences in EB concentration between MNP-exposed and control mice (**Figure 16**B), with 500 nm-exposed mice showing a trend toward lower values. Confocal microscopy findings also showed no signs of BBB disruption following MNP ingestion (**Figure 16**C). These findings suggest no disruption of BBB following MNP ingestion.

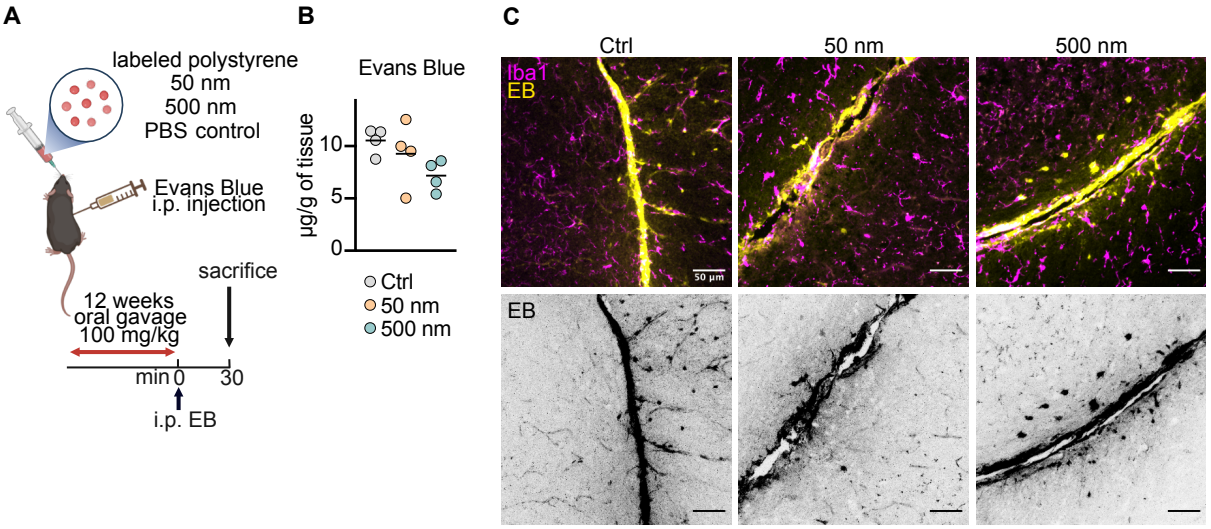

Figure 16 MNP ingestion caused no disruption in BBB: (A) Schematic representation of the experimental setup. **(B)** Colorimetric assay showing EB concentration in MNP-exposed and control brains, each dot represents an individual mouse, the horizontal line indicates the mean. n=4 per condition. Ordinary one-way ANOVA. **(C)** Representative images of immunofluorescence staining of the Brain, upper panel showing the EB (yellow) and Iba1 (magenta). lower panel showing the EB, Scale bars indicate 50 µm.

3.2.2.2 Absence of behavioral changes following chronic MNP ingestion

The presence of MNP in the brain, coupled with transcriptomic changes observed in microglia, raises questions about the potential impact of MNP ingestion on behavior. Therefore, a battery of tests was conducted to examine the effects of chronic MNP ingestion on behavior, including open field, novel object recognition, and social discrimination tests (**Figure 17**A).

The open field test assesses general locomotor activity and anxiety-like behavior, which is typically indicated by increased time spent in the periphery of the arena (**Figure 17**B). MNP-exposed mice showed no significant differences in total distance traveled (45-50 m) or velocity (5 cm/s) compared to controls over the test period (**Figure 17**C). All groups spent over 60 % of the time in motion, with 20 % of that time spent in the center of the field and the remaining 80 % at the borders, showing comparable center crossing counts (**Figure 17**C). These findings indicate normal motor function and no evidence of increased anxiety-like behavior following MNP ingestion.

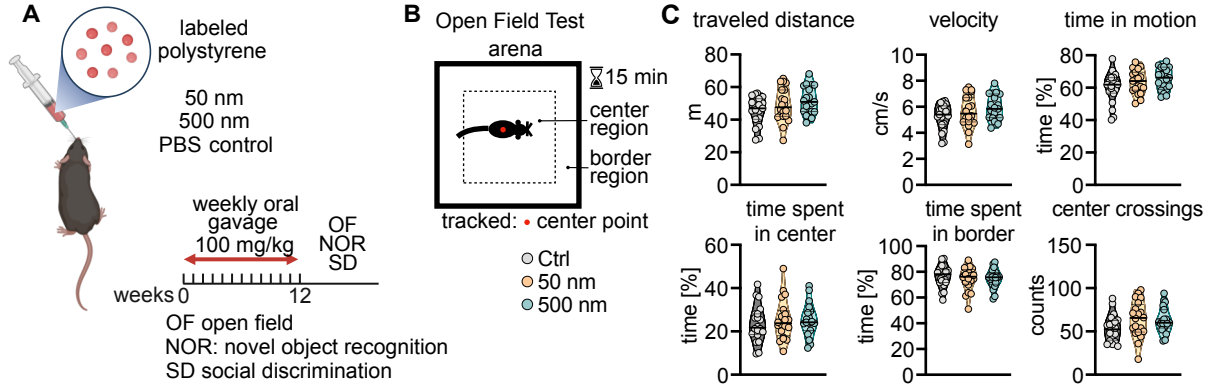

Figure 17 MNP ingestion does not trigger anxiety-like behavior: (A) Schematic representation of the experimental setup. **(B)** Schematic representation of the experimental design of the open field test. **(C)** Quantification of traveled distance (m), velocity (cm/s), time spent in motion (%), time spent in the center (%), time

spent in the border (%) and center crossing. Each dot represents an individual mouse, the horizontal line indicates the mean. n= 19-20 mice per condition. Ordinary one-way ANOVA.

The novel object recognition test evaluates memory and cognitive function by assessing each mouse's ability to distinguish between a novel and a familiar object (**Figure 18**A). The test consists of two trials, following a habituation period of three 5-minute sessions with two identical objects. In each trial, one of the habituation objects was replaced with a novel object. The discrimination index (DI) was calculated as the percentage of time spent exploring the novel object (time spent in the object zone) over the total exploration time, setting the chance level at 50 %. A DI above 50 % indicates a preference for the novel object, reflecting recognition memory, while a DI at or below 50 % suggests either no preference or a preference for the familiar object.

In the first trial, all groups displayed no significant deviation to the chance level, as analyzed by a one-sample t-test within each group, nor were there differences among groups (**Figure 18**B, trial 1). Similar to the first trail, all the mice showed no significant difference to the chance level in the second trail (**Figure 18**B, trial 2). However, the 50 nm-exposed group showed a higher preference than controls for the novel object (**Figure 18**B, trial 2).

The social discrimination test was conducted to assess memory and recognition by observing interactions with novel conspecifics (**Figure 18**C). The test consisted of two trials, following a habituation period of three 5-minute sessions with empty cages. In the first trial, a novel mouse was introduced in one of the empty cages to evaluate social behavior and initial recognition. In the second trial, a second, additional novel mouse was introduced to specifically test memory and recognition of the previously encountered mouse. Similar to the novel object recognition test, DIs were calculated to assess interaction time with each introduced mouse. In the first trial, each group showed a significant reduction in interaction to the chance level, indicating less interaction with the introduced mouse (**Figure 18**D, trial 1). In the second trial, control and 50 nm-exposed mice showed no preference between the two mice, whereas 500 nm-exposed mice showed a significant increase in interaction with the newly introduced mouse (**Figure 18**D, trial 2). However, no significant differences were observed among conditions for either trial.

In summary, MNP ingestion did not result in behavioral differences or motor function impairments compared to control mice. All groups showed no preference for novel objects and exhibited a reduced preference for conspecifics.

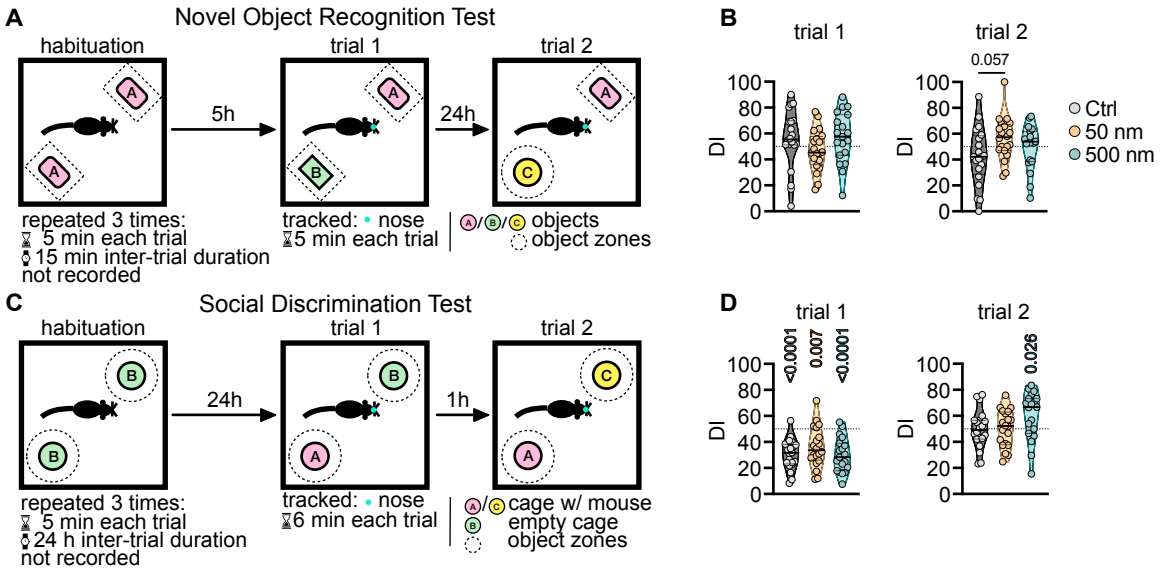

Figure 18 MNP exposed mice exhibited no alteration in memory and recognition: (A) Schematic representation of the experimental design of novel object recognition test. **(B)** DI for the first and second trial. Each dot represents an individual mouse, the horizontal line indicates the mean. n= 19-20 mice per condition. One-sample t-test within each group, Ordinary one-way ANOVA among the groups. **(C)** Schematic representation of the experimental design of social discrimination test. **(D)** DI for the first and second trial. Each dot represents an individual mouse, the horizontal line indicates the mean, the dashed line represents the chance level. n= 19-20 mice per condition. One-sample t-test within each group, ordinary one-way ANOVA among the groups.

3.2.3 Chronic exposure to MNP disrupts metabolic homeostasis

3.2.3.1 MNP-exposed livers show no sign of injury

To assess whether MNP ingestion may trigger liver fibrosis, Sirius Red staining, which specifically stains collagen, was performed (**Figure 19**A). Collagen deposition was observed surrounding the blood vessels; however, neither portal fibrosis nor bridging fibrosis was present, both of which are considered early stages of liver fibrosis (206). Additionally, quantitative reverse transcription polymerase chain reaction (qRT-PCR) analysis of fibrosis-associated genes, including transforming growth factor beta (*Tgfb1*), collagen type V alpha 1 chain (*Col5a1*), collagen type I alpha 1 chain (*Col1a1*), tenascin C (*Tnc*), and fibronectin (*Fn1*), revealed no significant differences compared to the control group (**Figure 19**B).

Furthermore, liver injury was assessed by measuring serum levels of the aminotransferase enzymes alanine aminotransferase (ALT) and aspartate aminotransferase (AST) using enzyme-linked immunosorbent assay (ELISA). ALT is primarily produced in the liver, making its elevation a key indicator of hepatocellular damage. In contrast, AST is expressed in both the liver and muscle tissue, meaning that increased AST levels may indicate either liver injury or muscle damage (207). The levels of both enzymes were comparable to those in the control mice (**Figure 19**C). The AST/ALT ratio, a widely used diagnostic index for liver function (207,208), showed no change among the conditions. In summary, these findings indicate that chronic MNP ingestion did not result in fibrosis or overt liver injury (**Figure 19**C).

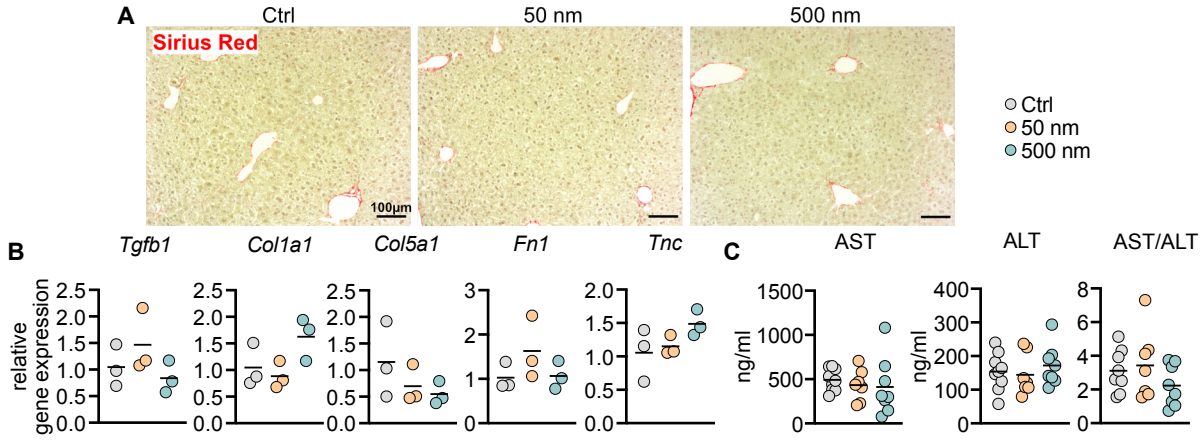

Figure 19 MNP ingestion does not cause liver injury: (A) Representative images of Sirius Red-stained liver sections. Scale bars indicate 100 µm. **(B)** Relative gene expression of fibrosis-related markers, normalized to housekeeping genes. n=3 per condition. **(C)** Serum levels of AST, ALT, and the AST/ALT ratio. n= 7-9 per condition. Each dot represents an individual mouse, the horizontal line indicates the mean. Ordinary one-way ANOVA.

3.2.3.2 MNP alter hepatic metabolism following chronic ingestion

Given the liver's central role in metabolic regulation and the accumulation of MNP in this organ, it was essential to assess MNP impact on liver metabolism to better understand their overall biological effects. Throughout the 12 weeks of MNP exposure (**Figure 4**A), no significant differences in body weight were observed among the groups. Both the 50 nm- and 500 nm-treated mice displayed normal weight gain during this period (**Figure 20**A). Additionally, liver weight relative to body weight after 12 weeks of chronic plastic treatment remained unchanged in both conditions compared to the control (**Figure 20**B).

The liver plays a major role in glycogen storage, which is a crucial energy resource. Periodic acid-Schiff's with hematoxylin (PAS-H) staining, used to visualize glycogen-containing granules, revealed a significant reduction in liver glycogen levels in mice exposed to 500 nm-PS particles (**Figure 20**C, D), while 50 nm-exposed livers showed no change compared to controls.

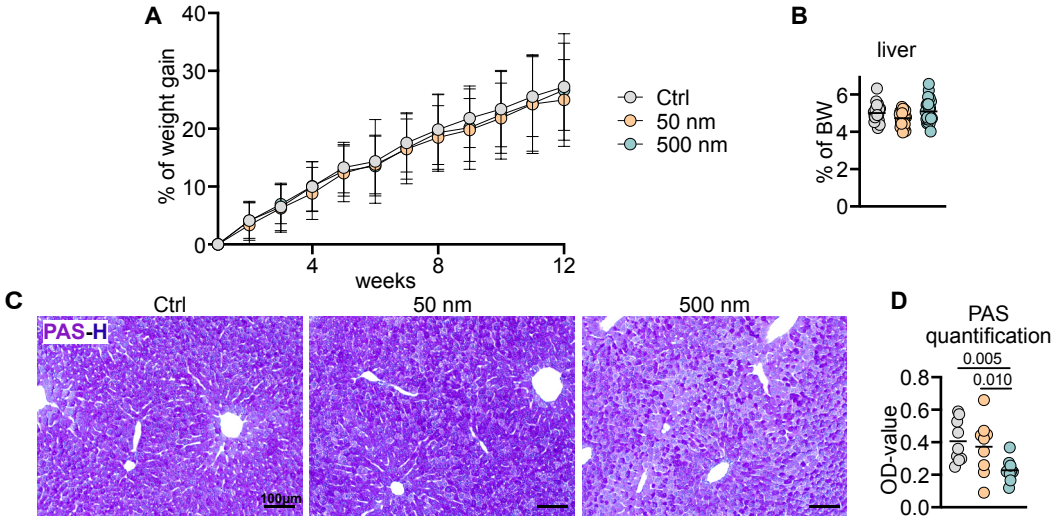

Figure 20 Microplastic-exposed livers exhibited reduced glycogen levels: (A) The percentage of body weight gain over 12 weeks of MNP exposure. n=33-39 per condition. **(B)** Relative liver weight (% body weight) following

12 weeks of MNP exposure. Each dot represents an individual mouse, the horizontal line indicates the mean. n=19-24 per condition. Kruskal-Wallis test **(C)** Representative images of PAS-H-stained liver sections. Scale bars indicate 100 µm. **(D)** Quantification of PAS-H staining intensity (optical density). Each dot represents an individual mouse, the horizontal line indicates the mean. n=9-10 per condition. Ordinary one-way ANOVA.

In addition to its role in glucose homeostasis, the liver plays an essential role in lipid metabolism, particularly in the storage and processing of triacylglycerol (TG) (209). Oil-Red-O (ORO) staining demonstrated a possible reduction in neutral lipids content in the livers of MNP-exposed mice (**Figure 21**).

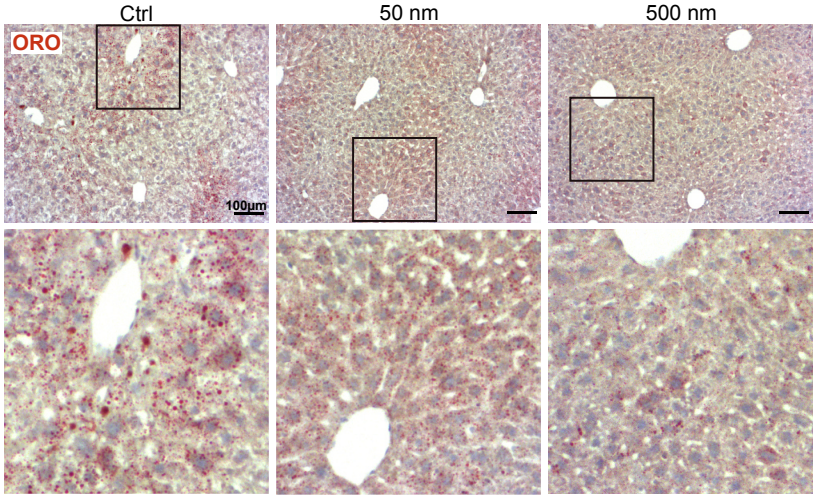

Figure 21 MNP ingestion impacts hepatic lipid storage: Representative picture of ORO-stained liver sections. Scale bars indicate 100 µm.

To further investigate lipid content, lipidomics analysis was performed on livers following chronic MNP ingestion, providing a comprehensive overview of lipid classes stored in the liver. This analysis covered neutral lipids, including TG, odd-chain TG (TG odd), diacylglycerol (DG), monoacylglycerol (MG) and cholesterol ester (CE). Additionally, phospholipids, such as phosphatidic acid (PA), phosphatidylglycerol (PG), phosphatidylcholine (PC), phosphatidylcholine ether (PC-O), phosphatidylethanolamine (PE), phosphatidylethanolamine ether (PE-O), phosphatidylserine (PS), lysophosphatidylcholine (LPC), lysophosphatidylcholine ether (LPC-O), and lysophosphatidylethanolamine (LPE) were checked as well. Furthermore, sphingolipids, including ceramide (Cer), hexosylceramide (HexCer), dihexosylceramide (DiHexCer), and sphingomyelin (SM) were analyzed. Lipidomics analysis revealed no significant changes in total lipid content between control and MNP-exposed groups (**Figure 22**A). However, a shift in lipid composition was observed, with a significant reduction in the relative abundance TG and TG odd, and a significant increase in the relative abundance SM, PE, and LPE in MNP-exposed livers compared to controls (**Figure 22**B, C). Additionally, the 500 nm-exposed group showed an increase in DG, CE, and LPC relative abundance relative to total lipids compared to controls (**Figure 22**B, C).

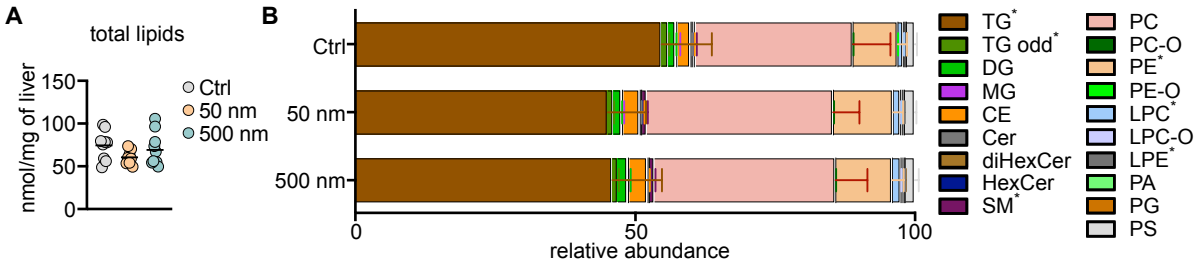

C

	q-value		
	Ctrl vs. 50 nm	Ctrl vs. 500 nm	50 nm vs. 500 nm
TG	0.0152	0.0152	0.2939
TG odd	0.005	0.005	0.283
DG	0.2480	0.0280	0.1076
MG	0.9841	0.9841	0.9841
CE	0.0864	0.0217	0.2921
Cer	0.0589	0.0589	0.9910
HexCer	0.4892	0.2900	0.5214
diHexCer	0.5752	0.2980	0.1871
SM	0.0028	0.0028	0.3275
LPC	0.0889	0.0055	0.1019
LPC-O	0.2494	0.2494	0.9770
LPE	0.0054	0.0005	0.0892
PA	0.9411	0.6705	0.6705
PC	0.1847	0.1847	0.7446
PC-O	0.4297	0.3313	0.6303
PE	0.0054	0.0103	0.1815
PE-O	0.053	0.0617	0.6879
PG	0.4078	0.2016	0.4816
PS	0.4379	0.5286	0.5986

Figure 22 MNP ingestion alters lipid composition in the liver: (A) Quantification of total lipid content in the liver. Each dot represents an individual mouse, and the horizontal line indicates the mean. n = 8-10 per condition. Ordinary one-way ANOVA. **(B)** Lipid class relative abundance in the liver. n = 8-10 per condition. **(C)** q-values for lipid class percentage comparisons after multiple testing correction.

To determine whether the observed shifts in lipid composition were due to actual lipid abundance shifts or a redistribution effect, absolute lipid concentrations were analyzed. PE, LPE, and SM levels increased significantly (**Figure 23**B, C), whereas TG odd levels decreased significantly in the MNP-exposed groups. Additionally, TG levels were lower in MNP-exposed livers compared to controls; however, this difference did not reach statistical significance (**Figure 23**A). Furthermore, LPC and LPC-O were increased in 500 nm-exposed livers compared to controls (**Figure 23**B).

These findings suggest that the alterations in lipid composition were driven by actual alterations in the abundances of TG, TG odd, PE, LPE, LPC, LPC-O and SM. However, the absolute abundances of DG and CE remained unchanged. across conditions, indicating that its proportional changes were a result of shifts in other lipid classes rather than a direct change in its abundance.

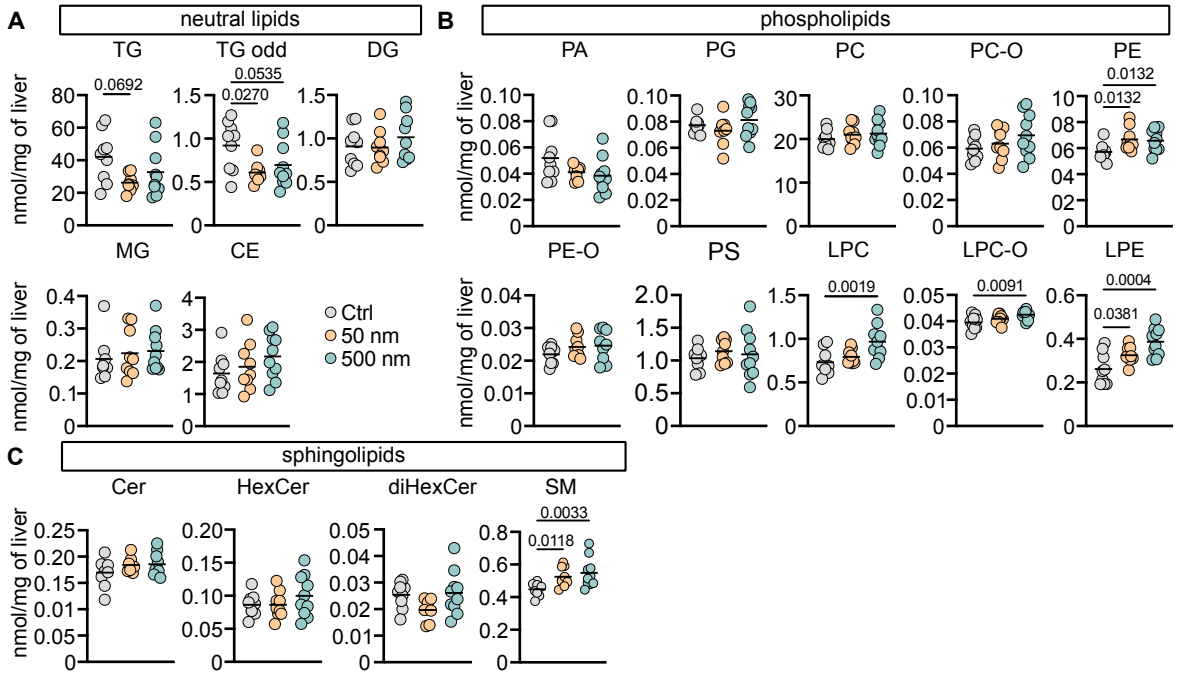

Figure 23 MNP ingestion impacts hepatic lipid abundance: (A) Absolute abundance of the neutral lipids in the liver. **(B)** Absolute abundance of the phospholipids in the liver. **(C)** Absolute abundance of the sphingolipids in the liver. Each dot represents an individual mouse, and the horizontal line indicates the mean. n = 8-10 per condition. Ordinary one-way ANOVA.

Since TG constitutes approximately 50% of total liver lipids (**Figure 22**B), a further assessment was conducted to examine the distribution of individual TG species (**Figure 24**). Several TG species, including TG 48:1 (a triacylglycerol species containing a total of 48 carbon atoms and a single double bond across its fatty acid chains), TG 48:2, TG 50:1, TG 50:3, TG 52:2, TG 54:3, TG 56:2, TG 56:4, and TG 58:4, were significantly reduced in MNP-exposed livers compared to controls. Additionally, TG 50:2 was decreased in the 50 nm-exposed group compared to both the 500 nm-exposed and control livers.

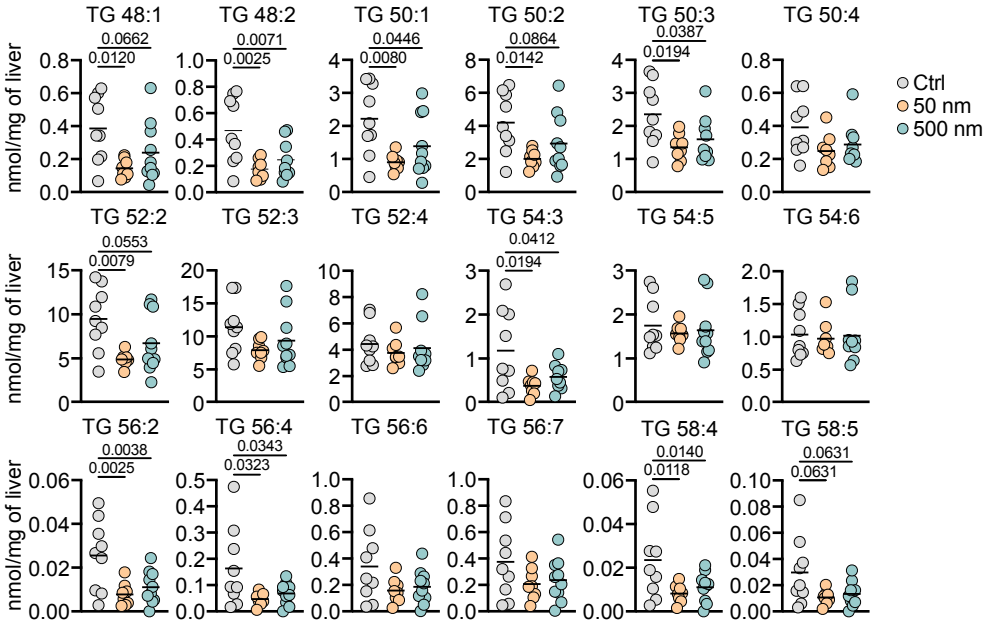

Figure 24 MNP ingestion affects the abundance of TG species: Absolute abundance of TG species in the liver. Each dot represents an individual mouse, and the horizontal line indicates the mean. n = 8-10 per condition. Ordinary one-way ANOVA.

Together, these findings indicate that MNP ingestion is associated with disruptions in glucose and lipid homeostasis

To investigate the molecular changes induced by MNP ingestion, single-nuclei RNA sequencing (snRNA-seq) was performed on sorted nuclei isolated from the livers of mice exposed to MNP for 12 weeks, alongside control mice (**Figure 4**A), using the 10x Genomics Chromium platform. After quality control, which involved removing low-quality nuclei based on unique gene counts (<600) and mitochondrial gene content (>30 %) as well as excluding doublets, a total of 37,774 high-quality nuclei were obtained for further analysis. Nuclei from all experimental conditions were combined and visualized using UMAP, where distinct cell populations were clustered based on their gene expression profiles and annotated accordingly, using marker genes identified in published scRNA-seq and snRNA-seq studies on the liver (210–212) (**Figure 25**A, B).

In detail, hepatocytes were identified by the expression of albumin (*Alb*), arginase 1 (*Arg1*), phosphoenolpyruvate carboxykinase 1 (*Pck1*), hemolytic complement (*Hc*) and homogentisate 1,2-dioxygenase (*Hgd*). Hepatic stellate cells were distinguished by the expression of bone morphogenetic protein 5 (*Bmp5*), neurexin 1 (*Nrxn1*), reelin (*Reln*), collagen type XIV alpha 1 chain (*Col14a1*), and platelet-derived growth factor receptor beta (*Pdgfrb*). Vascular endothelial cells were characterized by markers such as platelet and endothelial cell adhesion molecule 1 (*Pecam1*), cluster of differentiation 28 (*Cd28*), protein tyrosine phosphatase receptor type B (*Ptprb*), and coagulation factor VIII (*F8*), while liver sinusoidal endothelial cells were further distinguished by the additional expression of mannose receptor C-type 1 (*Mrc1*). KCs were identified by markers such as colony stimulating factor 1 receptor (*Csf1r*), adhesion G protein-coupled receptor E1 (*Adgre1*), V-set and immunoglobulin domain containing 4 (*Vsig4*), C-type lectin domain family 4 member F (*Clec4f*), and T-cell immunoglobulin and mucin domain containing 4 (*Timd4*), while dendritic cells (DCs) expressed interferon regulatory factor 8 (*Irf8*) and Fms-related receptor tyrosine kinase 3 (*Flt3*). Lymphocytes included T cells expressing Src kinase associated phosphoprotein 1 (*Skap1*), cluster of differentiation 226 (*CD226*), interleukin 2 receptor beta (*Il2rb*), T cell receptor beta constant 2 (*Trbc2*), and B-cell leukemia/lymphoma 11B (*Bcl11b*), and B cells characterized by early B cell factor 1 (*Ebf1*), immunoglobulin heavy constant delta (*Ighd*) and B and T lymphocyte attenuator (*Btla*). Lastly, cholanginocytes were marked by the expression of secreted phosphoprotein 1 (*Spp1*), epithelial cell adhesion molecule (*Epcam*), cystic fibrosis transmembrane conductance regulator (*Cftr*), SRY-box transcription factor 9 (*Sox9*), and protein phosphatase 2 regulatory subunit B beta (*Ppp2r2b).*

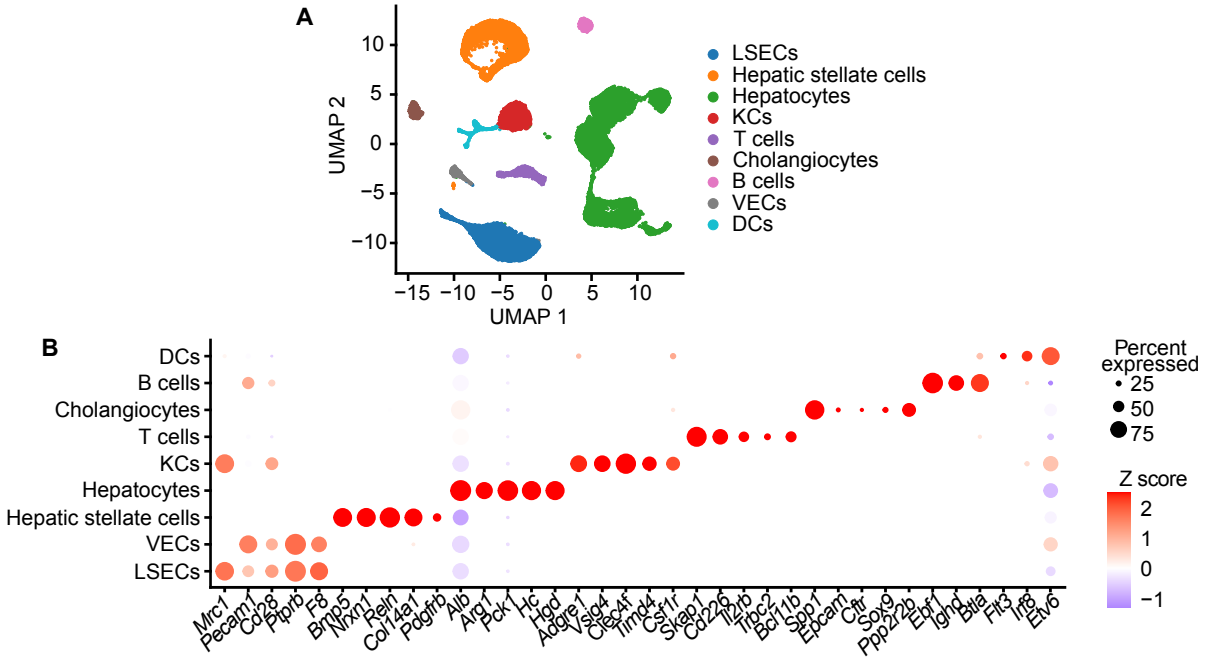

Figure 25 snRNA-Seq identifies distinct liver cell populations: (A) UMAP plot of annotated liver cell types. **(B)** Expression of marker genes across all cell types, visualized as a dot plot. Dot color represents the Z-score of gene expression, dot size indicates the percentage of cells expressing each marker within a given cluster.

Given their central role in metabolic regulation, hepatocytes (12200 nuclei in total) were selected for further analysis. DEGs between MNP-exposed and control hepatocytes were identified using an adjusted p-value threshold of ≤ 0.05, and a $\log_2$ fold change threshold of ≥ 0.75 or ≤ -0.75. Additionally, genes were considered only if expressed in more than 5% of the cells. This analysis revealed 155 and 125 downregulated genes and 297 and 298 upregulated genes in 50 nm- and 500 nm-exposed hepatocytes, respectively (**Figure 26**A-D). Among these, 76 downregulated genes and 174 upregulated genes were shared between both MNP groups.

ORA performed using DEGs revealed significant enrichment in pathways related to lipid metabolism and other metabolic processes. Among the upregulated genes following MNP ingestion, pathways associated with ‘lipid localization’, ‘small molecules catabolic process’ and ‘biological oxidations’ were prominently enriched (**Figure 26**E).

While ‘cholesterol homeostasis’, was upregulated in 500 nm-exposed hepatocytes, pathways involved in ‘xenobiotic metabolism’ regulation of lipid metabolism by Ppar alpha’ and ‘response to elevated platelet cytosolic Cas^{+}’ were upregulated in 50 nm-expose hepatocytes in compare to control (**Figure 26**E). conversely ‘humoral immune response was down regulated in 50 nm-exposed hepatocytes (**Figure 26**E).

Several key genes contributing to these enriched pathways were identified, particularly those involved in lipid metabolism and mobilization (**Figure 26**C, D). *Carboxylesterase 1f (Ces1f)*, *cytochrome P450 family 4 subfamily a polypeptide 14 (Cyp4a14)*, *acyl-CoA synthetase short-chain family member 3 (Acss3)*, *peroxisome proliferator-activated receptor gamma coactivator*

1 beta (Ppargc1b), *ATP-binding cassette sub-family A member 8a (Abca8a)*, *apolipoprotein A2 (Apoa2)*, and *paraoxonase 1 (Pon1)* were upregulated in both 50 nm- and 500 nm-exposed hepatocytes compared to controls. Additionally, *cytochrome P450 family 4, subfamily a polypeptide 10 (Cyp4a10)* and *acetyl-CoA acetyltransferase 3 (Acat3)* were specifically upregulated in the 500 nm-exposed group, while *peroxisome proliferator-activated receptor gamma (Pparg)*, *CD36 molecule (Cd36)*, *apolipoprotein E (Apoe)*, and *apolipoprotein H (Apoh)* were upregulated in the 50 m-exposed hepatocytes.

In contrast, *angiopoietin-like 8 (Angptl8)* was downregulated in both conditions. Further, *lipin 1 (Lpin1)*, *retinol Saturase (Retsat)*, *perilipin 2 (Plin2)*, and *angiopoietin-like 4 (Angptl4)* were downregulated in the 500 nm-exposed group, whereas *diacylglycerol o-acyltransferase 1 (Dgat1)* was downregulated in the 50 nm-exposed group.

Additionally, genes essential for glucose homeostasis exhibited significant expression changes. *Pyruvate carboxylase (Pcx)*, *insulin-like growth factor-binding protein 1 (Igfbp1)*, *insulin receptor substrate 2 (Irs2)*, *mitochondrial pyruvate carrier 1 (Mpc1)*, *pyruvate dehydrogenase kinase 1 (Pdk1)*, *nuclear factor, interleukin 3 (Nfil3)*, and *solute carrier family 16 member 7 (Slc16a7)* were consistently upregulated in both 50 nm- and 500 nm-exposed hepatocytes, suggesting a sustained metabolic response across conditions. In contrast, *glucokinase (Gck)* was specifically downregulated in 500 nm-exposed hepatocytes, while *triokinase and FMN cyclase (Tkfc)* was downregulated in both conditions compared to controls. Notably, *glycogen synthase 2 (Gys2)* and *dipeptidyl peptidase 4 (Dpp4)* were upregulated exclusively in the 500 nm-exposed group, further highlighting the metabolic impact of particle size on hepatocyte function.

Taken together, these findings indicate that chronic exposure to MNP induces significant changes in liver metabolic processes, particularly affecting lipid and glucose homeostasis. These disruptions were reflected in the observed reduction in glycogen and lipid storage, which were further supported by the molecular changes identified through snRNA-seq analysis.

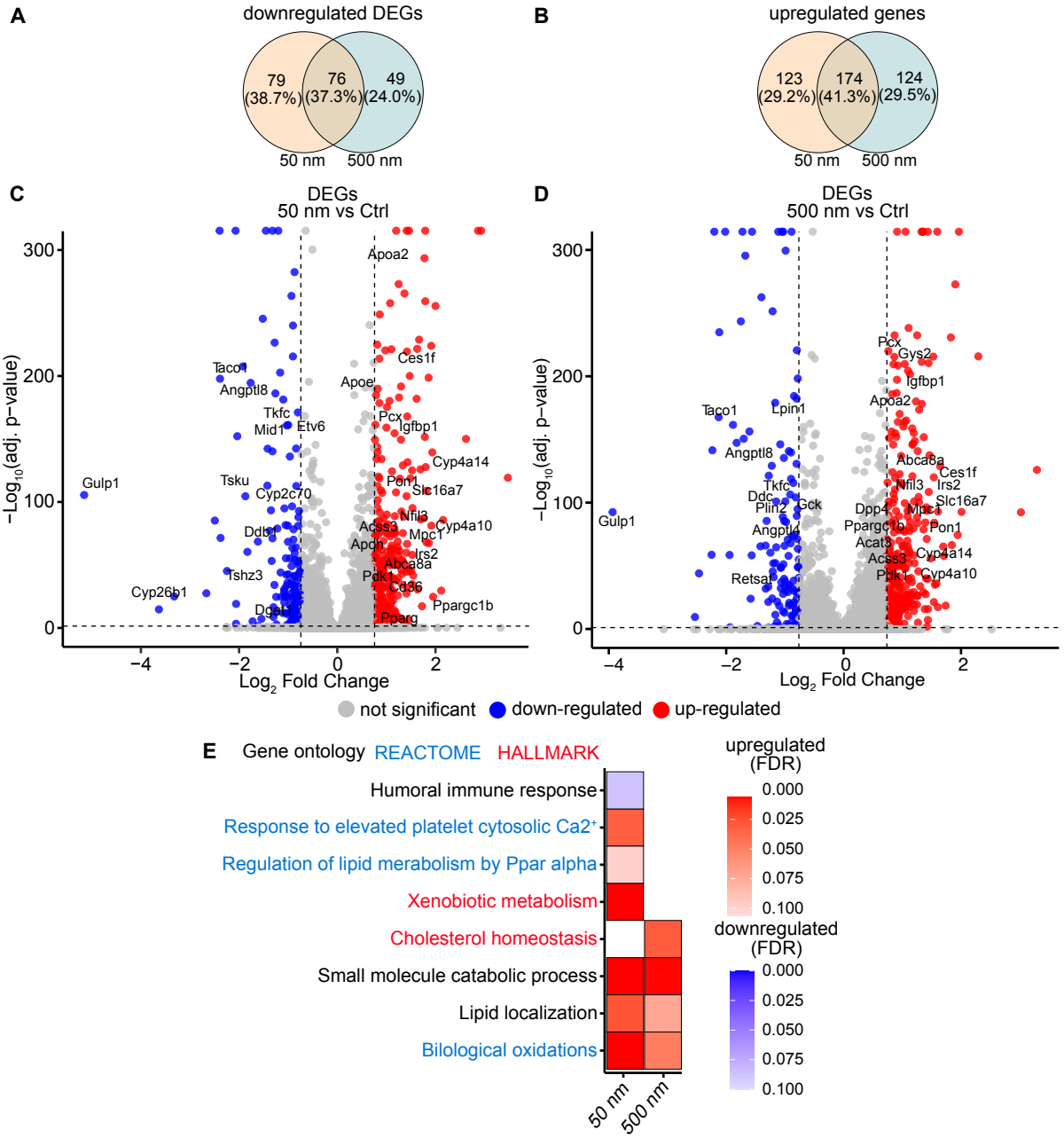

Figure 26 MNP-exposure alters hepatocyte gene expression: (A, B) Venn diagram showing DEG counts in 50 nm and 500 nm-exposed hepatocytes compared to control hepatocytes. **(C, D)** Volcano plots displaying DEGs between MNP-exposed and control hepatocytes, each dot represents a gene, with the x-axis showing the $\log_2$ fold change and the y-axis showing the $-\log_{10}$ adjusted p-value. Significantly upregulated genes (adjusted p-value ≤ 0.05, $\log_2$ fold change ≥ 0.75) are shown in red, downregulated genes (adjusted p-value ≤ 0.05, $\log_2$ fold change ≤ -0.75) are shown in blue, non-significant genes are displayed in gray. **(E)** heatmap displays significantly enriched pathways based on DEGs (DEGs: adjusted p-value ≤ 0.05, $\log_2$ fold change ≥ 0.75 or ≤ -0.75). Pathways enriched among upregulated genes are shown in red, while those enriched among downregulated genes are shown in blue. The color gradient reflects the false discovery rate (FDR)-adjusted significance, with more intense colors indicating stronger enrichment.

3.2.3.3 Chronic ingestion of MNP induces structural alterations in adipose tissue

The metabolic phenotype observed in the liver prompted further investigation into adipose tissue, another key metabolic organ. Given the well-established liver-adipose tissue crosstalk, where mediators such as free fatty acids, adipokines, hepatocytes and inflammatory signals

influence metabolism, disruptions in one organ may have profound systemic metabolic consequences.

Interestingly, gonadal white adipose tissue (gWAT) weight relative to body weight was significantly reduced following chronic MNP ingestion compared to controls (**Figure 27**A), suggesting a potential decrease in lipid storage. To explore the cause of this reduction, gWAT sections were stained with hematoxylin and eosin (H&E). Adipocyte size was then analyzed using AdipoQ (191), tool for evaluating adipocyte morphology and function. The results revealed an increase in the frequency of small-sized adipocytes, ≥ 5 x10^2 µm^2 &< 10 x10^2 µm^2, in 50 nm-exposed gWAT compared to controls **(Figure 27**B), further supporting the hypothesis of altered lipid storage and adipose tissue remodeling.

To further evaluate adipose tissue remodeling, histological analysis of gWAT sections was performed. H&E-stained sections revealed the presence of crown-like structures—macrophages encircling dead adipocytes—in mice exposed to both 50 nm and 500 nm PS particle (**Figure 27**C). Histological scoring reflected these findings, with exposed animals receiving higher scores than controls (**Figure 27**D), consistent with immune remodeling in adipose tissue.

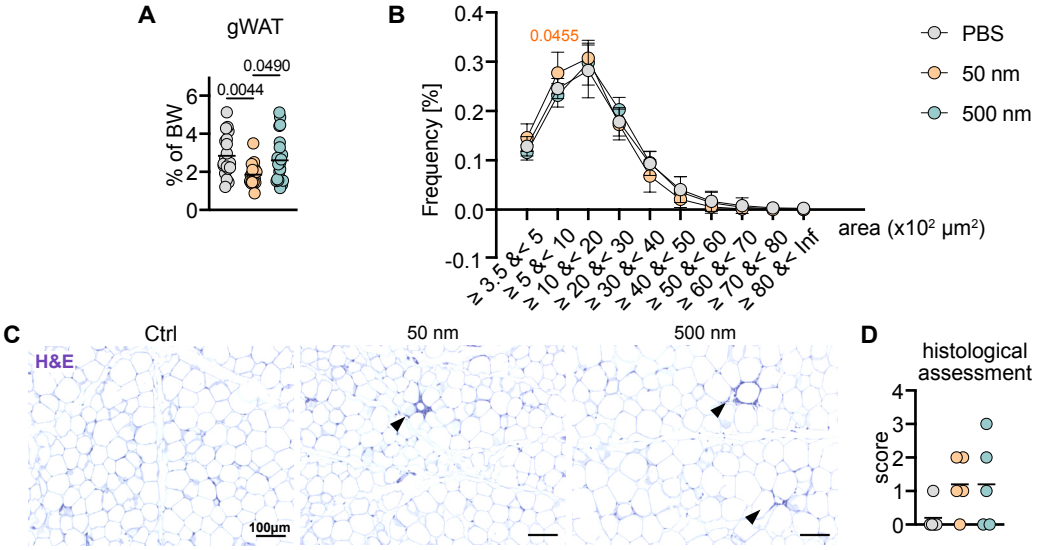

Figure 27 Chronic MNP ingestion is associated structural changes in adipose tissue: (A) Relative gWAT weight (% body weight) following 12 weeks of MNP exposure. Each dot represents an individual mouse, and the horizontal line indicates the mean. n= 20-21 per condition. Kruskal-Wallis test. **(B)** Adipocyte Size assessment using AdipoQ. n=9.10 per condition. Ordinary one-way ANOVA on each size. **(C)** Representative picture of H&E-stained gWAT sections, highlighting crown-like structures (arrows). Scale bars indicate 100 µm. **(D)** Histological assessment of H&E-stained gWAT sections. Each dot represents an individual mouse, and the horizontal line indicates the mean. n= 4-5 per condition. Kruskal-Wallis test.

Crown-like structures are primarily formed by monocyte-derived macrophages that infiltrate adipose tissue in response to inflammation, particularly CD11c$^+$ macrophages (213–215). Despite the occasional presence of crown-like structures, macrophage numbers, including TIM-4$^+$ (CD45$^+$ CD11b$^+$ F4/80$^+$ TIM-4$^+$), TIM-4$^-$ CD11c$^-$ (CD45$^+$ CD11b$^+$ F4/80$^+$ TIM-4$^-$ CD11c$^-$), and TIM-4$^-$ CD11c$^+$ (CD45$^+$ CD11b$^+$ F4/80$^+$ TIM-4$^-$ CD11c$^+$), were comparable

between MNP-exposed and control animals (**Figure 28**A, B). Furthermore, no monocyte infiltration into the tissue was detected **(Figure 28** B).

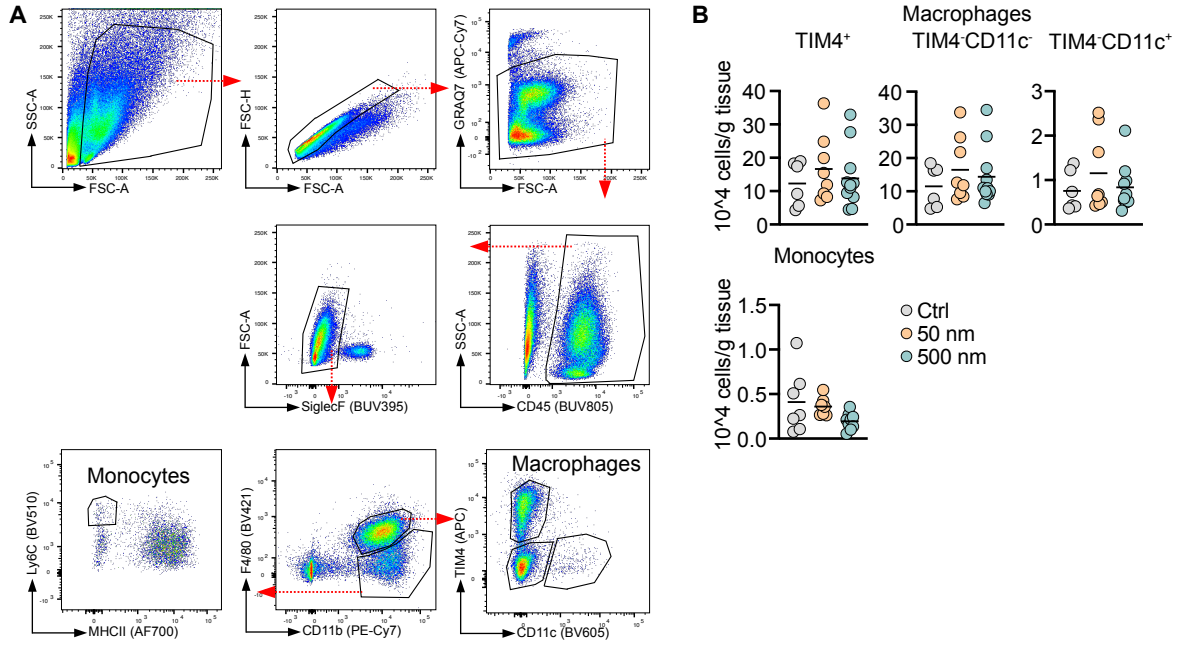

Figure 28 Chronic MNP ingestion does not change the abundance of immune cells in the gWAT: (A) Gating strategy of gWAT macrophages. **(B)** The abundance of TIM-4$^+$, TIM-4$^-$ CD11c$^-$ and TIM-4$^-$ CD11c$^+$ macrophages and monocytes. Each dot represents an individual mouse, the horizontal line indicates the mean. n= 6-11 per condition. Ordinary one-way ANOVA.

Brown adipose tissue (BAT), which plays a distinct metabolic role compared to gWAT, was next examined. While gWAT primarily stores energy in the form of fat, BAT is involved in thermogenesis by burning fat. Scoring of vacuole size in H&E-stained BAT sections revealed a significant reduction, suggesting decreased lipid storage in BAT of MNP-exposed mice (**Figure 29**A, B). However, BAT weight relative to body weight did not change following the chronic MNP ingestion (**Figure 29**C).

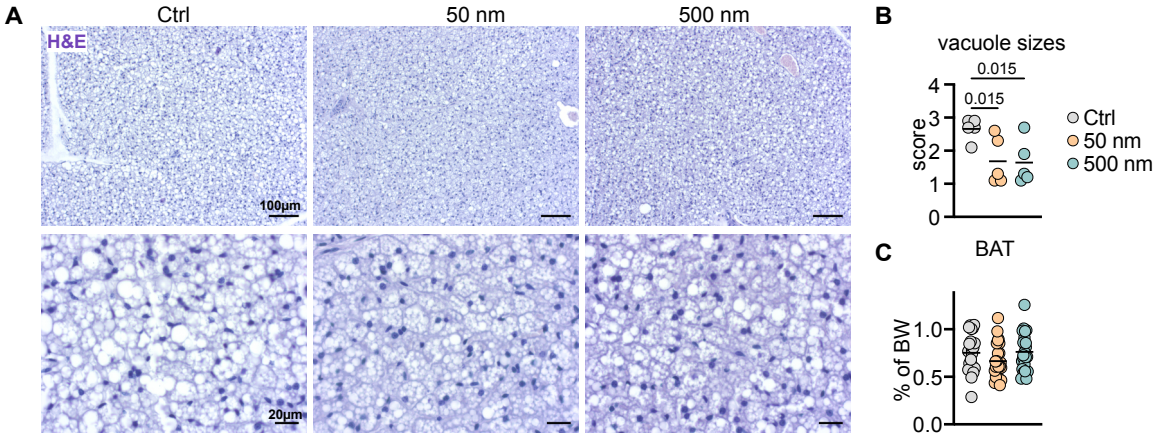

Figure 29 MNP ingestion affects vacuole sizes in BAT: (A) Representative picture of H&E-stained BAT sections Scale bars indicate 100 µm (upper panel), 20 µm (lower panel). **(B)** Scoring of vacuole size in H&E-stained BAT sections. n= 5 per condition **(C)** Relative BAT weight (% body weight) following 12 weeks of MNP exposure. n= 21-23 per condition. Each dot represents an individual mouse, and the horizontal line indicates the mean. Kruskal-Wallis test.

Overall, chronic ingestion of MNP induces inflammation in gWAT, as evidenced by the formation of crown-like structures. Additionally, structural changes in both gWAT and BAT suggest dysregulation of lipid homeostasis and storage.

3.2.3.4 Long term effects of MNP retention on the liver and adipose tissue

Given the long-term retention of MNP in the tissue (**Figure 10**B) and the metabolic disturbances observed after chronic exposure, liver structure and function were evaluated 26 weeks after the final gavage (**Figure 10**A). Relative liver weight (% of body weight) showed no change between MNP-exposed and control livers (**Figure 30**A).

PAS staining of the liver sections showed no differences in glycogen storage between the groups **(Figure 30**B, C). Sirius Red staining revealed occasional bridging fibrosis in the control and MNP-exposed livers (**Figure 30**D), suggesting that this may be an age-related effect. However, qRT-PCR analysis of fibrosis-related genes, including *Tgfb1, Col1a1, Col5a1, Fn1 and Tnc*, revealed no changes in expression levels between MNP-exposed and control livers (**Figure 30**E).

Although these findings suggest that chronic MNP ingestion does not induce a clear sign of fibrosis, serum biomarkers revealed subtle signs of hepatic stress. Interestingly, mice exposed to 50 nm MNP exhibited a tendency toward increased ALT levels relative to control mice, whereas 500 nm MNP exposure resulted in a slight increase in AST levels (**Figure 30**F). Moreover, the AST/ALT ratio was significantly elevated in the 500 nm-exposed mice serum (**Figure 30**F). These findings suggest that chronic MNP ingestion may cause subtle liver or muscle injury, as indicated by altered AST/ALT levels.

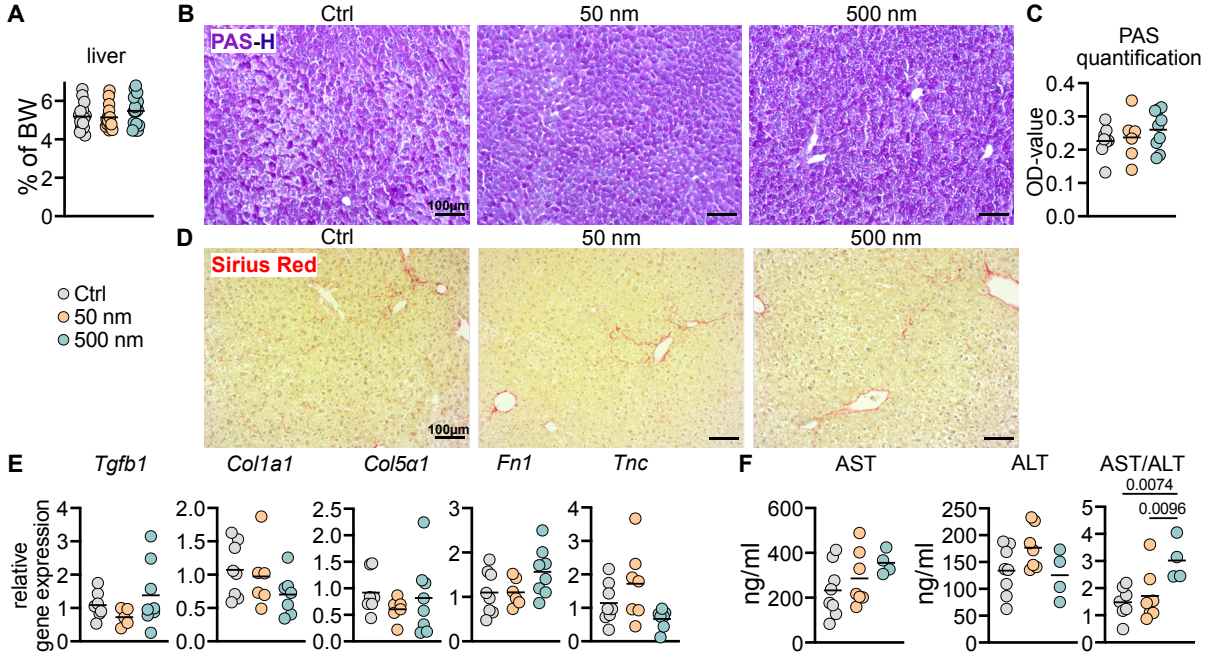

Figure 30 Long-term MNP retention does not induce liver fibrosis: (A) Relative liver weight (% body weight). Each dot represents an individual mouse, the horizontal line indicates the mean. n=15-17 per condition. Kruskal-Wallis test **(B)** Representative images of PAS-H-stained liver sections. Scale bars indicate 100 µm. **(C)** Quantification of PAS-H staining intensity (optical density). Each dot represents an individual mouse, the horizontal

line indicates the mean. n=6-8 per condition. Ordinary one-way ANOVA. **(D)** Representative images of Sirius Red-stained liver sections. Scale bars indicate 100 µm. **(E)** Relative gene expression of fibrosis-related markers, normalized to housekeeping genes. n=6-8 per condition. **(F)** Serum levels of AST, ALT, and the AST/ALT ratio. n= 4-8 per condition. Each dot represents an individual mouse, the horizontal line indicates the mean. Ordinary one-way ANOVA.

To further explore the systemic impact of long-term retention of MNP, adipose tissue was assessed for signs of tissue remodeling in MNP-exposed mice. Notably, crown-like structures persisted as a phenotype in gWAT of MNP-exposed mice, with these mice receiving significantly higher histological scores compared to controls (**Figure 31**A, B). However, the gWAT weight relative to body weight was comparable between MNP-exposed and control mice (**Figure 31**C).

In BAT, the previously observed reduction in vacuole size following MNP ingestion during the initial exposure was no longer evident (**Figure 31**D, F), suggesting an adaptive or compensatory response over time. Similarly, relative BAT weight remained unchanged compared to controls (**Figure 31**E).

Overall, these long-term data suggest that while overt injury is not apparent, persistent MNP retention induces mild hepatic stress and sustained adipose tissue remodeling.

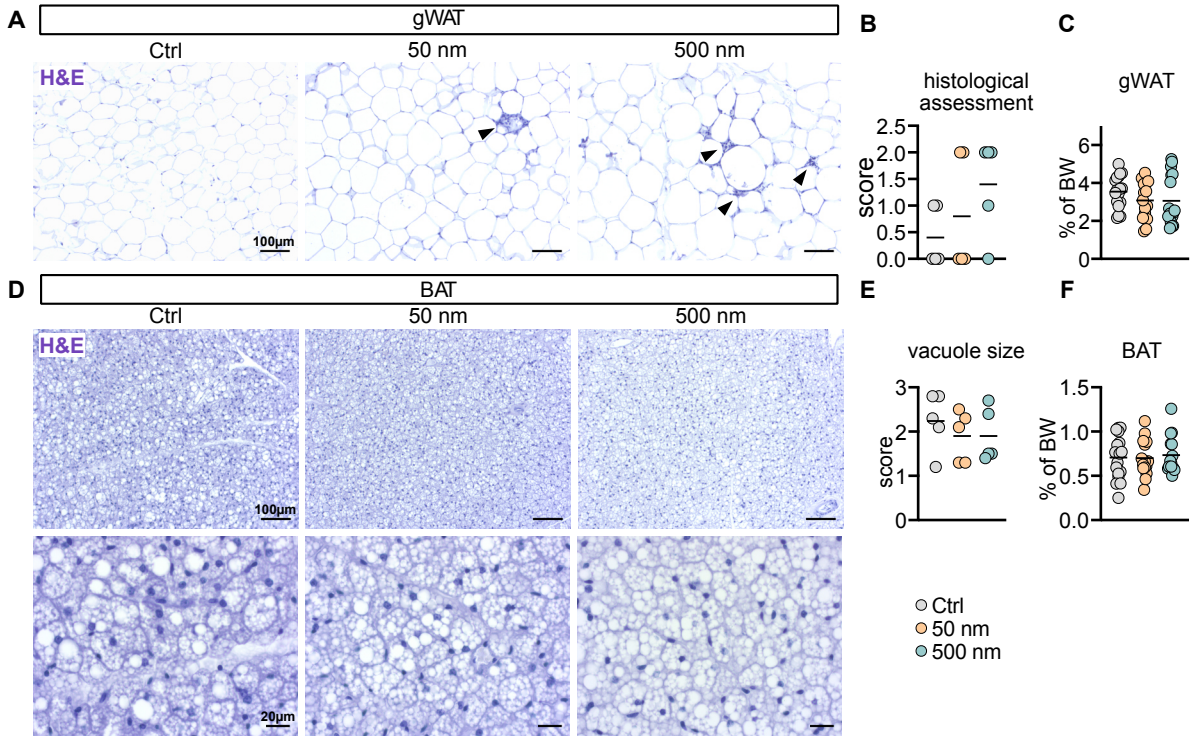

Figure 31 Long-term MNP retention induces adipose tissue remodeling: (A) Representative picture of H&E-stained gWAT sections, highlighting crown-like structures (arrows). Scale bars indicate 100 µm. **(B)** Histological assessment of H&E-stained gWAT sections. n= 5 per condition. **(C)** Relative gWAT weight (% body weight). n= n=15-17 per condition. Each dot represents an individual mouse, and the horizontal line indicates the mean. Kruskal-Wallis test. **(D)** Representative picture of H&E-stained BAT sections. Scale bars indicate 100 µm (upper panel), 20 µm (lower panel). **(E)** Scoring of vacuole size in H&E-stained BAT sections. n= 5 per condition. **(F)** Relative BAT weight (% body weight). n= n=15-17 per condition. Each dot represents an individual mouse, and the horizontal line indicates the mean. Kruskal-Wallis test.

3.2.3.5 Chronic low-dose MNP exposure disrupts glucose homeostasis

To evaluate whether MNP-induced metabolic alterations are dose-dependent, mice were exposed to lower doses (1 mg/kg or 10 mg/kg) for 12 weeks. In both titrations, liver-to-body weight ratios were unchanged compared to controls (**Figure 32**B, E).

To determine if the metabolic shift remains consistent, glycogen storage using PAS-H staining was assessed. Quantification of the staining revealed a similar trend as observed with 100 mg/kg MNP: chronic exposure to 10 mg/kg of 500 nm PS-particles led to a significant decrease in hepatic glycogen content, whereas 50 nm PS-particles showed no change (**Figure 32** C). However, mice receiving 1 mg/kg MNP did not show a reduction in glycogen levels compared to controls (**Figure 32** F).

These findings suggest that even at lower doses, plastic exposure can induce a shift in glucose homeostasis, highlighting a potential dose-dependent effect on metabolic regulation.

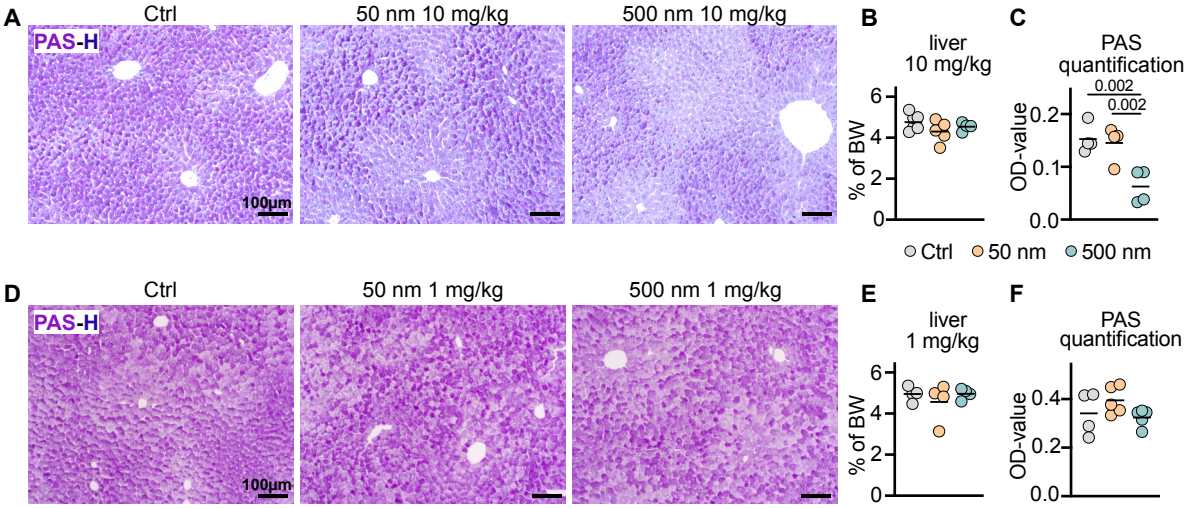

Figure 32 Chronic low-dose MNP exposure reduced hepatic glycogen storage: (A-C) Assessment of glycogen level in the liver following the ingestion of 10 mg/kg of MNP. (A) Representative images of PAS-H-stained liver sections following Scale bars indicate 100 µm. (B) Liver weight relative to body weight. (C) Quantification of PAS-H staining intensity (optical density). Each dot represents an individual mouse, the horizontal line indicates the mean. n= 4 per condition. Ordinary one-way ANOVA. **(D-F)** Assessment of glycogen level in the liver following the ingestion of 1 mg/kg of MNP. (AD Representative images of PAS-H-stained liver sections following Scale bars indicate 100 µm. (E) Liver weight relative to body weight. (F) Quantification of PAS-H staining intensity (optical density). Each dot represents an individual mouse, the horizontal line indicates the mean. n= 4-5 per condition. Ordinary one-way ANOVA.

3.2.3.6 Chronic ingestion of MNP in combination with high-fat diet aggravates obesity-related metabolic dysregulation

Given the observed changes in glucose and lipid homeostasis following chronic MNP ingestion, we aimed to explore the impact of an additional environmental stressor, such as a high-fat diet (HFD). HFD presents a significant challenge to modern societies, contributing to the increasing rates of obesity and other metabolic disorders (216–218). To evaluate the combined effect of MNP ingestion and HFD, a specific treatment paradigm was implemented (Figure 33A). Mice were gavaged with 50 nm and 500 m PS particles as described in the chronic ingestion model. Two weeks prior to the start of MNP exposure, the mice were

switched from chow diet to a control diet (CD, 13 kJ % fat) and maintained on it throughout the gavage period. After 8 weeks of MNP administration, the diet was switched to HFD (60 kJ % fat), which continued for 10 weeks. This included 4 weeks where HFD was provided simultaneously with MNP, followed by an additional 6 weeks on HFD after the final MNP gavage (**Figure 33**A).

Mice exposed to MNP displayed normal weight gain compared to control mice on CD. All mice began to gain weight noticeably upon starting HFD. However, there were no significant changes among the groups, with the 500 nm-treated mice showing a slight increase in weight gain on HFD (**Figure 33**B).

In terms of organ weight, while the liver and inguinal white adipose tissue (iWAT) weight relative to body weight was comparable across all conditions (Figure 33C). However, distinct weight changes were observed in gWAT and BAT. While 500 nm-exposed gWAT showed no significant differences, the relative weight of 50 nm-exposed gWAT was significantly reduced compared to both the control and 500 nm-exposed groups (**Figure 33**C). Additionally, BAT relative weight decreased following MNP ingestion, with a significant reduction observed specifically in the 50 nm-exposed group compared to control BAT (**Figure 33C**).

Further analysis of hepatic lipids using ORO staining revealed neutral lipid accumulation in both MNP-exposed and control animals. Interestingly, ORO-stained sections revealed a distinct lipid distribution when quantified as percentage of ORO^+ area. 50 nm-exposed livers exhibited a significant reduction in neutral lipid levels compared to controls, whereas 500 nm-exposed livers accumulated significantly more lipids than controls, suggesting a size-dependent disruption in lipid homeostasis **(Figure 33**D, E). These findings highlight that MNP exposure can exacerbate lipid dysregulation in the context of dietary stress.

Despite these lipid alterations, Sirius Red staining showed no signs of fibrosis in any of the groups indicating that chronic MNP exposure did not induce clear fibrotic changes in hepatic tissue when combined with HFD (**Figure 33**F).

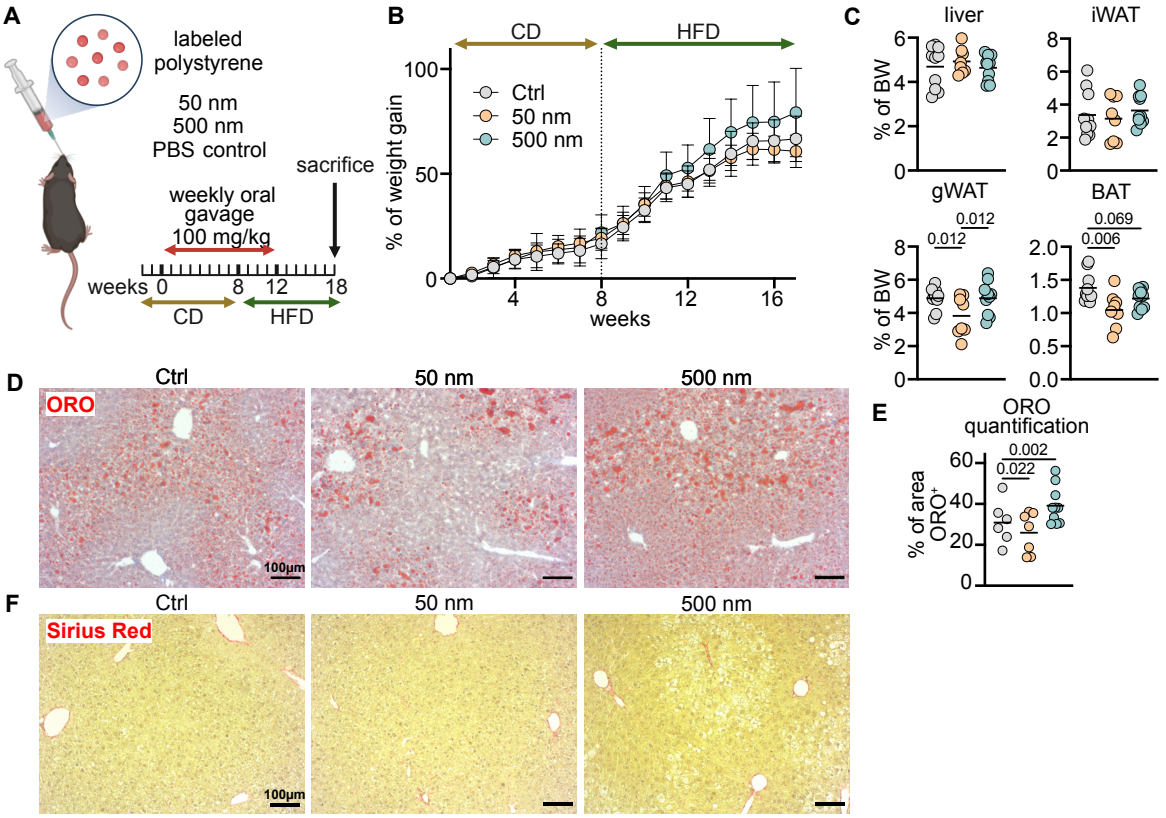

Figure 33 MNP-induced changes in weight gain and adipose tissue under HFD stress: (A) Schematic representation of the experimental setup. **(B)** The percentage of body weight gain over 18 weeks of MNP and HFD treatment. **(C)** Relative gWAT weight (% body weight). n= n=8-10 per condition. Each dot represents an individual mouse, and the horizontal line indicates the mean. Ordinary one-way ANOVA. **(D)** Representative picture of ORO-stained liver sections. Scale bars indicate 100 µm. **(E)** Quantification of ORO staining (% area). Each dot represents an individual mouse, the horizontal line indicates the mean. n= 3-5 per condition. Ordinary one-way ANOVA. **(F)** Representative images of Sirius Red-stained liver sections. Scale bars indicate 100 µm.

Glucose intolerance and insulin resistance are key indicators of metabolic disorders, including obesity (217). To assess these metabolic indicators, glucose tolerance tests (GTT) and insulin tolerance tests (ITT) were performed after 9-10 weeks on CD and after 9-10 weeks on HFD. After the CD and before transitioning to the HFD, fasting blood glucose levels showed no significant differences among the control, 50 nm- and 500 nm-exposed mice (Figure 34A). Additionally, GTT curves across all conditions displayed a typical pattern of glucose response and clearance, indicating normal glucose tolerance (Figure 34B). The ITT results also revealed comparable insulin sensitivity across all groups on CD (**Figure 34**C).

After 9-10 weeks on the HFD, however, fasting blood glucose levels were significantly higher in both 50 nm and 500 nm-exposed mice compared to controls (**Figure 34**D). In the GTT, the area under the curve (AUC) was significantly elevated in 50 nm-exposed mice compared to controls, suggesting impaired glucose tolerance, with a similar pattern observed in the 500 nm group (**Figure 34**E). Furthermore, ITT analysis indicated that 50 nm-exposed mice showed reduced insulin sensitivity compared to control mice, although this difference was not statistically significant (**Figure 34**F), while the 500 nm group exhibited insulin sensitivity similar to that of the controls.

Collectively, these findings suggest that MNP exposure may exacerbate HFD-induced metabolic dysfunction, aggravating the degree of glucose intolerance.

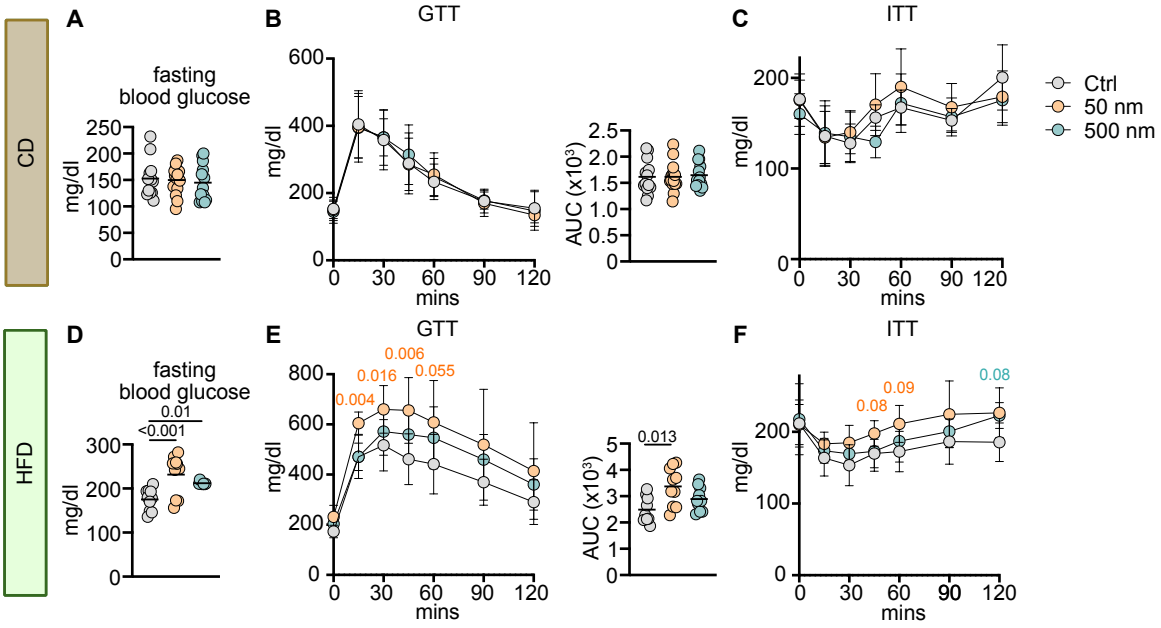

Figure 34 MNP ingestion aggravates the metabolic stress under HFD: (A) Fasting blood glucose levels after 9-10 weeks under CD diet. Each dot represents an individual mouse, the horizontal line indicates the mean. n= 13-15 per condition. Ordinary one-way ANOVA. **(B)** GTT after 9-10 weeks under CD diet (left), n= 13-15 per condition. Two-way ANOVA, AUC quantification (right). Each dot represents an individual mouse, the horizontal line indicates the mean. n= 13-15 per condition. Kruskal-Wallis test. **(C)** ITT after 9-10 weeks under CD diet. n= 8 per condition. Two-way ANOVA. **(D)** Fasting blood glucose levels after 9-10 weeks under HFD diet. Each dot represents an individual mouse, the horizontal line indicates the mean. n= 8-10 per condition. Ordinary one-way ANOVA. **(E)** GTT after 9-10 weeks under HFD diet (left), n= 8-10 per condition. Two-way ANOVA, AUC quantification (right). Each dot represents an individual mouse, the horizontal line indicates the mean. n= 8-10 per condition. Kruskal-Wallis test. **(F)** ITT after 9-10 weeks under HFD diet. n= 5 per condition. Two-way ANOVA.

3.2.4 Accumulation of MNP disrupts macrophages core functions

As demonstrated, macrophages, particularly KCs, are responsible for MNP uptake, leading to their accumulation over time following oral ingestion. To investigate molecular changes within KCs due to MNP accumulation, previously described snRNA-Seq data from sorted liver nuclei after chronic MNP exposure were further analyzed, focusing on the KC cluster (3,504 nuclei), which was subsequently subclustered into five distinct clusters (**Figure 35**A).

All clusters expressed canonical KC markers, including V-set and immunoglobulin domain containing 4 (*Vsig4*) and c-type lectin domain family 4-member f (*Clec4f)* (Figure 35B). However, cluster 4 uniquely expressed kinetochore Associated 1(*Kntc1*), suggesting that these cells are undergoing proliferation (**Figure 35**B). Thus, cluster 4 was excluded from further analysis and clusters 0, 1, 2, and 3 were combined for downstream assessment.

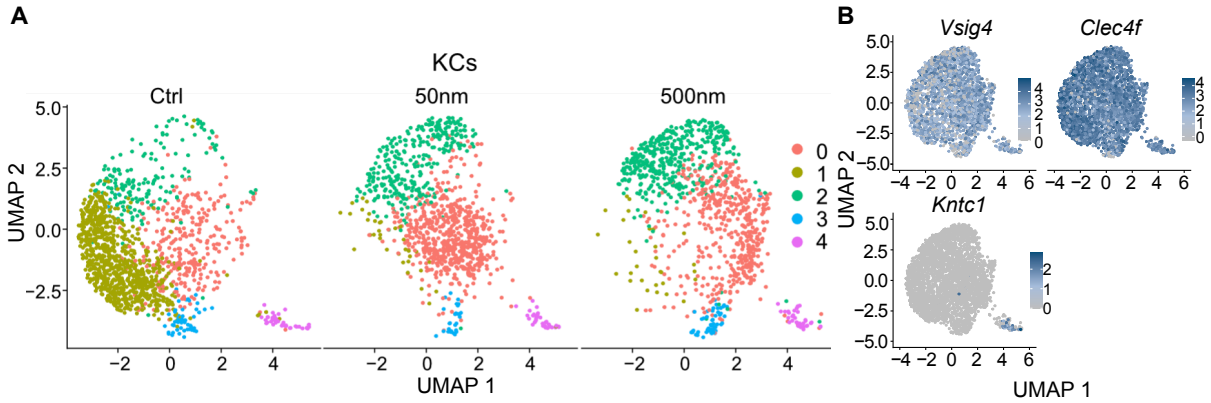

Figure 35 Subclustering of KCs following chronic MNP exposure: (A) UMAP plot of KCs subclusters. **(B)** Feature plot illustrating the expression of *Vsig4*, *Clec4f* and *Kntc1* in KCs.

DEGs in MNP-exposed KCs were identified, relative to controls, using an adjusted p-value threshold of ≤ 0.05, and a $\log_2$ fold change threshold of ≥ 0.35 or ≤ -0.35. Additionally, the gene need to be expressed in more than 5 % of the cells. This analysis revealed 70 and 79 downregulated genes and 130 and 144 upregulated genes in 50 nm- and 500 nm-exposed KCs, respectively (**Figure 36**A-D). Among these, 31 downregulated genes and 77 upregulated genes were shared between both MNP groups.

Several genes associated with the immune function of Kupffer cells (KCs) were affected by MNP exposure, particularly those involved in antigen presentation, complement system, and scavenger receptor activity. Notably, antigen presentation-related genes, including beta-2-microglobulin (*B2m*), histocompatibility 2 Q region locus 10 (*H2-Q10)*, and cathepsin L (*Ctsl*), were upregulated following MNP ingestion. Additionally, histocompatibility 2 D region locus 1 (*H2-D1*) and histocompatibility 2 T region locus 23 (*H2-T23*) were specifically upregulated in 500 nm-exposed KCs. In contrast, CD74 molecule (*Cd74*) and NLR family CARD domain containing 5 (*Nlrc5*) were downregulated in 50 nm-exposed KCs.

Among complement components, complement component 1q subcomponent alpha polypeptide (*C1qa*) was upregulated in MNP-exposed KCs, while complement component 1q subcomponent C chain (*C1qc*) and complement component 3 (*C3*) were specifically upregulated in 500 nm-exposed KCs.

Regarding scavenger receptors, T-cell immunoglobulin and mucin domain containing 4 (*Timd4*) was downregulated following MNP exposure, whereas Clec4f was downregulated specifically in 50 nm-exposed KCs. In contrast, *Cd163* was upregulated in 50 nm-exposed KCs.

MNP-exposed KCs exhibited signs of endoplasmic reticulum (ER) and oxidative stress, suggesting disruptions in protein homeostasis and redox balance, leading to increased cellular stress. Several genes, including heat shock protein 5 (*Hspa5*), mesencephalic astrocyte-derived neurotrophic factor (*Manf*), NADH ubiquinone oxidoreductase subunit A4 (*Ndufa4*), selenoprotein P (Selenop), serpin family A member 1A (*Serpina1a*), *Serpina1b*, *Serpina1c,*

and glutathione S-transferase alpha 3 (*Gsta3*), were upregulated following MNP ingestion. Furthermore, 500 nm-exposed KCs showed upregulation of glutathione peroxidase 1 (*Gpx1*) and thioredoxin-interacting protein (*Txnip*).

Additionally, several genes related to lipid and glucose homeostasis were altered, indicating potential metabolic adaptations in KCs. Genes involved in lipid transport, such as fatty acid-binding protein 1 (*Fabp1*), apolipoprotein C1 (*Apoc1*), apolipoprotein C3 (*Apoc3*), *Apoe*, *Apoh* as well as genes linked to fatty acid oxidation, including cytochrome P450 family 2 subfamily E member 1 (*Cyp2e1*) and cytochrome P450 family 3 subfamily A member 11 (*Cyp3a11*), were upregulated following MNP exposure. Similarly, key regulators of glucose homeostasis were affected, with aldolase B fructose-bisphosphate (*Aldob*) upregulated following MNP ingestion, while phosphoenolpyruvate carboxykinase 1 (*Pck1*) was specifically upregulated in 50 nm-exposed KCs.

For ORA, a less stringent DEG threshold (adjusted p-value threshold of ≤ 0.1 and a $\log_2$ fold change threshold of ≥ 0.25 or ≤ -0.25) was applied, allowing the inclusion of genes with borderline significance for exploratory analysis (**Figure 36**E). Under these settings, 113 and 100 genes were downregulated, while 195 and 205 genes were upregulated in 50 nm- and 500 nm-exposed KCs, respectively.

Similar to the observation based on the DEGs assessment, ORA revealed that chronic MNP ingestion alters KC function, impacting both macrophage core functions and metabolic pathways. MNP-exposed KCs showed an upregulation of pathways related to ‘binding and uptake of ligand by scavenger receptors’, ‘iron uptake and transfer’, ‘response to oxidative stress’, ‘cytoprotection by HMOX1’, ‘response to xenobiotic stimulus’, ‘chaperone mediated autophagy’, ‘lipid localization’, ‘glycogen metabolism’ and ‘cellular response to starvation’. Additionally, ‘lipid homeostasis’ was upregulated only following 500 nm-particles ingestion.

Conversely, MNP ingestion led to the downregulation of ‘mononuclear cell migration’, while ‘regulation of chemotaxis’ and ‘Fcγ receptor-dependent phagocytosis’ were specifically downregulated in 500 nm-exposed KCs.

Notably, ‘antigen processing and presentation’ showed opposing enrichment patterns between MNP-exposed groups: it was downregulated in 50 nm-exposed KCs but upregulated in 500 nm-exposed KCs.

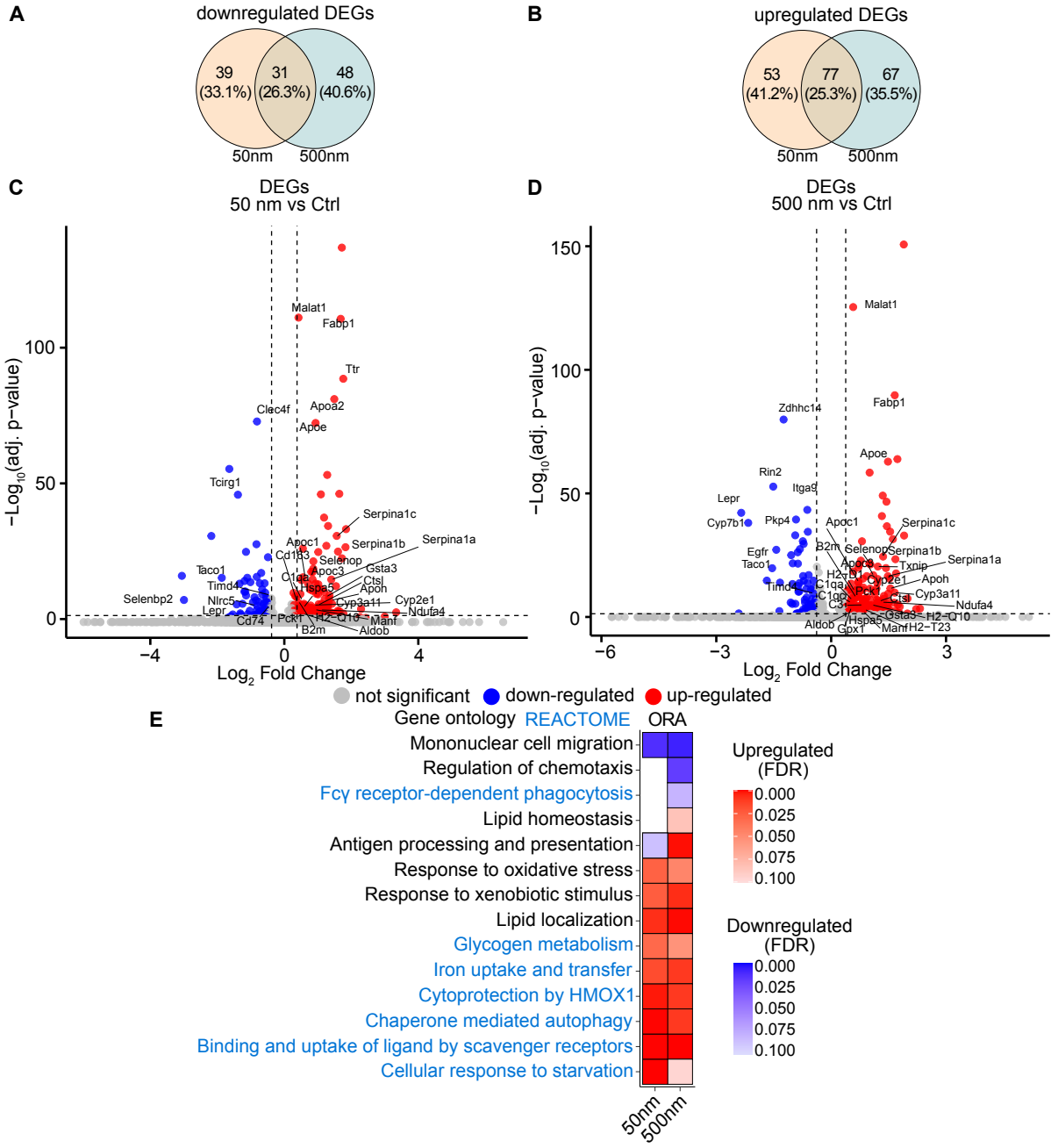

Figure 36 MNP ingestion alters KCs gene expression: (A, B) Venn diagram showing DEG counts in 50 nm and 500 nm-exposed KCs compared to controls. **(C, D)** Volcano plots displaying DEGs between MNP-exposed and control KCs, each dot represents a gene, with the x-axis showing the $\log_2$ fold change and the y-axis showing the $-\log_{10}$ adjusted p-value. Significantly upregulated genes (adjusted p-value ≤ 0.05, $\log_2$ fold change ≥ 0.38) are shown in red, downregulated genes (adjusted p-value ≤ 0.05, $\log_2$ fold change ≤ -0.38) are shown in blue, non-significant genes are displayed in gray. **(E)** heatmap displays significantly enriched pathways based on DEGs (DEGs: adjusted p-value ≤ 0.1, $\log_2$ fold change ≥ 0.25 or ≤ -0.25). Pathways enriched among upregulated genes are shown in red, while those enriched among downregulated genes are shown in blue. The color gradient reflects the false discovery rate (FDR)-adjusted significance, with more intense colors indicating stronger enrichment.

To further explore the changes in the KC-phenotype, specifically regarding phagocytosis and antigen presentation, the protein levels of key surface markers were assessed using flow cytometry following chronic MNP ingestion. These markers included CD64 (Fc gamma receptor I, FcγRI), CD32b (FcγRIIb), CD16.2 (FcγRIV), T-cell immunoglobulin and mucin domain-containing protein 4 (TIM-4), MER proto-oncogene tyrosine kinase (MerTK), all of

which play a major role in phagocytosis (219). Additionally, major histocompatibility complex class II (MHCII), which is essential for antigen presentation (220) was assessed as well. Although *Timd4* was downregulated following MNP ingestion, TIM-4 protein levels were not changes in both 50 nm- and 500 nm exposed KCs compared to control (**Figure 37**). Similarly, both CD64 and CD16.2 remained stable (**Figure 37**). Notably MerTK and CD32b levels decreased significantly in 500 nm-exposed KCs compared to both 50 nm-exposed and control KCs (Figure 37). Additionally, MHCII was significantly reduced in 50 nm- and 500 nm-exposed KCs (Figure 37).

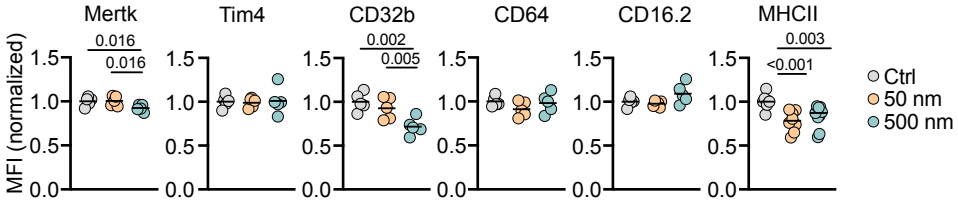

Figure 37 Chronic MNP ingestion alters phagocytic and antigen-presenting marker expression in KCs: Expression of immune markers in KCs (MFI normalized to control). Each dot represents an individual mouse, the horizontal line indicates the mean. n= 5-9 per condition. Ordinary one-way ANOVA.

Together, these findings suggest that MNP exposure broadly disrupts immune and metabolic functions in KCs. Notably, microplastic-exposed KCs showed a pronounced impact on phagocytosis at both the transcriptomic and protein levels, indicating a potential dysregulation in phagocytic capacity, which could impair pathogen clearance.

3.2.4.1 Microplastic accumulation compromises phagocytic function in macrophages

To investigate the altered phagocytic capacity described earlier—particularly the downregulation of 'Fcγ receptor-dependent phagocytosis'—KCs were assessed *in vivo*. This was done using an FcγR-mediated platelet depletion assay (**Figure 38**A). Here, mice ingested plastic for 12 weeks, while controls received PBS. After the last gavage, the baseline platelet counts were measured. Mice then received an i.p. injection of platelet-specific (clone 6A6) antibody of the IgG2c subclass (6A6-IgG2c) (221), promoting opsonization and rapid clearance of platelets by KCs (221). The platelet counts in the blood were monitored over 72 hours, during which control mice showed full platelet recovery. While the 50 nm-exposed mice displayed similar pattern to the control mice, the 500 nm-exposed group showed significantly higher platelet counts at 8 hours post-antibody injection, with elevated levels also observed at 4 and 24 hours (**Figure 38**B). These findings demonstrate a significant impairment in KCs phagocytosis and clearance of opsonized platelets following microplastic ingestion.

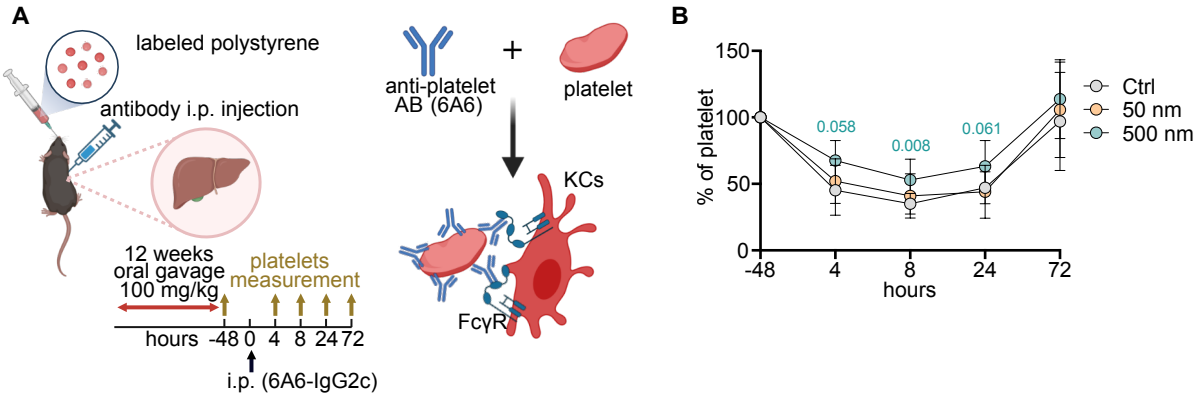

Figure 38 Chronic MNP exposure impairs FcγR-mediated phagocytosis in KCs: (A) Schematic representation of the experimental setup. **(B)** Platelets quantification (% of baseline) over 72 hours following 6A6-IgG2c injection. n= 7-12 per condition. Two-way ANOVA.

3.2.4.2 Chronic microplastic ingestion hinders bacterial clearance

After confirming that chronic microplastic ingestion impairs macrophage phagocytic capacity, it was essential to assess its broader implications for immune function, including its impact on bacterial clearance, as phagocytosis plays a critical role in pathogen removal (222).

To test this, mice chronically exposed to MNP were infected intravenously (i.v.), with *E. coli* K12 at a dose of $1x10^6$ CFU/20 g body weight. Infection progression was monitored over 24 hours (**Figure 39**A). Bacterial colony-forming units (CFU) were measured in the blood 2 hours post-infection. At 24 hours post-infection, mice were sacrificed, and CFU counts were assessed in the spleen and liver. All groups exhibited comparable weight loss over the 24 hours period, with no detection of bacteria in the blood 2 hours post-infection (**Figure 39**B). 24 hours post-infection, CFU counts showed no significant differences between MNP-exposed and control mice in the liver (**Figure 39**C), with no detectable bacteria in the spleen. These results indicate that, despite compromised phagocytic function in microplastic-exposed macrophages, bacterial progression and clearance in the liver was comparable to those of control mice.

To assess blood clearance efficacy within a short time frame, mice were injected i.v. with 1×10^7 CFU/20 g body weight of *E. coli*. Five minutes post-infection, mice were sacrificed, and bacterial load was quantified in vena cava blood, liver, and spleen (**Figure 39**D). Notably, CFU counts in the liver and spleen remained similar across groups; however, the blood of 500 nm-exposed mice showed significantly higher bacterial load compared to both 50 nm-exposed and control mice (**Figure 39**E).

Overall, these findings suggest that chronic microplastic-exposure impaired macrophage-dependent bacterial clearance, while nanoplastic-exposed mice showed no changes in clearance capacity.

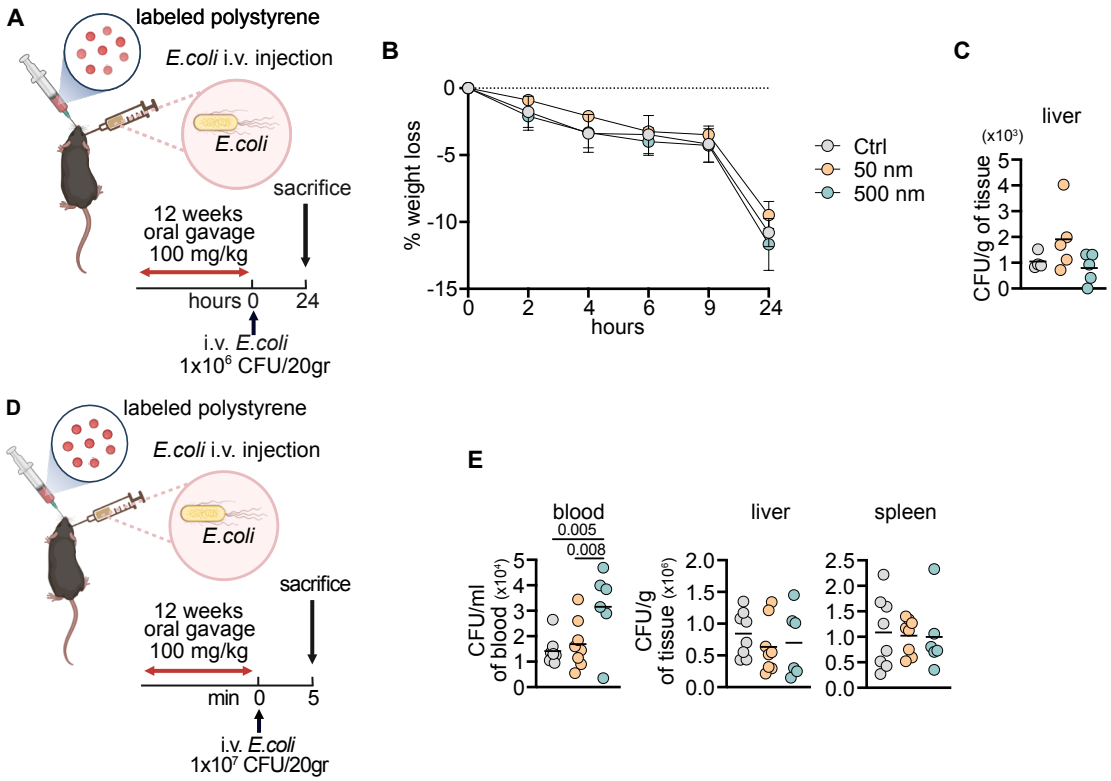

Figure 39 Chronic microplastic exposure impairs macrophage-mediated bacterial clearance: (A) Schematic representation of the experimental setup for 24 hours *E. coli* infection. **(B)** The percentage of body weight loss following *E. coli* infection. n= 4-5 per condition. Two-way ANOVA. **(C)** CFU counts quantification 24 hours post-infection in the liver (per gram of tissue). Each dot represents an individual mouse, the horizontal line indicates the mean. n= 4-5 per condition. Ordinary one-way ANOVA. **(D)** Schematic representation of the experimental setup for 5 minutes *E. coli* infection. **(E)** CFU counts quantification in the liver (per gram of tissue). Each dot represents an individual mouse, the horizontal line indicates the mean. n= 4-5 per condition. CFU counts quantification 5 minutes post-infection in the blood (per ml), liver and spleen (per gram of tissue). Each dot represents an individual mouse, the horizontal line indicates the mean. n= 6-8 per condition. Ordinary one-way ANOVA.

3.2.4.3 Microplastic ingestion impairs macrophage function in a recurrent malaria infection model

Since the 24-hour *E. coli* infection represents an acute infection, a chronic, recurring malaria infection model was chosen. This model provides a framework to assess immune responses and the phagocytic phenotype of macrophages (223), particularly in the spleen and liver, over an extended timeframe. After chronic ingestion of MNP, mice were infected intraperitoneally with *Plasmodium chabaudi*-infected red blood cells (*P. chabaudi*-iRBCs). Infection severity was measured by parasitemia, the percentage of iRBCs, and was monitored over 35 days, covering two peaks of parasitemia during the blood-stage malaria infection (**Figure 40**A). Parasitemia began to increase around 10 days post-infection (p.i. 10), with all groups showing comparable values. Although the 50 nm-exposed group exhibited slightly lower parasitemia levels, this difference was not statistically significant (**Figure 40**B, C). Notably, two of the 500 nm-exposed mice and one 50 nm-exposed mice exhibited a slower reduction in parasitemia between p.i. 10 and p.i. 17, at p.i. 14 (**Figure 40**B, C). During the second peak at

p.i. 21, the 500 nm-exposed group showed a significantly higher parasitemia values (**Figure 40**B, C), suggesting a decreased ability to clear iRBCs compared to controls.

Weight loss began around day p.i. 10 across all groups, indicating infection progression. Interestingly, the MNP-exposed mice recovered weight more rapidly, with 500 nm-exposed mice showing significant increase in weight compared to controls (**Figure 40**D).

These findings indicate that MNP accumulation may impair macrophage-mediated clearance of infected cells, leading to prolonged parasitemia and altered host recovery.

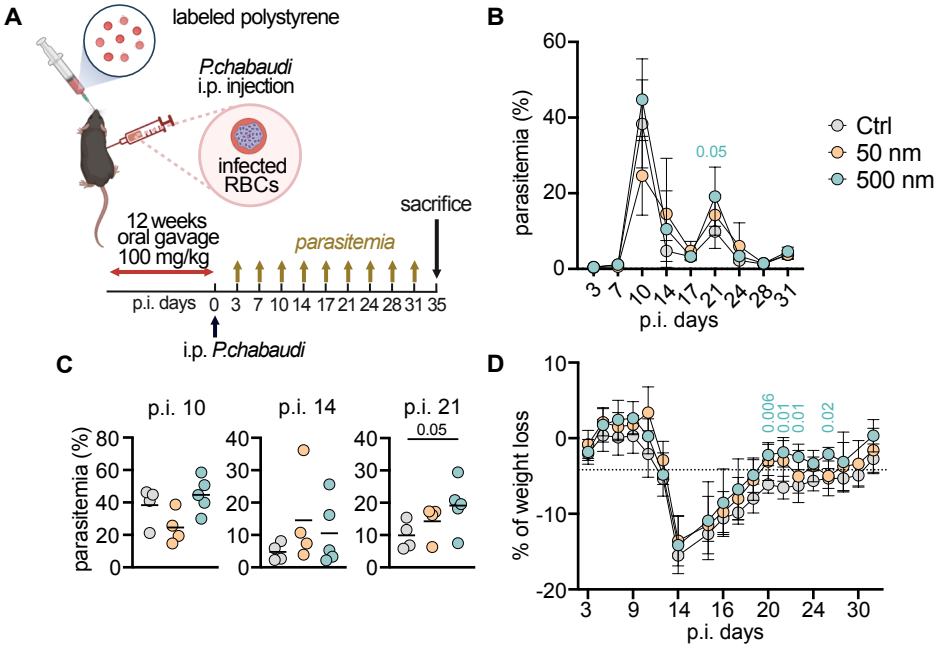

Figure 40 Chronic microplastic ingestion impairs iRBC clearance following malaria infection: (A) Schematic representation of the experimental setup for malaria infection. **(B)** Parasitemia levels following malaria infection. **(C)** Parasitemia levels at p.i. 10, p.i. 14 and p.i. 21. Each dot represents an individual mouse, the horizontal line indicates the mean. n= 4-5 per condition. Kruskal-Wallis test. **(D)** The percentage of body weight loss following malaria infection. n= 4-5 per condition. Two-way ANOVA.

3.2.4.4 MNP ingestion primes mice for autoimmune response

Another critical function of macrophages related to phagocytosis is the clearance of ACs through efferocytosis, a process that involves scavenger receptors such as MerTK (37,224). Impaired clearance of ACs has been linked to the onset of autoimmunity, as seen in conditions like SLE (225,226). Given that MerTK expression was found to be decreased on KCs exposed to 500 nm PS-particles (Figure 37), this finding prompted further investigation into the potential role of impaired macrophage function in promoting an autoimmune phenotype.

To investigate this, an *in vivo* model was utilized to assess macrophage function in the context of efferocytosis and its implications for autoimmunity. Specifically, a model inducing autoimmunity to apoptotic cell-derived self-antigens, as described by Duhlin et al. (193) was employed.

After chronic ingestion of MNP, male mice were administered weekly i.v. injections of apoptotic thymocytes ($2x10^7$ ACs/mouse) over five weeks to break immune tolerance (**Figure 41**A). To

assess memory responses, booster injections were administered on days 105 and 140 (d 105 and d 140). Serum levels of anti-DNA IgG autoantibodies were measured relative to a positive control serum, which was derived from the BXSB mice, a model known for developing lupus-like autoimmune disease and producing autoantibodies (227). As an additional control, sera from six- and nine-month-old mice were used to account for age-related changes.

Prior to ACs injections at d -5, all groups exhibited comparable anti-DNA IgG levels, with the exception of two 50 nm-exposed mice that showed elevated values (**Figure 41**B, C). Throughout the experiment, mice from different groups did not develop a robust autoimmune phenotype, and their anti-DNA IgG levels remained within the range of age-matched controls (**Figure 41**B, C). However, following the first and second booster injections, specifically at d 112 and d 149, one 50 nm-exposed mouse and one 500 nm-exposed mouse showed increased anti-DNA IgG levels (**Figure 41**B, C). Remarkably, the 500 nm-exposed mouse exhibited an eight-fold increase in anti-DNA IgG at d 149 (**Figure 41**B, C).

In summary, while the majority of MNP-exposed mice did not develop overt signs of systemic autoimmunity, approximately 10 % of exposed mice showed heightened anti-DNA IgG levels following AC challenge, suggestive of priming for autoreactivity.

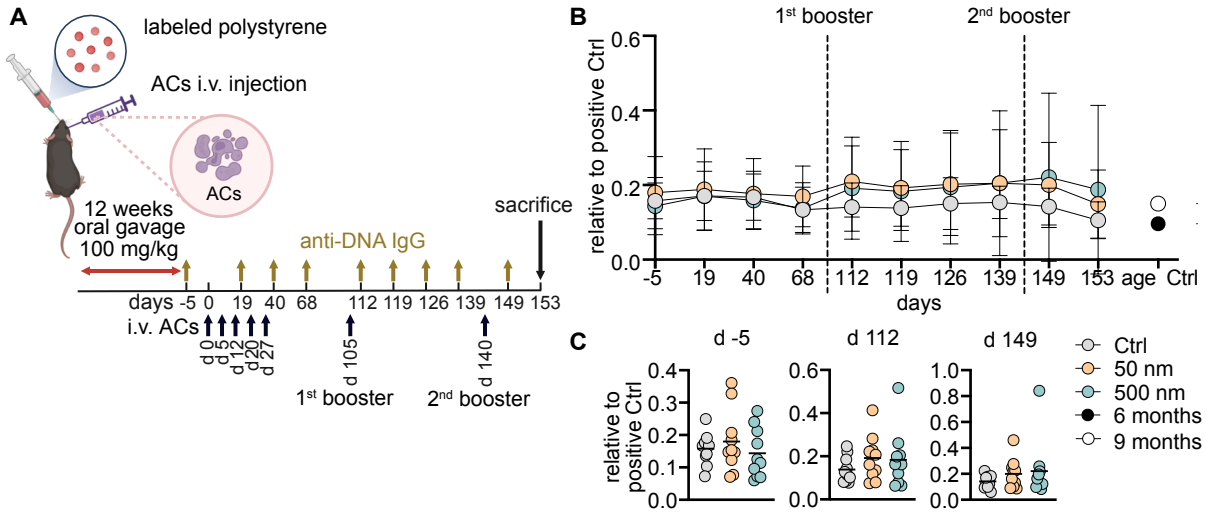

Figure 41 Chronic MNP ingestion impact on autoimmune response following ACs challenge: (A) Schematic representation of the experimental setup. **(B)** Serum anti-DNA IgG autoantibody levels relative to a positive control serum from the lupus-prone BXSB mouse model. Age-matched control sera were included to account for age-related changes. n=10 per condition. **(C)** Anti-DNA IgG levels at specific time points (days -5, 112, and 149). Each dot represents an individual mouse, with the horizontal line indicating the mean. Kruskal-Wallis test.

3.2.5 Ontogeny analysis reveals minor alterations in macrophage populations following chronic MNP ingestion

As demonstrated before, macrophages exhibited alterations in their phenotype, which may be due to their death and subsequent replenishment with monocytes-derived macrophages. To assess macrophage ontogeny, a double fate-mapping (DFM) model (*Tnfrsf11a*^{Cre}; *Rosa26*$^{LSL\text{-}YFP}$; *Ms4a3*^{FlpO}; *Rosa26*$^{FSF\text{-}tdTomato}$) was used (**Figure 42**A), in which DFM mice received either 50 nm-PS particles, 500 nm-PS particles or PBS for 12 weeks. The PS-particles used in the

DFM mice were unlabeled to avoid interference with the fluorescent protein signal. This model utilizes a combination of Cre-loxP and Flp-FRT recombination systems to achieve lineage tracing and dual fluorescent labelling. Specifically, the *Tnfrsf11a*^{Cre} drives Cre recombinase expression under the control of the *Tnfrsf11a* promoter, leading to the excision of the LSL (loxP-stop-loxP) cassette in the *Rosa26*$^{LSL\text{-}YFP}$ locus, thereby activating yellow fluorescent protein (YFP) expression in *Tnfrsf11a*-expressing cells, which are mainly tissue-resident macrophages (228). Additionally, the *Ms4a3*^{FlpO} allele drives Flp recombinase expression in *Ms4a3*-expressing cells, which are GMP-derived cells in bone marrow, allowing for the excision of the FSF (FRT-stop-FRT) cassette in the *Rosa26*$^{FSF\text{-}tdTomato}$ locus, resulting in tdTomato (tdT) expression. This dual-reporter system tracks EMP-derived macrophages (YFP-only) and monocyte-derived macrophages (tdT+ and YFP+), the latter expressing *Tnfrsf11a* during their differentiation into tissue-resident macrophages. However, tdT$^+$ macrophages may represent short lived, newly recruited macrophages.

In the liver, KCs remained predominantly EMP-derived, with 97 % YFP$^+$ labelling, despite the accumulation of MNP (**Figure 42**B). Notably, YFP$^+$ tdT$^+$ cells, indicative of monocyte-derived macrophages, increased significantly, from 10 % in the control mice to around 17 % in the MNP-exposed mice **(Figure 42**B).

In the spleen, macrophage subpopulations display distinct developmental origins. In control mice, approximately 80% of both CD163$^+$ RPM and MMM, as well as 68% of CD163$^-$ RPM, were derived from yolk-sac progenitors, while the remaining 20% and 32%, respectively, originated from monocytes. Both the WPM and MZM consist of three fractions. While WPM were 44 % YFP$^+$, 41 % tdT$^+$ and 15 % YFP$^+$ tdT$^+$, MZM were 16 % YFP$^+$, 68 % tdT$^+$ and 16 % YFP$^+$ tdT$^+$ (**Figure 42**C). In contrast to the KCs in the liver, the spleen exhibited altered macrophage ontogeny in the 500 nm-exposed mice, while 50 nm-exposed mice exhibited no significant differences. CD163$^+$ RPM, CD163$^-$ RPM and MMM showed 5-8 % shift from EMP-derived towards monocyte-derived macrophages (**Figure 42**C). However, the effect on WPM and MZM was minimal to non-existent.

In conclusion, the DFM model demonstrated that despite the accumulation of MNP in the liver and spleen, the impact on macrophage ontogeny was relatively minor in the spleen, and no changes were observed in KC following chronic MNP ingestion.

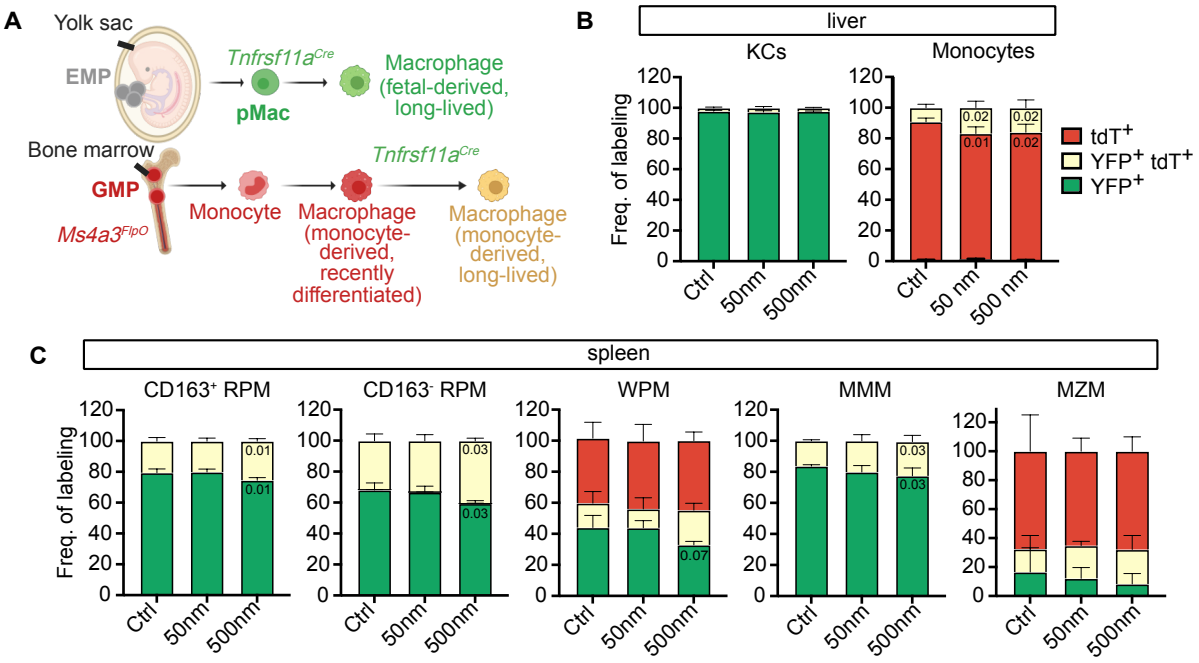

Figure 42 Chronic MNP ingestion exhibits minor influence on macrophage ontogeny: (A) Schematic representation of *Tnfrsf11a*^{Cre}; *Rosa26*$^{LSL\text{-}YFP}$; *Ms4a3*^{FlpO}; *Rosa26*$^{FSF\text{-}tdTomato}$ mouse model used to distinguish EMP-derived and monocytes-derived macrophages. **(B)** Frequency of labelling of KCs and monocytes in the liver. (**C)** Frequency of labelling of splenic macrophages. n= 4.5 per condition. Kruskal-Wallis test.

3.2.6 Chronic MNP ingestion alters gut microbiome diversity and composition

The oral ingestion of MNP directly affects the gut environment, suggesting that the microbiome may also be influenced. This prompted investigation into potential microbiome alterations and their implications for host health. To investigate microbiome changes after chronic MNP ingestion (**Figure 4**A), fecal and cecal samples were analyzed.

Alpha diversity analysis, which reflects the microbiome diversity within each condition, revealed a reduction in microbial diversity in the cecum of 50 nm-exposed mice compared to controls, while the fecal microbiome showed no changes in alpha diversity (**Figure 43**A). In contrast, 500 nm-exposed mice exhibited no changes in microbial diversity in either the cecum or feces.

To assess the impact of chronic MNP ingestion on the gut microbiome composition, beta diversity was evaluated using the Bray-Curtis dissimilarity index, which considers both species presence/absence and relative abundance.

In the cecum, both 50 nm and 500 nm PS-particles exposure groups exhibited a significant shift in microbial community composition compared to control mice (PERMANOVA, q-value of 0.052 and 0.046, respectively) (**Figure 43**B). These findings indicate that MNP ingestion altered the relative abundance of microbial taxa in the cecum.

In the fecal samples, neither 50 nm- nor 500 nm-exposed groups showed a significant difference compared to controls (PERMANOVA, q-value of 0.19 and 0.14, respectively) (**Figure 43**B).

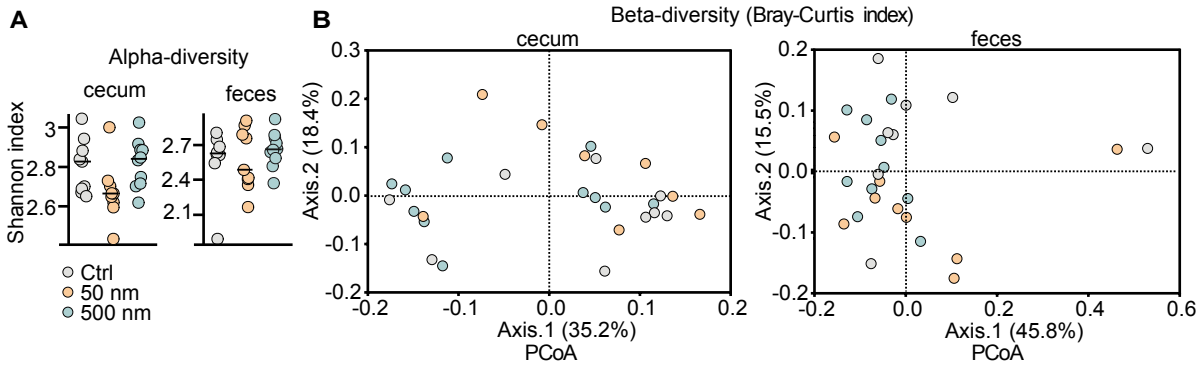

Figure 43 Chronic MNP ingestion alters microbiome diversity: (A) alpha diversity measures with Shannon index in cecum and feces, **(B)** PCoA plots showing the beta diversity with Bray-Curtis index for cecum and feces. n=8-10 per condition. PERMANOVA.

Furthermore, detailed analysis of bacterial species abundance highlighted specific shifts caused by MNP ingestion. In the cecum, MNP-exposed mice showed a significant increase in species such as *Oscillibacter*, *Faecalibacterium UBA 1819*, *Coriobacteriaceae UCG-002*, and *Ruminococcaceae UCG-005*. Conversely, *Eubacterium coprostanoligenes*, and *Christensenellaceae R-7 group* were decreased. Additionally, *Muribaculum* was increased in 500 nm-exposed group, while Mucispiillum was decreased. *Ruminococcaceae and Turicibacter* was decreased in 50 nm-exposed group compared to controls (**Figure 44**).

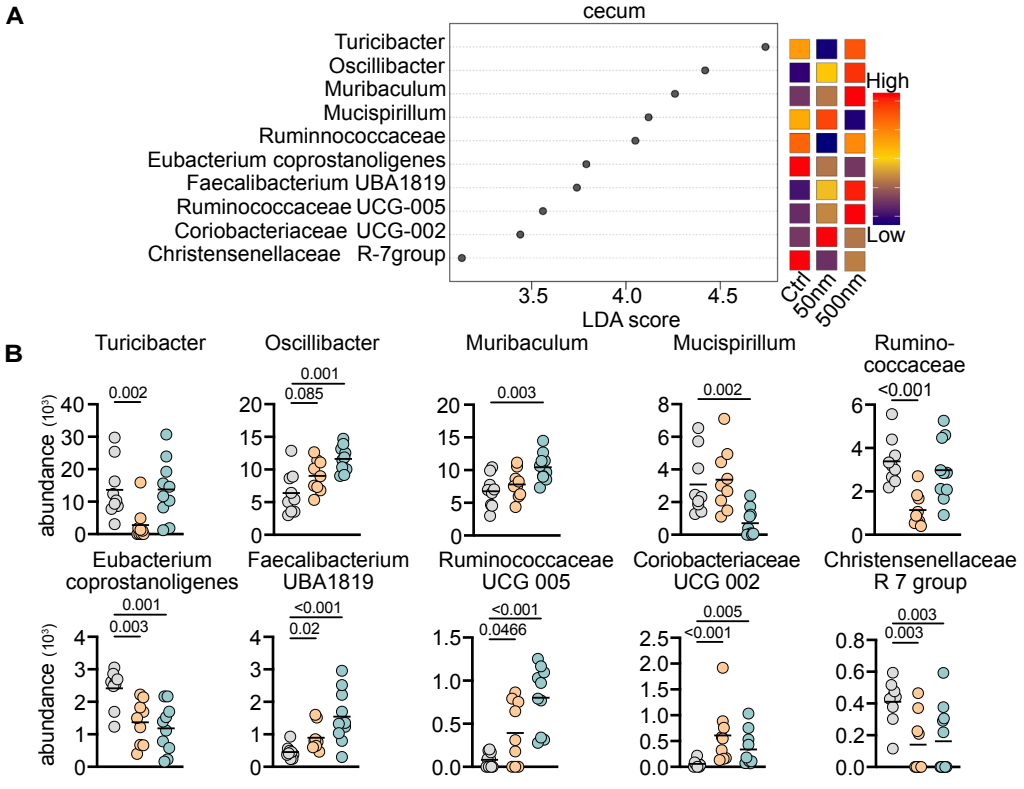

Figure 44 MNP ingestion alters cecal microbiota composition: (A) Heatmap of LDA scores generated by LEfSe analysis, highlighting differentially abundant bacterial taxa in MNP-exposed groups compared to controls. Taxa with an LDA score > 2and a significance threshold of $p < 0.05$ were considered significant **(B)** Abundance of selected bacterial species, n=8-10 per condition. Kruskal-Wallis test.

In the fecal samples, species such as *Oscillibacter* and *Clostridia UCG-014* were enriched in MNP-exposed mice, while *Lactobacillus* was reduced. Notably, 50 nm-exposed mice showed

distinct shifts compared to the 500 nm group, with *Coriobacteriaceae UCG-002* enriched, and *Ruminococcaceae, Turicibacter* and *Rikenellaceae RC9* reduced. Additionally, *Mucispirillum* was decreased in the 500 nm-exposed group.

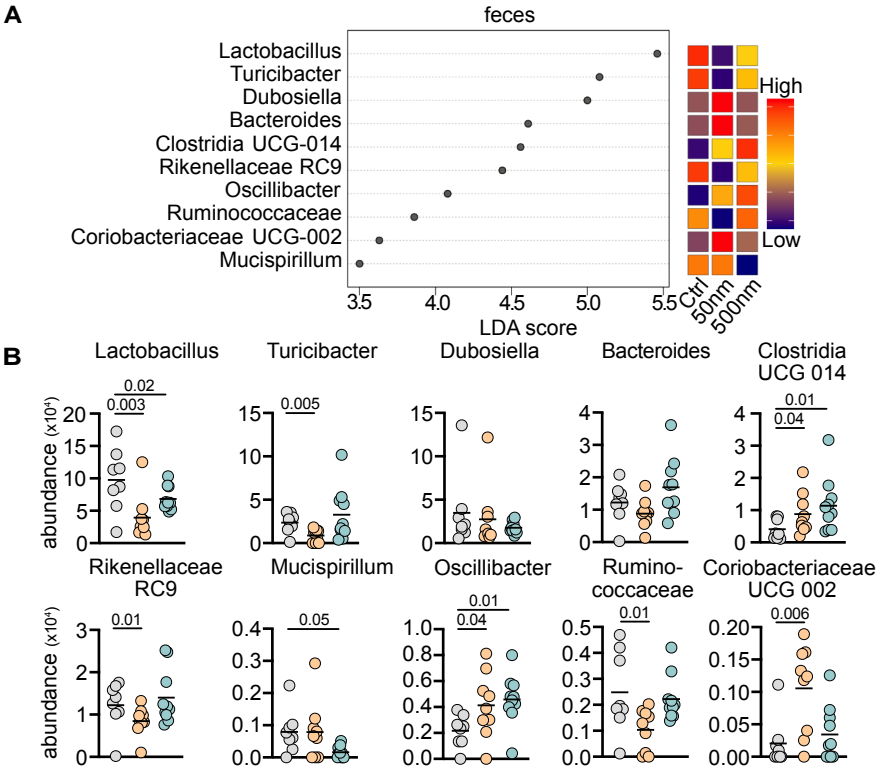

Figure 45 MNP ingestion alters fecal microbiota composition: (A) Heatmap of LDA scores generated by LEfSe analysis, highlighting differentially abundant bacterial taxa in MNP-exposed groups compared to controls. Taxa with an LDA score > 2and a significance threshold of $p < 0.05$ were considered significant **(B)** Abundance of selected bacterial species, n=8-10 per condition. Kruskal-Wallis test.

These findings suggest that exposure to 50 nm PS-particles leads to localized disruptions in microbial diversity within the cecum, while overall diversity in fecal samples remains stable. Abundance analysis highlights shifts in specific bacterial species following MNP ingestion, which may have significant implications for host metabolism and health.

4 Discussion

In an era where micro- and nanoplastic present escalating environmental and health concerns, this thesis explores their biological impacts, particularly on metabolic and immune functions. Plastic has become an integral part of modern life, with humans ingesting these particles in significant quantities through food, drinking water, and other sources (12,13,229,230). To address these concerns, we established a chronic ingestion model, where mice were exposed orally to MNP for 12 weeks. This model enabled us to investigate the effects of plastic accumulation in various organs on homeostatic functions over an extended period.

Weekly microplastic ingestion could range from 0.1–5 grams per person (19), equivalent to around 1.4 mg/kg to 70 mg/kg for a 70 kg individual. To reflect the broad range of microplastic intake, we selected doses of 100 mg/kg, 10 mg/kg and 1 mg/kg.

In this study, PS was used to investigate the effects of MNP ingestion. PS is the third most common plastic found in drinking water, while some studies claiming that it is the most common plastic in the ocean (231). Furthermore, PS is found to be common contaminant of food sources (12). The beads were modified with carboxyl groups, imparting a negative charge, a characteristic shown to enhance bioavailability in the brain relative to other modifications (232). However, given the diverse modifications of environmental plastics (233,234), this work serves as a starting point to better understand how plastics influence biological systems, highlighting the need for future studies with more environmentally relevant plastic models.

4.1 **Accumulation and long-term retention of MNP in tissue-resident macrophages**

This thesis demonstrated that MNP can cross the gut barrier and reach various organs, including the liver, spleen, and brain, consistent with previous reports (232,235). Notably, MNP were still detected in the liver six months after the last gavage, indicating the persistence of PS *in vivo*. This observation aligns with environmental studies suggesting the enduring nature of PS under natural conditions, highlighting its potential resistance to degradation both within biological systems and in the environment (236). These findings suggest that the effects of MNP ingestion may be long-lasting, raising concerns about potential cumulative harmful impacts over time.

Macrophages, key players in the immune system, are primarily responsible for clearing foreign particles (237). Consistent with earlier studies (238,239), we observed that MNP predominantly accumulated within macrophages across various organs. In both the liver and spleen, macrophages predominantly cleared MNP after chronic ingestion. Other immune cells, including DCs, granulocytes, and monocytes, also demonstrated the capacity to internalize MNP, with this phenomenon being more pronounced in the spleen.

Interestingly, endothelial cells, though considered non-professional phagocytes, internalized MNP in the liver, preferentially taking up 50 nm PS particles. This size-dependent uptake aligns with the known behavior of endothelial cells in particle internalization (240,241), and has been previously reported for plastic particles (242). It would be of interest to investigate the rate of MNP phagocytosis efficiency in endothelial cells in other organs, such as the spleen and lymph nodes to address whether non-professional phagocytes may also serve as a target for MNP.

Additionally, a plastic-associated signal was detected in lymphocytes, potentially B cells, suggesting possible MNP interaction or uptake. While this aligns with studies demonstrating that nanoparticles can target B cells in drug delivery models (243), further investigation is needed to confirm the nature of this interaction and to differentiate between true uptake and external association of MNP with the cell surface.

Unidentified cells in both the liver and spleen also accumulated MNP, warranting further investigation. Potential candidates for this unidentified cell population include hepatocytes, hepatic stellate cells (HSCs), and fibroblastic reticular cells (FRCs). Hepatocyte cell lines have demonstrated the ability to internalize MNP *in vitro* (244,245), and are known to engulf nanoparticles *in vivo* (246). Similarly, nanoparticles have been used to target HSCs and FRCs (247,248) implicating them as plausible contributors to MNP clearance.

4.2 **No evidence of systemic inflammation or cognitive impairment following chronic MNP ingestion**

Increases in pro-inflammatory cytokines such as IL-6, IL-1β, IL-23, and TNF-α have been reported in previous studies following MNP exposure (32,238,249), indicating an inflammatory state associated with MNP ingestion. However, no signs of systemic inflammation were observed in this study after chronic ingestion of MNP. Serum levels of key pro-inflammatory cytokines, including IL-1β, IL-1α, TNF-α, IL-23, and G-CSF, were not elevated, nor were the levels of chemokines such as CCL7 and CXCL5. These findings were consistent with those of Huang et al. (248), where no changes in mouse serum TNF-α and IL-6 levels were observed following microplastic ingestion

The discrepancy between these findings and previous reports may be due to differences between *in vitro* and *in vivo* models. While *in vitro* studies offer useful insights, they often exaggerate inflammatory responses because of their controlled and artificial conditions, which do not reflect the complex regulation in living organisms (250).

Interestingly, serum levels of IL-2R and IL-17A were reduced following chronic MNP ingestion, with IL-2R showing a significant decrease in mice exposed to 50 nm particles. While IL-2R is primarily expressed by activated T cells and regulatory T cells, IL-17A is produced by Th17 cells (251,252).

This reduction may indicate a suppressed immune state, as IL-2R plays a critical role in T cell activation and proliferation, particularly by supporting the growth and function of regulatory T cells (Tregs) and promoting immune homeostasis (252). Similarly, the downregulation of IL-17A, which has also been reported previously following MNP exposure *in vivo* (251), may further contribute to an altered immune state, giving that IL-17A is a key pro-inflammatory cytokine a crucial role in orchestrating immune responses (251).

In line with these findings, the absence of increased circulating immune cells, such as monocytes, neutrophils, further supports the conclusion of no systemic inflammation. Additionally, the immune cell composition in the liver and spleen remained comparable to controls, indicating no increased local tissue infiltration despite MNP accumulation.

An interesting aspect of nanoparticles is their ability to cross the blood-brain barrier (BBB) and reach the brain parenchyma, where they are subsequently captured by microglia. This phenomenon has also been reported in several studies (232,249,253). Interestingly, nanoparticles did reach the brain, though at lower levels than in the liver or spleen.

Although several reports have demonstrated BBB disruption after nanoparticle administration (205,254), Evans Blue assay confirmed its integrity following chronic MNP exposure. Many of these studies linked BBB disruption to specific experimental conditions, such as whole-body hyperthermia or exposure to high nanoparticle concentrations, which may not accurately represent typical physiological scenarios. Additionally, these studies often involved nanoparticles with different material compositions, such as emulsifying wax nanoparticles or metal-derived nanoparticles, rather than plastic-based MNP, which may reflect a material-specific phenotype.

Consistent with the intact BBB, no infiltration of circulating immune cells, such as monocytes and granulocytes, was observed in the MNP-treated brains. Microglia numbers were comparable among the groups as well.

scRNA-seq analysis revealed no significant changes in microglial phenotype following the ingestion of 50 nm PS particles. However, exposure to 500 nm PS particles led to the upregulation of *Hspa1a*, *Hsp90aa1*, and *Gadd45b*, indicating cellular stress (255,256). These findings align with previous reports describing changes in microglial phenotype upon microplastic exposure (32,236). However, these changes might also reflect artifacts introduced during enzymatic digestion of the brain tissue.

Notably, despite the downregulation of various genes in MNP-exposed microglia, no significant pathways were identified as downregulated in ORA, suggesting that the observed gene expression changes might not translate into broader functional alterations at the pathway level.

However, MNP ingestion showed no measurable behavioral deficits. Across a battery of behavioral tests, no significant differences were observed between MNP-exposed and control mice. In the open field test, MNP-treated mice displayed normal locomotion and no signs of increased anxiety-like behavior. The novel object recognition test also revealed no differences compared to controls. However, all experimental groups, including controls, showed no preference for the novel object, potentially reflecting an influence on recognition memory and exploratory behavior across all groups.

In the social discrimination test, a similar pattern emerged during the first trial when a novel conspecific was introduced. All groups exhibited reduced interaction time. Despite this, no differences were observed between MNP-exposed and control mice. In the second trial, while control and 50 nm-exposed mice showed no preference between the two introduced conspecifics, the 500 nm-exposed mice demonstrated a significant increase in interaction with the newly introduced mouse. This raises the possibility that weekly handling of the mice for 12 weeks, rather than the treatment itself, contributed to the observed behavioral changes in all experimental groups, as reflected by the lack of object preference in the NOR test and the reduced social interactions observed in the social discrimination test.

These findings stand in contrast to several previous studies reporting behavioral changes following MNP ingestion. Yang et al. (33), observed an anxiety-like phenotype following plastic ingestion, while Lee et al. (34) and this thesis found no evidence of such changes. Furthermore, Lee et al. reported no changes in social behavior, though all their experimental groups exhibited increased interaction with novel conspecifics. In contrast to the findings described in this thesis, both Yang et al. and Lee et al. documented impaired learning and memory, as demonstrated by the novel object recognition test and the Morris water maze, respectively.

These discrepancies may be attributed to differences in experimental methodologies, sample sizes, and the size and type of plastic particles used. For instance, Yang et al. used 500 nm and 2 µm particles without specifying the type of plastic, administering them daily for two months**.** This frequent handling may have influenced the behavioral outcomes. Similarly, Lee et al. tested only 2 µm polystyrene particles, which were administered twice weekly for two months, also involving more frequent handling than in our study. Notably, Yang et al. did not provide details on how control mice were handled, which could significantly affect the reliability of their behavioral test results.

In contrast, in this study both 50 nm and 500 nm particles were used, with the smaller size likely contributing to higher bioavailability in the brain. Additionally, our larger sample size provides greater statistical power and depth to our findings. To further refine future experiments, adopting a more consistent and less invasive delivery method, such as mixing

MNP with drinking water or food, could reduce handling-related variability and improve the conditions for behavioral assessments.

Altogether, despite the penetration of nanoplastic particles into the brain parenchyma, no measurable impact was observed within our treatment paradigm. Notably, microplastic particles induced a mild stress-like response at the transcriptome level, this response was mild and did not result in observable behavioral changes.

4.3 **Metabolic and structural disruptions following chronic MNP ingestion**

Chronic ingestion and accumulation of MNP in various organs, particularly the liver—a central metabolic hub—disrupted lipid homeostasis, potentially leading to metabolic dysregulation and impaired energy balance. Despite these alterations, no evidence of liver injury or fibrosis was observed.

MNP ingestion was associated with an increase in PE, LPE and SM. Moreover, LPC and LPC-O were elevated in microplastic-exposed livers. Many reports have linked the changes in those lipid classes levels to significant metabolic effects. While elevated PE and SM levels have been associated with the progression of NAFLD (257), LPE and LPC act as key mediators in lipid metabolism within hepatocytes, influencing lipid droplet formation and fatty acid transport (258,259). Additionally, LPC is considered a proinflammatory signaling molecule and has been linked to the development of atherosclerosis and autoimmune conditions (260–262).

Interestingly, a reduction in TG levels was observed as well in MNP-exposed livers, indicating alterations in energy balance and lipid metabolism. TG serve as a primary energy reservoir, and decreased levels could indicate shifts in lipid utilization and storage within hepatocytes. Reduced TG levels are often associated with enhanced lipid oxidation and improved metabolic efficiency (263,264).

Notably, snRNA-seq analysis revealed a similar pattern, as evidenced by the differential enrichment of metabolic pathways. Pathways involved in ‘lipid localization’, ‘biological oxidation’ and small molecule catabolic process’ were upregulated following MNP ingestion, indicating shifts in hepatic metabolic activity. These findings indicate a disrupted balance in lipid utilization and mobilization, aligning with the previously observed reduction in hepatic TG levels in MNP-exposed livers.

To further explore these metabolic disruptions at the gene level, DEGs associated with lipid and glucose homeostasis were further analyzed. The upregulation of *Ces1f, Cyp4a14, Cyp4a10, Acss3, Pparg, and Ppargc1b* suggests an enhanced lipid catabolism (265–271). *Ces1f* is known for its role in triglyceride hydrolysis, while *Cyp4a14* and *Cyp4a10* contribute to the hydroxylation of fatty acids, a key step in lipid peroxidation (266,271). *Acss3* participates in the conversion of short-chain fatty acids into acetyl-CoA, linking lipid metabolism to energy

production (268). Additionally, *Pparg* and *Ppargc1b* are key regulators of lipid metabolism, promoting fatty acid oxidation and mitochondrial biogenesis (272).

Additionally, the downregulation of *Dgat1, Angptl8*, *Angptl4*, and *Plin2* indicates a reduction in lipid storage and a decrease in lipoprotein lipase inhibition, reinforcing a metabolic shift that favors lipid utilization over accumulation (265,273,274).

Furthermore, the upregulation of *Apoa2*, *Apoe Apoh*, *Abca8a and Cd36***,** suggest an alteration in lipid mobilization and fatty acids uptake. While *Apoa2*, *Apoe and Apoh* are integral components of lipoproteins, playing essential roles in lipid transport, *Cd36* and *Abca8a* are crucial for lipid translocation across cellular membranes (275–277).

These changes collectively reflect a metabolic adaptation that prioritizes lipid breakdown and utilization over storage, potentially influencing overall lipid homeostasis.

In parallel with lipid metabolic changes, livers exposed to microplastic exhibited diminished glycogen storage, indicating a size-dependent impact on glucose homeostasis. Furthermore, the dysregulation in glucose homeostasis was consistent even at lower microplastic dose (10 mg/kg). These findings highlight the capacity of microplastic, even at reduced ingestion rates, to disrupt key metabolic processes, emphasizing their potential to induce significant metabolic alterations. However, the impact on TGs storage at these lower ingestion levels requires further investigation.

DEG analysis revealed significant disruptions in hepatic glucose homeostasis following MNP exposure, affecting insulin signaling, gluconeogenesis, glycolysis, and glycogen storage. The upregulation of *Igfbp1* and *Irs2* following MNP ingestion suggests dysregulation of insulin signaling, Additionally, the upregulation of *Pcx*, *Mpc1*, and *Pdk1* in MNP-exposed hepatocytes indicates a shift toward gluconeogenesis and altered mitochondrial glucose metabolism (278–280). *Pcx*, a key gluconeogenic enzyme, facilitates the conversion of pyruvate to oxaloacetate in the mitochondria, while *Pdk1* inhibits the pyruvate dehydrogenase complex, thereby limiting glycolysis and promoting glucose production. *Mpc1* further supports this metabolic adaptation by regulating pyruvate transport into mitochondria, ensuring its availability. Moreover, the upregulation of *Slc16a7*, a monocarboxylate transporter, suggests an increased reliance on alternative metabolic fuels such as lactate, reinforcing a shift in energy metabolism (281).

Of note, 500 nm-exposed hepatocytes exhibited a distinct metabolic signature, with the upregulation of *Gys2* and *Dpp4* alongside the downregulation of *Gck*. This pattern suggests a shift favoring glycogen storage and reduced glycolysis, potentially impairing glucose utilization. Given the observed reduction in hepatic glycogen stores in the 500 nm-exposed group, this expression signature may represent a compensatory response to replenish glycogen levels in an attempt to restore metabolic balance.

Interestingly, the microplastic-specific impact on glucose homeostasis correlates with the disruption of KCs phagocytic capacity. This finding suggests a potential role for KC-hepatocyte

crosstalk in metabolic regulation and highlights the impairments associated with microplastic accumulation in KCs.

Given the well-established inter-organ communication between the liver and adipose tissue, particularly in maintaining metabolic homeostasis (282), the metabolic changes observed in the liver were closely linked to structural and metabolic alterations in adipose tissue. Despite no evidence of plastic particle accumulation, chronic MNP ingestion induced the formation of crown-like structures in gWAT, which are hallmarks of pro-inflammatory responses and metabolic dysregulation (283).

Furthermore, both gWAT and BAT exhibited signs of reduced lipid storage following chronic MNP ingestion. In gWAT, this was reflected by decreased organ weight and an increased frequency of small-sized adipocytes, while in BAT, it manifested as reduced vacuole size. These findings indicate a dysregulation in lipid metabolism, consistent with the metabolic phenotype observed in the liver. This observed reduction in lipid storage in the gWAT and BAT may result from enhanced lipid utilization (284,285) or impaired lipid storage. However, the change observed in the BAT may be also due to an increase in thermogenic activity.

This metabolic dysregulation in both the liver and adipose tissue aligns with previous reports linking plastic ingestion to disruptions in lipid metabolism (27–29). Notably, studies by Deng et al. (28) and Lu et al. (29) demonstrated decreased hepatic lipid levels and signs of oxidative stress following exposure to microplastic ranging in size from 500 nm to 20 µm.

Taken together, these findings suggest that MNP ingestion significantly affects metabolism, particularly lipid homeostasis, while microplastic specifically disrupt glucose homeostasis. These alterations may impact the utilization of energy-producing molecules, contributing to systemic metabolic imbalance.

Despite the long-term retention of MNP in the liver, glycogen levels remained unchanged between groups 26 weeks after cessation of MNP ingestion, suggesting a resolution of cellular and metabolic stress over time. Notably, serum levels of ALT and AST were elevated in 50 nm- and 500 nm-exposed mice, respectively, although these increases were not statistically significant. Elevated ALT is more specific to liver injury, whereas AST can originate from other tissues, such as muscle or kidney, in addition to the liver. Therefore, the ALT elevation in 50 nm-exposed mice suggests liver injury, while the AST increase in 500 nm-exposed mice may indicate a non-hepatic source, although liver involvement cannot be ruled out (207,208). Increasing the sample size might be necessary to confirm these trends.

Despite the elevation of AST and ALT levels, the absence of fibrosis, showed by Sirius Red staining and qRT-PCR analysis of fibrosis-related genes, suggests that the liver injury induced by MNP ingestion for 12 weeks is not severe.

Crown-like structures, which were already observed following chronic MNP ingestion, remained present in gWAT even after 26 weeks of cessation, indicating a prolonged pro-

inflammatory state associated with MNP exposure. In contrast, the reduction in vacuolar size in BAT observed after chronic MNP ingestion was no longer evident at the 26-week time point, suggesting a reversible or adaptive response.

To further investigate the broad metabolic dysregulation, introducing an additional metabolic stressor, such as HFD, may exacerbate these imbalances, providing insight into potential synergistic effects between MNP and HFD. Both plastic particles and dietary fat are common components of modern diets (12,13,216–218,229,230,286), and their combined impact may amplify metabolic dysfunction, as suggested by studies linking long-term nanoparticles exposure in general to aggravated obesity (287).

Throughout the MNP-HFD treatment, MNP-exposed mice exhibited comparable weight gain to controls following HFD. However, gWAT weight was significantly reduced in MNP-exposed mice, mirroring the reduction observed with MNP ingestion alone. Notably, BAT weight, which remained unchanged after MNP ingestion alone, was also reduced following the combined MNP-HFD treatment. This suggests that HFD may aggravate the metabolic disruptions induced by MNP exposure, particularly in adipose tissue.

Although liver weight remained unchanged following HFD, hepatic lipid content was significantly altered in a size-dependent manner. 500 nm MNP-exposed livers exhibited increased lipid accumulation compared to controls, whereas 50 nm-exposed livers showed a significant reduction in hepatic lipid content. These findings indicate that larger particles may promote lipid deposition, while smaller particles may instead disrupt lipid storage mechanisms in the liver.

Critically, MNP exposure significantly exacerbated the metabolic disturbances induced by a high-fat diet (HFD), as evidenced by elevated fasting glucose levels in both 50 nm- and 500 nm-exposed mice. Notably, glucose intolerance was particularly worsened in the 50 nm-exposed group, suggesting a size-dependent effect on glucose homeostasis in the MNP-HFD treatment. additionally, 50 nm-exposed mice also exhibited reduced insulin sensitivity, though this effect did not reach statistical significance, suggesting an increase in insulin resistance. However, increasing the sample size may clarify whether this represents a biologically relevant impairment in insulin signaling.

To gain a comprehensive understanding of the metabolic impact of MNP ingestion, further investigations are needed to assess lipid levels in adipose tissue and serum, clarifying how MNP influence lipid storage and turnover. Additionally, serum metabolomics analysis could identify key mediators, such as leptin, that contribute to systemic metabolic dysregulation. Evaluating food intake, energy expenditure, and thermogenesis will also be crucial in uncovering the mechanisms underlying these metabolic changes, particularly in the context of combined MNP-HFD exposure.

4.4 **Functional disruptions in macrophages following chronic MNP ingestion**

Macrophages, particularly KCs, are essential for the uptake of MNP, with persistent accumulation observed even six months post-exposure, raising concerns regarding potential long-term impacts on macrophage immune and cellular functions.

Reflecting the metabolic changes in hepatocytes, MNP-exposed KCs exhibited a shift in their metabolic phenotype, marked by altered expression of key metabolic genes, including *Fabp1, Apoe, Apoh, Apoc1, Apoc3, Cyp2e1, Cyp3a11, Aldob and Pck1* These gene expression changes, alongside ORA-identified alterations in metabolic pathways, suggest that MNP ingestion disrupts the hepatic microenvironment, contributing to metabolic dysregulation in KCs.

Chronic exposure to stimuli, such as pathogens, has been shown to induce macrophage exhaustion, characterized by reduced phagocytosis and impaired antigen presentation (288). Consistent with these observations, MNP-exposed KCs exhibited a reduction in MHCII expression, a critical component of extracellular antigen presentation to $CD4^+$ T cells (220). In parallel, snRNA-seq analysis revealed upregulation of genes associated with antigen processing and presentation, such as *B2m, H2-Q10, H2-T23, H2-D1, and Ctsl*, which encode components of MHC class I (MHCI) and facilitate intracellular antigen presentation to $CD8^+$ T cells (220,289). However, 50 nm-exposed KCs showed downregulation of antigen presentation genes, such as *Cd74* and *Nlrc5* (290,291), a trend that was also evident in the pathway analysis.

This shift from extracellular (MHCII-mediated) to intracellular (MHCI-mediated) antigen presentation indicates a stress-related adaptation, likely driven by cellular stressors such as ER and oxidative stress (292,293). Supporting this, genes associated with ER and oxidative stress response, including *Hspa5*, *Manf*, *Ndufa4*, *Selenop*, *Serpina1a*, *Serpina1b, Serpina1 and Gsta3*, were upregulated in MNP-exposed KCs, with *Gpx1* and *Txnip* also being upregulated in 500 nm-exposed KCs. Notably, the upregulation of *Hspa5,* a key mediator of the unfolded protein response*,* aligns with cellular stress responses to environmental injury (294). In general, the increased expression of these stress-response genes suggests that MNP accumulation induces a cellular stress response and disrupts redox balance, contributing to metabolic and immunological adaptations following MNP ingestion (293,295–299).

Furthermore, cellular stress, particularly oxidative stress, has been linked to impaired phagocytosis (300), aligning with the observed impairment in phagocytic capacity of macrophages following microplastic ingestion.

At the molecular level, microplastic-exposed KCs exhibited reduction of phagocytosis-related proteins, including decreased expression of MerTK—a scavenger receptor critical for efferocytosis (301) —and CD32b, an inhibitory Fc receptor (302). *In vivo* assessment of FcγR-

mediated phagocytosis revealed a significant impairment in microplastic-exposed mice, while nanoplastic exposure did not alter phagocytic capacity, highlighting a size-dependent effect of MNP. Thus, the downregulation of CD32b may represent a compensatory attempt to balance the reduced phagocytosis, suggesting that microplastic exposure uniquely disrupts KC phagocytic capacity compared to nanoplastic.

4.5 Immune and autoimmune consequences of macrophage dysregulation following chronic MNP ingestion

Macrophages are pivotal components of innate immunity, serving as first responders during infections and playing critical roles in clearing bacteria and cellular debris (237). Dysregulation of phagocytosis following microplastic ingestion could profoundly impact infection outcomes. To explore these potential effects, a series of assays were conducted to assess the consequences of chronic MNP ingestion on macrophage function.

Bacteria clearance was assessed following *E. coli* infection, a well-characterized pathogen and a common cause of sepsis (303). Interestingly, microplastic-treated mice showed a reduced ability to clear *E. coli* from the blood within 5 minutes of infection, compared to both nanoplastic-treated and control mice, consistent with the previously observed impairment in phagocytic capacity following microplastic ingestion. Nevertheless, bacterial loads in the liver and spleen remained comparable between MNP-treated and control mice, possibly due to macrophages immobilizing bacteria rather than actively phagocytosing them. Further investigation is needed to confirm this mechanism, such as immunofluorescent staining to visualize the localization of bacteria within macrophages, assess phagocytic activity, and differentiate between surface-bound and internalized bacteria. Overall, these findings suggest that impaired macrophage function due to microplastic exposure may increase susceptibility to infections and raise the risk of developing sepsis as a severe complication.

Despite the impaired bacterial clearance observed at 5 minutes post-infection, MNP-exposed mice showed a comparable progression of infection at 24 hours post-infection compared to controls. A key difference between the two experiments was the bacterial dose administered; the 24 hours post-infection experiment used a lower dose of *E. coli* (1×10^6 CFU/20 g body weight) compared to the higher dose (1×10^7 CFU/20 g body weight) used in the 5 minutes post-infection experiment. By 2 hours post-infection, *E. coli* was cleared from the blood across all groups. At 24 hours post-infection, no *E. coli* was detected in the spleens of MNP-exposed mice, while the livers displayed bacterial load similar to controls. This comparable progression may be attributed to the longer post-infection interval and the lower bacterial dose used. Under these conditions, macrophages or other immune components, such as neutrophils (304), may have compensated for the impaired phagocytic capacity of macrophages.

While the *E. coli* infection model represents an acute infection, the malaria infection model offers a recurrent infection paradigm, enabling a broader assessment of the phagocytic capacity of hepatic and splenic macrophages over an extended timeframe (223). This extended timeframe covers two peaks of parasitemia during the blood-stage malaria infection, increasing the phagocytic burden on macrophages to clear iRBCs. Consistent with earlier findings, microplastic-ingested mice demonstrated an impaired phagocytic capacity. Microplastic-exposed mice showed similar parasitemia levels to controls at p.i. 10, but higher levels at the second peak (p.i. 21).

Notably, weight recovery following malaria infection revealed an interesting pattern. All groups exhibited a reduction in body weight as a response to the infection. However, MNP-exposed mice demonstrated faster weight recovery compared to controls, with the microplastic-ingested mice showing a statistically significant trend. During illness, reduced food intake combined with increased metabolic demands often induces a starvation-like state**.** Upon refeeding, the body prioritizes replenishing lost energy reserves, potentially resulting in weight gain—a phenomenon termed post-starvation hyperphagia (305). The pre-existing metabolic dysregulation associated with MNP exposure could affect the body's post-infection adaptive starvation response, enhancing the impact of post-starvation hyperphagia. This combined effect may underlie the accelerated weight recovery observed in MNP-exposed mice.

Another consequence of impaired macrophage phagocytic capacity is the potential development of autoimmune diseases, driven by reduced clearance of apoptotic cells (ACs) (225,226). The observed reduction in MerTK expression on KCs further supports this notion, indicating a compromised efferocytic capacity. Furthermore, the downregulation of CD32b is linked to the onset of autoimmune diseases (306).

To investigate whether microplastic-ingestion could trigger an autoimmune phenotype against self-antigens, a model was employed where thymocyte-derived ACs were used to overload the system, break tolerance, and apply immunological pressure (193). Following this treatment paradigm, the mice were assessed individually for any signs of autoreactivity. Of note, two nanoplastic-exposed mice already showed elevated levels of anti-DNA IgG prior to AC administration, potentially indicating a preexisting autoimmune reaction.

Throughout the tolerance-breaking phase**,** no increases in anti-DNA IgG levels were observed in any of the groups, likely reflecting the reduced susceptibility of male mice to autoimmune induction (307,308). However, after the first and second booster doses of ACs, one mouse from each plastic-exposed group exhibited elevated levels of anti-DNA IgG. While these results remain inconclusive, they offer valuable insights into the potential induction of autoimmunity following chronic MNP ingestion. One notable limitation of the autoimmune disease model was the use of males throughout the whole thesis, since they are known to be less susceptible to autoimmune diseases compared to females (307,308). To validate these

findings and further explore the autoimmune response, experiments using female mice, known to have higher susceptibility to autoimmune induction, are essential.

4.6 **Limited impact of MNP ingestion on macrophage ontogeny**

To investigate the impact of MNP accumulation on macrophage ontogeny, the DFM model was utilized to identify potential changes in their developmental dynamics. MNP accumulation may induce cellular stress, potentially leading to macrophage apoptosis and the recruitment of replacements.

In the liver, MNP-exposed KCs exhibited no changes in ontogeny compared to controls. However, monocytes displayed an increase in the YFP^+ tdT^+ fraction at the expense of the tdT^+ fraction, suggesting enhanced infiltration and differentiation into macrophages. Despite this, no changes were observed in the abundance of KCs or monocytes in the liver.

In the spleen, macrophage subpopulations exhibited distinct phenotypic changes in microplastic-exposed mice. $CD163^+$ RPMs, $CD163^-$ RPMs, and MMMs showed an increase in monocyte-derived macrophages at the expense of EMP-derived macrophages, although the differences were minor, with a maximum change of 8 %. In contrast, MZMs and WPMs showed no changes in ontogeny.

Given the lack of significant changes in the liver and only minor differences in the spleen, chronic MNP ingestion is unlikely to induce widespread apoptosis of resident macrophages. However, the DFM model does not account for the clonal expansion of macrophages within the tissue. To address this limitation, the Confetti mouse model would be a suitable alternative. The Confetti model is a multicolor lineage-tracing system in which individual cells are labeled with distinct fluorescent markers, enabling the monitoring of cell proliferation and lineage dynamics over time (309).

4.7 **The influence of MNP on microbiome composition and function**

The impact of plastics on the gut microbiome may be driven by their physicochemical properties, including their ability to adsorb environmental toxins, leach chemical additives, and provide surfaces for microbial colonization (310). In this treatment paradigm, chronic MNP ingestion appears to disrupt the gut microbiome, with distinct effects observed based on particle size. In nanoplastic-exposed mice, a reduction in microbial diversity within the cecum was noted, potentially affecting host metabolism and nutrient absorption (311). Specific shifts in cecal bacterial species point to broader implications for metabolic health, inflammatory regulation, and nutrient processing. For instance, reductions in *Christensenellaceae R-7 group* and *Ruminococcaceae* in MNP-treated mice may impair anti-inflammatory functions and short-chain fatty acid (SCFA) production, thereby influencing immune modulation and metabolic health (312–314). Conversely, an enrichment of species such as *Oscillibacter*,

Muribaculum, *Coriobacteriaceae*, and *Faecalibacterium*—generally associated with beneficial roles in gut health and metabolism—was observed (315–318). However, *Oscillibacter* has also been linked to compromised gut barrier function, adding complexity to its role (319).

Interestingly, despite fecal samples showing no changes in alpha and beta diversity, the abundance of specific bacterial species was altered following chronic MNP ingestion. Reductions in *Lactobacillus*, *Turicibacter*, *Ruminococcaceae*, and *Rikenellaceae RC9* in MNP-exposed mice may impact glucose and lipid homeostasis as well as immune regulation (320–323). Similarly, *Mucispirillum*, which supports mucosal health, was reduced in microplastic-ingested mice (324). On the other hand, nanoplastic ingestion led to increased abundance of *Coriobacteriaceae UCG-002* and *Bacteroides*, which may affect epithelial barrier function (325,326). Consistent with this, the increase in *Oscillibacter* abundance in MNP-exposed mice is further associated with impaired gut barrier integrity (319).

Overall, these microbiome changes highlight the potential impact of chronic MNP ingestion on metabolic and immune states as well as gut barrier function, emphasizing the need for further investigation into these complex interactions. Specially that nanoparticles have been linked to diet-induced obesity through aggravating intestinal mucus layer damage and microbiota dysbiosis (287).

4.8 **Implications of chronic MNP ingestion for public health and policy**

The growing prevalence of MNP in daily life poses an emerging public health concern due to increased exposure through food and air (12,13,229,230,327). This thesis, alongside accumulating published evidence, highlights the hazardous nature of MNP, showing their potential to disrupt key biological processes, leading to immune dysregulation and metabolic disorders.

Chronic MNP-exposure was shown to impair macrophage function, particularly phagocytic capacity, thereby increasing susceptibility to infections. This, in turn, may exacerbate disease progression and prolong recovery times. Furthermore, the observed link between MNP ingestion and an increase in autoimmune induction raises concerns about the potential correlation between plastic pollution and the rising incidence of autoimmune diseases (328), warranting further investigation.

MNP ingestion was associated with metabolic dysregulation, which was further aggravated under metabolic stress induced by HFD. Obesity, like other diseases including cardiovascular disease, diabetes mellitus, and non-alcoholic fatty liver disease, is strongly linked to metabolic syndrome (329). Thus, the ingestion of MNP may aggravate the progression and severity of these disorders. This highlights the significant challenge posed by increasing plastic pollution and subsequent uptake, especially when combined with preexisting metabolic dysregulation, potentially placing a substantial burden on public health systems (217,218).

Hence, allocating more resources to investigate the potential effects of MNP ingestion across various disease conditions is critical for developing a comprehensive understanding of their synergistic impacts. In particular, autoimmune diseases and cancer metastasis warrant focused attention, as macrophages play a pivotal role in the progression and regulation of these conditions (225,226,330). This could provide valuable insights into how MNP influence macrophage function in disease settings, further elucidating their broader implications for public health.

5 References

1. Baekeland LH. Original papers: The synthesis, constitution, and uses of bakelite. Ind Eng Chem [Internet]. 1909 Mar 1 [cited 2024 Dec 20];1(3):149–61. Available from: https://pubs.acs.org/sharingguidelines
2. PlascticsEurope. Plastics-the Facts 2021 An analysis of European plastics production, demand and waste data.
3. Geyer R, Jambeck JR, Law KL. Production, use, and fate of all plastics ever made. Sci Adv [Internet]. 2017 Jul 7 [cited 2024 Dec 20];3(7). Available from: https://www.science.org/doi/10.1126/sciadv.1700782
4. Javed H. Microplastics: An overview. In: Toxicology and Human Health: Environmental Exposures and Biomarkers [Internet]. Springer Nature; 2023 [cited 2024 Dec 20]. p. 75–82. Available from: https://doi.org/10.1007/978-981-99-2193-5_4
5. da Costa JP, Santos PSM, Duarte AC, Rocha-Santos T. (Nano)plastics in the environment - Sources, fates and effects. Vols 566–567, Science of the Total Environment. Elsevier B.V.; 2016. p. 15–26.
6. Cole M, Galloway TS. Ingestion of Nanoplastics and Microplastics by Pacific Oyster Larvae. Environ Sci Technol [Internet]. 2015 Dec 15 [cited 2024 Dec 20];49(24):14625–32. Available from: https://pubs.acs.org/sharingguidelines
7. Cole M, Lindeque P, Fileman E, Halsband C, Galloway TS. The impact of polystyrene microplastics on feeding, function and fecundity in the marine copepod Calanus helgolandicus. Environ Sci Technol [Internet]. 2015 Jan 20 [cited 2024 Dec 20];49(2):1130–7. Available from: https://pubs.acs.org/sharingguidelines
8. Peng L, Fu D, Qi H, Lan CQ, Yu H, Ge C. Micro- and nano-plastics in marine environment: Source, distribution and threats — A review. Vol. 698, Science of the Total Environment. Elsevier B.V.; 2020. p. 134254.
9. Efimova I, Bagaeva M, Bagaev A, Kileso A, Chubarenko IP. Secondary microplastics generation in the sea swash zone with coarse bottom sediments: Laboratory experiments. Front Mar Sci [Internet]. 2018 Sep 5 [cited 2024 Dec 20];5(SEP):313. Available from: www.frontiersin.org
10. Almeida M, Martins MA, Soares AMV, Cuesta A, Oliveira M. Polystyrene nanoplastics alter the cytotoxicity of human pharmaceuticals on marine fish cell lines. Environ Toxicol Pharmacol. 2019 Jul 1;69:57–65.
11. Hernandez LM, Yousefi N, Tufenkji N. Are there nanoplastics in your personal care products? Environ Sci Technol Lett [Internet]. 2017 Jul 1 [cited 2024 Dec 20];4(7):280–5. Available from: https://pubs.acs.org/sharingguidelines

12. Toussaint B, Raffael B, Angers-Loustau A, Gilliland D, Kestens V, Petrillo M, et al. Review of micro- and nanoplastic contamination in the food chain [Internet]. Vol. 36, Food Additives and Contaminants - Part A Chemistry, Analysis, Control, Exposure and Risk Assessment. Taylor and Francis Ltd.; 2019 [cited 2024 Nov 14]. p. 639–73. Available from: https://pubmed.ncbi.nlm.nih.gov/30985273/
13. Smith M, Love DC, Rochman CM, Neff RA. Microplastics in Seafood and the Implications for Human Health [Internet]. Vol. 5, Current environmental health reports. Springer; 2018 [cited 2024 Nov 14]. p. 375–86. Available from: https://link.springer.com/article/10.1007/s40572-018-0206-z
14. Koelmans AA, Mohamed Nor NH, Hermsen E, Kooi M, Mintenig SM, De France J. Microplastics in freshwaters and drinking water: Critical review and assessment of data quality. Vol. 155, Water Research. Elsevier Ltd; 2019. p. 410–22.
15. Boyle K, Örmeci B. Microplastics and nanoplastics in the freshwater and terrestrial environment: A review [Internet]. Vol. 12, Water (Switzerland). MDPI AG; 2020 [cited 2024 Dec 22]. p. 2633. Available from: www.mdpi.com/journal/water
16. Waring RH, Harris RM, Mitchell SC. Plastic contamination of the food chain: A threat to human health? [Internet]. Vol. 115, Maturitas. Elsevier Ireland Ltd; 2018 [cited 2021 Jun 25]. p. 64–8. Available from: http://www.maturitas.org/article/S0378512218303505/fulltext
17. Bouwmeester H, Hollman PCH, Peters RJB. Potential Health Impact of Environmentally Released Micro- and Nanoplastics in the Human Food Production Chain: Experiences from Nanotoxicology [Internet]. Vol. 49, Environmental Science and Technology. American Chemical Society; 2015 [cited 2021 Jun 25]. p. 8932–47. Available from: https://pubs.acs.org/doi/abs/10.1021/acs.est.5b01090
18. Cox KD, Covernton GA, Davies HL, Dower JF, Juanes F, Dudas SE. Human Consumption of Microplastics. Environ Sci Technol [Internet]. 2019 Jun 18 [cited 2024 Dec 20];53(12):7068–74. Available from: https://pubs.acs.org/sharingguidelines
19. Senathirajah K, Attwood S, Bhagwat G, Carbery M, Wilson S, Palanisami T. Estimation of the mass of microplastics ingested – A pivotal first step towards human health risk assessment. J Hazard Mater [Internet]. 2021 Feb 15 [cited 2024 Nov 14];404(Pt B). Available from: https://pubmed.ncbi.nlm.nih.gov/33130380/
20. Leslie HA, van Velzen MJM, Brandsma SH, Vethaak AD, Garcia-Vallejo JJ, Lamoree MH. Discovery and quantification of plastic particle pollution in human blood. Environ Int. 2022 May 1;163:107199.
21. Horvatits T, Tamminga M, Liu B, Sebode M, Carambia A, Fischer L, et al. Microplastics detected in cirrhotic liver tissue. EBioMedicine [Internet]. 2022 Aug 1 [cited 2024 Dec 23];82. Available from: https://pubmed.ncbi.nlm.nih.gov/35835713/

22. Jenner LC, Rotchell JM, Bennett RT, Cowen M, Tentzeris V, Sadofsky LR. Detection of microplastics in human lung tissue using μFTIR spectroscopy. Science of the Total Environment. 2022 Jul 20;831:154907.
23. Ragusa A, Notarstefano V, Svelato A, Belloni A, Gioacchini G, Blondeel C, et al. Raman Microspectroscopy Detection and Characterisation of Microplastics in Human Breastmilk. Polymers (Basel) [Internet]. 2022 Jul 1 [cited 2024 Dec 23];14(13). Available from: https://pubmed.ncbi.nlm.nih.gov/35808745/
24. Garcia MA, Liu R, Nihart A, El Hayek E, Castillo E, Barrozo ER, et al. Quantitation and identification of microplastics accumulation in human placental specimens using pyrolysis gas chromatography mass spectrometry. Toxicological Sciences [Internet]. 2024 Apr 29 [cited 2024 Dec 23];199(1):81–8. Available from: https://academic.oup.com/toxsci/article/199/1/81/7609801
25. Roslan NS, Lee YY, Ibrahim YS, Tuan Anuar S, Yusof KMKK, Lai LA, et al. Detection of microplastics in human tissues and organs: A scoping review. J Glob Health [Internet]. 2024 Aug 23 [cited 2025 Feb 27];14:04179. Available from: https://pmc.ncbi.nlm.nih.gov/articles/PMC11342020/
26. Huang J, Sun X, Wang Y, Su J, Li G, Wang X, et al. Biological interactions of polystyrene nanoplastics: Their cytotoxic and immunotoxic effects on the hepatic and enteric systems. Ecotoxicol Environ Saf. 2023 Oct 1;264:115447.
27. Silva AH, Locatelli C, Filippin-Monteiro FB, Martin P, Liptrott NJ, Zanetti-Ramos BG, et al. Toxicity and inflammatory response in Swiss albino mice after intraperitoneal and oral administration of polyurethane nanoparticles. Toxicol Lett. 2016 Mar 30;246:17–27.
28. Deng Y, Zhang Y, Lemos B, Ren H. Tissue accumulation of microplastics in mice and biomarker responses suggest widespread health risks of exposure. Sci Rep [Internet]. 2017 Apr 24 [cited 2021 Jun 25];7(1):1–10. Available from: www.nature.com/scientificreports
29. Lu L, Wan Z, Luo T, Fu Z, Jin Y. Polystyrene microplastics induce gut microbiota dysbiosis and hepatic lipid metabolism disorder in mice. Science of the Total Environment. 2018 Aug 1;631–632:449–58.
30. Luo T, Wang C, Pan Z, Jin C, Fu Z, Jin Y. Maternal Polystyrene Microplastic Exposure during Gestation and Lactation Altered Metabolic Homeostasis in the Dams and Their F1 and F2 Offspring. Environ Sci Technol [Internet]. 2019 Sep 17 [cited 2024 Dec 24];53(18):10978–92. Available from: https://pubs.acs.org/doi/abs/10.1021/acs.est.9b03191
31. Moon H, Jeong D, Choi JW, Jeong S, Kim H, Song BW, et al. Microplastic exposure linked to accelerated aging and impaired adipogenesis in fat cells. Scientific Reports

2024 14:1 [Internet]. 2024 Oct 13 [cited 2024 Dec 27];14(1):1–14. Available from: https://www.nature.com/articles/s41598-024-74892-6

32. Mahmud F, Sarker DB, Jocelyn JA, Sang QXA. Molecular and Cellular Effects of Microplastics and Nanoplastics: Focus on Inflammation and Senescence [Internet]. Vol. 13, Cells. Multidisciplinary Digital Publishing Institute (MDPI); 2024 [cited 2024 Nov 15]. p. 1788. Available from: https://www.mdpi.com/2073-4409/13/21/1788/htm
33. Yang Q, Dai H, Cheng Y, Wang B, Xu J, Zhang Y, et al. Oral feeding of nanoplastics affects brain function of mice by inducing macrophage IL-1 signal in the intestine. Cell Rep [Internet]. 2023 Apr 25 [cited 2023 Apr 27];42(4). Available from: https://doi.org/10.1016/j.celrep.2023.112346
34. Lee CW, Hsu LF, Wu IL, Wang YL, Chen WC, Liu YJ, et al. Exposure to polystyrene microplastics impairs hippocampus-dependent learning and memory in mice. J Hazard Mater. 2022 May 15;430:128431.
35. Huang H, Hou J, Liao Y, Wei F, Xing B. Polyethylene microplastics impede the innate immune response by disrupting the extracellular matrix and signaling transduction. iScience [Internet]. 2023 Aug 18 [cited 2024 Dec 13];26(8):107390. Available from: https://pmc.ncbi.nlm.nih.gov/articles/PMC10405319/
36. Kuroiwa M, Yamaguchi SI, Kato Y, Hori A, Toyoura S, Nakahara M, et al. Tim4, a macrophage receptor for apoptotic cells, binds polystyrene microplastics via aromatic-aromatic interactions. Science of the Total Environment. 2023 Jun 1;875:162586.
37. Moon B, Yang S, Moon H, Lee J, Park D. After cell death: the molecular machinery of efferocytosis [Internet]. Vol. 55, Experimental and Molecular Medicine. Springer Nature; 2023 [cited 2024 Nov 2]. p. 1644–51. Available from: https://doi.org/10.1038/s12276-023-01070-5
38. Chen G, Feng Q, Wang J. Mini-review of microplastics in the atmosphere and their risks to humans. Vol. 703, Science of the Total Environment. Elsevier B.V.; 2020. p. 135504.
39. Junaid M, Liu S, Yue Q, Wei M, Wang J. Trophic transfer and interfacial impacts of micro(nano)plastics and per-and polyfluoroalkyl substances in the environment. Vol. 465, Journal of Hazardous Materials. Elsevier B.V.; 2024. p. 133243.
40. Sun R, Liu M, Xiong F, Xu K, Huang J, Liu J, et al. Polystyrene micro- and nanoplastics induce gastric toxicity through ROS mediated oxidative stress and P62/Keap1/Nrf2 pathway. Science of the Total Environment. 2024 Feb 20;912:169228.
41. Özcan O, Erdal H, Çakırca G, Yönden Z. Oxidative stress and its impacts on intracellular lipids, proteins and DNA. Journal of Clinical and Experimental Investigations [Internet]. 2015 Nov 6 [cited 2024 Dec 23];6(3):331–6. Available from: www.jceionline.org

42. Hou J, Lei Z, Cui L, Hou Y, Yang L, An R, et al. Polystyrene microplastics lead to pyroptosis and apoptosis of ovarian granulosa cells via NLRP3/Caspase-1 signaling pathway in rats. Ecotoxicol Environ Saf. 2021 Apr 1;212:112012.
43. Li Z, Zhu S, Liu Q, Wei J, Jin Y, Wang X, et al. Polystyrene microplastics cause cardiac fibrosis by activating Wnt/β-catenin signaling pathway and promoting cardiomyocyte apoptosis in rats. Environmental Pollution. 2020 Oct 1;265:115025.
44. Jung BK, Han SW, Park SH, Bae JS, Choi J, Ryu KY. Neurotoxic potential of polystyrene nanoplastics in primary cells originating from mouse brain. Neurotoxicology. 2020 Dec 1;81:189–96.
45. Metschnikoff E. Lecture on Phagocytosis and Immunity. BMJ. 1891;1(1570):213–7.
46. Metchnikov E. Untersuchungen ueber die mesodermalen Phagocyten einiger Wirbeltiere. Biologisches Centralblatt. 1883;3:560–5.
47. Arroyo Portilla C, Tomas J, Gorvel JP, Lelouard H. From Species to Regional and Local Specialization of Intestinal Macrophages. Vol. 8, Frontiers in Cell and Developmental Biology. Frontiers Media S.A.; 2021. p. 1910.
48. Kierdorf K, Prinz M, Geissmann F, Gomez Perdiguero E. Development and function of tissue resident macrophages in mice [Internet]. Vol. 27, Seminars in Immunology. Academic Press; 2015 [cited 2023 Jan 5]. p. 369–78. Available from: /pmc/articles/PMC4948121/
49. Saraiva Camara NO, Braga TT. Macrophages in the Human Body: A Tissue Level Approach. Macrophages in the Human Body: A Tissue Level Approach. Elsevier; 2022. 1–309 p.
50. van Furth R, Cohn ZA, Hirsch JG, Humphrey JH, Spector WG, Langevoort HL. The mononuclear phagocyte system: a new classification of macrophages, monocytes, and their precursor cells. Bull World Health Organ [Internet]. 1972 [cited 2019 May 7];46(6):845–52. Available from: http://www.ncbi.nlm.nih.gov/pubmed/4538544
51. Bain CC, Bravo-Blas A, Scott CL, Gomez Perdiguero E, Geissmann F, Henri S, et al. Constant replenishment from circulating monocytes maintains the macrophage pool in the intestine of adult mice. Nat Immunol [Internet]. 2014 Jan 1 [cited 2023 Jan 4];15(10):929–37. Available from: https://pubmed.ncbi.nlm.nih.gov/25151491/
52. Epelman S, Lavine KJ, Beaudin AE, Sojka DK, Carrero JA, Calderon B, et al. Embryonic and adult-derived resident cardiac macrophages are maintained through distinct mechanisms at steady state and during inflammation. Immunity [Internet]. 2014 Jan 16 [cited 2023 Jan 4];40(1):91–104. Available from: https://pubmed.ncbi.nlm.nih.gov/24439267/
53. Calderon B, Carrero JA, Ferris ST, Sojka DK, Moore L, Epelman S, et al. The pancreas anatomy conditions the origin and properties of resident macrophages. Journal of

Experimental Medicine [Internet]. 2015 Sep 21 [cited 2023 Jan 4];212(10):1497–512. Available from: https://pubmed.ncbi.nlm.nih.gov/26347472/

54. Tamoutounour S, Guilliams M, MontananaSanchis F, Liu H, Terhorst D, Malosse C, et al. Origins and functional specialization of macrophages and of conventional and monocyte-derived dendritic cells in mouse skin. Immunity [Internet]. 2013 Nov 14 [cited 2023 Jan 4];39(5):925–38. Available from: https://pubmed.ncbi.nlm.nih.gov/24184057/
55. Ji RP, Phoon CKL, Aristizábal O, McGrath KE, Palis J, Turnbull DH. Onset of cardiac function during early mouse embryogenesis coincides with entry of primitive erythroblasts into the embryo proper. Circ Res [Internet]. 2003 Feb 7 [cited 2019 May 31];92(2):133–5. Available from: http://www.ncbi.nlm.nih.gov/pubmed/12574139
56. Palis J, Robertson S, Kennedy M, Wall C, Keller G. Development of erythroid and myeloid progenitors in the yolk sac and embryo proper of the mouse. Development [Internet]. 1999 Nov [cited 2019 May 5];126(22):5073–84. Available from: http://www.ncbi.nlm.nih.gov/pubmed/10529424
57. McGrath KE, Koniski AD, Malik J, Palis J. Circulation is established in a stepwise pattern in the mammalian embryo. Blood [Internet]. 2003 Mar 1 [cited 2023 Jan 3];101(5):1669–76. Available from: https://pubmed.ncbi.nlm.nih.gov/12406884/
58. Gomez Perdiguero E, Klapproth K, Schulz C, Busch K, Azzoni E, Crozet L, et al. Tissue-resident macrophages originate from yolk-sac-derived erythro-myeloid progenitors. Nature [Internet]. 2015 Feb 26 [cited 2022 Dec 8];518(7540):547–51. Available from: /pmc/articles/PMC5997177/
59. McGrath KE, Frame JM, Fegan KH, Bowen JR, Conway SJ, Catherman SC, et al. Distinct Sources of Hematopoietic Progenitors Emerge before HSCs and Provide Functional Blood Cells in the Mammalian Embryo. Cell Rep [Internet]. 2015 Jun 30 [cited 2023 Jan 3];11(12):1892–904. Available from: https://pubmed.ncbi.nlm.nih.gov/26095363/
60. Mass E, Ballesteros I, Farlik M, Halbritter F, Gunther P, Crozet L, et al. Specification of tissue-resident macrophages during organogenesis. Science (1979) [Internet]. 2016 Sep 9 [cited 2019 May 9];353(6304):aaf4238–aaf4238. Available from: http://www.ncbi.nlm.nih.gov/pubmed/27492475
61. Stremmel C, Schuchert R, Wagner F, Thaler R, Weinberger T, Pick R, et al. Yolk sac macrophage progenitors traffic to the embryo during defined stages of development. Nat Commun [Internet]. 2018 Dec 8 [cited 2018 Jan 16];9(1):75. Available from: http://www.nature.com/articles/s41467-017-02492-2
62. Merad M, Manz MG, Karsunky H, Wagers A, Peters W, Charo I, et al. Langerhans cells renew in the skin throughout life under steady-state conditions. Nat Immunol [Internet].

2002 Dec 1 [cited 2023 Jan 3];3(12):1135–41. Available from: https://pubmed.ncbi.nlm.nih.gov/12415265/

63. Jenkins SJ, Ruckerl D, Cook PC, Jones LH, Finkelman FD, Van Rooijen N, et al. Local macrophage proliferation, rather than recruitment from the blood, is a signature of T H2 inflammation. Science (1979) [Internet]. 2011 Jun 10 [cited 2023 Jan 3];332(6035):1284–8. Available from: https://pubmed.ncbi.nlm.nih.gov/21566158/
64. Jakubzick C, Gautier EL, Gibbings SL, Sojka DK, Schlitzer A, Johnson TE, et al. Minimal differentiation of classical monocytes as they survey steady-state tissues and transport antigen to lymph nodes. Immunity [Internet]. 2013 Sep 19 [cited 2023 Jan 3];39(3):599–610. Available from: https://pubmed.ncbi.nlm.nih.gov/24012416/
65. Hashimoto D, Chow A, Noizat C, Teo P, Beasley MB, Leboeuf M, et al. Tissue-resident macrophages self-maintain locally throughout adult life with minimal contribution from circulating monocytes. Immunity [Internet]. 2013 Apr 18 [cited 2023 Jan 3];38(4):792–804. Available from: https://pubmed.ncbi.nlm.nih.gov/23601688/
66. Ajami B, Bennett JL, Krieger C, Tetzlaff W, Rossi FMV. Local self-renewal can sustain CNS microglia maintenance and function throughout adult life. Nat Neurosci [Internet]. 2007 Dec [cited 2023 Jan 3];10(12):1538–43. Available from: https://pubmed.ncbi.nlm.nih.gov/18026097/
67. A-Gonzalez N, Castrillo A. Origin and specialization of splenic macrophages. Cell Immunol. 2018 Aug 1;330:151–8.
68. Bertrand JY, Jalil A, Klaine M, Jung S, Cumano A, Godin I. Three pathways to mature macrophages in the early mouse yolk sac. Blood [Internet]. 2005 Nov [cited 2023 Jan 3];106(9):3004–11. Available from: https://pubmed.ncbi.nlm.nih.gov/16020514/
69. Mukouyama YS, Chiba N, Mucenski ML, Satake M, Miyajima A, Hara T, et al. Hematopoietic cells in cultures of the murine embryonic aorta-gonad-mesonephros region are induced by c-Myb. Current Biology [Internet]. 1999 Jul 29 [cited 2023 Jan 3];9(15):833–6. Available from: http://biomednet.com/elecref/0960982200900833
70. Dege C, Fegan KH, Creamer JP, Berrien-Elliott MM, Luff SA, Kim D, et al. Potently Cytotoxic Natural Killer Cells Initially Emerge from Erythro-Myeloid Progenitors during Mammalian Development. Dev Cell [Internet]. 2020 Apr 20 [cited 2023 Jan 4];53(2):229-239.e7. Available from: https://pubmed.ncbi.nlm.nih.gov/32197069/
71. Epelman S, Lavine KJ, Beaudin AE, Sojka DK, Carrero JA, Calderon B, et al. Embryonic and adult-derived resident cardiac macrophages are maintained through distinct mechanisms at steady state and during inflammation. Immunity [Internet]. 2014 Jan 16 [cited 2023 Jan 4];40(1):91–104. Available from: https://pubmed.ncbi.nlm.nih.gov/24439267/

72. Guilliams M, De Kleer I, Henri S, Post S, Vanhoutte L, De Prijck S, et al. Alveolar macrophages develop from fetal monocytes that differentiate into long-lived cells in the first week of life via GM-CSF. Journal of Experimental Medicine [Internet]. 2013 [cited 2023 Jan 4];210(10):1977–92. Available from: https://pubmed.ncbi.nlm.nih.gov/24043763/
73. Hoeffel G, Chen J, Lavin Y, Low D, Almeida FF, See P, et al. C-Myb+ Erythro-Myeloid Progenitor-Derived Fetal Monocytes Give Rise to Adult Tissue-Resident Macrophages. Immunity [Internet]. 2015 Apr 21 [cited 2023 Jan 4];42(4):665–78. Available from: /pmc/articles/PMC4545768/
74. Medvinsky A, Dzierzak E. Definitive hematopoiesis is autonomously initiated by the AGM region. Cell [Internet]. 1996 Sep 20 [cited 2023 Jan 4];86(6):897–906. Available from: https://pubmed.ncbi.nlm.nih.gov/8808625/
75. Boisset JC, Van Cappellen W, Andrieu-Soler C, Galjart N, Dzierzak E, Robin C. In vivo imaging of haematopoietic cells emerging from the mouse aortic endothelium. Nature [Internet]. 2010 Feb 14 [cited 2023 Jan 4];464(7285):116–20. Available from: https://www.nature.com/articles/nature08764
76. Christensen JL, Wright DE, Wagers AJ, Weissman IL. Circulation and Chemotaxis of Fetal Hematopoietic Stem Cells. Douglas Melton, editor. PLoS Biol [Internet]. 2004 Mar 16 [cited 2023 Jan 4];2(3):e75. Available from: https://dx.plos.org/10.1371/journal.pbio.0020075
77. Cassado A dos A, Dâ€™ImpÃ©rio Lima MR, Bortoluci KR. Revisiting Mouse Peritoneal Macrophages: Heterogeneity, Development, and Function. Front Immunol [Internet]. 2015 May 19 [cited 2019 May 12];6:225. Available from: http://www.ncbi.nlm.nih.gov/pubmed/26042120
78. Chakarov S, Lim HY, Tan L, Lim SY, See P, Lum J, et al. Two distinct interstitial macrophage populations coexist across tissues in specific subtissular niches. Science [Internet]. 2019 Mar 15 [cited 2019 May 31];363(6432):eaau0964. Available from: http://www.sciencemag.org/lookup/doi/10.1126/science.aau0964
79. Cox N, Geissmann F. Macrophage ontogeny in the control of adipose tissue biology [Internet]. Vol. 62, Current Opinion in Immunology. Elsevier Ltd; 2020 [cited 2023 Jan 4]. p. 1–8. Available from: https://pubmed.ncbi.nlm.nih.gov/31670115/
80. Sierro F, Evrard M, Rizzetto S, Melino M, Mitchell AJ, Florido M, et al. A Liver Capsular Network of Monocyte-Derived Macrophages Restricts Hepatic Dissemination of Intraperitoneal Bacteria by Neutrophil Recruitment. Immunity [Internet]. 2017 Aug 15 [cited 2019 May 12];47(2):374-388.e6. Available from: http://www.ncbi.nlm.nih.gov/pubmed/28813662

81. Ginhoux F, Jung S. Monocytes and macrophages: developmental pathways and tissue homeostasis. Nat Rev Immunol [Internet]. 2014 Jun 23 [cited 2019 May 11];14(6):392–404. Available from: http://www.ncbi.nlm.nih.gov/pubmed/24854589
82. McGrath KE, Frame JM, Palis J. Early hematopoiesis and macrophage development [Internet]. Vol. 27, Seminars in Immunology. Academic Press; 2015 [cited 2023 Jan 5]. p. 379–87. Available from: /pmc/articles/PMC4856633/
83. Migliaccio G, Migliaccio AR, Petti S, Mavilio F, Russo G, Lazzarot D, et al. Human Embryonic Hemopoiesis Kinetics of Progenitors and Precursors Underlying the Yolk Sac-+ Liver Transition.
84. Ivanovs A, Rybtsov S, Welch L, Anderson RA, Turner ML, Medvinsky A. Highly potent human hematopoietic stem cells first emerge in the intraembryonic aorta-gonad-mesonephros region. Journal of Experimental Medicine [Internet]. 2011 Nov 21 [cited 2023 Jan 6];208(12):2417–27. Available from: /pmc/articles/PMC3256972/
85. Aorta-associated CD34+ hematopoietic cells in the early human embryo - PubMed [Internet]. [cited 2023 Jan 6]. Available from: https://pubmed.ncbi.nlm.nih.gov/8547678/
86. Bian Z, Gong Y, Huang T, Lee CZW, Bian L, Bai Z, et al. Deciphering human macrophage development at single-cell resolution. Nature [Internet]. 2020 Jun 25 [cited 2023 Jan 6];582(7813):571–6. Available from: https://doi.org/10.1038/s41586-020-2316-7
87. Hoeksema MA, Glass CK. Nature and nurture of tissue-specific macrophage phenotypes [Internet]. Vol. 281, Atherosclerosis. Elsevier Ireland Ltd; 2019 [cited 2023 Jan 6]. p. 159–67. Available from: /pmc/articles/PMC6399046/
88. Gordon S, Plüddemann A. Tissue macrophages: heterogeneity and functions. BMC Biol [Internet]. 2017 [cited 2019 May 7];15(1):53. Available from: http://www.ncbi.nlm.nih.gov/pubmed/28662662
89. Mass E, Nimmerjahn F, Kierdorf K, Schlitzer A. Tissue-specific macrophages: how they develop and choreograph tissue biology. Nature Reviews Immunology 2023 [Internet]. 2023 Mar 15 [cited 2023 Mar 17];1–17. Available from: https://www.nature.com/articles/s41577-023-00848-y
90. Kierdorf K, Erny D, Goldmann T, Sander V, Schulz C, Perdiguero EG, et al. Microglia emerge from erythromyeloid precursors via Pu.1-and Irf8-dependent pathways. Nat Neurosci [Internet]. 2013 Mar 20 [cited 2023 Jan 6];16(3):273–80. Available from: https://www.nature.com/articles/nn.3318
91. Li Q, Barres BA. Microglia and macrophages in brain homeostasis and disease. Nat Rev Immunol [Internet]. 2018 Apr 20 [cited 2019 Dec 11];18(4):225–42. Available from: http://www.ncbi.nlm.nih.gov/pubmed/29151590

92. Cunningham CL, Martínez-Cerdeño V, Noctor SC. Microglia regulate the number of neural precursor cells in the developing cerebral cortex. Journal of Neuroscience [Internet]. 2013 Mar 6 [cited 2023 Jan 6];33(10):4216–33. Available from: https://www.jneurosci.org/content/33/10/4216

93. Checchin D, Sennlaub F, Levavasseur E, Leduc M, Chemtob S. Potential role of microglia in retinal blood vessel formation. Invest Ophthalmol Vis Sci [Internet]. 2006 Aug [cited 2023 Jan 6];47(8):3595–602. Available from: https://pubmed.ncbi.nlm.nih.gov/16877434/

94. Fantin A, Vieira JM, Gestri G, Denti L, Schwarz Q, Prykhozhij S, et al. Tissue macrophages act as cellular chaperones for vascular anastomosis downstream of VEGF-mediated endothelial tip cell induction. Blood [Internet]. 2010 Aug 5 [cited 2023 Jan 6];116(5):829–40. Available from: https://pubmed.ncbi.nlm.nih.gov/20404134/

95. Squarzoni P, Oller G, Hoeffel G, Pont-Lezica L, Rostaing P, Low D, et al. Microglia Modulate Wiring of the Embryonic Forebrain. Cell Rep [Internet]. 2014 Sep 11 [cited 2023 Jan 7];8(5):1271–9. Available from: http://dx.doi.org/10.1016/j.celrep.2014.07.042

96. Ueno M, Fujita Y, Tanaka T, Nakamura Y, Kikuta J, Ishii M, et al. Layer v cortical neurons require microglial support for survival during postnatal development. Nat Neurosci [Internet]. 2013 May [cited 2023 Jan 7];16(5):543–51. Available from: https://pubmed.ncbi.nlm.nih.gov/23525041/

97. Stevens B, Allen NJ, Vazquez LE, Howell GR, Christopherson KS, Nouri N, et al. The Classical Complement Cascade Mediates CNS Synapse Elimination. Cell [Internet]. 2007 Dec 14 [cited 2023 Jan 7];131(6):1164–78. Available from: https://pubmed.ncbi.nlm.nih.gov/18083105/

98. Schafer DP, Lehrman EK, Kautzman AG, Koyama R, Mardinly AR, Yamasaki R, et al. Microglia Sculpt Postnatal Neural Circuits in an Activity and Complement-Dependent Manner. Neuron [Internet]. 2012 May 24 [cited 2023 Jan 7];74(4):691–705. Available from: https://pubmed.ncbi.nlm.nih.gov/22632727/

99. Stephan AH, Barres BA, Stevens B. The complement system: An unexpected role in synaptic pruning during development and disease [Internet]. Vol. 35, Annual Review of Neuroscience. Annu Rev Neurosci; 2012 [cited 2023 Jan 7]. p. 369–89. Available from: https://pubmed.ncbi.nlm.nih.gov/22715882/

100. Safaiyan S, Kannaiyan N, Snaidero N, Brioschi S, Biber K, Yona S, et al. Age-related myelin degradation burdens the clearance function of microglia during aging. Nat Neurosci [Internet]. 2016 Aug 1 [cited 2023 Jan 7];19(8):995–8. Available from: https://www.nature.com/articles/nn.4325

101. Hoshiko M, Arnoux I, Avignone E, Yamamoto N, Audinat E. Deficiency of the microglial receptor CX3CR1 impairs postnatal functional development of thalamocortical synapses in the barrel cortex. Journal of Neuroscience [Internet]. 2012 Oct 24 [cited 2023 Jan 7];32(43):15106–11. Available from: https://pubmed.ncbi.nlm.nih.gov/23100431/
102. Li Y, Du XF, Liu CS, Wen ZL, Du JL. Reciprocal Regulation between Resting Microglial Dynamics and Neuronal Activity In Vivo. Dev Cell [Internet]. 2012 Dec 11 [cited 2023 Jan 7];23(6):1189–202. Available from: http://dx.doi.org/10.1016/j.devcel.2012.10.027
103. Palis J. Primitive and definitive erythropoiesis in mammals [Internet]. Vol. 5 JAN, Frontiers in Physiology. Frontiers Media SA; 2014 [cited 2023 Jan 7]. Available from: /pmc/articles/PMC3904103/
104. Willekens FLA, Werre JM, Kruijt JK, Roerdinkholder-Stoelwinder B, Groenen-Döpp YAM, Van Den Bos AG, et al. Liver Kupffer cells rapidly remove red blood cell-derived vesicles from the circulation by scavenger receptors. Blood [Internet]. 2005 Mar 1 [cited 2023 Jan 7];105(5):2141–5. Available from: https://pubmed.ncbi.nlm.nih.gov/15550489/
105. Horst AK, Tiegs G, Diehl L. Contribution of Macrophage Efferocytosis to Liver Homeostasis and Disease. Front Immunol [Internet]. 2019 Nov 14 [cited 2025 Jan 3];10:502121. Available from: www.frontiersin.org
106. Guilliams M, Scott CL. Liver macrophages in health and disease. Immunity [Internet]. 2022 Sep 13;55(9):1515–29. Available from: http://www.ncbi.nlm.nih.gov/pubmed/36103850
107. Balmer ML, Slack E, De Gottardi A, Lawson MAE, Hapfelmeier S, Miele L, et al. The liver may act as a firewall mediating mutualism between the host and its gut commensal microbiota. Sci Transl Med [Internet]. 2014 May 21 [cited 2024 Dec 31];6(237). Available from: https://pubmed.ncbi.nlm.nih.gov/24848256/
108. Lee WY, Moriarty TJ, Wong CHY, Zhou H, Strieter RM, Van Rooijen N, et al. An intravascular immune response to Borrelia burgdorferi involves Kupffer cells and iNKT cells. Nat Immunol [Internet]. 2010 [cited 2024 Dec 31];11(4):295–302. Available from: https://pubmed.ncbi.nlm.nih.gov/20228796/
109. Wang Y, van der Tuin S, Tjeerdema N, van Dam AD, Rensen SS, Hendrikx T, et al. Plasma cholesteryl ester transfer protein is predominantly derived from Kupffer cells. Hepatology [Internet]. 2015 Dec 1 [cited 2023 Jan 7];62(6):1710–22. Available from: https://pubmed.ncbi.nlm.nih.gov/26174697/
110. Remmerie A, Scott CL. Macrophages and lipid metabolism. Cell Immunol [Internet]. 2018 Aug 1 [cited 2024 Dec 31];330:27. Available from: https://pmc.ncbi.nlm.nih.gov/articles/PMC6108423/

111. Bonnardel J, T'Jonck W, Gaublomme D, Browaeys R, Scott CL, Martens L, et al. Stellate Cells, Hepatocytes, and Endothelial Cells Imprint the Kupffer Cell Identity on Monocytes Colonizing the Liver Macrophage Niche. Immunity [Internet]. 2019 Oct 15 [cited 2025 Jan 5];51(4):638-654.e9. Available from: https://pubmed.ncbi.nlm.nih.gov/31561945/
112. Marrone G, Shah VH, Gracia-Sancho J. Sinusoidal communication in liver fibrosis and regeneration. J Hepatol [Internet]. 2016 Sep [cited 2019 May 30];65(3):608–17. Available from: http://www.ncbi.nlm.nih.gov/pubmed/27151183
113. Schmidt-Arras D, Rose-John S. IL-6 pathway in the liver: From physiopathology to therapy. J Hepatol [Internet]. 2016 Jun [cited 2019 Apr 15];64(6):1403–15. Available from: http://www.ncbi.nlm.nih.gov/pubmed/26867490
114. Diehl KL, Vorac J, Hofmann K, Meiser P, Unterweger I, Kuerschner L, et al. Kupffer Cells Sense Free Fatty Acids and Regulate Hepatic Lipid Metabolism in High-Fat Diet and Inflammation. Cells [Internet]. 2020 Oct 8 [cited 2025 Jan 5];9(10). Available from: https://pubmed.ncbi.nlm.nih.gov/33050035/
115. Peraldi P, Spiegelman B. TNF-α and insulin resistance: Summary and future prospects. Mol Cell Biochem [Internet]. 1998 [cited 2025 Jan 5];182(1–2):169–75. Available from: https://link.springer.com/article/10.1023/A:1006865715292
116. Morgantini C, Jager J, Li X, Levi L, Azzimato V, Sulen A, et al. Liver macrophages regulate systemic metabolism through non-inflammatory factors. Nat Metab [Internet]. 2019 Apr 25 [cited 2019 May 19];1(4):445–59. Available from: http://www.nature.com/articles/s42255-019-0044-9
117. Odegaard JI, Ricardo-Gonzalez RR, Red Eagle A, Vats D, Morel CR, Goforth MH, et al. Alternative M2 activation of Kupffer cells by PPARdelta ameliorates obesity-induced insulin resistance. Cell Metab [Internet]. 2008 Jun [cited 2019 May 19];7(6):496–507. Available from: http://www.ncbi.nlm.nih.gov/pubmed/18522831
118. Westphalen K, Gusarova GA, Islam MN, Subramanian M, Cohen TS, Prince AS, et al. Sessile alveolar macrophages communicate with alveolar epithelium to modulate immunity. Nature [Internet]. 2014 Jan 19 [cited 2023 Jan 7];506(7489):503–6. Available from: https://www.nature.com/articles/nature12902
119. MacLean JA, Xia W, Pinto CE, Zhao L, Liu HW, Kradin RL. Sequestration of inhaled particulate antigens by lung phagocytes: A mechanism for the effective inhibition of pulmonary cell-mediated immunity. American Journal of Pathology [Internet]. 1996 Feb [cited 2023 Jan 8];148(2):657–66. Available from: /pmc/articles/PMC1861667/?report=abstract
120. Backer R, Schwandt T, Greuter M, Oosting M, Jüngerkes F, Tüting T, et al. Effective collaboration between marginal metallophilic macrophages and CD8+ dendritic cells in

the generation of cytotoxic T cells. Proc Natl Acad Sci U S A [Internet]. 2010 Dec 29 [cited 2025 Jan 2];107(1):216–21. Available from: https://www.pnas.org/doi/abs/10.1073/pnas.0909541107

121. You Y, Myers RC, Freeberg L, Foote J, Kearney JF, Justement LB, et al. Marginal Zone B Cells Regulate Antigen Capture by Marginal Zone Macrophages. The Journal of Immunology [Internet]. 2011 Feb 15 [cited 2025 Jan 2];186(4):2172–81. Available from: https://dx.doi.org/10.4049/jimmunol.1002106
122. Röszer T. Adipose Tissue Immunometabolism and Apoptotic Cell Clearance. Cells 2021, Vol 10, Page 2288 [Internet]. 2021 Sep 2 [cited 2024 Dec 31];10(9):2288. Available from: https://www.mdpi.com/2073-4409/10/9/2288/htm
123. Suganami T, Ogawa Y. Adipose tissue macrophages: their role in adipose tissue remodeling. J Leukoc Biol [Internet]. 2010 Jul 1 [cited 2024 Dec 31];88(1):33–9. Available from: https://dx.doi.org/10.1189/jlb.0210072
124. Pridans C, Raper A, Davis GM, Alves J, Sauter KA, Lefevre L, et al. Pleiotropic Impacts of Macrophage and Microglial Deficiency on Development in Rats with Targeted Mutation of the Csf1r Locus . The Journal of Immunology [Internet]. 2018 Nov 1 [cited 2023 Jan 8];201(9):2683–99. Available from: https://pubmed.ncbi.nlm.nih.gov/30249809/
125. Wei S, Lightwood D, Ladyman H, Cross S, Neale H, Griffiths M, et al. Modulation of CSF-1-regulated post-natal development with anti-CSF-1 antibody. Immunobiology [Internet]. 2005 Aug 19 [cited 2023 Jan 8];210(2–4):109–19. Available from: https://pubmed.ncbi.nlm.nih.gov/16164017/
126. Cox N, Crozet L, Holtman IR, Loyher PL, Lazarov T, White JB, et al. Diet-regulated production of PDGFcc by macrophages controls energy storage. Science (1979) [Internet]. 2021 Jul 2 [cited 2021 Jul 2];373(6550):eabe9383. Available from: https://www.sciencemag.org/lookup/doi/10.1126/science.abe9383
127. Chawla A, Boisvert WA, Lee CH, Laffitte BA, Barak Y, Joseph SB, et al. A PPARγ-LXR-ABCA1 pathway in macrophages is involved in cholesterol efflux and atherogenesis. Mol Cell [Internet]. 2001 [cited 2023 Jan 8];7(1):161–71. Available from: https://pubmed.ncbi.nlm.nih.gov/11172721/
128. Chiaranunt P, Tai SL, Ngai L, Mortha A. Beyond Immunity: Underappreciated Functions of Intestinal Macrophages. Vol. 12, Frontiers in Immunology. Frontiers Media S.A.; 2021. p. 3866.
129. Bain CC, Schridde A. Origin, differentiation, and function of intestinal macrophages. Front Immunol [Internet]. 2018 Nov 27 [cited 2023 Jan 8];9(NOV). Available from: https://pubmed.ncbi.nlm.nih.gov/30538701/

130. Morhardt TL, Hayashi A, Ochi T, Quirós M, Kitamoto S, Nagao-Kitamoto H, et al. IL-10 produced by macrophages regulates epithelial integrity in the small intestine. Sci Rep [Internet]. 2019 Dec 1 [cited 2023 Jan 8];9(1). Available from: https://pubmed.ncbi.nlm.nih.gov/30718924/
131. De Schepper S, Verheijden S, Aguilera-Lizarraga J, Viola MF, Boesmans W, Stakenborg N, et al. Self-Maintaining Gut Macrophages Are Essential for Intestinal Homeostasis. Cell [Internet]. 2018 Oct 4 [cited 2023 Jan 8];175(2):400-415.e13. Available from: https://pubmed.ncbi.nlm.nih.gov/30173915/
132. Viola MF, Boeckxstaens G. Intestinal resident macrophages: Multitaskers of the gut. Neurogastroenterology & Motility [Internet]. 2020 Aug 28 [cited 2023 Jan 8];32(8):e13843. Available from: https://onlinelibrary.wiley.com/doi/10.1111/nmo.13843
133. Goritzka M, Makris S, Kausar F, Durant LR, Pereira C, Kumagai Y, et al. Alveolar macrophage-derived type I interferons orchestrate innate immunity to RSV through recruitment of antiviral monocytes. Journal of Experimental Medicine [Internet]. 2015 May 4 [cited 2023 Jan 7];212(5):699–714. Available from: https://pubmed.ncbi.nlm.nih.gov/25897172/
134. Mould KJ, Jackson ND, Henson PM, Seibold M, Janssen WJ. Single cell RNA sequencing identifies unique inflammatory airspace macrophage subsets. JCI Insight [Internet]. 2019 Mar 7 [cited 2023 Jan 7];4(5). Available from: https://pubmed.ncbi.nlm.nih.gov/30721157/
135. Krenkel O, Tacke F. Liver macrophages in tissue homeostasis and disease. Nat Rev Immunol [Internet]. 2017 May 20 [cited 2019 May 3];17(5):306–21. Available from: http://www.ncbi.nlm.nih.gov/pubmed/28317925
136. Laskin DL, Sunil VR, Gardner CR, Laskin JD. Macrophages and Tissue Injury: Agents of Defense or Destruction? 2011;
137. Ho MS. Microglia in parkinson's disease. In: Advances in Experimental Medicine and Biology [Internet]. Springer New York LLC; 2019 [cited 2023 Jan 7]. p. 335–53. Available from: https://pubmed.ncbi.nlm.nih.gov/31583594/
138. Hansen D V., Hanson JE, Sheng M. Microglia in Alzheimer's disease [Internet]. Vol. 217, Journal of Cell Biology. Rockefeller University Press; 2018 [cited 2023 Jan 7]. p. 459–72. Available from: /pmc/articles/PMC5800817/
139. Sekar A, Bialas AR, De Rivera H, Davis A, Hammond TR, Kamitaki N, et al. Schizophrenia risk from complex variation of complement component 4. Nature [Internet]. 2016 Feb 11 [cited 2023 Jan 7];530(7589):177–83. Available from: https://pubmed.ncbi.nlm.nih.gov/26814963/

140. Clarke BE, Patani R. The microglial component of amyotrophic lateral sclerosis [Internet]. Vol. 143, Brain. Oxford University Press; 2020 [cited 2023 Jan 7]. p. 3526–39. Available from: https://academic.oup.com/brain/article/143/12/3526/6016135
141. Rademakers R, Baker M, Nicholson AM, Rutherford NJ, Finch N, Soto-Ortolaza A, et al. Mutations in the colony stimulating factor 1 receptor (CSF1R) gene cause hereditary diffuse leukoencephalopathy with spheroids. Nat Genet [Internet]. 2012 Feb [cited 2023 Jan 7];44(2):200–5. Available from: /pmc/articles/PMC3267847/
142. Oosterhof N, Chang IJ, Karimiani EG, Kuil LE, Jensen DM, Daza R, et al. Homozygous Mutations in CSF1R Cause a Pediatric-Onset Leukoencephalopathy and Can Result in Congenital Absence of Microglia. Am J Hum Genet [Internet]. 2019 May 2 [cited 2023 Jan 7];104(5):936–47. Available from: /pmc/articles/PMC6506793/
143. Mass E, Jacome-Galarza CE, Blank T, Lazarov T, Durham BH, Ozkaya N, et al. A somatic mutation in erythro-myeloid progenitors causes neurodegenerative disease. Nature [Internet]. 2017 Sep 21 [cited 2023 Jan 7];549(7672):389–93. Available from: /pmc/articles/PMC6047345/
144. Han D, Liu H, Gao Y. The role of peripheral monocytes and macrophages in ischemic stroke. Neurological Sciences 2020 41:12 [Internet]. 2020 Oct 3 [cited 2025 Jan 10];41(12):3589–607. Available from: https://link.springer.com/article/10.1007/s10072-020-04777-9
145. Pedragosa J, Salas-Perdomo A, Gallizioli M, Cugota R, Miró-Mur F, Briansó F, et al. CNS-border associated macrophages respond to acute ischemic stroke attracting granulocytes and promoting vascular leakage. Acta Neuropathol Commun [Internet]. 2018 Aug 9 [cited 2025 Jan 10];6(1):76. Available from: https://actaneurocomms.biomedcentral.com/articles/10.1186/s40478-018-0581-6
146. Suzuki T, Trapnell BC. Pulmonary Alveolar Proteinosis Syndrome [Internet]. Vol. 37, Clinics in Chest Medicine. W.B. Saunders; 2016 [cited 2023 May 3]. p. 431–40. Available from: /pmc/articles/PMC5902187/
147. Yan J, Li S, Li S. The role of the liver in sepsis. Int Rev Immunol [Internet]. 2014 Nov 2 [cited 2025 Jan 3];33(6):498–510. Available from: https://pubmed.ncbi.nlm.nih.gov/24611785/
148. Li D, Wu M. Pattern recognition receptors in health and diseases. Signal Transduction and Targeted Therapy 2021 6:1 [Internet]. 2021 Aug 4 [cited 2025 Jan 10];6(1):1–24. Available from: https://www.nature.com/articles/s41392-021-00687-0
149. Areschoug T, Gordon S. Scavenger receptors: role in innate immunity and microbial pathogenesis. Cell Microbiol [Internet]. 2009 Aug 1 [cited 2025 Jan 10];11(8):1160–9. Available from: https://onlinelibrary.wiley.com/doi/full/10.1111/j.1462-5822.2009.01326.x

150. Geijtenbeek TBH, Gringhuis SI. Signalling through C-type lectin receptors: shaping immune responses. Nature Reviews Immunology 2009 9:7 [Internet]. 2009 Jul [cited 2025 Jan 10];9(7):465–79. Available from: https://www.nature.com/articles/nri2569
151. Sikder MH, Asadazzuaman M, Hossen MJ, Matin MA, Rahman M, Ahmed MS, et al. The role of macrophages in tuberculosis. Recent Advancements in Microbial Diversity: Macrophages and their Role in Inflammation. 2022 Jan 1;397–415.
152. Guirado E, Schlesinger LS, Kaplan G. Macrophages in Tuberculosis: Friend or Foe. Semin Immunopathol [Internet]. 2013 Sep [cited 2025 Mar 8];35(5):563. Available from: https://pmc.ncbi.nlm.nih.gov/articles/PMC3763202/
153. Chua CLL, Ng IMJ, Yap BJM, Teo A. Factors influencing phagocytosis of malaria parasites: the story so far. Malaria Journal 2021 20:1 [Internet]. 2021 Jul 16 [cited 2025 Jan 11];20(1):1–15. Available from: https://malariajournal.biomedcentral.com/articles/10.1186/s12936-021-03849-1
154. Chua CLL, Brown G, Hamilton JA, Rogerson S, Boeuf P. Monocytes and macrophages in malaria: protection or pathology? Trends Parasitol. 2013 Jan 1;29(1):26–34.
155. Crutcher JM, Hoffman SL. Malaria. Medical Microbiology [Internet]. 1996 [cited 2025 Jan 11]; Available from: https://www.ncbi.nlm.nih.gov/books/NBK8584/
156. Terpstra V, Van Berkel TJC. Scavenger receptors on liver Kupffer cells mediate the in vivo uptake of oxidatively damaged red blood cells in mice. Blood [Internet]. 2000 Mar 15 [cited 2025 Jan 11];95(6):2157–63. Available from: https://dx.doi.org/10.1182/blood.V95.6.2157
157. Dilillo DJ, Ravetch J V. Fc-Receptor Interactions Regulate Both Cytotoxic and Immunomodulatory Therapeutic Antibody Effector Functions. Cancer Immunol Res [Internet]. 2015 Jul 1 [cited 2025 Jan 10];3(7):704–13. Available from: /cancerimmunolres/article/3/7/704/467731/Fc-Receptor-Interactions-Regulate-Both-Cytotoxic
158. Takai T. Fc receptors and their role in immune regulation and autoimmunity. J Clin Immunol [Internet]. 2005 Jan [cited 2025 Jan 10];25(1):1–18. Available from: https://link.springer.com/article/10.1007/s10875-005-0353-8
159. Wieland A, Ahmed R. Fc Receptors in Antimicrobial Protection. Curr Top Microbiol Immunol [Internet]. 2019 [cited 2025 Jan 10];423:119–50. Available from: https://link.springer.com/chapter/10.1007/82_2019_154
160. Laassili C, Ben El Hend F, Benzidane R, Oumeslakht L, Aziz AI, El Fatimy R, et al. Fc receptors act as innate immune receptors during infection? Front Immunol. 2023 Jul 26;14:1188497.

161. Pisetsky DS. Pathogenesis of autoimmune disease. Nature Reviews Nephrology 2023 19:8 [Internet]. 2023 May 10 [cited 2025 Jan 11];19(8):509–24. Available from: https://www.nature.com/articles/s41581-023-00720-1
162. Yang S, Zhao M, Jia S. Macrophage: Key player in the pathogenesis of autoimmune diseases. Front Immunol. 2023 Feb 14;14:1080310.
163. Grajchen E, Hendriks JJA, Bogie JFJ. The physiology of foamy phagocytes in multiple sclerosis. Acta Neuropathologica Communications 2018 6:1 [Internet]. 2018 Nov 19 [cited 2025 Jan 11];6(1):1–21. Available from: https://actaneurocomms.biomedcentral.com/articles/10.1186/s40478-018-0628-8
164. Bogie JFJ, Stinissen P, Hellings N, Hendriks JJA. Myelin-phagocytosing macrophages modulate autoreactive T cell proliferation. J Neuroinflammation [Internet]. 2011 Jul 25 [cited 2025 Jan 11];8(1):1–13. Available from: https://jneuroinflammation.biomedcentral.com/articles/10.1186/1742-2094-8-85
165. Dietrich P, Hellerbrand C. Non-alcoholic fatty liver disease, obesity and the metabolic syndrome. Best Pract Res Clin Gastroenterol. 2014;28(4):637–53.
166. Xu GX, Wei S, Yu C, Zhao SQ, Yang WJ, Feng YH, et al. Activation of Kupffer cells in NAFLD and NASH: mechanisms and therapeutic interventions. Front Cell Dev Biol. 2023 May 16;11:1199519.
167. Hardy T, Oakley F, Anstee QM, Day CP. Nonalcoholic Fatty Liver Disease: Pathogenesis and Disease Spectrum. Annu Rev Pathol [Internet]. 2016 May 23 [cited 2025 Jan 3];11:451–96. Available from: https://pubmed.ncbi.nlm.nih.gov/26980160/
168. Baeck C, Wehr A, Karlmark KR, Heymann F, Vucur M, Gassler N, et al. Pharmacological inhibition of the chemokine CCL2 (MCP-1) diminishes liver macrophage infiltration and steatohepatitis in chronic hepatic injury. Gut [Internet]. 2012 Mar [cited 2025 Jan 3];61(3):416–26. Available from: https://pubmed.ncbi.nlm.nih.gov/21813474/
169. Pradere JP, Kluwe J, De Minicis S, Jiao JJ, Gwak GY, Dapito DH, et al. Hepatic macrophages but not dendritic cells contribute to liver fibrosis by promoting the survival of activated hepatic stellate cells in mice. Hepatology [Internet]. 2013 Oct [cited 2025 Jan 3];58(4):1461–73. Available from: https://pubmed.ncbi.nlm.nih.gov/23553591/
170. Neyrinck AM, Cani PD, Dewulf EM, De Backer F, Bindels LB, Delzenne NM. Critical role of Kupffer cells in the management of diet-induced diabetes and obesity. Biochem Biophys Res Commun. 2009 Jul 31;385(3):351–6.
171. Lanthier N, Molendi-Coste O, Horsmans Y, Van Rooijen N, Cani PD, Leclercq IA. Kupffer cell activation is a causal factor for hepatic insulin resistance. Am J Physiol Gastrointest Liver Physiol [Internet]. 2010 Jan [cited 2025 Jan 5];298(1):107–16. Available from: https://journals.physiology.org/doi/10.1152/ajpgi.00391.2009

172. Clementi AH, Gaudy AM, van Rooijen N, Pierce RH, Mooney RA. Loss of Kupffer cells in diet-induced obesity is associated with increased hepatic steatosis, STAT3 signaling, and further decreases in insulin signaling. Biochimica et Biophysica Acta (BBA) - Molecular Basis of Disease. 2009 Nov 1;1792(11):1062–72.
173. Rai RM, Loffreda S, Karp CL, Yang SQ, Lin HZ, Diehl AM. Kupffer cell depletion abolishes induction of interleukin-10 and permits sustained overexpression of tumor necrosis factor alpha messenger RNA in the regenerating rat liver. Hepatology [Internet]. 1997 [cited 2025 Jan 5];25(4):889–95. Available from: https://journals.lww.com/hep/fulltext/1997/04000/kupffer_cell_depletion_abolishes_induction_of.17.aspx
174. Papackova Z, Palenickova E, Dankova H, Zdychova J, Skop V, Kazdova L, et al. Kupffer cells ameliorate hepatic insulin resistance induced by high-fat diet rich in monounsaturated fatty acids: The evidence for the involvement of alternatively activated macrophages. Nutr Metab (Lond) [Internet]. 2012 Mar 22 [cited 2024 Dec 31];9(1):1–15. Available from: https://nutritionandmetabolism.biomedcentral.com/articles/10.1186/1743-7075-9-22
175. Weisberg SP, McCann D, Desai M, Rosenbaum M, Leibel RL, Ferrante AW. Obesity is associated with macrophage accumulation in adipose tissue. Journal of Clinical Investigation [Internet]. 2003 Dec 15 [cited 2023 Jan 8];112(12):1796–808. Available from: https://pubmed.ncbi.nlm.nih.gov/14679176/
176. Kanda H, Tateya S, Tamori Y, Kotani K, Hiasa KI, Kitazawa R, et al. MCP-1 contributes to macrophage infiltration into adipose tissue, insulin resistance, and hepatic steatosis in obesity. Journal of Clinical Investigation [Internet]. 2006 Jun 1 [cited 2023 Jan 8];116(6):1494–505. Available from: https://pubmed.ncbi.nlm.nih.gov/16691291/
177. Weisberg SP, Hunter D, Huber R, Lemieux J, Slaymaker S, Vaddi K, et al. CCR2 modulates inflammatory and metabolic effects of high-fat feeding. Journal of Clinical Investigation [Internet]. 2006 [cited 2023 Jan 8];116(1):115–24. Available from: https://pubmed.ncbi.nlm.nih.gov/16341265/
178. Cinti S, Mitchell G, Barbatelli G, Murano I, Ceresi E, Faloia E, et al. Adipocyte death defines macrophage localization and function in adipose tissue of obese mice and humans. J Lipid Res [Internet]. 2005 Nov [cited 2025 Jan 3];46(11):2347–55. Available from: https://pubmed.ncbi.nlm.nih.gov/16150820/
179. Moore KJ, Freeman MW. Scavenger receptors in atherosclerosis: beyond lipid uptake. Arterioscler Thromb Vasc Biol [Internet]. 2006 Aug [cited 2025 Jan 5];26(8):1702–11. Available from: https://pubmed.ncbi.nlm.nih.gov/16728653/
180. Castillo-Armengol J, Fajas L, Lopez-Mejia IC. Inter-organ communication: a gatekeeper for metabolic health.

181. Stanya KJ, Jacobi D, Liu S, Bhargava P, Dai L, Gangl MR, et al. Direct control of hepatic glucose production by interleukin-13 in mice. J Clin Invest [Internet]. 2013 Jan 2 [cited 2025 Jan 6];123(1):261–71. Available from: https://pubmed.ncbi.nlm.nih.gov/23257358/
182. Rui L. Energy Metabolism in the Liver. Compr Physiol [Internet]. 2014 [cited 2025 Jan 6];4(1):177. Available from: https://pmc.ncbi.nlm.nih.gov/articles/PMC4050641/
183. Kharitonenkov A, Shiyanova TL, Koester A, Ford AM, Micanovic R, Galbreath EJ, et al. FGF-21 as a novel metabolic regulator. J Clin Invest [Internet]. 2005 Jun [cited 2025 Jan 6];115(6):1627–35. Available from: https://pubmed.ncbi.nlm.nih.gov/15902306/
184. Davis EM, Sandoval DA. Glucagon-Like Peptide-1: Actions and Influence on Pancreatic Hormone Function. Compr Physiol [Internet]. 2020 Apr 1 [cited 2025 Jan 6];10(2):577–95. Available from: https://pubmed.ncbi.nlm.nih.gov/32163198/
185. Ferrell JM, Chiang JYL. Bile acid receptors and signaling crosstalk in the liver, gut and brain. Liver Res. 2021 Sep 1;5(3):105–18.
186. Kir S, Beddow SA, Samuel VT, Miller P, Previs SF, Suino-Powell K, et al. FGF19 as a postprandial, insulin-independent activator of hepatic protein and glycogen synthesis. Science [Internet]. 2011 Mar 25 [cited 2025 Jan 6];331(6024):1621–4. Available from: https://pubmed.ncbi.nlm.nih.gov/21436455/
187. Oh KJ, Lee DS, Kim WK, Han BS, Lee SC, Bae KH. Metabolic Adaptation in Obesity and Type II Diabetes: Myokines, Adipokines and Hepatokines. Int J Mol Sci [Internet]. 2016 Jan 1 [cited 2025 Jan 6];18(1):8. Available from: https://pmc.ncbi.nlm.nih.gov/articles/PMC5297643/
188. Albillos A, de Gottardi A, Rescigno M. The gut-liver axis in liver disease: Pathophysiological basis for therapy. J Hepatol. 2020 Mar 1;72(3):558–77.
189. Aboghazleh R, Boyajian SD, Atiyat A, Udwan M, Al-Helalat M, Al-Rashaideh R. Rodent brain extraction and dissection: A comprehensive approach. MethodsX. 2024 Jun 1;12:102516.
190. Schafer DP, Lehrman EK, Heller CT, Stevens B. An engulfment assay: a protocol to assess interactions between CNS phagocytes and neurons. J Vis Exp [Internet]. 2014 Jun 8 [cited 2025 Feb 23];(88). Available from: https://pubmed.ncbi.nlm.nih.gov/24962472/
191. Sieckmann K, Winnerling N, Huebecker M, Leyendecker P, Silva Ribeiro DJ, Gnad T, et al. AdipoQ-a simple, open-source software to quantify adipocyte morphology and function in tissues and in vitro. Mol Biol Cell [Internet]. 2022 Oct 1 [cited 2025 Feb 12];33(12). Available from: https://pubmed.ncbi.nlm.nih.gov/35947507/
192. Pfaffl MW. Quantification strategies in real-time PCR. 2004;

193. Duhlin A, Chen Y, Wermeling F, Sedimbi SK, Lindh E, Shinde R, et al. Selective Memory to Apoptotic Cell–Derived Self-Antigens with Implications for Systemic Lupus Erythematosus Development. The Journal of Immunology [Internet]. 2016 Oct 1 [cited 2023 Aug 17];197(7):2618–26. Available from: www.jimmunol.org/cgi/doi/10.4049/jimmunol.1401129
194. Hughes TK, Wadsworth MH, Gierahn TM, Do T, Weiss D, Andrade PR, et al. Second-Strand Synthesis-Based Massively Parallel scRNA-Seq Reveals Cellular States and Molecular Features of Human Inflammatory Skin Pathologies. Immunity. 2020 Oct 13;53(4):878-894.e7.
195. Gierahn TM, Wadsworth MH, Hughes TK, Bryson BD, Butler A, Satija R, et al. Seq-Well: portable, low-cost RNA sequencing of single cells at high throughput. Nature Methods 2017 14:4 [Internet]. 2017 Feb 13 [cited 2025 Jan 14];14(4):395–8. Available from: https://www.nature.com/articles/nmeth.4179
196. Macosko EZ, Basu A, Satija R, Nemesh J, Shekhar K, Goldman M, et al. Highly Parallel Genome-wide Expression Profiling of Individual Cells Using Nanoliter Droplets. Cell [Internet]. 2015 May 30 [cited 2025 Feb 24];161(5):1202–14. Available from: https://pubmed.ncbi.nlm.nih.gov/26000488/
197. Neuberger-Castillo L, Hamot G, Marchese M, Sanchez I, Ammerlaan W, Betsou F. Method Validation for Extraction of DNA from Human Stool Samples for Downstream Microbiome Analysis. Biopreserv Biobank [Internet]. 2020 Apr 1 [cited 2025 Feb 23];18(2):102–16. Available from: https://pubmed.ncbi.nlm.nih.gov/31999474/
198. Kable ME, Chin EL, Storms D, Lemay DG, Stephensen CB. Tree-Based Analysis of Dietary Diversity Captures Associations Between Fiber Intake and Gut Microbiota Composition in a Healthy US Adult Cohort. J Nutr [Internet]. 2022 Mar 1 [cited 2025 Feb 23];152(3):779–88. Available from: https://pubmed.ncbi.nlm.nih.gov/34958387/
199. Junkins EN, McWhirter JB, McCall LI, Stevenson BS. Environmental structure impacts microbial composition and secondary metabolism. ISME Communications 2022 2:1 [Internet]. 2022 Feb 3 [cited 2025 Feb 23];2(1):1–10. Available from: https://www.nature.com/articles/s43705-022-00097-5
200. Seel W, Reiners S, Kipp K, Simon MC, Dawczynski C. Role of Dietary Fiber and Energy Intake on Gut Microbiome in Vegans, Vegetarians, and Flexitarians in Comparison to Omnivores-Insights from the Nutritional Evaluation (NuEva) Study. Nutrients [Internet]. 2023 Apr 1 [cited 2025 Feb 23];15(8). Available from: https://pubmed.ncbi.nlm.nih.gov/37111133/
201. Bolyen E, Rideout JR, Dillon MR, Bokulich NA, Abnet CC, Al-Ghalith GA, et al. Reproducible, interactive, scalable and extensible microbiome data science using

QIIME 2. Nature Biotechnology 2019 37:8 [Internet]. 2019 Jul 24 [cited 2025 Feb 23];37(8):852–7. Available from: https://www.nature.com/articles/s41587-019-0209-9

202. Callahan BJ, McMurdie PJ, Rosen MJ, Han AW, Johnson AJA, Holmes SP. DADA2: High-resolution sample inference from Illumina amplicon data. Nature Methods 2016 13:7 [Internet]. 2016 May 23 [cited 2025 Feb 23];13(7):581–3. Available from: https://www.nature.com/articles/nmeth.3869
203. Gierahn TM, Wadsworth MH, Hughes TK, Bryson BD, Butler A, Satija R, et al. Seq-Well: portable, low-cost RNA sequencing of single cells at high throughput. Nature Methods 2017 14:4 [Internet]. 2017 Feb 13 [cited 2025 Jan 14];14(4):395–8. Available from: https://www.nature.com/articles/nmeth.4179
204. Becht E, McInnes L, Healy J, Dutertre CA, Kwok IWH, Ng LG, et al. Dimensionality reduction for visualizing single-cell data using UMAP. Nat Biotechnol [Internet]. 2018 Dec 3 [cited 2019 Apr 8];37(1):38–44. Available from: http://www.ncbi.nlm.nih.gov/pubmed/30531897
205. Sharma HS, Sharma A. Nanoparticles aggravate heat stress induced cognitive deficits, blood-brain barrier disruption, edema formation and brain pathology [Internet]. Vol. 162, Progress in Brain Research. Prog Brain Res; 2007 [cited 2024 Nov 8]. p. 245–73. Available from: https://pubmed.ncbi.nlm.nih.gov/17645923/
206. Venkatesh SK, Torbenson MS. Liver fibrosis quantification. Abdom Radiol (NY) [Internet]. 2022 Mar 1 [cited 2025 Feb 11];47(3):1032. Available from: https://pmc.ncbi.nlm.nih.gov/articles/PMC9538706/
207. Lee AS, Persoff J, Lange SM. LIVER FUNCTION TESTS. In: Mayo Clinic Medical Manual [Internet]. CRC Press; 2006 [cited 2024 Dec 1]. p. 373–87. Available from: https://www.ncbi.nlm.nih.gov/books/NBK482489/
208. NYBLOM H. HIGH AST/ALT RATIO MAY INDICATE ADVANCED ALCOHOLIC LIVER DISEASE RATHER THAN HEAVY DRINKING. Alcohol and Alcoholism [Internet]. 2004 Jul 1 [cited 2024 Dec 1];39(4):336–9. Available from: https://academic.oup.com/alcalc/article-lookup/doi/10.1093/alcalc/agh074
209. Mashek DG. Hepatic lipid droplets: A balancing act between energy storage and metabolic dysfunction in NAFLD [Internet]. Vol. 50, Molecular Metabolism. Elsevier GmbH; 2021 [cited 2024 Dec 9]. p. 101115. Available from: https://pmc.ncbi.nlm.nih.gov/articles/PMC8324678/
210. Su Q, Kim SY, Adewale F, Zhou Y, Aldler C, Ni M, et al. Single-cell RNA transcriptome landscape of hepatocytes and non-parenchymal cells in healthy and NAFLD mouse liver. iScience. 2021 Nov 19;24(11):103233.
211. Carlessi R, Denisenko E, Boslem E, Köhn-Gaone J, Main N, Abu Bakar NDB, et al. Single-nucleus RNA sequencing of pre-malignant liver reveals disease-associated

hepatocyte state with HCC prognostic potential. Cell Genomics [Internet]. 2023 May 10 [cited 2024 Nov 29];3(5). Available from: http://www.cell.com/article/S2666979X23000678/fulltext

212. Andrews TS, Atif J, Liu JC, Perciani CT, Ma XZ, Thoeni C, et al. Single-Cell, Single-Nucleus, and Spatial RNA Sequencing of the Human Liver Identifies Cholangiocyte and Mesenchymal Heterogeneity. Hepatol Commun [Internet]. 2022 Apr 1 [cited 2024 Nov 29];6(4):821–40. Available from: https://pmc.ncbi.nlm.nih.gov/articles/PMC8948611/
213. Li X, Ren Y, Chang K, Wu W, Griffiths HR, Lu S, et al. Adipose tissue macrophages as potential targets for obesity and metabolic diseases. Front Immunol. 2023 Apr 19;14:1153915.
214. Nakajima S, Koh V, Kua LF, So J, Davide L, Lim KS, et al. Accumulation of CD11c+CD163+ Adipose Tissue Macrophages through Upregulation of Intracellular 11β-HSD1 in Human Obesity. The Journal of Immunology [Internet]. 2016 Nov 1 [cited 2025 Feb 12];197(9):3735–45. Available from: https://dx.doi.org/10.4049/jimmunol.1600895
215. Stefanovic-Racic M, Yang X, Turner MS, Mantell BS, Stolz DB, Sumpter TL, et al. Dendritic cells promote macrophage infiltration and comprise a substantial proportion of obesity-associated increases in CD11c + cells in adipose tissue and liver. Diabetes [Internet]. 2012 Sep [cited 2025 Feb 12];61(9):2330–9. Available from: https://pmc.ncbi.nlm.nih.gov/articles/PMC3425427/
216. Duan Y, Zeng L, Zheng C, Song B, Li F, Kong X, et al. Inflammatory links between high fat diets and diseases. Front Immunol. 2018 Nov 13;9(NOV):424482.
217. Teodoro JS, Varela AT, Rolo AP, Palmeira CM. High-fat and obesogenic diets: Current and future strategies to fight obesity and diabetes [Internet]. Vol. 9, Genes and Nutrition. Springer Verlag; 2014 [cited 2024 Dec 2]. p. 406. Available from: http://link.springer.com/10.1007/s12263-014-0406-6
218. Blüher M. Obesity: global epidemiology and pathogenesis [Internet]. Vol. 15, Nature Reviews Endocrinology. Nature Publishing Group; 2019 [cited 2024 Dec 18]. p. 288–98. Available from: https://www.nature.com/articles/s41574-019-0176-8
219. Hirayama D, Iida T, Nakase H. The phagocytic function of macrophage-enforcing innate immunity and tissue homeostasis [Internet]. Vol. 19, International Journal of Molecular Sciences. MDPI AG; 2018 [cited 2024 Dec 9]. p. 92. Available from: https://pmc.ncbi.nlm.nih.gov/articles/PMC5796042/
220. Pishesha N, Harmand TJ, Ploegh HL. A guide to antigen processing and presentation [Internet]. Vol. 22, Nature Reviews Immunology. Nature Research; 2022 [cited 2024 Dec 4]. p. 751–64. Available from: https://www.nature.com/articles/s41577-022-00707-2

221. Wöhner M, Brechtelsbauer S, Friedrich N, Vorsatz C, Bulang J, Liang C, et al. Tissue niche occupancy determines the contribution of fetal- versus bone-marrow-derived macrophages to IgG effector functions. Cell Rep [Internet]. 2024 Feb 27 [cited 2025 Feb 18];43(2). Available from: https://pubmed.ncbi.nlm.nih.gov/38354088/
222. Fu YL, Harrison RE. Microbial Phagocytic Receptors and Their Potential Involvement in Cytokine Induction in Macrophages [Internet]. Vol. 12, Frontiers in Immunology. Frontiers Media S.A.; 2021 [cited 2024 Oct 28]. p. 662063. Available from: www.frontiersin.org
223. Chua CLL, Ng IMJ, Yap BJM, Teo A. Factors influencing phagocytosis of malaria parasites: the story so far [Internet]. Vol. 20, Malaria Journal. BioMed Central Ltd; 2021 [cited 2024 Dec 12]. p. 1–15. Available from: https://malariajournal.biomedcentral.com/articles/10.1186/s12936-021-03849-1
224. Nishi C, Toda S, Segawa K, Nagata S. Tim4- and MerTK-Mediated Engulfment of Apoptotic Cells by Mouse Resident Peritoneal Macrophages. Mol Cell Biol [Internet]. 2014 Apr 1 [cited 2024 Nov 2];34(8):1512–20. Available from: https://pubmed.ncbi.nlm.nih.gov/24515440/
225. Vinuesa CG, Sanz Ĩ, Cook MC. Dysregulation of germinal centres in autoimmune disease [Internet]. Vol. 9, Nature Reviews Immunology. Nat Rev Immunol; 2009 [cited 2024 Nov 2]. p. 845–57. Available from: https://pubmed.ncbi.nlm.nih.gov/19935804/
226. Mahajan A, Herrmann M, Muñoz LE. Clearance deficiency and cell death pathways: A model for the pathogenesis of SLE [Internet]. Vol. 7, Frontiers in Immunology. Frontiers Media S.A.; 2016 [cited 2024 Nov 2]. p. 1. Available from: www.frontiersin.org
227. Almizraq RJ, Frias Boligan K, Loriamini M, McKerlie C, Branch DR. (NZW × BXSB) F1 male mice: An unusual, severe and fatal mouse model of lupus erythematosus. Front Immunol. 2022 Sep 23;13:977698.
228. Mass E, Ballesteros I, Farlik M, Halbritter F, Gunther P, Crozet L, et al. Specification of tissue-resident macrophages during organogenesis. Science (1979) [Internet]. 2016 Sep 9 [cited 2019 May 9];353(6304):aaf4238–aaf4238. Available from: http://www.ncbi.nlm.nih.gov/pubmed/27492475
229. KD C, GA C, HL D, JF D, F J, SE D. Human Consumption of Microplastics. Environ Sci Technol [Internet]. 2019 [cited 2024 Nov 14];53(12). Available from: https://pubmed.ncbi.nlm.nih.gov/31184127/
230. Alberghini L, Truant A, Santonicola S, Colavita G, Giaccone V. Microplastics in Fish and Fishery Products and Risks for Human Health: A Review [Internet]. Vol. 20, International Journal of Environmental Research and Public Health. MDPI; 2023 [cited 2024 Nov 14]. p. 789. Available from: https://pmc.ncbi.nlm.nih.gov/articles/PMC9819327/

231. Eriksen M, Lebreton LCM, Carson HS, Thiel M, Moore CJ, Borerro JC, et al. Plastic Pollution in the World's Oceans: More than 5 Trillion Plastic Pieces Weighing over 250,000 Tons Afloat at Sea. Dam HG, editor. PLoS One [Internet]. 2014 Dec 10 [cited 2024 Dec 23];9(12):e111913. Available from: https://dx.plos.org/10.1371/journal.pone.0111913
232. Walczak Peter J M Hendriksen Ruud A Woutersen Meike van der Zande Anna K Undas Richard Helsdingen Hans H J van den Berg Ivonne M C M Rietjens Hans Bouwmeester AP. Bioavailability and biodistribution of differently charged polystyrene nanoparticles upon oral exposure in rats.
233. Zhao S, Ward JE, Danley M, Mincer TJ. Field-Based Evidence for Microplastic in Marine Aggregates and Mussels: Implications for Trophic Transfer. Environ Sci Technol [Internet]. 2018 Oct 2 [cited 2024 Nov 14];52(19):11038–48. Available from: https://pubs.acs.org/doi/full/10.1021/acs.est.8b03467
234. Vaughan R, Turner SD, Rose NL. Microplastics in the sediments of a UK urban lake. Environmental Pollution. 2017 Oct 1;229:10–8.
235. Liang B, Zhong Y, Huang Y, Lin X, Liu J, Lin L, et al. Underestimated health risks: polystyrene micro- and nanoplastics jointly induce intestinal barrier dysfunction by ROS-mediated epithelial cell apoptosis. Part Fibre Toxicol [Internet]. 2021 Dec 1 [cited 2024 Nov 15];18(1):20. Available from: https://particleandfibretoxicology.biomedcentral.com/articles/10.1186/s12989-021-00414-1
236. Degradation Rates of Plastics in the Environment | Enhanced Reader [Internet]. [cited 2024 Nov 15]. Available from: moz-extension://7a5a33a8-2c13-4045-be9e-2fa47ae8d9a1/enhanced-reader.html?openApp&pdf=https%3A%2F%2Fpubs.acs.org%2Fdoi%2Fpdf%2F10.1021%2Facssuschemeng.9b06635%3Fref%3Dvi_green-chemistry-2021
237. Gordon S, Plüddemann A. Tissue macrophages: Heterogeneity and functions [Internet]. Vol. 15, BMC Biology. BioMed Central Ltd.; 2017 [cited 2024 Nov 18]. p. 1–18. Available from: https://bmcbiol.biomedcentral.com/articles/10.1186/s12915-017-0392-4
238. Merkley SD, Moss HC, Goodfellow SM, Ling CL, Meyer-Hagen JL, Weaver J, et al. Polystyrene microplastics induce an immunometabolic active state in macrophages. Cell Biol Toxicol [Internet]. 2022 Feb 1 [cited 2024 Nov 15];38(1):31–41. Available from: https://link.springer.com/article/10.1007/s10565-021-09616-x
239. Stock V, Böhmert L, Lisicki E, Block R, Cara-Carmona J, Pack LK, et al. Uptake and effects of orally ingested polystyrene microplastic particles in vitro and in vivo. Arch

Toxicol [Internet]. 2019 Jul 1 [cited 2024 Nov 15];93(7):1817–33. Available from: https://link.springer.com/article/10.1007/s00204-019-02478-7

240. Wiewrodt R, Thomas AP, Cipelletti L, Christofidou-Solomidou M, Weitz DA, Feinstein SI, et al. Size-dependent intracellular immunotargeting of therapeutic cargoes into endothelial cells. Blood [Internet]. 2002 Feb 1 [cited 2024 Nov 18];99(3):912–22. Available from: https://dx.doi.org/10.1182/blood.V99.3.912
241. Zhang S, Li J, Lykotrafitis G, Bao G, Suresh S. Size-dependent endocytosis of nanoparticles. Advanced Materials [Internet]. 2009 Jan 26 [cited 2024 Nov 18];21(4):419–24. Available from: https://pubmed.ncbi.nlm.nih.gov/19606281/
242. Cho Y, Seo EU, Hwang KS, Kim H, Choi J, Kim HN. Evaluation of size-dependent uptake, transport and cytotoxicity of polystyrene microplastic in a blood-brain barrier (BBB) model. Nano Converg [Internet]. 2024 Dec 1 [cited 2024 Nov 18];11(1):40. Available from: https://nanoconvergencejournal.springeropen.com/articles/10.1186/s40580-024-00448-z
243. Du J, Zhang YS, Hobson D, Hydbring P. Nanoparticles for immune system targeting. Vol. 22, Drug Discovery Today. Elsevier Ltd; 2017. p. 1295–301.
244. Johnston HJ, Semmler-Behnke M, Brown DM, Kreyling W, Tran L, Stone V. Evaluating the uptake and intracellular fate of polystyrene nanoparticles by primary and hepatocyte cell lines in vitro. Toxicol Appl Pharmacol [Internet]. 2010 Jan 1 [cited 2024 Nov 18];242(1):66–78. Available from: https://linkinghub.elsevier.com/retrieve/pii/S0041008X09004074
245. Englert FH, Mueller FA, Dugershaw-Kurzer B, Kissling VM, Boentges S, Gupta GS, et al. Environmentally relevant UV-light weathering of polystyrene micro- and nanoplastics promotes hepatotoxicity in a human cell line. Environ Sci Nano [Internet]. 2023 May 3 [cited 2024 Nov 18];10(6):1644–59. Available from: https://pubs.rsc.org/en/content/articlehtml/2023/en/d3en00044c
246. Understanding nanoparticle-liver interactions in nanomedicine | Enhanced Reader [Internet]. [cited 2024 Nov 18]. Available from: moz-extension://7a5a33a8-2c13-4045-be9e-2fa47ae8d9a1/enhanced-reader.html?openApp&pdf=https%3A%2F%2Fwww.wilhelm-lab.com%2Fwp-content%2Fuploads%2F2024%2F07%2FEODD_2024.pdf
247. Vivero-Escoto JL, Vadarevu H, Juneja R, Schrum LW, Benbow JH. Nanoparticle mediated silencing of tenascin C in hepatic stellate cells: Effect on inflammatory gene expression and cell migration. J Mater Chem B [Internet]. 2019 Nov 27 [cited 2024 Nov 18];7(46):7396–405. Available from: https://pubs.rsc.org/en/content/articlehtml/2019/tb/c9tb01845j

248. Fairchild RL. Fibroblastic reticular cells orchestrate long-term graft survival following recipient treatment with CD40 ligand-targeted costimulatory blockade [Internet]. Vol. 132, Journal of Clinical Investigation. American Society for Clinical Investigation; 2022 [cited 2024 Nov 18]. Available from: https://pubmed.ncbi.nlm.nih.gov/36519546/
249. Kwon W, Kim D, Kim HY, Jeong SW, Lee SG, Kim HC, et al. Microglial phagocytosis of polystyrene microplastics results in immune alteration and apoptosis in vitro and in vivo. Science of the Total Environment. 2022 Feb 10;807:150817.
250. Bernardette Martínez-Rizo A, Fosado-Rodríguez R, César Torres-Romero J, César Lara-Riegos J, Alberto Ramírez-Camacho M, Ly Arroyo Herrera A, et al. Models in vivo and in vitro for the study of acute and chronic inflammatory activity: A comprehensive review. Int Immunopharmacol [Internet]. 2024 Jun 30 [cited 2025 Feb 24];135. Available from: https://pubmed.ncbi.nlm.nih.gov/38788446/
251. Chen K, Kolls JK. Interluekin-17A (IL17A). Gene [Internet]. 2017 May 30 [cited 2025 Feb 24];614:8. Available from: https://pmc.ncbi.nlm.nih.gov/articles/PMC5394985/
252. Ross SH, Cantrell DA. Signaling and Function of Interleukin-2 in T Lymphocytes. Annu Rev Immunol [Internet]. 2018 Apr 26 [cited 2025 Feb 24];36:411. Available from: https://pmc.ncbi.nlm.nih.gov/articles/PMC6472684/
253. Gaspar L, Bartman S, Coppotelli G, Ross JM. Acute Exposure to Microplastics Induced Changes in Behavior and Inflammation in Young and Old Mice. Int J Mol Sci [Internet]. 2023 Aug 1 [cited 2025 Feb 28];24(15):12308. Available from: https://www.mdpi.com/1422-0067/24/15/12308/htm
254. Lockman PR, Koziara JM, Mumper RJ, Allen D. Nanoparticle Surface Charges Alter Blood–Brain Barrier Integrity and Permeability. J Drug Target [Internet]. 2004 [cited 2025 Feb 23];12(9–10):635–41. Available from: https://www.tandfonline.com/doi/abs/10.1080/10611860400015936
255. Guan Y, Zhu X, Liang J, Wei M, Huang S, Pan X. Upregulation of HSPA1A/HSPA1B/HSPA7 and Downregulation of HSPA9 Were Related to Poor Survival in Colon Cancer. Front Oncol [Internet]. 2021 Oct 26 [cited 2025 Feb 5];11:749673. Available from: www.frontiersin.org
256. Liebermann DA, Hoffman B. Gadd45 in stress signaling. J Mol Signal [Internet]. 2008 Sep 12 [cited 2025 Feb 5];3:15. Available from: https://pmc.ncbi.nlm.nih.gov/articles/PMC2563007/
257. Shama S, Jang H, Wang X, Zhang Y, Shahin NN, Motawi TK, et al. Phosphatidylethanolamines Are Associated with Nonalcoholic Fatty Liver Disease (NAFLD) in Obese Adults and Induce Liver Cell Metabolic Perturbations and Hepatic Stellate Cell Activation. Int J Mol Sci [Internet]. 2023 Jan 1 [cited 2025 Feb 23];24(2). Available from: https://pubmed.ncbi.nlm.nih.gov/36674549/

258. Hollie NI, Cash JG, Matlib MA, Wortman M, Basford JE, Abplanalp W, et al. Micromolar changes in lysophosphatidylcholine concentration cause minor effects on mitochondrial permeability but major alterations in function. Biochim Biophys Acta [Internet]. 2014 [cited 2025 Feb 23];1841(6):888–95. Available from: https://pubmed.ncbi.nlm.nih.gov/24315825/

259. Yamamoto Y, Sakurai T, Chen Z, Inoue N, Chiba H, Hui SP. Lysophosphatidylethanolamine Affects Lipid Accumulation and Metabolism in a Human Liver-Derived Cell Line. Nutrients [Internet]. 2022 Feb 1 [cited 2025 Feb 23];14(3). Available from: https://pubmed.ncbi.nlm.nih.gov/35276938/

260. Zahednasab H, Balood M, Harirchian MH, Mesbah-Namin SA, Rahimian N, Siroos B. Increased autotaxin activity in multiple sclerosis. J Neuroimmunol [Internet]. 2014 [cited 2025 Feb 23];273(1–2):120–3. Available from: https://pubmed.ncbi.nlm.nih.gov/24984830/

261. Lehto LJ, Albors AA, Sierra A, Tolppanen L, Eberly LE, Mangia S, et al. Lysophosphatidyl Choline Induced Demyelination in Rat Probed by Relaxation along a Fictitious Field in High Rank Rotating Frame. Front Neurosci [Internet]. 2017 Aug 3 [cited 2025 Feb 23];11(AUG). Available from: https://pubmed.ncbi.nlm.nih.gov/28824359/

262. Schmitz G, Ruebsaamen K. Metabolism and atherogenic disease association of lysophosphatidylcholine. Atherosclerosis [Internet]. 2010 Jan [cited 2025 Feb 23];208(1):10–8. Available from: https://pubmed.ncbi.nlm.nih.gov/19570538/

263. Comizio R, Pietrobelli A, Tan YX, Wang Z, Withers RT, Heymsfield SB, et al. Total body lipid and triglyceride response to energy deficit: relevance to body composition models. Am J Physiol [Internet]. 1998 [cited 2025 Feb 24];274(5). Available from: https://pubmed.ncbi.nlm.nih.gov/9612244/

264. Lei S, Sun RZ, Wang D, Gong MZ, Su XP, Yi F, et al. Increased hepatic fatty acids uptake and oxidation by LRPPRC-driven oxidative phosphorylation reduces blood lipid levels. Front Physiol [Internet]. 2016 Jul 12 [cited 2025 Feb 24];7(JUL):195086. Available from: www.frontiersin.org

265. Sylvers-Davie KL, Davies BSJ. Regulation of lipoprotein metabolism by ANGPTL3, ANGPTL4, and ANGPTL8. Am J Physiol Endocrinol Metab [Internet]. 2021 Oct 1 [cited 2025 Feb 16];321(4):E493. Available from: https://pmc.ncbi.nlm.nih.gov/articles/PMC8560382/

266. Lian J, Nelson R, Lehner R. Carboxylesterases in lipid metabolism: from mouse to human. Protein Cell [Internet]. 2017 Feb 1 [cited 2025 Feb 16];9(2):178. Available from: https://pmc.ncbi.nlm.nih.gov/articles/PMC5818367/

267. Zhang X, Li S, Zhou Y, Su W, Ruan X, Wang B, et al. Ablation of cytochrome P450 omega-hydroxylase 4A14 gene attenuates hepatic steatosis and fibrosis. Proc Natl Acad Sci U S A [Internet]. 2017 Mar 21 [cited 2025 Feb 16];114(12):3181–5. Available from: https://pubmed.ncbi.nlm.nih.gov/28270609/
268. Ma Y, Nenkov M, Chen Y, Press AT, Kaemmerer E, Gassler N. Fatty acid metabolism and acyl-CoA synthetases in the liver-gut axis. World J Hepatol [Internet]. 2021 Nov 27 [cited 2025 Feb 16];13(11):1512. Available from: https://pmc.ncbi.nlm.nih.gov/articles/PMC8637682/
269. Hoeks J, Hesselink MKC, Russell AP, Mensink M, Saris WHM, Mensink RP, et al. Peroxisome proliferator-activated receptor-γ coactivator-1 and insulin resistance: Acute effect of fatty acids. Diabetologia [Internet]. 2006 Oct 1 [cited 2025 Feb 16];49(10):2419–26. Available from: https://link.springer.com/article/10.1007/s00125-006-0369-2
270. Tsai TH, Chen E, Li L, Saha P, Lee HJ, Huang LS, et al. The constitutive lipid droplet protein PLIN2 regulates autophagy in liver. Autophagy [Internet]. 2017 Jul 3 [cited 2025 Feb 16];13(7):1130. Available from: https://pmc.ncbi.nlm.nih.gov/articles/PMC5529083/
271. Hardwick JP. Cytochrome P450 omega hydroxylase (CYP4) function in fatty acid metabolism and metabolic diseases. Biochem Pharmacol. 2008 Jun 15;75(12):2263–75.
272. Gervois P, Torra IP, Fruchart JC, Staels B. Regulation of lipid and lipoprotein metabolism by PPAR activators. Clin Chem Lab Med [Internet]. 2000 [cited 2025 Feb 16];38(1):3–11. Available from: https://pubmed.ncbi.nlm.nih.gov/10774955/
273. Tsai TH, Chen E, Li L, Saha P, Lee HJ, Huang LS, et al. The constitutive lipid droplet protein PLIN2 regulates autophagy in liver. Autophagy [Internet]. 2017 Jul 3 [cited 2025 Feb 16];13(7):1130. Available from: https://pmc.ncbi.nlm.nih.gov/articles/PMC5529083/
274. Yen CLE, Stone SJ, Koliwad S, Harris C, Farese R V. DGAT enzymes and triacylglycerol biosynthesis. J Lipid Res [Internet]. 2008 [cited 2025 Feb 16];49(11):2283. Available from: https://pmc.ncbi.nlm.nih.gov/articles/PMC3837458/
275. Yang C, Yuan H, Gu J, Xu D, Wang M, Qiao J, et al. ABCA8-mediated efflux of taurocholic acid contributes to gemcitabine insensitivity in human pancreatic cancer via the S1PR2-ERK pathway. Cell Death Discovery 2021 7:1 [Internet]. 2021 Jan 11 [cited 2025 Feb 16];7(1):1–12. Available from: https://www.nature.com/articles/s41420-020-00390-z
276. Chen Y, Zhang J, Cui W, Silverstein RL. CD36, a signaling receptor and fatty acid transporter that regulates immune cell metabolism and fate. J Exp Med [Internet]. 2022

Jun 6 [cited 2025 Feb 16];219(6):e20211314. Available from: https://pmc.ncbi.nlm.nih.gov/articles/PMC9022290/

277. McLeod RS, Yao Z. Assembly and Secretion of Triglyceride-Rich Lipoproteins. Biochemistry of Lipids, Lipoproteins and Membranes: Sixth Edition. 2016;459–88.
278. Deng X, Wang Q, Cheng M, Chen Y, Yan X, Guo R, et al. Pyruvate dehydrogenase kinase 1 interferes with glucose metabolism reprogramming and mitochondrial quality control to aggravate stress damage in cancer. J Cancer [Internet]. 2020 [cited 2025 Feb 16];11(4):962. Available from: https://pmc.ncbi.nlm.nih.gov/articles/PMC6959030/
279. Gray LR, Sultana MR, Rauckhorst AJ, Oonthonpan L, Tompkins SC, Sharma A, et al. Hepatic Mitochondrial Pyruvate Carrier 1 is Required for Efficient Regulation of Gluconeogenesis and Whole-body Glucose Homeostasis. Cell Metab [Internet]. 2015 Oct 6 [cited 2025 Feb 16];22(4):669. Available from: https://pmc.ncbi.nlm.nih.gov/articles/PMC4754674/
280. Yu S, Meng S, Xiang M, Ma H. Phosphoenolpyruvate carboxykinase in cell metabolism: Roles and mechanisms beyond gluconeogenesis. Mol Metab. 2021 Nov 1;53:101257.
281. Bosshart PD, Kalbermatter D, Bonetti S, Fotiadis D. Mechanistic basis of L-lactate transport in the SLC16 solute carrier family. Nature Communications 2019 10:1 [Internet]. 2019 Jun 14 [cited 2025 Feb 16];10(1):1–11. Available from: https://www.nature.com/articles/s41467-019-10566-6
282. Wang F, So KF, Xiao J, Wang H. Organ-organ communication: The liver's perspective. Theranostics [Internet]. 2021 [cited 2025 Feb 13];11(7):3317. Available from: https://pmc.ncbi.nlm.nih.gov/articles/PMC7847667/
283. Howe LR, Subbaramaiah K, Hudis CA, Dannenberg AJ. Molecular pathways: Adipose inflammation as a mediator of obesity-associated cancer. Clinical Cancer Research [Internet]. 2013 Nov 15 [cited 2024 Dec 1];19(22):6074–83. Available from: /clincancerres/article/19/22/6074/208657/Molecular-Pathways-Adipose-Inflammation-as-a
284. Hoeke G, Kooijman S, Boon MR, Rensen PCN, Berbeé JFP. Role of Brown Fat in Lipoprotein Metabolism and Atherosclerosis [Internet]. Vol. 118, Circulation Research. Lippincott Williams and Wilkins; 2016 [cited 2024 Dec 1]. p. 173–82. Available from: https://pubmed.ncbi.nlm.nih.gov/26837747/
285. Palacios-Marin I, Serra D, Jimenez-Chillarón J, Herrero L, Todorčević M. Adipose Tissue Dynamics: Cellular and Lipid Turnover in Health and Disease. Nutrients [Internet]. 2023 Sep 1 [cited 2025 Feb 13];15(18):3968. Available from: https://pmc.ncbi.nlm.nih.gov/articles/PMC10535304/
286. Wang L, Wang H, Zhang B, Popkin BM, Du S. Elevated fat intake increases body weight and the risk of overweight and obesity among chinese adults: 1991–2015 trends.

Nutrients [Internet]. 2020 Nov 1 [cited 2024 Dec 2];12(11):1–13. Available from: https://pmc.ncbi.nlm.nih.gov/articles/PMC7694029/

287. Zhu X, Zhao L, Liu Z, Zhou Q, Zhu Y, Zhao Y, et al. Long-term exposure to titanium dioxide nanoparticles promotes diet-induced obesity through exacerbating intestinal mucus layer damage and microbiota dysbiosis. Nano Res [Internet]. 2021 May 1 [cited 2024 Dec 23];14(5):1512–22. Available from: https://doi.org/10.1007/s12274-020-3210-1
288. Chen S, Lai SWT, Brown CE, Feng M. Harnessing and Enhancing Macrophage Phagocytosis for Cancer Therapy. Vol. 12, Frontiers in Immunology. Frontiers Media S.A.; 2021. p. 635173.
289. Ohtsuka M, Inoko H, Kulski JK, Yoshimura S. Major histocompatibility complex (Mhc) class Ib gene duplications, organization and expression patterns in mouse strain C57BL/6. BMC Genomics [Internet]. 2008 Apr 17 [cited 2025 Feb 19];9:178. Available from: https://pmc.ncbi.nlm.nih.gov/articles/PMC2375909/
290. Beswick EJ, Reyes VE. CD74 in antigen presentation, inflammation, and cancers of the gastrointestinal tract. World Journal of Gastroenterology : WJG [Internet]. 2009 Jun 21 [cited 2025 Feb 19];15(23):2855. Available from: https://pmc.ncbi.nlm.nih.gov/articles/PMC2699002/
291. Yao Y, Wang Y, Chen F, Huang Y, Zhu S, Leng Q, et al. NLRC5 regulates MHC class I antigen presentation in host defense against intracellular pathogens. Cell Research 2012 22:5 [Internet]. 2012 Apr 10 [cited 2025 Feb 19];22(5):836–47. Available from: https://www.nature.com/articles/cr201256
292. Granados DP, Tanguay PL, Hardy MP, Caron É, de Verteuil D, Meloche S, et al. ER stress affects processing of MHC class I-associated peptides. BMC Immunol [Internet]. 2009 Feb 16 [cited 2024 Dec 9];10(1):10. Available from: https://bmcimmunol.biomedcentral.com/articles/10.1186/1471-2172-10-10
293. Preynat-Seauve O, Coudurier S, Favier A, Marche PN, Villiers C. Oxidative stress impairs intracellular events involved in antigen processing and presentation to T cells. Cell Stress Chaperones [Internet]. 2003 Jun [cited 2025 Feb 19];8(2):162. Available from: https://pmc.ncbi.nlm.nih.gov/articles/PMC514868/
294. Falahatpisheh H, Nanez A, Montoya-Durango D, Qian Y, Tiffany-Castiglioni E, Ramos KS. Activation profiles of HSPA5 during the glomerular mesangial cell stress response to chemical injury. Cell Stress Chaperones [Internet]. 2007 Sep [cited 2025 Feb 19];12(3):209. Available from: https://pmc.ncbi.nlm.nih.gov/articles/PMC1971237/
295. Oslowski CM, Hara T, O'Sullivan-Murphy B, Kanekura K, Lu S, Hara M, et al. Thioredoxin-interacting protein mediates ER stress-induced β cell death through

initiation of the inflammasome. Cell Metab [Internet]. 2012 Aug 8 [cited 2025 Feb 19];16(2):265. Available from: https://pmc.ncbi.nlm.nih.gov/articles/PMC3418541/

296. Geraghty P, Baumlin N, Salathe MA, Foronjy RF, D'Armiento JM. Glutathione Peroxidase-1 Suppresses the Unfolded Protein Response upon Cigarette Smoke Exposure. Mediators Inflamm [Internet]. 2016 [cited 2025 Feb 19];2016. Available from: https://pubmed.ncbi.nlm.nih.gov/28070146/
297. Dubois V, Gheeraert C, Vankrunkelsven W, Dubois-Chevalier J, Dehondt H, Bobowski-Gerard M, et al. Endoplasmic reticulum stress actively suppresses hepatic molecular identity in damaged liver. Mol Syst Biol [Internet]. 2020 May [cited 2025 Feb 19];16(5):e9156. Available from: https://pmc.ncbi.nlm.nih.gov/articles/PMC7224309/
298. Yoshida K, Kusama K, Tamura K, Fukushima Y, Ohmaru-Nakanishi T, Kato K. Alpha-1 antitrypsin-induced endoplasmic reticulum stress promotes invasion by extravillous trophoblasts. Int J Mol Sci [Internet]. 2021 Apr 1 [cited 2025 Feb 19];22(7):3683. Available from: https://pmc.ncbi.nlm.nih.gov/articles/PMC8037753/
299. Yu Y, Liu DY, Chen XS, Zhu L, Wan LH. MANF: A Novel Endoplasmic Reticulum Stress Response Protein-The Role in Neurological and Metabolic Disorders. Oxid Med Cell Longev [Internet]. 2021 [cited 2025 Feb 19];2021. Available from: https://pubmed.ncbi.nlm.nih.gov/34745419/
300. Anderson HA, Englert R, Gursel I, Shacter E. Oxidative stress inhibits the phagocytosis of apoptotic cells that have externalized phosphatidylserine. Cell Death & Differentiation 2002 9:6 [Internet]. 2002 May 24 [cited 2025 Feb 19];9(6):616–25. Available from: https://www.nature.com/articles/4401013
301. Scott RS, McMahon EJ, Pop SM, Reap EA, Caricchio R, Cohen PL, et al. Phagocytosis and clearance of apoptotic cells is mediated by MER. Nature [Internet]. 2001 May 10 [cited 2024 Dec 4];411(6834):207–11. Available from: https://www.nature.com/articles/35075603
302. Nimmerjahn F, Ravetch J V. Fcγ receptors as regulators of immune responses [Internet]. Vol. 8, Nature Reviews Immunology. Nature Publishing Group; 2008 [cited 2024 Dec 10]. p. 34–47. Available from: https://www.nature.com/articles/nri2206
303. Bonten M, Johnson JR, van den Biggelaar AHJ, Georgalis L, Geurtsen J, de Palacios PI, et al. Epidemiology of *Escherichia coli* Bacteremia: A Systematic Literature Review. Clinical Infectious Diseases [Internet]. 2021 Apr 8 [cited 2024 Dec 14];72(7):1211–9. Available from: https://academic.oup.com/cid/article/72/7/1211/5836974
304. Wang H, Kim SJ, Lei Y, Wang S, Wang H, Huang H, et al. Neutrophil extracellular traps in homeostasis and disease. Signal Transduction and Targeted Therapy 2024 9:1 [Internet]. 2024 Sep 20 [cited 2025 Feb 20];9(1):1–40. Available from: https://www.nature.com/articles/s41392-024-01933-x

305. Dulloo AG, Jacquet J, Girardier L. Poststarvation hyperphagia and body fat overshooting in humans: A role for feedback signals from lean and fat tissues. American Journal of Clinical Nutrition [Internet]. 1997 Mar 1 [cited 2024 Dec 13];65(3):717–23. Available from: http://ajcn.nutrition.org/article/S0002916523176441/fulltext
306. Smith KGC, Clatworthy MR. FcγRIIB in autoimmunity and infection: evolutionary and therapeutic implications. Nat Rev Immunol [Internet]. 2010 [cited 2025 Mar 7];10(5):328. Available from: https://pmc.ncbi.nlm.nih.gov/articles/PMC4148599/
307. Voskuhl R. Sex differences in autoimmune diseases [Internet]. Vol. 2, Biology of Sex Differences. BioMed Central; 2011 [cited 2024 Dec 14]. p. 1–21. Available from: https://bsd.biomedcentral.com/articles/10.1186/2042-6410-2-1
308. Fairweather D, Beetler DJ, McCabe EJ, Lieberman SM. Mechanisms underlying sex differences in autoimmunity. Journal of Clinical Investigation [Internet]. 2024 Sep 17 [cited 2024 Dec 14];134(18). Available from: https://www.jci.org/articles/view/180076
309. Tay TL, Mai D, Dautzenberg J, Fernández-Klett F, Lin G, Sagar S, et al. A new fate mapping system reveals context-dependent random or clonal expansion of microglia. Nat Neurosci [Internet]. 2017 Jun 1 [cited 2024 Dec 16];20(6):793–803. Available from: https://www.nature.com/articles/nn.4547
310. Cai Z, Li M, Zhu Z, Wang X, Huang Y, Li T, et al. Biological Degradation of Plastics and Microplastics: A Recent Perspective on Associated Mechanisms and Influencing Factors. Microorganisms [Internet]. 2023 Jul 1 [cited 2025 Feb 25];11(7):1661. Available from: https://pmc.ncbi.nlm.nih.gov/articles/PMC10386651/
311. Wu W, Lu H, Cheng J, Geng Z, Mao S, Xue Y. Undernutrition Disrupts Cecal Microbiota and Epithelium Interactions, Epithelial Metabolism, and Immune Responses in a Pregnant Sheep Model. Microbiol Spectr [Internet]. 2023 Apr 13 [cited 2024 Dec 16];11(2). Available from: https://journals.asm.org/doi/10.1128/spectrum.05320-22
312. Goodrich JK, Waters JL, Poole AC, Sutter JL, Koren O, Blekhman R, et al. Human genetics shape the gut microbiome. Cell [Internet]. 2014 Nov 6 [cited 2024 Dec 16];159(4):789–99. Available from: https://pubmed.ncbi.nlm.nih.gov/25417156/
313. Pan T, Zheng S, Zheng W, Shi C, Ning K, Zhang Q, et al. Christensenella regulated by Huang-Qi-Ling-Hua-San is a key factor by which to improve type 2 diabetes. Front Microbiol. 2022 Oct 12;13:1022403.
314. Venegas DP, De La Fuente MK, Landskron G, González MJ, Quera R, Dijkstra G, et al. Short chain fatty acids (SCFAs)mediated gut epithelial and immune regulation and its relevance for inflammatory bowel diseases. Vol. 10, Frontiers in Immunology. Frontiers Media S.A.; 2019. p. 424615.
315. Gut bacteria may reduce cholesterol and lower heart disease risk | National Institutes of Health (NIH) [Internet]. [cited 2024 Dec 16]. Available from:

https://www.nih.gov/news-events/nih-research-matters/gut-bacteria-may-reduce-cholesterol-lower-heart-disease-risk?utm_source=chatgpt.com

316. Zhu Y, Chen B, Zhang X, Akbar MT, Wu T, Zhang Y, et al. Exploration of the Muribaculaceae Family in the Gut Microbiota: Diversity, Metabolism, and Function [Internet]. Vol. 16, Nutrients. Multidisciplinary Digital Publishing Institute (MDPI); 2024 [cited 2024 Dec 16]. p. 2660. Available from: https://www.mdpi.com/2072-6643/16/16/2660/htm
317. Martín R, Rios-Covian D, Huillet E, Auger S, Khazaal S, Bermúdez-Humarán LG, et al. Faecalibacterium: a bacterial genus with promising human health applications [Internet]. Vol. 47, FEMS Microbiology Reviews. Oxford University Press; 2023 [cited 2024 Dec 16]. Available from: https://dx.doi.org/10.1093/femsre/fuad039
318. Maioli TU, Borras-Nogues E, Torres L, Barbosa SC, Martins VD, Langella P, et al. Possible Benefits of Faecalibacterium prausnitzii for Obesity-Associated Gut Disorders. Vol. 12, Frontiers in Pharmacology. Frontiers Media S.A.; 2021. p. 740636.
319. Lam YY, Ha CWY, Campbell CR, Mitchell AJ, Dinudom A, Oscarsson J, et al. Increased gut permeability and microbiota change associate with mesenteric fat inflammation and metabolic dysfunction in diet-induced obese mice. PLoS One [Internet]. 2012 Mar 23 [cited 2024 Dec 17];7(3):34233. Available from: www.plosone.org
320. Ji ZH, Xie WY, Zhao PS, Ren WZ, Jin HJ, Yuan B. Kombucha polysaccharide alleviates DSS-induced colitis in mice by modulating the gut microbiota and remodeling metabolism pathways. Frontiers in Microbiomes. 2024 Feb 7;3:1341824.
321. Anderson ST, Paschos GK. The role for the microbiome in the regulation of the circadian clock and metabolism. In: Nutritional Epigenomics. Elsevier; 2019. p. 231–48.
322. Lynch JB, Gonzalez EL, Choy K, Faull KF, Jewell T, Arellano A, et al. Gut microbiota Turicibacter strains differentially modify bile acids and host lipids. Nat Commun [Internet]. 2023 Dec 1 [cited 2024 Dec 16];14(1):1–15. Available from: https://www.nature.com/articles/s41467-023-39403-7
323. Un-Nisa A, Khan A, Zakria M, Siraj S, Ullah S, Tipu MK, et al. Updates on the Role of Probiotics against Different Health Issues: Focus on Lactobacillus [Internet]. Vol. 24, International Journal of Molecular Sciences. MDPI; 2023 [cited 2024 Dec 16]. p. 142. Available from: https://pmc.ncbi.nlm.nih.gov/articles/PMC9820606/
324. Herp S, Durai Raj AC, Salvado Silva M, Woelfel S, Stecher B. The human symbiont Mucispirillum schaedleri: causality in health and disease [Internet]. Vol. 210, Medical Microbiology and Immunology. Springer Science and Business Media Deutschland GmbH; 2021 [cited 2024 Dec 17]. p. 173–9. Available from: https://doi.org/10.1007/s00430-021-00702-9

325. Zhang Z, Li D, Xie F, Muhetaer G, Zhang H. The cause-and-effect relationship between gut microbiota abundance and carcinoid syndrome: a bidirectional Mendelian randomization study. Front Microbiol [Internet]. 2023 Dec 22 [cited 2024 Dec 17];14:1291699. Available from: https://gwas.mrcieu.ac.uk/
326. Wu S, Powell J, Mathioudakis N, Kane S, Fernandez E, Sears CL. Bacteroides fragilis enterotoxin induces intestinal epithelial cell secretion of interleukin-8 through mitogen-activated protein kinases and a tyrosine kinase-regulated nuclear factor-κB pathway. Infect Immun [Internet]. 2004 Oct [cited 2024 Dec 17];72(10):5832–9. Available from: https://pmc.ncbi.nlm.nih.gov/articles/PMC517603/
327. Cao G, Cai Z. Getting Health Hazards of Inhaled Nano/Microplastics into Focus: Expectations and Challenges [Internet]. Vol. 57, Environmental Science and Technology. American Chemical Society; 2023 [cited 2024 Dec 18]. p. 3461–3. Available from: https://doi.org/10.1021/acs.est.3c00029
328. Agmon-Levin N, Lian Z, Shoenfeld Y. Explosion of autoimmune diseases and the mosaic of old and novel factors. Vol. 8, Cellular and Molecular Immunology. 2011. p. 189–92.
329. Neeland IJ, Lim S, Tchernof A, Gastaldelli A, Rangaswami J, Ndumele CE, et al. Metabolic syndrome. Nat Rev Dis Primers [Internet]. 2024 Dec 1 [cited 2024 Dec 18];10(1):1–22. Available from: https://www.nature.com/articles/s41572-024-00563-5
330. Mantovani A, Marchesi F, Di Mitri D, Garlanda C. Macrophage diversity in cancer dissemination and metastasis. Cellular & Molecular Immunology 2024 21:11 [Internet]. 2024 Oct 14 [cited 2024 Dec 20];21(11):1201–14. Available from: https://www.nature.com/articles/s41423-024-01216-z

6 Appendix

6.1 List of figures

6.2 List of tables

6.3 **Abbreviations**

PE	Polyethylene
PP	Polypropylene
PS	Polystyrene
PVC	Polyvinyl chloride
PET	Polyethylene terephthalate
MNP	Micro-and nanoplastic
ACs	Apoptotic cells
KCs	Kupffer cells
ROS	Reactive oxygen species
AVs	Alveolar macrophages
HSCs	Hematopoietic stem cells
AGM	Aorta-gonad-mesonephros
PPARδ	Peroxisome proliferator-activated receptor delta
IL-6	Interleukin-6
TNFa	Tumor necrosis factor-alpha
IL-1β	Interleukin-1 beta
IL-13	Interleukin-13
IL-12	Interleukin-12
IL-10	Interleukin-10
oxLDL	Oxidized low-density lipoprotein
ATMs	Adipose tissue macrophages
SR-A	Scavenger receptor class A
CSF1R	Colony-stimulating factor 1 receptor
PAP	Pulmonary alveolar proteinosis
GM–CSF	Granulocyte–macrophage colony-stimulating factor
FGF21	Fibroblast growth factor 21
VLDL	Very low density lipoprotein
GLP-1	Glucagon-like peptide 1
FXR	Farnesoid X receptor
FGF 15/19	Fibroblast growth factor 15/19
RNS	Reactive nitrogen species
NF-κB	Nuclear factor κB
BBB	Blood brain barrier
PRR	Pattern recognition receptors
PAMP	Pathogen-associated molecular patterns
TLRs	Toll-like receptors

CLRs	C-type lectin receptors
NLRs	NOD-like receptors
FcRs	Fc receptors
iRBCs	Infected red blood cells
SLE	Systemic Lupus Erythematosus
MS	Multiple sclerosis
TGFβ1	Transforming growth factor-beta 1
PDGF	Platelet-derived growth factor
NAFLD	Non-alcoholic fatty liver disease
NASH	Non-alcoholic steatohepatitis
EDTA	Ethylenediaminetetraacetic acid
HRP	Horseradish Peroxidase conjugated
ELISA	Enzyme-linked immunosorbent assay
DAPI	4′,6-Diamidino-2-phenylindole dihydrochloride
FBS	Fetal bovine serum
PMSF	Phenylmethylsulfonyl fluoride
RPMs	Red pulp macrophages
MZMs	Marginal zone macrophages
MMMs	Marginal metallophilic macrophages
WPMs	White pulp macrophages
IL-1α	Interleukin-1αlpha
IL-18	Interleukin-18
IL-22	Interleukin-22
IL-23	Interleukin-23
G-CSF	Granulocyte colony-stimulating factor
RANKL	Receptor activator of nuclear factor κb ligand
BAFF	B-cell activating factor
CCL7	C-C motif chemokine ligand 7
CXCL5	C-X-C motif chemokine ligand 5
cDCs	Conventional dendritic cells
NKs	Natural killers
UMAP	Uniform manifold approximation and projection
DEGs	Deferential expressed genes
ORA	Over representation analysis
EB	Evans Blue
i.p.	Intraperitoneal
i.v.	Intravenous
OFT	Open field test

NOR	Novel object recognition
SD	Social discremination
DI	Discrimination index
qRT-PCR	Quantitative Reverse Transcription Polymerase Chain Reaction
PAS-H	Periodic acid-Schiff's with hematoxylin
ORO	Oil-Red-O
HE	Hematoxylin and eosin
TG	Triacylglycerol
TG odd	Triacylglycerol odd-chain
DG	Diacylglycerol
MG	Monoacylglycerol
CE	Cholesterol ester
PA	Phosphatidic acid
PG	Phosphatidylglycerol
PC	Phosphatidylcholine
PC-O	Phosphatidylcholine ether
PE	Phosphatidylethanolamine
PE-O	Phosphatidylethanolamine ether
PS	Phosphatidylserine
LPC	Lysophosphatidylcholine
LPC-O	Lysophosphatidylcholine ether
LPE	Lysophosphatidylethanolamine
Cer	Ceramide
HexCer	Hexosylceramide
DiHexCer	Dihexosylceramide
SM	Sphingomyelin
gWAT	Gonadal white adipose tissue
iWAT	Inguinal white adipose tissue
BAT	Brown adipose tissue
HFD	High-fat diet
CD	Control diet
GTT	Glucose tolerance test
ITT	Insulin tolerance test
AUC	Area under the curve
MHCII	Major histocompatibility complex class II
TIM-4	T-cell immunoglobulin and mucin domain-containing protein 4
snRNA-seq	Single-nuclei RNA sequencing
scRNA-seq	Single-cell RNA sequencing

LSECs	Liver sinusoidal endothelial cells
VECs	Vascular endothelial cells
ER	Endoplasmic reticulum
p.i.	post-infection
DFM	Double fate-mapping (
YFP	Yellow fluorescent protein
tdT	TdTomato
Tregs	Regulatory T cells

6.4 **Contributions**

I acknowledge the important contributions of others to the experiments and figures presented in this thesis:

Frederike Graelmann (University of Bonn, LIMES institute) performed the PAS staining assessment (Figure 20 D), the lipidomics experiment and the initial analysis of the liver FACS data (Figure 5) under my supervision.

Nele Kronau and Theresa Eulgem performed the ORO staining in Figure 21 and Figure 33, respectively, under my supervision.

Katharina Sieckmann (University of Bonn, institute of innate immunity, the lab of Prof. Dagmar Wachten) performed the quantitative RT-PCR on the liver and the AdipoQ analysis on gWAT.

Dr. Katharina Mauel and Marie-Louise Diefenbach-Wilke (University of Bonn, LIMES institute) accessed performing the Malaria infection model (Figure 40).

Dr. Fabrizio Musacchio (DZNE, the lab of Prof. Martin Fuhrmann) performed the behavioral analysis.

Dr. Nelli Blank-Stein (University of Bonn, LIMES Institute) performed the scRNA-seq on the brain and snRNA-seq on the liver.

Dr. Lisa Maria Steinheuer (University of Bonn, Institute for Experimental Oncology, the lab of Prof. Kevin Thurley) performed the analysis of scRNA-seq on the brain and snRNA-seq on the liver.

Dr. Waldemar Seel (Institute of Nutritional and Food Sciences, Bonn university, the lab of Prof. Marie-Christine Simon) performed the microbiome analysis.

6.5 **List of publications**

Makdissi N, Viola M, Steinheuer L, Blank-Stein N, Taveras E, Musacchio F, Sieckmann K, Kardinal R, Deveuve Q, Graelmann F, Mauel K, Kronau N, Thomas J, Bejarano D, Högler S, Yaghmour M, Schultze J, Thiele C, Kenner L, Schlitzer A, Nimmerjahn F, Dagmar W, Fuhrmann M, Thruley K, Mass E. (2025). Size-dependent plastic exposure disrupts macrophage function and tissue-specific metabolism. Nature (preprint). doi: 10.21203/rs.3.rs-6204281/v1.

Makdissi N, Hirschmann D, Frolov A, Sado I, Nikolka F, Cheng J, Blank-Stein N, Viola MF, Yaghmour M, Arnold P, Bonaguro L, Becker M, Thiele C, Meissner F, Hiller K, Beyer M, Mass E. Kupffer cells control neonatal hepatic metabolism via Igf1 signaling. bioRxiv (preprint) doi: 10.1101/2025.02.19.638983

Makdissi N. Macrophage Development and Function. Methods Mol Biol. 2024;2713:1-9. doi: 10.1007/978-1-0716-3437-0_1

Makdissi N, Mass E. Of myeloid cells and fibroblasts-A love story. Immunity. 2021 Jul 13;54(7):1371-1373. doi: 10.1016/j.immuni.2021.06.016

Müller L, Nasr AR, Jux B, Makdissi N, Trowbridge JW, Schmidt SV, Schultze JL, Quast T, Schulte-Schrepping J, Kolanus W, Mass E. Differential impact of high-salt levels in vitro and in vivo on macrophage core functions. Mol Biol Rep. 2024 Feb 24;51(1):343. doi: 10.1007/s11033-024-09295-x

Kayvanjoo AH, Splichalova I, Bejarano DA, Huang H, Mauel K, Makdissi N, Heider D, Tew HM, Balzer NR, Greto E, Osei-Sarpong C, Baßler K, Schultze JL, Uderhardt S, Kiermaier E, Beye M, Schlitzer A, Mass E (2023) Fetal liver macrophages contribute to the hematopoietic stem cell niche by controlling granulopoiesis. elife. 2024 Mar 25:13:e86493. doi: 10.7554/eLife.86493.

Huang H, Splichalova I, Balzer N, Seep L, Franco Taveras E, Radwaniak C, Acil K, Mauel K, Blank-Stein N, Makdissi N, Zurkovic J, Kayvanjoo A, Wunderling K, Jessen M, Yaghmour M, Ulas T, Schultze JL, Liu Z, Ginhoux F, Beyer M, Thiele C, Hasenauer J, Wachten D, Mass E (2023) Developmental programming of Kupffer cells by maternal obesity causes fatty liver disease in the offspring. Nature (preprint). doi:10.21203/rs.3.rs-3242837/v1

6.6 **Acknowledgments**

First and foremost, I would like to express my deepest gratitude to my supervisor, Prof. Dr. Elvira Mass, for her invaluable guidance, continuous support, and insightful feedback throughout my PhD journey. Her mentorship has not only shaped my scientific skills but also inspired me to grow both personally and professionally.

I am equally grateful to the members of my Thesis Advisory Committee, Prof. Dr. Falk Nimmerjahn and Prof. Dr. Martin Fuhrmann. Their constructive suggestions, thoughtful discussions, and critical insights were instrumental in refining the direction of my research and strengthening this thesis.

I further wish to sincerely acknowledge the members of my doctoral committee — Prof. Dr. Elvira Mass, Prof. Dr. Dagmar Wachten, Prof. Dr. Waldemar Kolanus, and Prof. Dr. Martin Fuhrmann — for kindly serving as evaluators of my dissertation and offering their valuable perspectives.

I am also thankful to the Research Training Group 1873 and the Bonner Forum Biomedizin Program for their financial support and dedication to fostering innovative research.

My heartfelt appreciation goes to all members of the Mass Lab for creating a stimulating, collaborative, and supportive environment that has made this journey truly enjoyable and enriching.

In particular, I would like to thank Conny, who has stood by me from the very beginning until the very end. Your unwavering support, care, and willingness to help unconditionally have left a lasting impact on me, both scientifically and personally. I am deeply grateful for everything you have done.

A special thanks to Nelli, Kati, and Eliana— We started this journey side by side, and I firmly believe that you were the cornerstone upon which the lab's foundation was laid. I am grateful that our relationship grew beyond being colleagues, evolving into friendships and a sense of family. I will always cherish the memories and moments we shared.

To Marina—my first student, my NanoGlia buddy, and a dear friend—thank you for your support and for making countless memorable moments, including the infamous “Barbie joke”. Your friendship has been a constant source of joy and motivation.

I would also like to thank Mohamed—moving to a new country and starting fresh can be challenging, but early on, we found a strong friendship that made the transition easier. I am grateful for the support, shared experiences, and the laughs along the way.

Most importantly, I want to express my deepest gratitude to my beloved partner and best friend, Sally. You have been my greatest supporter, the one who believed in me the most, even in moments when I doubted myself. Your unwavering love, encouragement, and

countless sacrifices have made it possible for me to become who I am today. Words cannot fully express how grateful I am for your presence in my life.

And to our wonderful son, Theo—you are my greatest joy and motivation. Every step of this journey has been for you, and I hope to make you proud.